Heriot-Watt University, Edinburgh UK

Doctoral Thesis

Modelling Thin Films and Droplets Using Smoothed Particle Hydrodynamics

Author:
Nowoghomwenma Noel Ehigiamusoe

Supervisor:
Dr. Yeaw-Chu Lee

A thesis submitted in fulfilment of the requirements for the degree of Doctor of Philosophy in the

Department of Mechanical Engineering

Computational Engineering Research Group

School of Engineering and Physical Sciences

November 2017

Declaration of Authorship

I, Nowoghomwenma Noel Ehigiamusoe, declare that this thesis titled, 'Modelling Thin Films and Droplets Using Smoothed Particle Hydrodynamics' and the work presented in it are my own. I confirm that:

- This work was done wholly or mainly while in candidature for a research degree at this University.
- Where any part of this thesis has previously been submitted for a degree or any other qualification at this University or any other institution, this has been clearly stated.
- Where I have consulted the published work of others, this is always clearly attributed.
- Where I have quoted from the work of others, the source is always given. With the exception of such quotations, this thesis is entirely my own work.
- I have acknowledged all main sources of help.
- Where the thesis is based on work done by myself jointly with others, I have made clear exactly what was done by others and what I have contributed myself.

Signed: _____

Date: _____

"Thanks to my solid academic training, today I can write hundreds of words on virtually any topic without possessing a shred of information, which is how I got a good job in journalism."

Dave Barry

"I wouldn't take my life for a heart made of vapour."

Ehigiamusoe Noel

"God will never give a man a finished woman. The male was created by God to create what he wants. The woman you're looking for does not exist, she has to be created. Your job is to take the raw materials you married & cultivate it into the woman you desire."

Myles Munroe Monday

"I can see that your mouth speak that which your heart never command."

Ehigiamusoe Noel

"I am the first to say, that there is still many ways in which Europe need to improve and of the tasks of reforming Europe does not end with yesterdays agreement."

David Cameron

"Any man can treat a lady right for one night, but it takes a great man to treat her right for the rest of her life."

David Avocado Wolfe

"Even if everyone is doing it, wrong is never right. Evil, error and darkness will never be truth, even if popular."

Russel M. Nelson

"How determined are you to win your race?"

Ehigiamusoe Noel

"If making you happy costs me my happiness, I can't afford you!"

Ehigiamusoe Noel

"It's not how much we give, but how much love we put into giving!"

Ehigiamusoe Noel

"When God blesses you financially, don't raise your standard of living. Raise your standard of giving"

Mark Batterson

"A woman's loyalty is tested when her man has nothing, while the man's loyalty is tested when he has everything"

Marriage Couselling

"The greatest threat to freedom is the absence of criticism."

Wole Soyinke

"If someone shows you their true colours, don't try to repaint them."

Power of Positivity

"Never let a day come and go, when you cannot define clearly what you have accomplished."

Pastor Faith Oyedepo

"Life is like riding a bicycle. To keep balance, you must keep moving."

Aibert Einstein

"Begin at the beginning," the King said gravely, "and go on till you come to the end; then stop."

Lewis Caroll, Alice in Wonderland.

"The simplification of anything is always sensational." G.K. Chesterton, (1874-1936).

"It isn?t that they can't see the solution. It is that they can't see the problem." G.K. Chesterton, (1874-1936).

Abstract

The small scale and length of time, in addition to the exciting phenomena (such as the inner processes within the fluid) presented by droplets and thin films, make experimental observations difficult and, thus require the need for computational models capable of reproducing these processes in engineering. Current computational models are dominated by Finite Element and Finite Volume methods; whilst this has advanced to a high level of improvement and understanding, they however, lack the capacity to capture large deformations adequately and applied on complex systems, which is mainly due to its dependence on their mesh requirements. The present research proposed and developed a new method of solving thin films and droplet problems using a full Lagrangian approach known as Smoothed Particle Hydrodynamics (SPH). SPH solves the continuum set of conservation equations and provides the ability to accurately track the fluid or material history throughout its lifetime. The thesis explores and develops new and novel single phase SPH models to reliably treat and handle the dynamic nature of surface tension effects over long simulation time scales. In particular, Intermolecular Interaction Force (IIF), Continuum Surface Force (CSF), Contact Line Force (CLF) and Disjoining Pressure (DP) models are developed and applied on a variety of surface tension dominated flow problems and the results, where possible, are validated against known analytical and experimental findings, which include investigations of droplet oscillation, wetting on substrate, contact angle hysteresis and thin film rivulet flows to highlight the capability of the proposed developed SPH methodology and models. The SPH solver is developed from scratch using C++ to maximise extensibility of the methodology and computational performance.

Acknowledgements

I wish to express my sincerest appreciation and gratitude to my supervisor, Dr. Yeaw Chu Lee for his invaluable and very useful advice and guidance. Your tremendous mentoring spirit have contributed substantially to the successful birthing of this thesis.

I am extremely thankful to my dear wife Mrs Imwenghomwen Lilian Ehigiamusoe for her support, prayers and sacrifices/sleepless nights, words cannot describe how grateful I am. I would also like to thank my siblings, family member and friends for their prayers throughout this period, your love and sacrifice are priceless. I wish to thank also my colleagues in the **Computational Engineering Research Group (CERG)**; Odin Du'Plessis, Alasdair McKean, Peter Szabo, Samat Maxutov and Mehroz Sana. Special thanks to Brother Ife, Onne Ambrose Okpu, Obina Unuoha, Christy Etukudor, Victor Ude and others too numerous to mention, for their moral support.

Finally, I will like to thank all my colleagues at Ambrose Alli University, Ekpoma, University of Benin and friends at the Winner Chapel in Edinburgh: Your encouragement and perfectly timed social breaks are greatly appreciated. I wish to also thank my employer Ambrose Alli University, Ekpoma for recommending me and **Tertiary Education Trust Fund (TETFUND)** of Nigeria for providing the scholarship without which it wouldn't have been possible. Above all, I wish to thank God Almighty for given me the grace to finish this race. To HIM alone be all the Praise and Glory.

List of Publications and Grant Awards

Papers under Peer Review

1. Ehigiamusoe N. N., Maxutov S. and Lee Y. C. Oscillating Droplet Using Smoothed Particle Hydrodynamics, International Journal for Numerical Methods in Fluids, 2017. (Positive feedback received on the 29^{th} of September 2017).

Conference presentation

1. Ehigiamusoe N. N. and Lee Y. C. Droplet Oscillation and Contact Angle Hysteresis using Smoothed Particle Hydrodynamics: The 24^{th} Annual SCI-CSCST Conference on "Novel Materials and Surface for Future Engineering" held at Northumbria University, Newcastle-upon-Tyne, United Kingdom, from 23^{rd} - 24^{th} June 2017.

2. Ehigiamusoe N. N. and Lee Y. C. Simulating Surface Tension of Oscillating Droplet with Smoothed Particle Hydrodynamics: The 7^{th} International Conference on Computational Methods (ICCM) held at Berkeley California, United State of America, from 1^{st} - 4^{th} August, 2016.

3. Ehigiamusoe N. N and Lee Y. C. Surface Tension Dominant flow of Droplet using SPH: 1^{st} Smoothed Particle Hydrodynamics UK Symposium, STFC Daresbury Laboratory, 28^{th} September 2015.

Conference/Workshop attended

1. 12^{th} International SPHERIC/Training Workshop (SPHERIC) held at University of Vigo, Ourense, Spain, from 12^{th} - 15^{th} June 2017.

2. 2^{nd} DualSPHysics Users Workshop held at University of Manchester, United Kingdom, from 6^{th} - 7^{th} December 2016.

3. Attended the 27^{th} Scottish Fluid Mechanics Conference, University of St Andrews, 15^{th} June 2014.

4. GPU computing with CUDA, Heriot-Watt University, 1^{st} - 2^{nd} September 2014.

5. Introduction to High Performance Computing by ARCHER, Heriot-Watt University, 3^{rd} September 2014.

Grant Awards

1. Santander Global Mobility Grant 2017: To attend the 12th International SPHERIC Workshop 2017, held in Spain, between the 12^{th} - 15^{th} June 2017.

2. Annual Fund Grant 2016: To attend the 7^{th} International Conference on Computational Methods (ICCM) held at Berkeley California, United State of America, from 1^{st} - 4^{th} August, 2016.

Contents

List of Figures

List of Tables

Abbreviations

ALE	Arbitrary Lagrangian-Eulerian
BC	Boundary Condition
CFD	Computational Fluid Dynamics
CFL	Courant-Friedrichs-Lewy
CLF	Contact Line Force
CSF	Continuum Surface Force
CSM	Computational Solid Mechanics
DEM	Diffuse Element Method
DPD	Dissipative Particle Dynamics
DSMC	Direct Simulation Monte Carlo
EFG	Element Free Garlekin
EOS	Equation of State
FAS	Full Approximation Storage
FEA	Finite Element Analysis
FEM	Finite Element Method
FDM	Finite difference Method
FLIC	Fluid-in-Cell
FMG	Full Multi Grid
FVM	Finite Volume Method
HVI	High Velocity Impact
IC	Initial Condition
IIF	Inter-particle Interaction Force
ISPH	Incompressible Smoothed Particle Hydrodynamics
LBE	Lattice Boltzmann Equation

MAC	Marker-and-Cell
MD	Molecular Dynamics
MHD	Magnetic Hydrodynamics
MLPG	Meshless Local Petrov-Garlekin
MLS	Moving Least Square
MPM	Mesh-free Particle Methods
MPS	Moving Particle Semi-implicit
MWS	Mesh-free Weak-Strong Form
NRS	Neighbour Range Search
N-S	Navier-Stokes
ODE	Ordinary Differential Equation
PDE	Partial Differential Equation
PIC	Particle-in-Cell
PIM	Point Interpolation Method
RBF	Radial Basis Function
RKPM	Reproduced Kernel Particle Method
SPH	Smoothed Particle Hydrodynamics
WCSPH	Weakly Compressible Smoothed Particle Hydrodynamics
XSPH	Extended Smoothed Particle Hydrodynamics

Physical Constants

Constant Name	**Symbol**		**Constant Value (with units)**
Speed of Light	c_o	=	$2.997\ 924\ 58 \times 10^8$ (ms^{-1}) (exact)
Gravity	g	=	9.81 (ms^{-2})
Density of water	ρ	=	1000.0 (kgm^{-3})
Viscosity of water	μ	=	10^{-3} $(\mathrm{kgm}^{-1}\mathrm{s}^{-1})$
Kinematic viscosity of water	ν	=	10^{-6} $(\mathrm{m}^2\mathrm{s}^{-1})$
Surface tension coefficient of water	σ	=	0.0728 (Nm^{-1})

Symbols

Symbol	Name	Unit
B_O	Bond number	mkg^{-1}
p	Pressure	Pa
V	Volume	m^3
h	Smoothing length	m
I	Unit tensor	
m	Particle mass	kg
N	Number of particles	
$\mathbf{q}$	Heat flux	$\mathrm{J/m^2s}$
Re	Reynolds number	
t	Time	s
Δt	Time stepping	s
T	Temperature	K
e	Internal energy	J/kg
L_x	Length of substrate	m
H_y	Height of source	m
$\vec{\mathbf{v}}$	Particle velocity	m/s
v_{in}	Inlet flow rate velocity	m/s
W	Smoothing function	m^{-3}
$\mathbf{r}$	Particle position	m
dx	Initial particle separation in X-axis	m
dy	Initial particle separation in Y-axis	m
P	Power	W (Js^{-1})

ω	Angular frequency	rads^{-1}
η_d	Dynamic viscosity	kg/m s
ν	Kinematic viscosity	m^2/s
ρ	Particle density	$\mathrm{kg/m}^3$
σ	Surface tension coefficient	N/m
μ	Viscosity	kg/m s
τ	Viscous stress tensor	$\mathrm{kg/m\ s}^2$
ψ	Inclination angle	$^\circ$

Dedications

To my children,

Nowoghomwenma Jessica, Desmond, Michael, and David.

To the memory of my beloved late parents,

Pa Ogbonmwan Ehigiamusoe and Mrs Ehigiamusoe
Omosumwen Janet

Chapter 1

Introduction

> "Begin at the beginning," the King said gravely, "and go on till you come to the end; then stop."
>
> Lewis Caroll, Alice in Wonderland.

1.1 Background

A thin film or droplet flow is a layer of material ranging from fractions of a nanometer (monolayer) to several micrometers in thickness or diameter. They are composed of common liquid such as water or oil, rheological complex materials such as polymers solution or melts or complex mixtures of phases or components. These thin film or droplet entities are ubiquitous in nature and technology, so an understanding of their mechanics is important in applications [3] such as Engineering, Biophysics, Geology and Physics, when they are subjected to the action of various mechanical, thermal or structural factors, they exhibit interesting dynamic phenomena.

Some examples of these phenomena are wave steeping, wave propagation and development of chaotic response [4], erection of hole, spreading of front and development of fingers [5, 6], gravity current under water or lava flows [7–12] membrane as linings in mammalian lungs [13–15], tear film in the eye [5, 16]. Now, what is making this phenomenon exciting, is the present of surface tension acting at the free-surface and which is having a dominant force compared to other internal forces, thus making it have greater impact on the shape and properties of the flow.

To model this surface tension force, accurate prediction of fluid-fluid and fluid-solid interactions are required. Multiphase multicomponent flows are encountered in many applications, with their numerical continuum-scale modelling complicated by the strong non-linearity of the Navier-Stokes (N-S) equation describing the flow [17]. Like for instance, the fluid-solid interaction of molecules present additional challengers because their molecule interaction cannot be adequately describe by the standard (no slip) boundary conditions commonly used in conjunction with the Navier-Stokes equation for simulating the fluid dynamics. Hence in dealing with thin film and droplet modelling, it is necessary to simplify the analysis, but the develop analysis must still have some of the important physical properties of the origin problem.

One sure way of doing this is to adapt the Smoothed Particle Dynamics (SPH) methodology (see the work of Liu [18]). It is a mesh free, Lagrangian based formulation that was originally devised independently by Gingold & Monaghan and Lucy in the late seventies for modelling astrophysical phenomena for compressible flow, but was later extended to truly incompressible flow as a result of improvement in the method. SPH is a method for obtaining approximate numerical solution of the equations of fluid dynamics by replacing the fluid with a set of particles; these set of particles possess material properties and interact with each other within the range controlled by a weighted or smoothing kernel function and these particles are now used in turn to discretise the governing equations. Due to SPH mesh free nature, it is ideal for solving fluid flow phenomena with moving interfaces and complex shape. The most attractive features of SPH are its abilities to naturally handle problems with extremely large deformations [19] and changes in morphology [20, 21], which are the reasons it is being used here to explore thin film and droplet phenomena.

1.2 Aims and Objectives

The present work aims to improve the capabilities for modelling thin film and liquid droplet with the novel Lagrangian based approach of SPH to elevate limitations imposed by the traditional grid based lubrication approximation approaches. The key objectives of this study are listed below:

1. To develop an efficient capable Smoothed Particle Hydrodynamics solver from scratch which most be written in C++ programming language.

2. To validate the developed solver and bench-mark against known numerical/theoretical results before a droplet flow over a topography is undertaken.

3. To check the capability of the solver for modelling and handling surface tension in single-phase flow correctly in two-dimensions.

4. To incorporate accurate prediction of curvature formulation for single-phase in two-dimensions.

5. To implement the modified contact line force (CLF) model for single-phase in Smoothed Particle Hydrodynamics to contact angle control in two-dimensions.

6. To implement the disjoining pressure model for single-phase for the first time in Smoothed Particle Hydrodynamics for contact angle control in two-dimensions.

7. To implement the modified IIF model for single-phase in Smoothed Particle Hydrodynamics for contact angle hysteresis and for the first time in thin film flow in two-dimensions.

Chapter 2

Background

"Everything has been thought of before, but the problem is to think of it again."

Johann Wolfgang Goethe, (1749-1832).

This chapter sets out the relevant background on literature review for this work.

2.1 Surface Tension

For a long time now, detergent and soap have been known to mankind. The Babylonian clay cylinders have the earliest evidence dating back from 2800 BC of the use of the soap-like substance. The ingredients for making soap which consist of water, cassia oil and alkali were written on a Babylonian clay tablet around 2200 BC. Also, capture in 1550 BC is the ancient Egyptian who bathed frequently with a soap-like substance made from vegetable and animal oils mixed with alkali salts. The Soap got its name from Mount Sapo which is an ancient Romans place where animals are sacrificed. When rain washes down the mountain a mix of animal tallow and wood ash goes into the clay soil, a women discovered that it is easier to clean the clothes with this soap [22]. In 79 AD, a bar of scented soap factory was established in the ruin of Pompeii, while in the 19th century, Pierre Simon and Thomas Young introduced surface tension phenomenon, which is known to be responsible for the cleaning of the

clothes. Figure 2.1 illustrate the physical origin of surface tension, where molecules at the free surface are unhappy due to missing half of their cohesive interactions, thus leading to the liquid molecules having an unfavourable energy state.

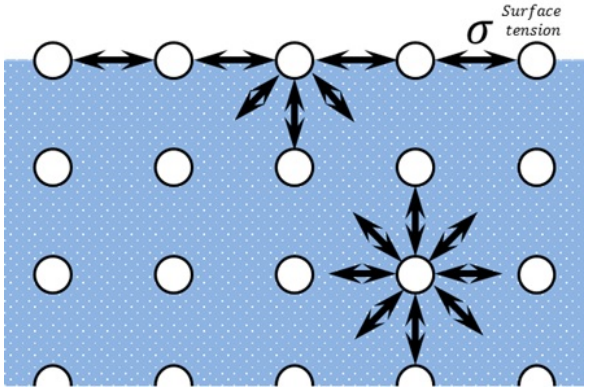

FIGURE 2.1: The hungry molecule at the free-surface due to its missing half cohesive interactions leading to unfavourable energy state.

Intermolecular force of attraction that molecules of liquid exert on one another is majorly responsible for surface tension effect and this is described as the attractive force or stickiness between molecules of the same fluid which is called cohesive forces. However, if the attraction is between unlike molecules, like liquid will often make contact with solid, such as glass, then additional forces of attraction this time is coming into play, which is called adhesive forces. Now, at the bulk (interior) of the fluid (see Figure 2.1), the molecules experience an attractive force equally in every direction by its neighbouring molecules, thus giving a resultant force effect of zero. However, for those molecules located at the surface which lack some neighbouring molecules, they experience unbalance forces that are pulling them into the medium (fluid). This is the basic reason why liquid adjust their shape in order to expose the minimum possible surface area [22], for instance, in the absence of gravity, water forms a homogeneous spherical droplet as can be seen in Figure 2.2. The free surface of this liquid droplet where surface tension phenomenon occurs is a visible intermix or skinning boundary layer between liquid and gas (for instance air) with a thickness of roughly a few molecular diameter [23].

2.1.1 Mechanical Definition

There are two form by which surface tension present itself, first is surface energy and second is a surface force. In the case of surface energy, which is important for creating surfaces, work is required to do this. The Figure 2.3 below illustrate what

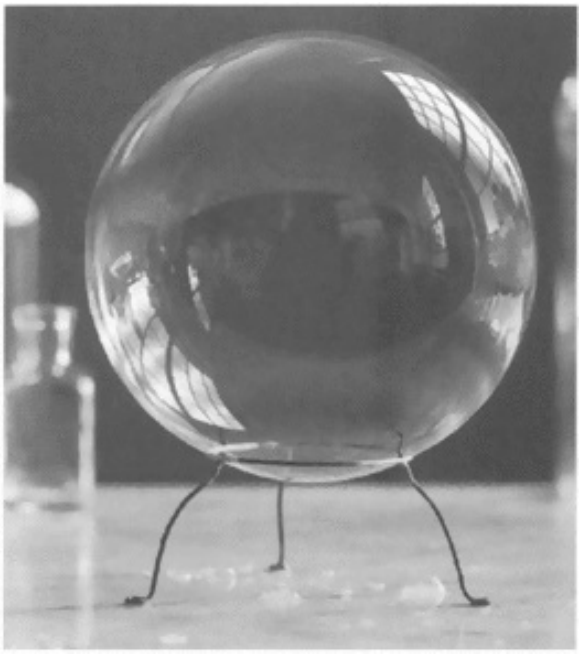

FIGURE 2.2: The homogenous spherical droplet [24].

happened when a metal frame tie with a moving string is immersed into a soap solution. Immediately the metal frame is removed from the soap solution, a soap film is created between the frame and the string, which pull the movable string inward, trying to minimise the surface area as a result of surface tension.

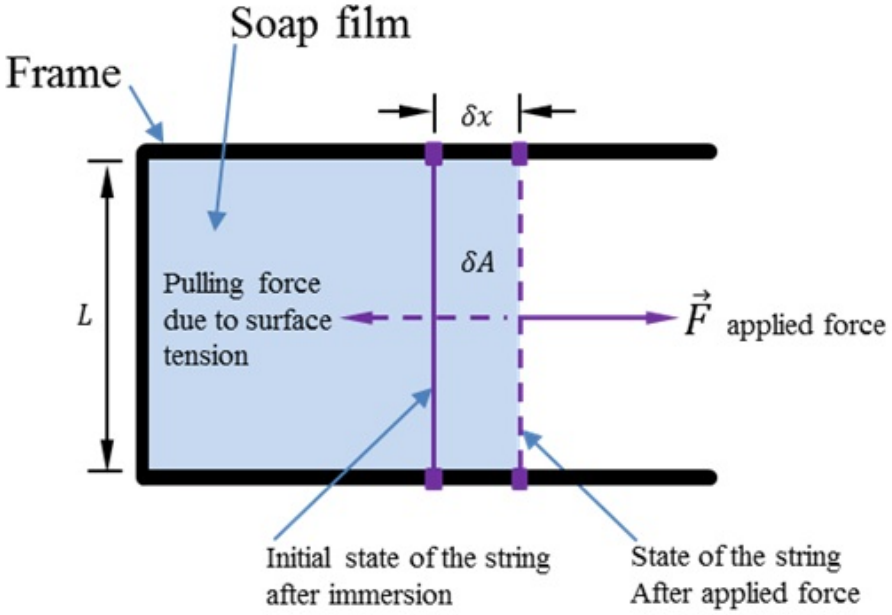

FIGURE 2.3: The soap film exerting a force on the string thus minimising the surface area.

Now, if a force ($\vec{\mathbf{F}}$) is applied to the movable string in the direction (dash line) shown, then work is done to increase the surface area, which upon release, the soap film pulls it back in the direction (solid line) shown, thereby decreasing the surface area again. This work done is proportional to the number of molecules pulled to the additional surface area which can be represented mathematically as follows:

$$\delta W = \sigma \delta A, \tag{2.1}$$

where σ with unit (mN/m^2) is the surface (or interfacial) tension, $\delta W$and δA are the work done and change in surface area respectively. The increase area δA from Figure 2.3 is given as follows:

$$\delta A = L \delta x. \tag{2.2}$$

Now, from Figure 2.3, it can be seen that this following formulation hold:

$$\delta W = \vec{\mathbf{F}} \delta x, \tag{2.3}$$

where δW is the work done by pulling the string from the initial position (solid line) to the new position (dash line) with the force ($\vec{\mathbf{F}}$). So, therefore it follows that:

$$\vec{\mathbf{F}} = \sigma L. \tag{2.4}$$

It is possible to achieve more complex soap/water films by using different complex frames such as spiral, hanging chain and cubic shape like the one shown in Figure 2.4.

Looking at the ideas of surface tension (σ) as having a shrinking interface (see Figure 2.5) that creates a pressure difference between the environment and the liquid droplet, the force due to this pressure difference $\pi r^2 \Delta p$ and that of surface tension $2\pi r\sigma$ can be in equilibrium as follows:

$$\begin{aligned} \pi r^2 \Delta p &= 2\pi r \sigma, \\ \Delta p &= \frac{2\sigma}{r}. \end{aligned} \tag{2.5}$$

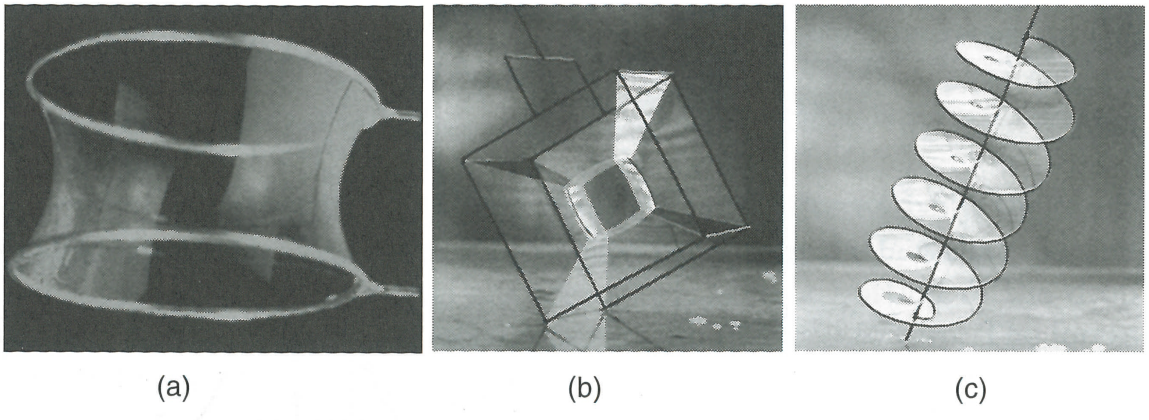

FIGURE 2.4: The soap film on complex frame. (a) Hanging (b) Cubic (c) Spiral frames respectively [24]

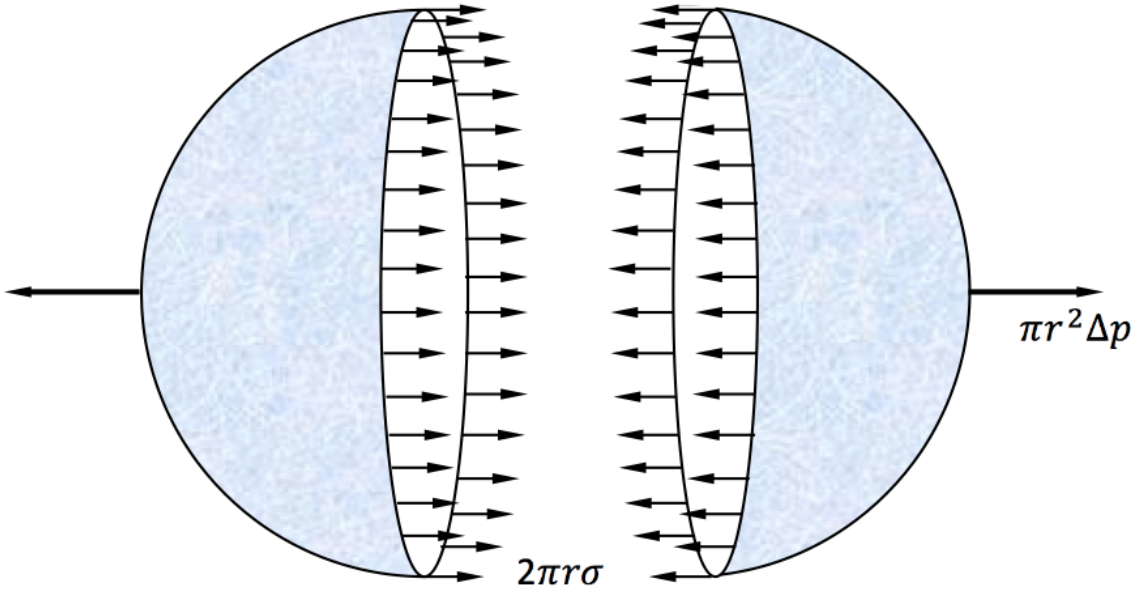

FIGURE 2.5: The surface tension force $2\pi r\sigma$ along the circumference of a spherical droplet. This force is balanced by the pressure difference $\pi r^2 \Delta p$, since the droplet is at equilibrium.

If a soap bubble with spherical shape is involved, then the above equation becomes the popular well-known equation of Young and Laplace, given as:

$$\Delta p = \frac{4\sigma}{r} \quad \text{if soap bubble thickness is negligible,} \tag{2.6}$$

$$\Delta p = \sigma\left(\frac{1}{r_1}+\frac{1}{r_2}\right) \quad \text{if the soap bubble has thickness,} \tag{2.7}$$

where r_1 and r_2 represent the principal radii of the curvature of bubble surface. From the above equation, it is clear that as the radius becomes smaller, the corresponding pressure increases. To demonstrate this effect, two different sized bubbles connected together as seen in Figure 2.6, will experience the discharge of the smaller bubble drop into the bigger bubble drop because it is at a higher pressure. Practically, this phenomenon is useful in the industry where oil mixes with water to form an emulsion, where smaller drop vanishes into bigger drop due to their higher pressure becoming thermodynamically unstable.

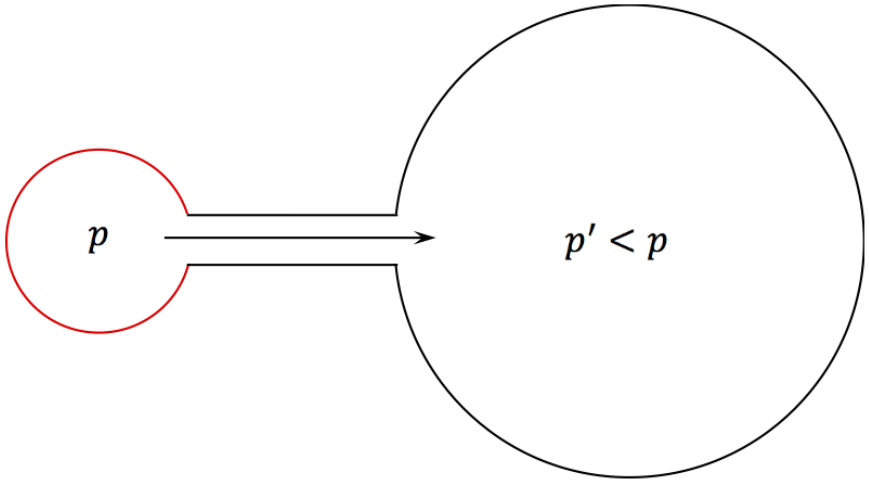

FIGURE 2.6: The smaller bubble vanishing into the large bubble due to its high pressure compared to large bubble with low pressure.

Surface tension as a force has a remarkable effect in nature, which makes it possible for most insects and spider to walk on the water surface. The water surface acts like an elastic membrane that stretches similar to the skin of a drum, with the strength of the membrane varying depending on the different liquids used e.g. it is far less in soapy water than in pure water, thus allowing the insects to walk on the surface without getting wet. The weight of these insects is supported mainly by surface tension while buoyancy which is necessary for floating objects, in this case, is negligible. However, had the water be polluted with detergent, these insects would have been drown due to lower surface tension resulting from the presence of detergent in the water. Figure 2.7 (a) shows the picture of a spider walking on water surface because it is supported by a strong elastic membrane which exerts a set of forces (see Figure 2.7 (b)) at

each point on the surface that is either parallel or at an angle to the surface. This phenomenon is replicated in the floatation of some tiny dense objects say needle/blade on the water surface provided that the object has the right shape. Due to the surface membrane, there are cohesive forces which act between molecules of the substance without chemical bonding. Substances that reduce the surface tension of liquid are called surfactant. Once few drop of detergent is added to the water, the needle or blade sink instantly due to the presence of surfactant in the washing liquid.

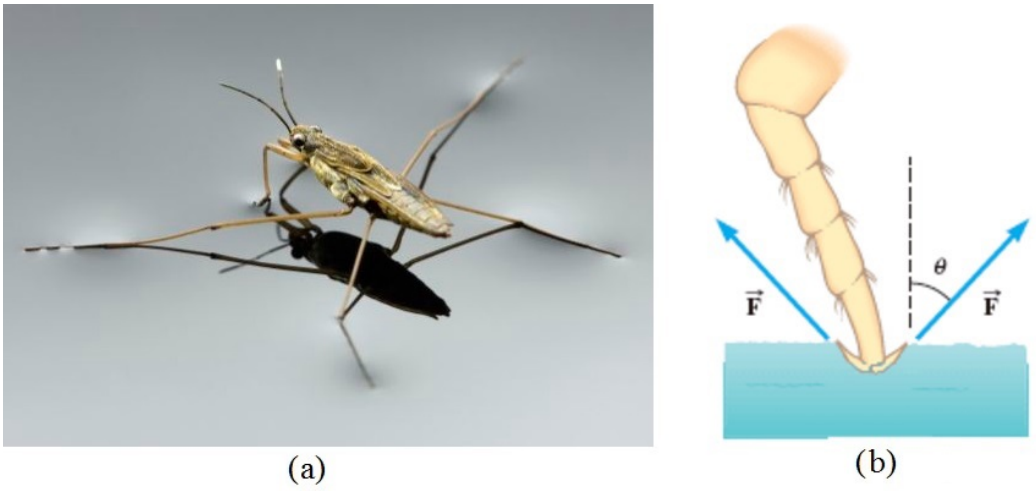

FIGURE 2.7: (a) The spider walking on the water surface due to surface tension (b) An exploded view of the forces acting on the water surface: [24].

From the above, surface tension phenomena, in general, can then be defined as "any fluid surface with an elastic tendency which makes it to acquire minimum surface area possible". In other words, the fluid surface behaves as if it is covered with an elastic stretched membrane, thus setting up an unbalance force which result in tension at the surface. Its dimension is either force per unit length or energy per unit area and they are equivalent to each other. Surface or interfacial tension has become a constant controlling and measuring variable in many industrial processes for deciding the quality of a product. A very good example is the use of pesticide in leaves, whereby the retention time is necessary in order to have good result. The pesticide must stay on the leafs for a certain amount of time to have the desire effect. Also, in the protecting of metals or concrete from rust or penetration by water are some of the other areas of application in the industries.

2.1.2 Marangoni Forces

Once the surface tension of any interface is varied, there will be a tangential (shear) force created and this effect is called Marangoni force [25, 26]. This effect could come from temperature variation or inhomogeneous material properties which have to do with the chemical concentration at the interface. There is a direct relationship between surface tension and temperature. Generally, surface tension decreases with increasing temperature and this is one of the reasons why hot water is preferred for washing clothes and ourselves than cold water. Liquid at rest will always be set in motion by the presence of shear surface force unless it is balanced by other forces. To illustrate Marangoni effect, a soap-powered boat toy which is made from a piece of cardboard, wood or polystyrene is cut out in a shape as shown in Figure 2.8. The toy boat is driven around the water surface by a piece of soap or camphor drop or hang at the rear end (indicated by letter r). As the soap or camphor dissolved, the surface tension of the water surface behind the boat is lower, thus creating an unbalance larger surface tension at the front end (indicated by letter f) which pulls the boat forward. This exciting phenomenon will certainly come to an end when the soap or camphor concentration all over the water surface will be the same.

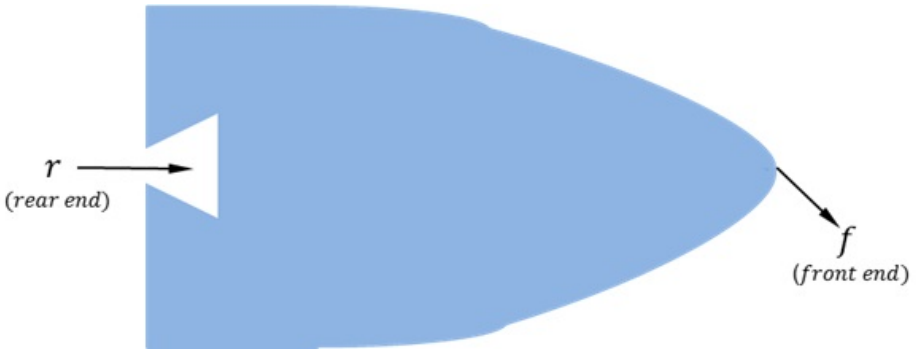

FIGURE 2.8: Shape of a toy boat with pea at the rear end fitted with soap or camphor.

However, this effect will not be observed if a static soap bubble under gravity is involved. This is due to the elastic reaction by the soap bubble skin which stretches once there is a variation in surface tension in order to balance variation that has just happened. As previously mentioned, the temperature increases significantly as the surface tension decreases [27] and this is shown in Figure 2.9, where a linear graph is noticed. The surface tension of water is 0.0728 Nm^{-1} at 25^{o}C, which is a force of 0.0728 N required to break a 1 m long water surface, provided the operating temperature is 25^{o}C. More details about the effect of temperature on surface tension

can be found in the literature [28, 29]. Also, the surface tension of various liquids at room temperature and some molten metals at their melting temperature [30] is shown in Table 2.1.

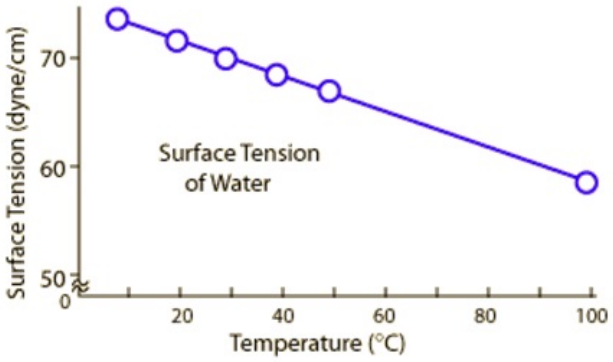

FIGURE 2.9: Graph of surface tension against temperature [31].

TABLE 2.1: (a) Surface tension of different liquids at 20^{o}C and Metals at melting point [31].

Liquid/air, σ	**mNm**$^{-1}$
benzene	28.1–29.03 (28.88)
ether	16.96
ethanol	22.52
n-heptane	20.40
mercury	476.0
n-pentane	16.0
Metals, σ	**mNm**$^{-1}$
Caesium	70
Platinum	195
Gold	197
Aluminium	914
Silver	966
Titanium	1650
Iron	1872
Tungsten	2500

The tears of wine phenomena are the first Marangoni flows considered by James Thomson in 1855. The phenomenon called tears of wine is observed as a clear liquid ring appearing close to the top of a glass of wine, from which droplets constantly

form and the drop keep falling back into the wine. It is mostly common with wine containing high alcoholic content. It is also sometimes referred to as church windows, curtains, or wine legs. Now, wine generally is a mixture of alcohol and water with the alcohol having a lower surface tension than water. If alcohol is mixed with water non-uniformly, the region of lower concentration of alcohol will pull on the surrounding fluid more strongly than the region of higher alcohol concentration, i.e. the fluid tends to move away from the region of higher alcohol concentration. This is demonstrated by spreading a thin film of water on a smoothed surface and allowing a drop of alcohol to fall at the center of the film. Immediately, the drop of alcohol touching the thin film, the liquid at that region will gush out.

A similar effect happens, when the wine is poured into a glass cup just like the one shown in Figure 2.10. At the region where the wine meets the side of the glass, the liquid begins to climb the side of the glass due to capillary action. As this happen, both alcohol and water evaporate from the climbing film, but with the alcohol evaporating faster due to its higher vapour pressure. This lead to decrease in the concentration of alcohol with a corresponding increase in the surface tension of the liquid, thereby causing more liquid to be drawn up from the bulk of the wine, which is at a higher concentration of alcohol having lower surface tension. This makes the wine to move up the side of the glass to form a droplet which falls back due to its own weight. The intensity of this phenomenon is largely based on the alcoholic content, which can be eliminated totally by covering the wine glass, so as to prevent the alcohol from evaporating. Sometimes, the sweetness or quality of a wine is judged by this effect and may find it use in a technical application such as moving the water droplet around.

2.1.3 Wetting of Interfaces

Apart from the interface between liquid and air, which have been examined previously, the interface between liquid and liquid or liquid and solid pose another interesting phenomenon. To illustrate this, let consider an oil lens over water as shown schematically in Figure 2.11.

In order to represent the contact line of the three-phase, the surface tension per unit length will be denoted with σ_{12}, σ_{13}, σ_{23} while the corresponding angles will be θ_1, θ_2, θ_3 respectively between the phase. For the three-phase to be in equilibrium, the following conditions must be satisfy, that is:

FIGURE 2.10: Tears of wine on the glass cup [32].

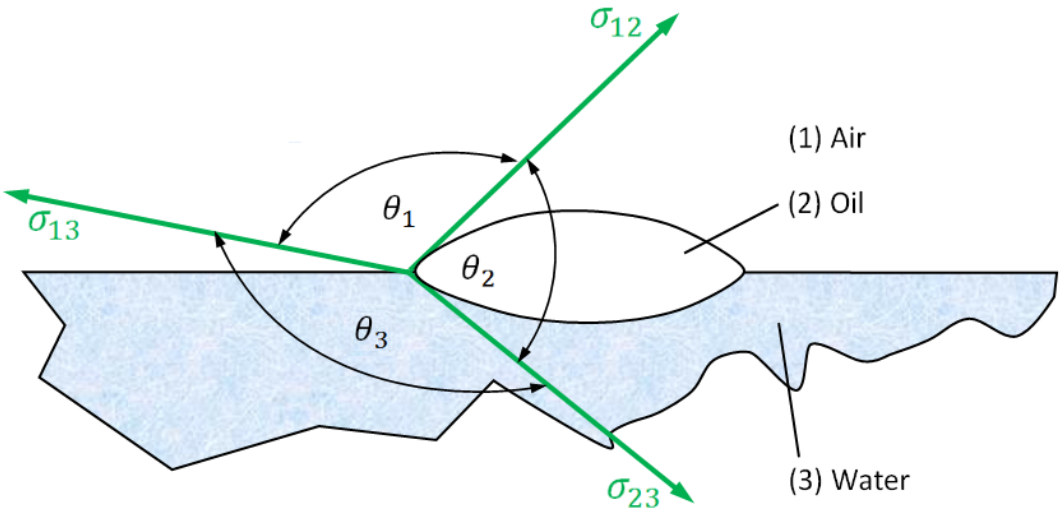

FIGURE 2.11: Triple point of oil lens on water surface.

$$\frac{\sin\theta_1}{\sigma_{12}} = \frac{\sin\theta_2}{\sigma_{23}} = \frac{\sin\theta_3}{\sigma_{13}}. \tag{2.8}$$

The above equation (2.8) comes from the application of sine law to the triangle generated by the three surface tension forces at the contact line. Now, the contact angle is the most important single parameter that describe the interaction between fracture surfaces (rough surface) and the flowing liquid. Also the contact angle, which a motionless liquid drop makes with a substrate is a demonstration of the symmetry between adhesive and cohesive forces. Furthermore, the equilibrium (intrinsic) contact angle of a liquid on a pure and molecularly uniform surfaces (e.g., surface of mineral grains) is a function of the interplay between the liquid-vapour, solid-liquid, and solid-vapour interfacial energies [33]. Lets consider the interaction between the liquid and solid, with the liquid drop making an angle θ (contact angle) with the smoothed solid substrate as show schematically in Figure 2.12.

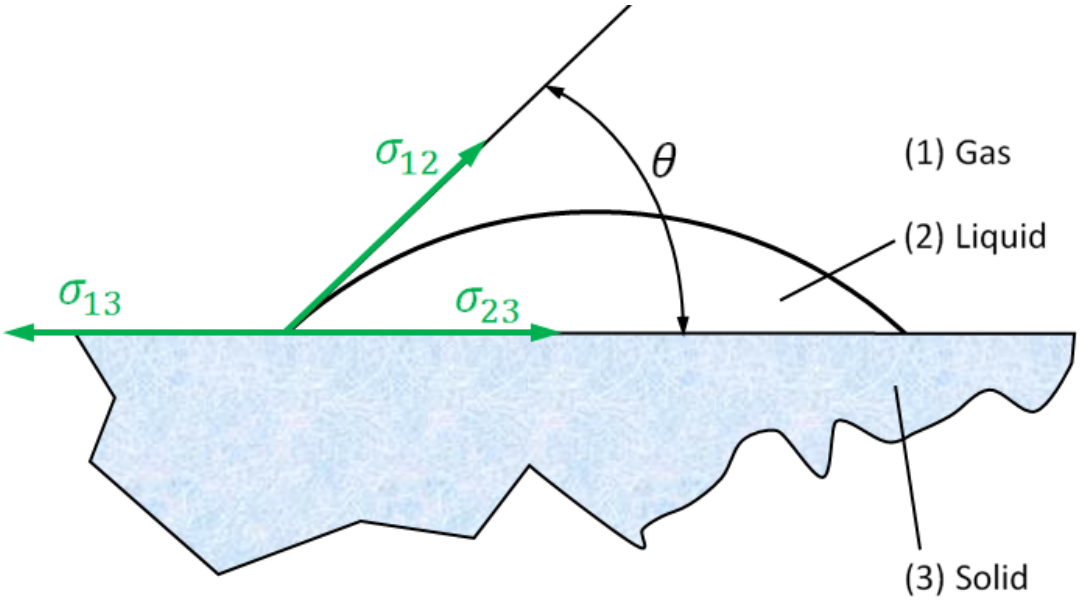

FIGURE 2.12: Liquid drop on smooth substrate.

However, most normal surfaces including rupture faces (rough surface) are neither clean nor smooth, and the solid-vapour and solid-liquid interfacial energies are not homogeneous throughout the surfaces. Therefore, the supposed contact angle a liquid makes with a geometrically and/or chemically heterogeneous surface is deemed different from the inherent values [33]. Now, following Young's relation, the equilibrium equation describing the horizontal component of the three forces per unit length along the contact line at the triple point can be given as:

$$\sigma_{13} = \sigma_{23} + \sigma_{12} \cos\theta. \tag{2.9}$$

Although this equation (2.9) initially faced serious divert opinion by Bikerman [29], because Young's only expressed his ideas in words without any proof of hypotheses. However, with further research, it has become the most pioneering formulation up to date [34], with the contact angle between the three phases been determined by the physical and chemical characteristic of each phase. Furthermore, depending on the magnitude of the contact angle, it is possible to have total wetting (total spreading with $\theta \approx 0^o$), partial-wetting (partial spreading with $0 < \theta < 180^o$) and non-wetting (complete non-spreading with $\theta \approx 180^o$) with applications in [35, 36]. With better understanding of wetting phenomenon, it is possible to turn wettable substrate to non-wettable substrate. Lets take for example, water spreading ordinarily when placed in glass, but if this glass is coated with a thin fluorinated layer like Teflon, then the glass (Teflon) becomes a non-wettable glass when water is pour on it. Details of this phenomenon will be discussed fully in Chapter 6. Wetting have numerous significant applications in the industry and also in our daily life, some of the examples are summarized in Table 2.2.

TABLE 2.2: Areas of wetting application in industries [35, 36].

1. The climbing liquid in plants.
2. Anti-frosting.
3. Automobile industry (processing tyres against slippery road and glasses against the de-wetting of water.
4. Chemical industry (paints, ink, coating etc).
5. Soil science (absorption of liquid in porous media).
6. Construction industry (protecting metals and concrete from water).

2.1.4 Thin Films, Rivulets and Droplets

Droplets and thin films entities are ubiquitous in nature and technology [3]. A fluid is defined as a substance that cannot support shear stress in static equilibrium or more intuitively, a substance that flow because it cannot resist deformation [37]. In order to keep it in place, it have to be kept in tank or other container, which explain the

reason why the interaction of fluids with solid boundaries plays a major role in fluid simulation. Solid (or liquid) body, which exhibits a significantly lower geometrical extension in one dimension than in the remaining two spatial dimensions, is called thin film. The properties of this film or coating have to differ significantly from that of bulk. A thin film substrate is a layer of material applied with thin film technology. A substrate is an underlying material or layer of material upon which other materials or processes are carried out [38]. Thin film finds application in many fields of endeavour like engineering, geology, geophysics, volcanology, spray coating, printing, biophysics and fabrication integrated circuit and photovoltaic (See Table 2.3 below for more details). For example in the LCD application, the fabrication of this display requires conductive, transparent, and luminescent or fluorescent films as well as dielectric and insulating layers to be deposited on the substrate whereas in the case of optical memories, it requires the deposit of organic polymer materials as a storage media and protective overcoats [39]. On the other hand, a drop or droplet is a little pile of liquid that is partially or entirely covered by free surfaces. It can be formed by the accumulation of liquid at the bottom end of a tube or other surface boundary, thus resulting in a hanging drop called pendant drop. Once this drop exceeds a certain size, it becomes unstable and will then detached itself. They may also be formed by vapour condensation or atomization of bigger mass of liquid. Generally, because liquid exhibit surface tension, they are able to form droplet. Details of the effect of surface tension has been discussed in Section 2.1.

So many researchers have worked on thin film or falling films either as under gravity, rivulet or droplet. Gaskel *et al.* [40] studied the gravity-driven flow of continuous thin liquid films on non-porous substrate with topography. In their work, a range of two and three dimensional problem were explored by using an efficient multi-gird solver to analyse the domain and then obtain solution which are in excellent agreement with the experimental results of Decre and Baret [41]. Liu *et al.* [42] also look on experimental investigation into three-dimensional (3-D) secondary instabilities of falling flowing films to understand the transition to complex disorganized patterns, they came up with some qualitative agreement, but concluded that many of their observations need to be interpreted. Huppert [8] worked on silicon oil release under viscous gravity current on an incline rigid plane using the lubrication-theory approximation approach with the major aim of determining the theoretical spreading considerations and shapes of this two-dimensional and axisymmetric flow. Their theoretical results agree well with the experimental findings by Didden & Maxworthy [43]. Fermigier *et al.* [44] study both the experimental and theoretical evolution of a two-dimensional patterns

of a detailed geometry of the Rayleigh-Taylor instability of silicon oil but this time underside of a horizontal plane and overlying a fluid of lower density (gas) by first using the lubrication hypothesis and then deriving an evolution equation for the interface. They observed that the nonlinear growth cause by this instability leads to the development of pattern with distinct symmetries, only at very short time agreed well with literature [45], however at large time they concluded that the resulting secondary instability will need to be investigated further.

Veremieiev *et al.* [7] looked at inertial thin film flow on planar surfaces featuring topography for both two and three dimensions by employing a staggered mesh arrangement for the dependent variable and then solving the resulting equation set with an efficient full approximation storage (FAS) algorithm and full multi grid (FMG) technique together with error controlled automatic adaptive time-stepping and proper treatment of the associated nonlinear convective terms. Their results were found to be in agreement with experimental data and predictions from the finite element analysis.

In another situation, Baxter *et al.* [47] however studied three dimensional thin film flows over and around an obstacle on an incline plane by using the boundary element method in which the work of Blyth and Pozrikidis [48] was extended in order to get the analysis for film flow over and around large obstacle. This they made possible by using the Hermitian radial basis function (RBF) in their implementation. Thiele and Knobloch [49] consider thin liquid films on a slightly incline heated plate and observed that at sufficiently large Marangoni number, the film breaks up into a periodic array of drops, which slide down the substrate when the substrate was slightly incline. Their results were compared with that of VanHook *et al.* [50] who studied long-wavelength surface-tension-driven Benard convection both experimentally and theoretically, where they used a two-layer model to developed a two-layer nonlinear theory capable of predicting deformation effect on the interface temperature profile; and that depending on the thin liquid depths, the experimental results were in good agreement with their developed model than the one-layer model. Comparison were also made with A. Oron and S. G. Bankoff [51, 52] who worked on the de-wetting of a heated coated solid surface by an evaporating liquid film under conjoining/disjoining pressures by using the attractive and repulsive molecular forces governed by the 3-4 power-law potential, as against the Lennard-Jones 3-9 potential. Their major focus was to study the evolution of this evaporating liquid film up till its end life. Their approach was capable of handling both volatile and nonvolatile isothermal thin liquid films, with the nonvolatile case given rise to static steady states makeup of liquid

TABLE 2.3: Areas of Applications of Thin Film Technology [39, 46].

Areas	**Description**
Engineering/ Processing	Tribological Applications: Protective coatings to reduce wear, corrosion and erosion, low friction coatings
	Hard coatings for cutting tools
	Surface passivation
	Protection against high temperature corrosion
	Self-supporting coatings of refractory metals for rocket nozzles, crucibles, pipes
	Decorative coatings
	Catalysing coatings
Optics	Anti-reflex coatings ("Multicoated Optics")
	Highly reflecting coatings (laser mirrors)
	Interference filters
	Beam splitter and thin film polarizers
	Integrated optics
Optoelectronics	Photo-detectors
	Image transmission
	Optical memories
	LCD/TFT
Electronics	Passive thin film elements (Resistors, Condensers, Interconnects)
	Active thin film elements (Transistors, Diodes)
	Integrated Circuits (VLSI, very Large Scale Integrated Circuit)
	CCD (charge Coupled Device)
Cryotechnics	Sure re-conducting thin films, switches, memories
	SQUIDS (Superconducting Quantum Interference Devices)
New Materials	Superhard carbon ("Diamond")
	Amorphous silicon
	Metastable phases: Metallic glasses
	Ultrafine powders (diameter < 10nm)
	Spheroidization of high melting point materials (diameter 1-500um
	High purity semiconductors (GaAs)
Alternative Energies	Solar collectors and solar cells
	Thermal management of architectural glasses and foils
	Thermal insulation (metal coated foils)

Continuation of Table 2.3

Areas	**Description**
Magnetic Applications	Audio, video and computer memories
	Magnetic read/write heads
Sensorics	Data acquisition in aggressive environments and media
	Telemetry
	Biological Sensorics
Biomedicine	Biocompatible implant coatings
	Neurological sensors
	Claddings for depot Pharmacia

ridges with thin films separation while the volatile case lead to a long time evolution of thin film flattening and subsequent vanishing. Grotberg [53] and Edwards *et al.* [54] worked on the effect of adding different surfactant concentration on thin film. In their findings, they observed that fingering phenomena depend greatly on the thickness of the thin film and on whether the concentration of the surfactant solution was above or below the micelle value.

The process of de-wetting causes ruptures in standing films and flowing fluids to form rivulets and dry arches. The advancing edge may take differing shapes depending on different parameters. This has been well studied and documented [5, 6, 8, 55]. For a static film sitting on a substrate, ruptures causes holes, droplets or areas without fluid to form if the local surface tension of the substrate is decreased by a residue or oily deposit. The surface of fluid bounding the rupture is governed by competing forces of gravity and surface tension. Gravity acts to smooth the fluid by a net force causing the perimeter of the hole to decrease whilst surface tension opposes this to minimise the fluid's surface area thus increasing the perimeter of the hole.

The balancing of these forces represents a stable rupture. However if the radius is greater than this equilibrium value, the rupture grows. Conversely, the rupture collapses if the radius of the rupture is smaller than the equilibrium value. A critical film thickness exists above which no rupture is stable and the fluid flows back into a homogeneous structure as the rupture collapses. This thickness is defined by the wetting angle made between the intersection of the substrate and the inside of the fluid surface. The characteristic velocity with which a rupture's radius increases at is related to the surface tension and wetting angle and is inversely proportional to the resistance of flow, dynamic viscosity, η_d, (see [56]).

For dynamic films, more complex structures may arise from the de-wetting process. For example if the substrate on which the film is placed is tilted at an angle until the leading edge of the fluid has a gravitationally induced acceleration then fingers may form as the fluid slides down the slope [8]. Tilting is necessary since for a discrete amount of fluid, there will be a symmetric outward gravitational force that will only drive the fluid as long as the surface tension remains unbalanced. This happens for example when a drop is applied to a horizontal impermeable surface [57]. For a highly viscous fluid the structures resemble a saw tooth structure whereas for a low viscosity fluid, long fingers form (see Figure 2.13).

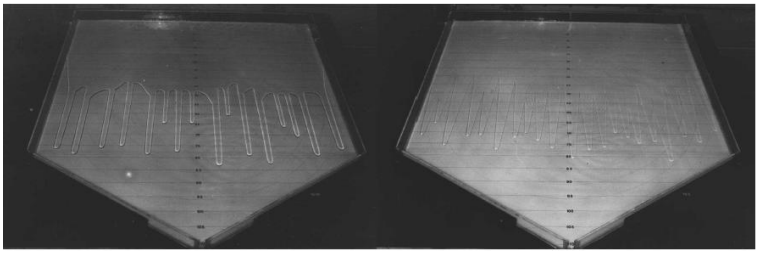

FIGURE 2.13: Fluid film flow down a substrate. Left: Fingering rivulets result from large substrate gradients and rapidly flowing or low viscosity fluids. Right: Saw tooth waves result from low substrate gradients and slowly flowing or high viscosity fluids [8].

A model for the evolution of a dry arch in fluid flow is briefly described (see Figure 2.14) by Podgorski [55]. Details of other thin film mechanical instabilities include the study by Liu *et al.* [42] who investigated the long scale growth of two and three dimensional instabilities from a driven thin film flow down a slope. It was found that an unsteady harmonic existed for a region where growing perturbations of consecutive waves were in phase after which the correlation broke down at a distance where a chaotic region existed.

For slightly different conditions, setting different values for the parameters of driving frequency, Reynolds number and angle of inclination produced an out of phase relationship for the consecutive waves at a larger displacement from the source. Another experiment by Hocking *et al.* [58], involving thin films flowing down a plane whose progress was tracked by monitoring the fluid-gas interface as it developed, compared the flows of different materials and concluded that a silicon-oil solution produced a saw-tooth like pattern of triangular waves as a leading edge of the interface while glycerine produced a far more vertically inclined flow of thin fingers. These differing outcomes were due to the disparity between Reynolds numbers. Another example by Fermigier *et al.* [44] previewed the formations of a thin layer of fluid sandwiched

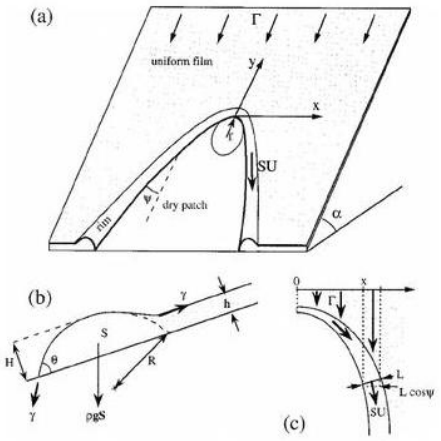

FIGURE 2.14: A dry arch forms over an area of low surface tension. The evolution of the arch is parameterised as a function of ψ [55].

between a lower density fluid and the underside of a ridged translucent plate. The gravitational instability implied by the former condition powered the instabilities. These instabilities were found to be axisymmetric. By analysing these problems mathematically, a more specific analysis can be wrought. However the description of the fluid is given in terms of coupled equations of interacting forces and effects, so a simplified model that predicts results retaining validity in the experimental case is needed. As is usual, asymptotic perturbations are fundamental in reducing and untangling complete equations. Taking an interest in long scale phenomena in this case affords the suppression of fluid variations parallel to the direction of the flow. The instabilities normal to the flow are instead focused on, in addition it is assumed that these variations happen over a long time scale.

Also, Kalliadasis *et al.* [59] worked on the steady free-surface of thin film flow over topography in the present of external body force by using the lubrication approximation couple with simplifying the equations of motion to a single nonlinear partial differential equation for the free-surface evolution in time and space. They were able to show that three dimensionless constants which are depth, width and steepness attributes governed the problem. From their computational model, it reveals that the free-surface develops a ridge just before the gate to the trench or departure from the hump and that for outstanding depth of sharp substrate attributes, the ridge becomes larger. They concluded that this effect is caused by capillary pressure gradient induced by the surface curvature and can be suppressed either with finite width or outstanding vertical component of gravity. As a follow up to Kalliadasis *et al.* [59], a study of the stability of free-surface thin-film flows over topography was carried out

by Kalliadasis and Homsy [60]. Kalliadasis and Homsy [60], concluded that unlike the contact line problem where instability grows into a well-defined rivulet, in their own analysis the ridge is surprisingly stable over a wide range of relevant parameters. This they attributed to the capillary ridge been governed by the rearrangement of the fluid flow in the direction toward the net pressure gradient induced by surface tension at high wavenumbers and by topography at low wavenumbers.

Furthermore, Craster and Matar[6] looked at a review of the dynamics and stability of thin liquid films. In their review, a wide rang of issues starting from wave pattern in films flows down a windowpane, de-wetting droplet and fingering of viscous flows down a slope were detailed. More insight into the de-wetting, thermos-capillary and surfactant-driven films, films flowing over an object, falling films, and the fast rotating substrate and evaporating films were discussed. The paper concluded with exciting research avenues and open problem in the area of fluid mechanics.

Schmuki and Laso [61] presented a visualisation experiment to explain the classification of flow regimes. The main focus of their study was to set-up constraints on the stable state flow rate so as to delineate the existence of various flow regimes. In their experiments, the liquid was dispatched to the top edge of an inclined smooth surface at a constant flow rate using a narrow tubing. Figure 2.15 illustrate photos taken at different flow rates with difference wettability. They observed that for a well-wetting liquid, the substrate is completely wetted by the flow without any dry spots as shown in Figure 2.15 (a). In the case of a non-wetting liquid, they observed that at the lowest flow rate in the experiment, a train of equally distributed "sliding drops"Figure 2.15 (b) were found. As the flow rate increased, the sliding drops begin to join to form a straight rivulet as shown in Figure 2.15 (c)). With further increase in the flow rate, the straight rivulet resulted in a meandering rivulet that split into multiple smaller rivulets as shown in (Figure 2.15 (d)).

Another interesting phenomenon is the impact of droplet on liquid and solid substrate especially in the field of annealing, spray cooling, quenching and painting, meteorology and ink-jet printing etc. Worthington [62–64] was the first to have investigate droplet impact from the scientific view. Since then, several studies and published articles have been released using various drop impact conditions, such as low or high speed, cold or hot surfaces and shallow or deep liquids. Depending on these conditions, various phenomenon can arise: drop splashing with a crown [65, 66], drop spreading on solid substrate [67–71], the so-called Worthington jet [72, 73], and droplet bouncing may be observed [74–77] etc. Savva *et al.* [78] study two-dimensional droplet spreading

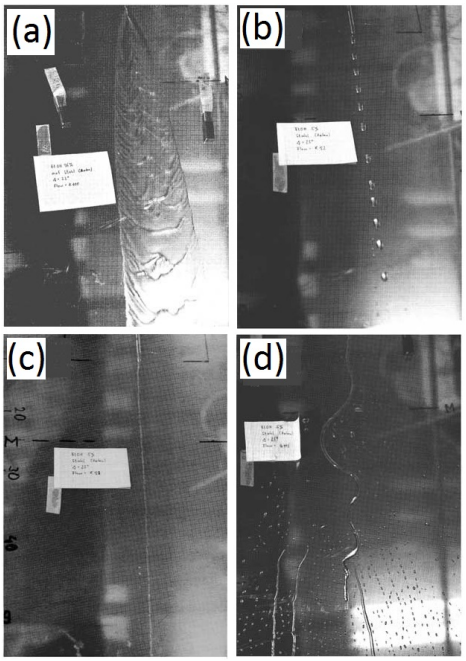

FIGURE 2.15: Snapshots of different flow regimes from experiments conducted by Schmuki and Laso [61]: (a) wavy film flow, (b) sliding drops, (c) straight rivulet and (d) meandering rivulets.

over the random topographical substrate with theoretical formulation using statistical approaches by representing the substrate families as motionless functions. In their conclusion, substrate roughness prevent wetting, thus making the droplet to slide without spreading once equilibrium is reached. Also, their theoretical predictions agreed well with numerical experiments.

Similarly, Muller *et al.* [79] observed that when a water droplet is placed on a normal flat silicone surface, and a silicone substrate coated with germanium nano-pyramids, the advancing contact angle will increase monotonically from approximate 40^o to 55^o respectively. Furthermore, Dettre and Johnson [80] concluded that the apparent contact angle of a droplet depends on the nature of the surface and that it values is greater in rough surfaces than in smoothed surface. Gaskel *et al.* [81] however worked on efficient and accurate time adaptive multi grid simulations of droplet spreading by using the full approximate storage (FAS) multi grid algorithm to solve the droplet spreading flow which was modelled as a coupled set of nonlinear lubrication equations. In their approach, the method was initially validated against a range of analytical and existing numerical predictions before using it for the new three dimensional flows consisting of droplet spreading.

For the numerical simulation of surface tension with mesh base method, Schwartz and

Eley [82] studied the simulation of droplet motion on low-energy and heterogeneous surfaces for a time-dependent three-dimensional liquid droplet using the lubrication approach. They carried out simulation both on a uniform and non-uniform substrate, only to notice that the spreading rates in the uniform substrate were independent of the contact angle until the droplet stabilizes, while in the non-uniform substrate makeup of two materials with wide different in contact angle, the drop break up due to the action of the wetting force. Their simulation result agreed well with experimental observations although with a time-scale correction. As a further study, Schwartz [83] also worked on hysteretic effects in droplet motions on heterogeneous substrates with direct numerical simulation by using the lubrication approach for both homogeneous and heterogeneous substrates. In the homogeneous substrate, it revealed that there is the need for time-scale correction for it to be in good agreement when compared with a report from experimental results. He treated two set of problem, one with natural driven motion and the other with force cyclical motion and concluded that if the contact angle is sufficiently high, the droplet can locate numerous different stable positions, depending on the previous history of its motion.

In the work of Malkin *et al.* [84], the effect of droplet size on the rheological properties of highly concentrated water-in-oil emulsions was studied. They found that by varying the droplet size, the emulsions are non-Newtonian liquids with flow curves of the low shear rate at the Newtonian domain. Also, the effect of time was studied, where they found that the emulsion behaves like rheopectic fluid due to prolonged shearing, thereby resulting in increase viscosity at the low shear rate domain.

2.2 Numerical Methods

Numerical simulation is a vital scientific tool for validating and predicting phenomena by using approximate discrete equations for compact computation of the continuum fields. Numerical simulation helps to transform the major attributes of a problem in physics into a segmented (discretized) form of mathematics, and then integrate and solves the task using a computer. When its solutions are compared with the results from experimental experts, there is a strong agreement. Since the advent of computers with more computing resources, numerical simulation are now becoming more important in every fields making it a suitable tool for solving complex problems with little or no approximations and assumptions, compare to the traditional methods such as

Finite Element, Finite Difference and Finite Volume methods, which have more hypothesis. In recent scientific research, numerical modelling has become an alternative approach that can be used to safe cost, instead of doing elaborate, time-consuming and harmful experiments for clients [18]. Also numerical modelling is more convenient, has its provides complete and clear data compared to traditional method. Numerical simulation with the help of powerful computer can deliver verifiable results, present understanding to underlying physics and also help to explain or discover new ideas. According to Liu [18], numerical simulation play important duty by acting as a bridge between experiment and theory, and this is illustrated as shown in Figure 2.16.

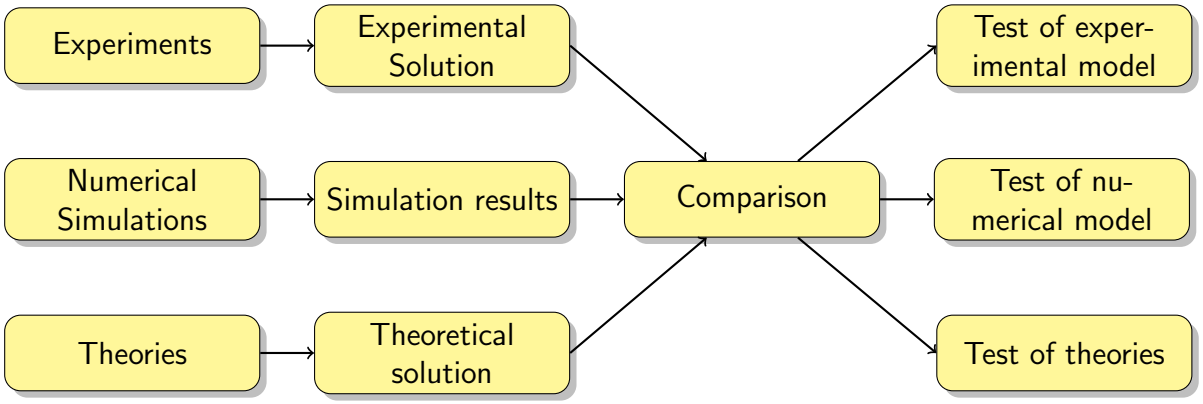

FIGURE 2.16: The Numerical Simulation link between experiment and theory.

There are two fundamental approaches for describing the physical governing equations: the Eulerian and Lagrangian methods. The Eulerian description is a spatial description and is physically represented by the gird or mesh that is fixed while the Lagrangian description is a material description and is physically represented by packets of particles that are free to move with the mesh. Numerical simulation can be mesh based or mesh free method. For the mesh based method, it involves the use of either a fixed grid where the materials flow across the fixed grid or a moving mesh where the materials are attached to the moving mesh. Prominent examples of the mesh based methods are, finite element method (FEM) which uses a Lagrangian based formulation and the finite difference method (FDM) which uses Eulerian based formulation [85] because of its early foundation, but for large deformation, the mesh based method need corrective treatment, like re-zoning or remeshing [18], however this lead to reduction in both accuracy and efficiency in terms of computational time and cost. In contrast to meshed based methods, the mesh free method do not require any grid or mesh, but rather it proposes the use of particles alone to model the phenomenon. This method has the advantage of keeping a complete physical properties (like mass,

velocity, pressure e.t.c) of the particles and since the particles carries these physical properties, extremely large deformation can be handled very easily. Other merit of this method is that the code implemented is also very easy.

2.2.1 Mesh based methods

These two description which are Eulerian and Lagrangian Method are examined as follows.

2.2.1.1 Eulerian Grid

The Eulerian grid method is fixed in space, which mean the simulated object locate and move across the fixed mesh cells. In this way all grid nodes and mesh cells remain spatially fixed in space and do not change with time while the materials are flowing across the mesh. This is illustrated in Figure 2.17 (a) - (b) below. The flux of mass, momentum and energy across mesh cell boundaries are simulated to compute the distribution of mass, velocity, energy, etc. in the problem domain. The shape and volume of the mesh cell remain unchanged in the entire process of the computation. Because the Eulerian grid is fixed in space and time, large deformation in the object do not cause any deformation in the mesh cell itself. Eulerian methods are dominant in area of computational fluid dynamic where the flow of the material dominates. However, so many disadvantages are associated with this method, there are:-

1. Because the movement of the material cannot be tracked using a fixed mesh, it is difficult to analyse the time history of field variables at fix point on the material
2. Complicated geometry of material cannot be treated with ease using Eulerian method. Usually it require expensive numerical mapping
3. It is difficult to determine accurately the free surfaces, deformable boundaries and moving material interfaces because the method only track mass, momentum and energy flux across the mesh cell boundaries
4. Large computational domain is required in order to cover the entire area to which the material can possibly flow. Also it may require much coarse grid for

computational efficiency at the expenses of the resolution of domain discretization and the accuracy of the solution.

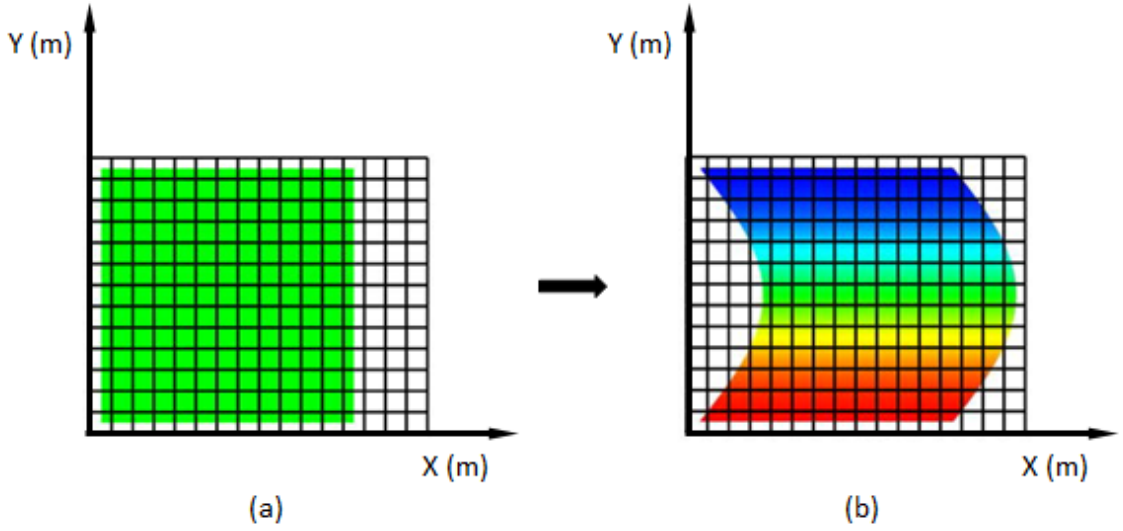

FIGURE 2.17: Eulerian Grid mesh cells grid is fixed in space and does not move or deform with time. The material moves/ flow across the fixed mesh cells.

2.2.1.2 Lagrangian Grid

Contrary to the Eulerian grid, the Lagrangian grid is fixed to or attached on the material in the entire computational process, and therefore it moves with the material as illustrated below in Figure 2.18 (a) - (b). The Lagrangian grid method offers several advantages, which are:-

1. The entire time history of all the field variable at the material point can easily be tracked because the fixed grid is moving with the material.
2. Irregular or complicated geometries can be treated conveniently with ease by using an irregular mesh.
3. No additional grid domain is required beyond the problem domain since the grid is only required within the problem domain and this make the Lagrangian method to be computationally efficient
4. It is possible to automatically track boundary conditions at the free surface, moving boundaries, and material interfaces by placing some grid node at the boundaries and material interfaces.

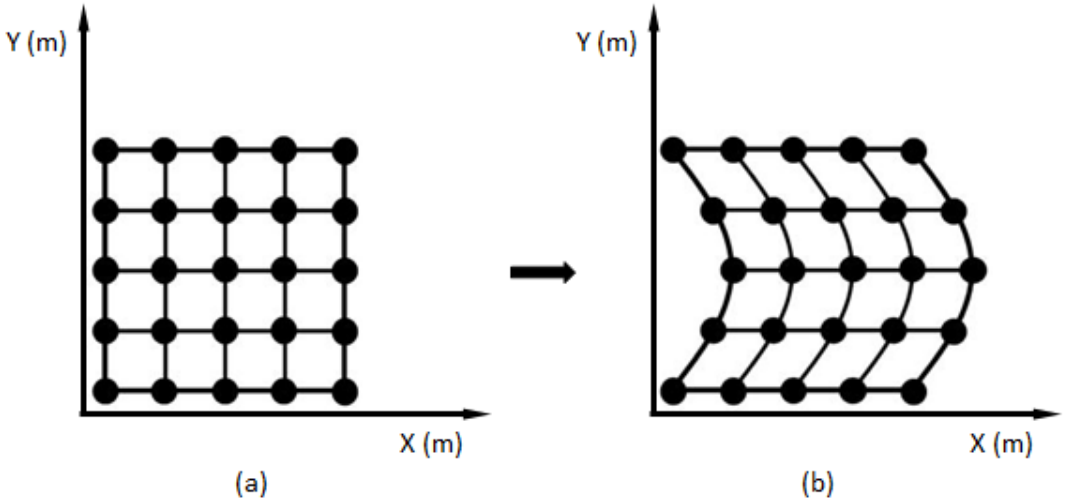

FIGURE 2.18: Lagrangian mesh cells grid is fixed or attached to the material as it moves.

5. It is easy to manipulate since no convective term exists in the related partial differential equations. This make the code conceptually simpler and faster, as no computational effort is necessary for dealing with the convective terms.

Because of the above advantages, Lagrangian methods are very popular and are successful in solving computational solid mechanics (CSM) problem where the deformation is not as large as that experience in fluid flows. However Lagrangian method are practically very difficult to apply for cases with extremely distorted mesh, because their formulation is always based on mesh. For a heavily distorted mesh, the accuracy of the formulation and the solution are severely effected. Also if the smallest element size is too small, the computation might breakdown. So a possible way to enhance the Lagrangian computation is by re-zoning or re-meshing the problem domain. Re-zoning the mesh involves overlaying the old distorted mesh with a new undistorted mesh, so that the following-up computation can be performed on the new undistorted mesh. The physical properties in the new mesh cells are approximated from the old mesh cells through calculating the mass, momentum, and energy transport in a Eulerian description. However, the re-zoning procedures in Lagrangian computation can be tedious and very time consuming. Also with frequent re-zoning, Lagrangian code tend to resemble Eulerian code in an overall sense. Therefore even if there are good advantages in Lagrangian grid based method, the disadvantages can result in numerical difficulties when simulating events of extremely large deformation. For this reason, a Lagrangian numerical method whose solution does not depend on mesh and is not affected by heavy movement of the grid node is desirable. Table 2.4 below show the

similarities and differences between both methods, while Table 2.5 shows summary of Lagrangian and Eulerian description of mass, momentum and energy equations.

TABLE 2.4: Comparisons of Lagrangian and Eulerian methods [18].

	Lagrangian Methods	**Eulerian Methods**
Grid	Attached on the moving material	Fixed in the space
Track	Movement of any point on materials	Mass, momentum and energy flux across grid nodes and mesh cell boundary
Time history	Easy to obtain time-history data at a point attached on materials	Difficult to obtain time-history data at a point attached on materials
Moving boundary and interface	Easy to track	Difficult to track
Irregular geometry	Easy to model	Difficult to model with good accuracy
Large deformation	Easy to handle	Difficult to handle
Grid size	No extra grid beyond the problem domain is needed	Additional grid space is required

TABLE 2.5: Conservation equations in PDE form in the Lagrangian and Eulerian description [18].

Mass	**Lagrangian description**	**Eulerian description**
Mass	$\frac{D\rho}{Dt} = -\rho\frac{\partial v^\beta}{\partial x^\beta}$	$\frac{\partial \rho}{\partial t} + v^\beta\frac{\partial \rho}{\partial x^\beta} = -\rho\frac{\partial v^\beta}{\partial x^\beta}$
Momentum	$\frac{Dv^\beta}{Dt} = -\frac{1}{\rho}\frac{\partial p}{\partial x^\beta}$	$\frac{\partial v^\beta}{\partial t} + v^\alpha\frac{\partial v^\beta}{\partial x^\alpha} = -\frac{1}{\rho}\frac{\partial p}{\partial x^\beta}$
Energy	$\frac{De}{Dt} = -\frac{p}{\rho}\frac{\partial v^\beta}{\partial x^\beta}$	$\frac{\partial e}{\partial t} + v^\beta\frac{\partial e}{\partial x^\beta} = -\frac{p}{\rho}\frac{\partial v^\beta}{\partial x^\beta}$

2.2.1.3 Numerical Discretisation

In order to solve the governing equation of the fluid motion, first their numerical analogue must be generated. This is done by a process referred to as discretisation. In the discretisation process, each term within the partial differential equation describing the flow is written in such a manner that the computer can be programmed to calculate it. There are various techniques for numerical discretisation which are described below:-

Finite Difference Method

Finite difference method utilizes the Taylor series expansion to write the derivatives of a variable as the differences between values of the variable at various points in space or time. The Finite Difference Method (FDM) is use to give approximate solutions for differential equations and is based on a finite number of nodal points or grids [86]. FDM can be classified in two way by the geometrical relationship of points which is forward, backward or central difference and by the accuracy of the expression, for instance central difference is second-order accurate, whereas both forward and backward difference are first-order accurate. In order to apply this discretisation method to the whole flow field, many points are place in the domain to be simulated. Then, at each of these points, the derivatives of the flow variables are written in the difference form, relating the values of the variable at each point to its neighbouring points. Once this process is applied to all the points in the domain, a set of equations are obtained which are solved numerically [87, 88].

Finite-Element Method

In the Finite Element Method (FEM), the fluid domain in consideration is divided into finite number of sub-domain known as elements which is represented by discrete nodes connected by a mesh. A history of the early development of the technique has been written by Meek [89] and the pioneering work in this area can be attributed to the authors [90–93]. The governing equations are estimated at the nodes and the mesh defines the connectivity of the nodes. It is a Lagrangian method in which the mesh and nodes move with the material of interest. This means material boundaries and mass conservation are naturally handled by the location of the nodes and mesh representing the material. By varying mesh densities, the efficiency of the method can be improved. Though this will increase the computational time and cost [94]. Additional efficiency is gained because nodes and mesh are only required in material volumes and not for voids. This requirement for the nodes to be joined by a mesh to define the connectivity is the main down fall of this method. Large material deformations can cause extreme distortion of the mesh to the point where the model will fail to converge. Also the computational method fails if the mesh size is too small. Although there are methods such as the Arbitrary Lagrangian-Eulerian (ALE) approaches that can improve the performance of FEM models in situations of extreme deformation, which is a re-zoning or remeshing step to avoid the mesh distorting too much, by transferring the

field variables from the existing distorted mesh onto a newly generated non-distorted mesh via an Eulerian representation of the model. However this lead to reduction in both accuracy and efficiency in terms of computational time and cost. Figure 2.19 shows the Archimedes' problem (circa 250 B.C.): rectification of the circle as limit of inscribed regular polygons, where the black ring circles represent the computational nodes whilst the mesh is represented by the straight solid blue lines.

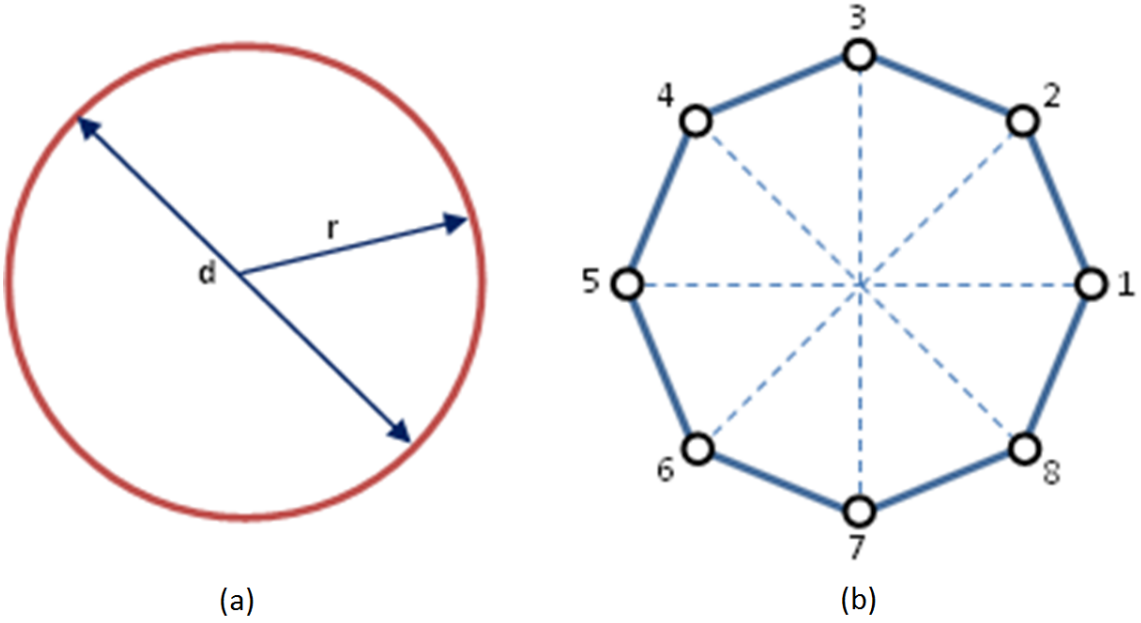

FIGURE 2.19: Showing (a) the circumference of a circle and (b) the Finite Element Method of approximating it.

Finite Volume Method

The Finite-Volume Method (FVM) is a method for representing and evaluating partial differential equations in the form of algebraic equations [95, 96]. It is the most popular method in CFD because it can resolve some of the problem experience in both FDM and FEM. The method is a meshed approach, but operates in Eulerian frame and is based on non-overlapping infinitesimal control volumes which are generated by grid points where their values are calculated at discrete places on the meshed geometry. The term "Finite volume" refers to the small volume surrounding each node point on a mesh. In the finite volume method, volume integrals in a partial differential equation that contain a divergence term are converted to surface integrals, using the divergence theorem. These terms are then evaluated as fluxes at the surfaces of each finite volume. Because the flux entering a given volume is identical to that

leaving the adjacent volume, these methods are conservative (see Figure 2.20 below). Another advantage of the finite volume method is that it is easily formulated to allow for unstructured meshes. FVM is used in many Engineering Applications because it is capable of modelling Heat Transfer, Mass Transfer and Fluid Mechanics [97]. This method can be less efficient than FEA because the mesh has to cover the entire computational domain rather than just existing where material is present as with FEA. Representing geometry with features of different size scales can also be problematic because the mesh is typically of a constant density.

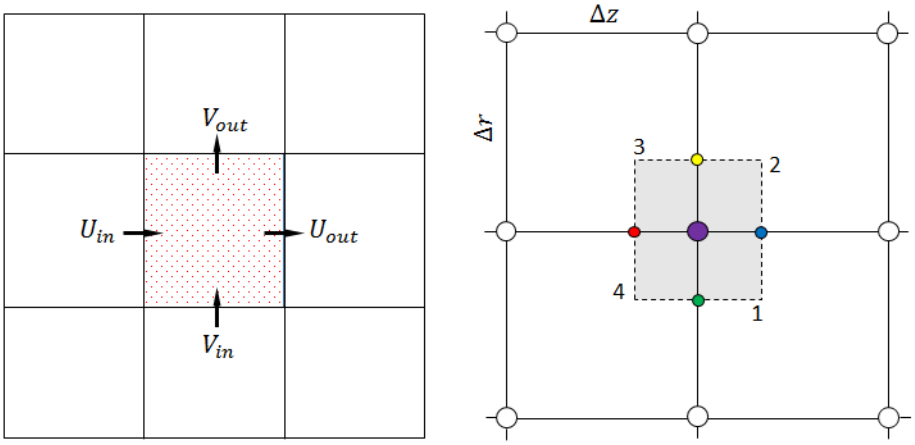

FIGURE 2.20: Finite Volume Method in 2 Dimensions

2.2.2 Mesh-Free Methods

The traditional grid based numerical method has great limitation with regards to the grid generation which is not a direct process, thereby making it an expensive task, both in terms of computational time and mathematical complexity. Mesh free methods have greater opportunities and are more promising in their ability to handle large deformations, advanced materials, complex geometry, nonlinear material behaviour, discontinuities and singularities [18]. Mesh free particle methods (MPM) is one of the example that uses the particles to represent the physical object or a portion of the domain with Table 2.6 highlighting its merits. For Computational Fluid Dynamics (CFD) problems, materials properties such as mass, momentum, energy, position, etc. are computed at each particle. Some examples of these methods are shown in Table 2.7. Mesh free methods can be applied to solid mechanics as well as fluid dynamics, though share some similarities with the grid based method, they differs in their method of approximation. See Table 2.8 for a summary of these methods and their methods of approximation.

TABLE 2.6: Merits of Mesh Free Methods.

1. Its offers stable and accurate numerical solution for integral equations of PDEs.
2. Its has the capacity to defines all kinds of boundary conditions with a set of arbitrary nodes.
3. Convenient to model large deformations.
4. Convenient to model inhomogeneities.
5. Convenient to model shockwaves.
6. Convenient to model free surfaces.
7. Convenient to model high impact velocity.
8. Convenient to model explosion.
9. Convenient to model moving materials interfaces deformation boundaries.

TABLE 2.7: Some typical particle methods [2].

Methods
Molecular dynamics (MD)
Monte Carlo
Direct Simulation Monte Carlo (DSMC)
Dissipative particle dynamics (DPD)
Lattice gas Cellular Automata
Lattice Boltzmann equation (LBE)
Partilce-in-Cell (PIC)
Marker-and-Cell (MAC)
Fluid-in-Cell (FLIC)
Moving Particle Semi-implicit (MPS)
Discrete element method (DEM)
Vortex methods
Smoothed Particle Hydrodynamics (SPH)

TABLE 2.8: Some typical meshfree methods in chronological order [2].

Methods	**Methods of Approximation**
Smoothed particle hydrodynamics	Integral representation
Finite point method	Finite difference representation
Diffuse element method (DEM)	Moving least square (MLS) approximation Garlekin method
Element free Garlekin (EFG) method	MLS approximation Garlekin method
Reproduced kernel particle method (RKPM)	Integral representation Garlekin method
HP-cloud method	MLS approximation Partition of unity
Free mesh method	Garlekin method
Meshless local Petrov-Garlekin (MLPG) method	MLS approximation Petrov-Garlekin method
Point interpolation method (PIM)	Point interpolation (Radial and Polynomial basis), Garlekin method, Petrov-Garlekin method
Meshfree weak-strong form (MWS)	MLS, PIM, radial PIM (RPIM), Collocation plus Petrov-Garlekin

2.2.2.1 Smoothed Particle Hydrodynamics (SPH) Method

Traditionally, the behaviour of complex physical systems have been tested by two well-known techniques which are the experimental techniques, where one disturbs the system in some controlled manner and observes its behaviour, and the theoretical approach, in which one uses analytical mathematical techniques to determine the behaviour consistent with well-established physical law. But with advances in computers and computing power, the advantages of using numerical simulation is increasing obvious and apparent. The Figure 2.21 and 2.22 below shows the SPH representation of particles.

SPH development

Smoothed-particle hydrodynamics (SPH) is a computational mesh free method, originally developed by Lucy [98] and Gingold & Monaghan [99], to investigate astrophysical problems. It has since been extended and used in various fields of research, including, ballistics, volcanology, and oceanography. SPH is fully Lagrangian, that

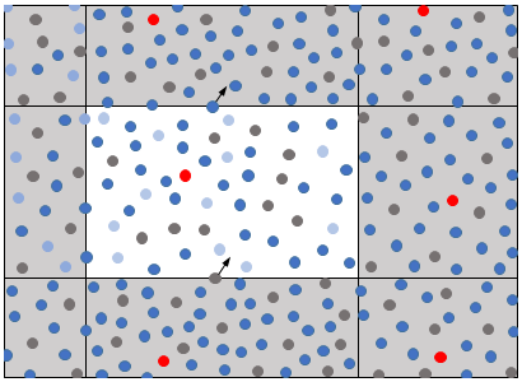

FIGURE 2.21: Showing the particles deploy within the cells

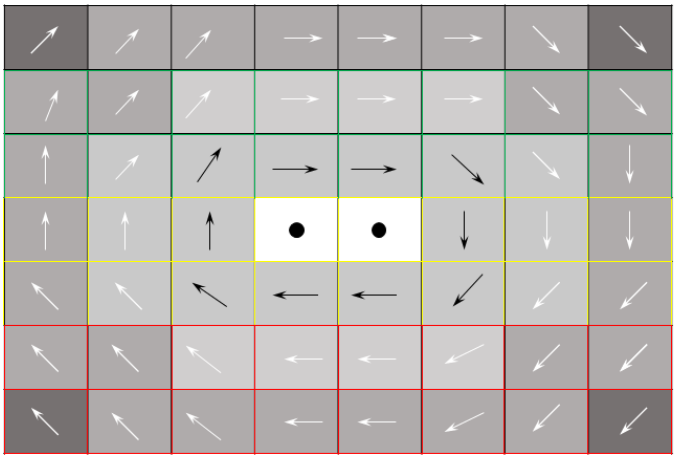

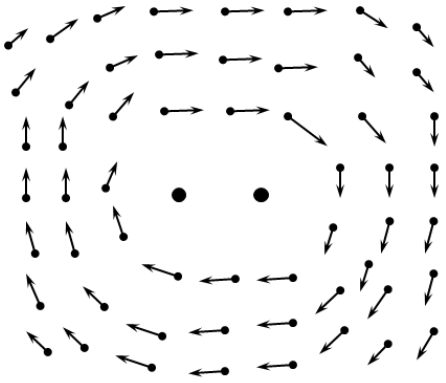

FIGURE 2.22: Showing the particles movement within the domain

is; a grid free method, in which the fluid is represented by particles which carry materials properties, typically of fixed mass, follow the fluid motion and are then used to discretize the governing equations. Like every other method, the approximation is carried out by using a suitable kernel function to represent the spatial derivatives of the continuous field in discrete form [100] originating from the interaction with the neighbouring particles. This particle is used as an interpolation or sampling point for the numerical purposes of the calculations but has the physical interpretation of a material quantity depending on the scale of the simulation, for example it may be thought of as a molecule or a batch of molecules which move with independent velocities many orders of magnitude smaller than the batch velocity. Since particle methods deal so easily with free surfaces and deformations, they are ideal for modelling fluids and fragmenting or highly deforming solids.

The method has been improved repeatedly, as of the early 1990s, where it was applied firstly to weakly compressible hydrodynamics (WCSPH); Morris *et al.* [101], Szewc

et al. [102], then to strongly compressible (Sigalotti *et al.*, [103]) and truly incompressible (ISPH) (Cummins and Rudman, [104]; Shao S. and Lo E. [105]; Xu Rui [106]) hydrodynamics. Another interesting improvement is the XSPH variant, where the particles moves with velocity close to the average velocity within its neighborhood, thus ensuring ordering particles distribution without introducing dissipation, like in the work of Monaghan [107]. Because it is possible to formulate SPH to converse mass, momentum, and energy exactly and also relatively easy to incorporate complicated physical effects into it, this makes SPH an extremely versatile method to be applied to a vast range of problems. Although the error in result can sometimes be substantially larger than that obtained using traditional methods tailored for a specific problem, the main attractions of SPH is its potential to predict highly strained motions without utilizing any computational mesh or grid, on the basis of a collection of macroscopic particles.

SPH has being discredited by many theoricists and modelling specialists, because of the relatively 'experimental' nature of its initial evolvements, but recently it is regarded as the most popular and reliable mesh free method due to further improvements, which provided it with a number of properties which are deemed essential to the trustworthiness of a numerical method [18]. Another attractive advantage of the approach is the consistency of the method with both Lagrangian and Hamiltonian Mechanics. SPH has being applied to dam break, elastic flow (Swegle [108]), quasi-incompressible hydrodynamics (Monaghan [107]), gravity current (Monaghan and kocharyan [4]), Magneto-hydrodynamics, fracture of brittle solids (Benz & Asphaug [109]) and most recently the convergence properties of SPH by (Di Lisio *et al.*., [110]; Ben Moussa, [111]).

Some notable SPH researchers, like J. J. Monaghan [112] proposed that a constant smoothing length, h, is useful, but acknowledging the facts that in more complication problem, it is necessary to allow h to vary with time as in case of Gingold & Monaghan [99] or with both time and position as in case of Wood [113]. While G. V. Bicknell [114] proposed that the inaccuracy in SPH is cause both by approximation to the pressure gradient and replacing the interpolation points by integral sum. P. W Randles *et al.* [115] proposed the use of conservation smoothing for removing tensile instability and damping, boundary algorithms for removing material interface and also scalar and tensor models for removing fracture and fragmentations.

Furthermore, Pozorski and Wawrenczuk [116] developed a Poisson's solver algorithm.

They suggested solving the Poisson's equation related to velocity divergence and density variation simultaneously. However their method was unable to resolve difficulties associated with particle clustering and density error accumulation. M. Ellero *et al.* [117] introduced the SHAKE algorithm of molecular dynamics to constraint the density variation, while correcting the density error, by modifying particle position iteratively, their method produces relatively large particle clustering than that of weakly compressible SPH method. However as oppose to previous methods, it does not require solving the pressure Poisson's equation in order to get the divergence-free velocity field. However X. Y. Hu and Adam [118] proposed fractional time-step to enforce density variation and velocity divergence-free condition at each full time-step with their result in good agreement with analytical or reference from literature. Though the method increases coding complexity slightly, there was the need to superimpose the negative pressure with a constant positive reference pressure to overcome stability problems that may arise. X. Y. Hu and Adam [119] proposed the constant-density approach for the incompressible multi-phase SPH. This method correct the intermediate density error by adjusting the half-time step velocity with exact projection without the previous time-step restriction to the reference pressure and allow the simulation of flow with unprecedented high density ratio. Numerical examples were investigated and compared with analytical solution and previous results. The results show that the method can be applied to single and multi-phase flows with a wide range of density and viscosity ratios.

Due to the nature of SPH having a mesh free features, the method can be applied to complicated phenomena, not only because of its versatile nature, but also that it is based on Lagrangian formulation with particle approximation. A compact summarized of its application is given below in Table 2.9.

Smoothed particle hydrodynamics is a fantastic multi-tasking and easy approach for numerical fluid dynamics. SPH just like any other numerical methods, has its advantages and disadvantages, but it must be said that the advantages out-way its disadvantages. The following Table 2.10 and Table 2.11 below highlight these facts as follows:

Applications in Surface Tension

More recently, SPH has found diverse applications in modelling fluid flow problems in addition to those with moving interfaces Szewc *et al.* [149]. The primary advantage

TABLE 2.9: Areas of Applications of SPH Techniques [18].

Areas	**Specific examples**
Astrophysics	Cloud fragmentations and collisions [120]
	Collapse and formation of galaxies [121--124]
	Cosmology [125, 126]
	Evolution of the universe [127]
	Moon formation and impacts problems [128]
	Stellar collisions [19, 129–133]
	Supernovas explosion [134, 135]
Fluid Dynamics	Free-surface flows [107, 136, 137]
	Gravity currents [138, 139]
	Heat conduction [140]
	Multi-phase [4]
	Underwater explosions [141]
Magneto-Hydrodynamics	Alfvenic waves propagation [142]
	Development of expansive wave in a magnetic cloud [143]
	Magnetic colapse of gas clouds [144]
Solid Mechanics	Fractures simulation [109]
	Impact problems [145]
	Impacts of solids simualtion [146]
	Metal forming [147]
	Study of brittle soilds [148]

of SPH over the Eulerian approach is that the fluid, describe by particles, is naturally suitable for complex geometries and issues arising from free-surface flows. Numerous approaches to precisely model surface tension has been reported (Brackbill *et al.* [150], Nugent and Posch [151] and Tartakovsky and Meakin [152]) and they can be broken down to two main methodologies.

The first approach is the Continuous Surface Force (CSF) which takes into account the curvature of the surface of the fluid, Brackbill *et al.* [150] and was made famous by Muller *et al.* [153], who proposed a single-phase method to track and model surface tension of droplets in SPH with the aid of different kernels. Though the approach is relatively fast, with usefulness/applicability in computer graphics, it lacks accuracy that is needed to solve realistic and practical physical problems. Das and Das [34] examined multiphase flow of droplets moving down an inclined plane. The surface tension was model using the CSF method, while for the tracking of the moving contact line, they proposed the diffuse interface model. However, to resolve the particle

TABLE 2.10: Advantages of SPH [18].

1. The ease with which it can provide a large dynamic range in spatial resolution and density, as well as an automatically adaptive resolution, are unmatched in Eulerian methods.
2. SPH has excellent conservation properties, not only for energy and linear momentum but also for angular momentum. This later is not assured in Eulerian methods automatically, although it is fulfilled for well-resolved flows at an acceptable level.
3. By coupling SPH with self-gravity, the total energy is exactly conserved. This is manifestly not true for most mesh-based approaches to hydrodynamics.
4. Because SPH approach is completely mesh-free, it is Galilean invariant and free of any error from advection alone. Also, it can be applied to complicated geometric shape and a large area of space that are completely devoid of particles.
5. SPH numerical code implementation tends to be more comparatively simple and transparent. Also, the scheme is characterized by an amazing robustness which makes it impossible for example, for negative densities or temperature to occur in SPH by construction, whereas it is a problem in mesh-based methods.
6. Conservation of mass is assured without extra calculations.
7. SPH formulation involve solving the pressure from nearest neighbour particles rather than solving a linear sets of equations.
8. SPH can use to simulate free surface for two-phase interacting fluid directly.
9. It an exact solution to the continuity equation.
10. Resolution follows mass, natural compatibility with N-body codes.
11. ZERO dissipation.
12. Advection is done accurately.
13. EXACT conservation of mass, momentum, angular momentum, energy and entropy.
14. A guaranteed minimum energy state.
15. Dissipation terms must be explicitly added to treat discontinuities.

penetration (fluid particle going through the solid wall) and clumping (fluids particle joining together) problems, they employed the inter-particle Leonard-Jones force [18].

The second approach major on the Inter-particle Interaction Force (IIF) which was proposed by Tartakovsky and Meakin [152] for a porous media problem, that consist of attractive and repulsive forces between the fluid particles, thereby making surface tension forces to exist even within the bulk of the fluid. Due to these unbalanced forces within the bulk of the fluid, they make the droplet to be very sensitive to the contact line especially at small contact angles. For the surface tension model using

TABLE 2.11: Disadvantages of SPH [18].

1. The limited accuracy of SPH in multi-dimensional flows is its major disadvantages. These noises originate from the approximation of local kernel interpolants which occurs by summing overs small set of nearest neighbours. In 1D dimensional problem, the noise is reasonably small compared to a multi-dimensional problem where particle motion has a much higher degree of freedom, thereby creating an unbalanced force because the neighbouring particle pairs do not cancel out in all directions simultaneously. Because of this, jittering of the particle motion begin, giving rise to serious inaccuracy, which messes up this technique, especially for subsonic flow and also leads to slow rate of convergence.
2. Another general issue is that the artificial viscosity is operating at a level outside of the shocks, this makes the numerical model to have a high numerical viscosity, which tends to limits Reynolds number that could be reached with this techniques.
3. SPH is prone to fluid instabilities across contact discontinuities, such as the Kelvin-Helmholtz instabilities. These are usually found to be suppressed in their growth.
4. Methods can be crude (need a good switch).
5. Exact conservation no guarantee of accuracy.
6. Screw-ups indicated by noise rather than code crash.
7. Historical difficulties incorporating magnetic fields (MHD).

IIF, the particle pressure is computed using the Van der Walls equation of state ([151] , [154]) which consist of three control variables that need to be tuned. Akinci *et al.* [155] studied using a multi-phase approach where they employed a combine surface tension model comprising of the cohesion and surface area minimisation terms to model the fluid and air particles while an adhesion model is introduced for fluid and solid particles. This lead to a method which is expensive in terms of computational time and cost.

In the present study, a single-phase modified CSF and IIF approaches are developed to precisely model surface tension dominated flow of droplets. The proposed CSF methodology introduces the use of a modified curvature model, where the formulation will be verified against known results numerically and those in literature. The CSF approach is employed to investigate the case of an oscillating droplet and spreading with real fluid properties, while the IIF approach is employed to investigate the case of an oscillating droplet, spreading, contact angle hysteresis and thin film flow; the former aims simplify and eliminate the use of tuning parameters that may result in unphysical and unrealistic interactions. However, for complex movement, the former

is inadequate while the latter can handle such situation. Throughout all the models used, Wendland kernel is employed especially for the CSF method to reduce the effect of tensile instability due to its soft repulsive stability effect [156].

Chapter 3

SPH Methodology

"It is not wise to violate the rules until you know how to observe them."

T.S. Eliot, (1888-1965).

3.1 Introduction

SPH was originally designed for astrophysics for simulating galaxy formation where there were no boundaries and restrictions imposed by numerical mesh, by Lucy 1977, Gingold & Monaghan 1977, but later turned out to be very useful for many other applications. However, for this method to be applied to other fields, especially for engineering related problems, there need to be a boundary (details of this boundary conditions will be discussed later in this Chapter 3). SPH describes a fluid by replacing its continuum properties with locally smoothed quantities at discrete Lagrangian locations which are without grid or mesh. This smoothed quantity used to approximate the continuum properties is called smoothed kernel and it depends on two parameters which are the interpolation distance, $(r - r')$ (the separation between particles), and the smoothing length, h (characteristic length), details of this kernel will be discussed later in this Chapter 3.

3.2 General Formulation of SPH Method

In the SPH approach, particles are used as interpolation points of field variables, from which the governing equations are solved using a smoothing function (kernel) to weigh particle interactions.

The use of a smoothing function is central to the workings of SPH, because it defines the catchment area or support domain for combining the particle properties , that is, the connectivity normally provided by a mesh. The central concept of a smoothing function encapsulates that particles further away from the particle of interest will have less effect on the behaviour of that particle because of their monotonically decreasing nature. The smoothing function represented by, W, depends on the separation, $(r-r')$, between the particle position, r of interest (the point where the system equations are being evaluated) and the neighbouring particle position, r', that is being used in the estimation and its smoothing length, h. The smoothing length defines the extent of the support domain of the kernel for a particle as shown in Figure 3.1.

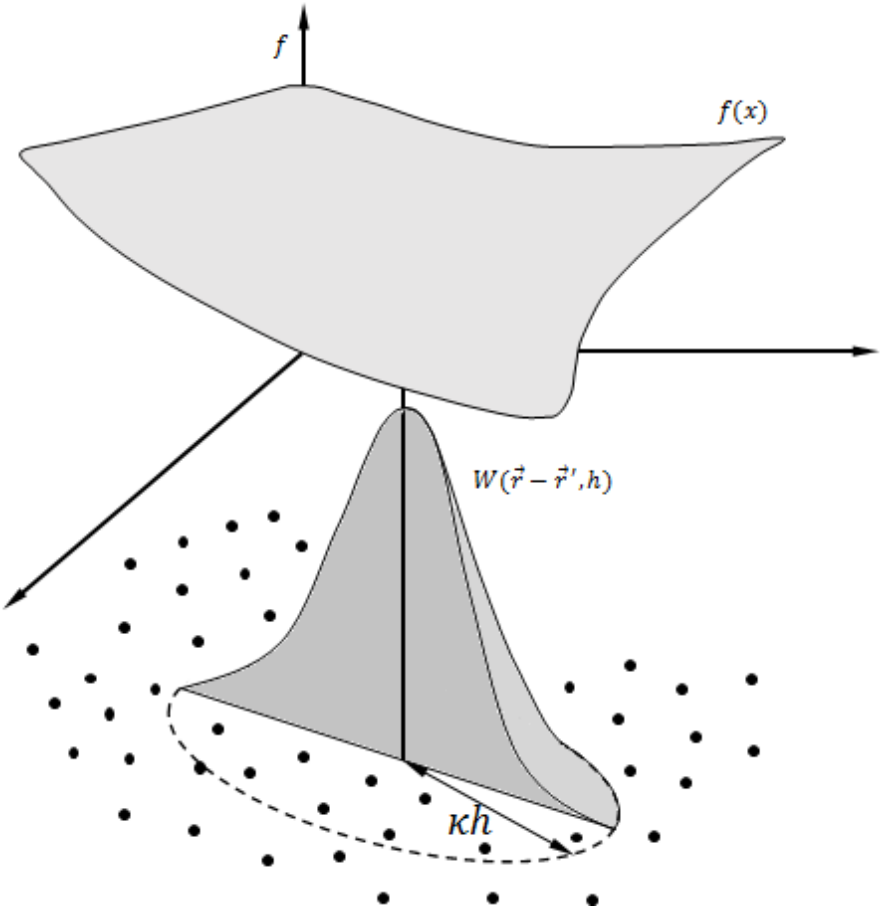

FIGURE 3.1: Kernel approximation of field function f.

3.3 SPH Method of Approximation

Generally, SPH method of approximation can be achieved in two main steps. The first is the kernel approximation, while the second is particle approximation of the field function.

3.3.1 Kernel Aproximation

The equation sets in SPH are determined in a continuous form called the kernel approximation. This approximation is based on the following identity:

$$f(r) = \int_{\Omega} f(r')\delta(r - r')dr', \tag{3.1}$$

$$\delta(r - r') = \begin{cases} 1 & \text{if } r = r', \\ 0 & \text{if } r \neq r', \end{cases} \tag{3.2}$$

where $f(r)$ is as arbitrary scaler continuous function being estimated, Ω represents the computational volume and $\delta(r - r')$ is the Dirac delta. This gives an exact answer for continuous functions and is not an estimate since $f(r')\delta(r-r')$ will only give a non-zero answer when $r = r'$. For approximations of discrete functions, a function other than the Dirac delta is required to allow interpolation of the discrete values. The Dirac delta has only point support and so will not interpolate the values from neighbouring particles which are used once the equations are discretised (see Subsection 3.3.3). The described smoothing functions however have a larger support domain that allows the interpolation between particles. Replacing the Dirac delta in Equation (3.1) with a smoothing function $W(r - r', h)$ results in the approximation being rewritten as:

$$f(r) \approx \int_{\Omega} f(r')W(r - r', h)dr'. \tag{3.3}$$

In SPH, the kernel approximation operator is marked by the angle brackets <> [157] and therefore Equation (3.3) is again rewritten as:

$$< f(r) >= \int_{\Omega} f(r')W(r - r', h)dr'. \tag{3.4}$$

Now, for the $W(r - r', h)$ function to be consider as a kernel, its must satisfy several criteria [158], which are:

1. Delta function property:

$$\lim_{h \to 0}[W(r - r', h)] = \delta(r - r'). \tag{3.5}$$

2. The function must only have compact support:

$$W(r - r', h) = 0 \qquad when \quad |r - r'| > kh, \tag{3.6}$$

   where k is a scaling factor (see Figure 3.1) used to define the spread of the function. This is important from a computational stand point rather than a theoretical one since calculating an infinite support domain would not be possible. While $h = \eta \times dx$, where, η is referred to as the coupling constant or expansion ratio in some SPH literature and dx is the initial particle spacing. This coupling constant, η, will be discussed in more detail in Chapter 4.

3. Across its support domain the function must integrate to one. This is the normalisation criterion:

$$\int_{\Omega} [W(r - r', h)] dr' = 1. \tag{3.7}$$

   Note however that the normalization condition $\sum_j W(r - r_j, h)V_j = 1$ in the discretized form is only valid for cases at the bulk of the fluid where the particles are well ordered, but not valid when the particles are randomly distributed or close to the boundaries or free surface [159].

4. The smoothing function should be positive within its support domain. This is required because it will be used in the method to model a physical system. A negative value of the smoothing function will result in unrealistic properties such as negative density and energy. This is not a theoretical requirement however simply a demand of the modelled process:

$$W(r - r', h) \geq 0. \tag{3.8}$$

5. The smoothing function should be a symmetric function. This means that the value of the function depends only on the separation of two particles and not their relative orientations:

$$\int_{\Omega}(r-r')[W(r-r',h)]dr'=0. \tag{3.9}$$

6. The weight applied to a particle should decrease as its distance from the central particle increases. This results in a function that monotonically decreases from its centre point.

7. The function should be continuous in nature and be smooth enough to avoid inaccuracies due to disordered or bunched particles.

A lot of different kernels have been used in literature; Lucy [98] used a bell shaped function in his early paper in the field by using the terminology broadening functions to refer to what is commonly now called smoothing function, and σ for the support domain, kh and $r = |r - r'|$ to describe the separation between particles. Some commonly used kernel functions in the literature will be discussed later in this chapter.

As $W(r-r',h)$ diverges from the Dirac delta $\delta(r-r')$, its support domain increases and the errors in the approximation increase. Recall the first criterion of the smoothing function Equation (3.5), which states as follow:

$$\lim_{h\to 0}[W(r-r',h)]=\delta(r-r'). \tag{3.10}$$

This indicates that the errors present in the approximation will be related to the smoothing length, h, of the chosen function. The error between Equations (3.1) and (3.4) as a result of this approximation can be obtained by using Taylor series expansion of $f(r')$ about (r) in Equation (3.4), as follows:

$$\begin{aligned} < f(r) > &= \int_{\Omega}[f(r)+f'(r)(r'-r)+B((r'-r)^2)]W(r-r',h)dr', \\ &= f(r)\int_{\Omega}W(r-r',h)dr' \\ &\quad +f'(r)\int_{\Omega}(r'-r)W(r-r',h)dr'+B(h^2). \end{aligned} \tag{3.11}$$

From Equation (3.11), it follows that $\int_\Omega W(r-r',h)dr'$ is unity and $\int_\Omega (r'-r)W(r-r',h)dr'$ is zero, as shown in Equation (3.7), and Equation (3.9), respectively. Using this information, Equation (3.11) now reduces to:

$$< f(r) > \quad = \quad f(r) + B(h^2), \tag{3.12}$$

where B is the remainder.

From Equation (3.12), it can be seen that the error in the kernel approximation is second order accurate $O(h^2)$ [19, 157]. The ability of the kernel approximation to accurately approximate an arbitrary polynomial is also largely dependent on the chosen smoothing function and how many of its moments satisfy the following conditions [18]:

$$\begin{cases} M_0 = \int_\Omega [W(r-r',h)]dr' & = 1 \\ M_1 = \int_\Omega (r-r')[W(r-r',h)]dr' & = 0 \\ M_2 = \int_\Omega (r-r')^2[W(r-r',h)]dr' & = 0 \\ ..... = ... & = 0 \\ ..... = ... & = 0 \\ ..... = ... & = 0 \\ ..... = ... & = 0 \\ M_n = \int_\Omega (r-r')^n[W(r-r',h)]dr' & = 0, \end{cases} \tag{3.13}$$

where M_0 and M_1 are the normalization and symmetric function criteria and have to be satisfied by any smoothing function. Therefore the basic SPH kernel approximation method can accurately reproduce a first order function and so can replicate any arbitrary linear relationship. This accuracy assessment only holds when the support domain of the smoothing function is completely within the computational domain. An example of when this is not the case is when the support domain crosses a domain boundary as illustrated for $1D$ space in Figure 3.2.

In this situation the smoothing function is cut off by the boundary and so can no longer satisfy the normalization and symmetric function criteria (M_0 and M_1), and therefore cannot replicate a constant value in the following Equations (3.14) and (3.15)

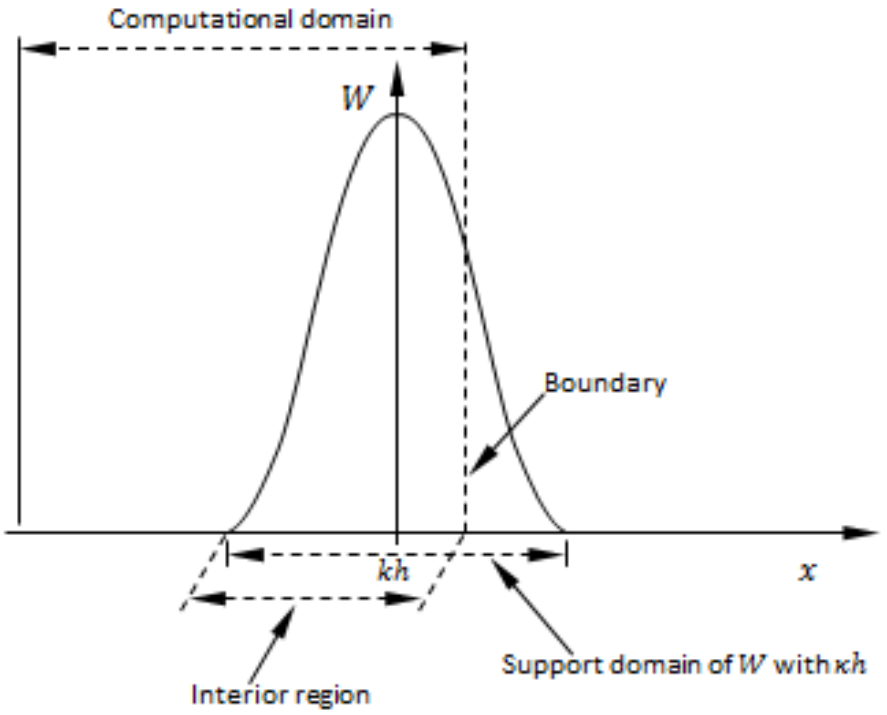

FIGURE 3.2: Truncation of a SPH smoothing function by a computational domain boundary.

$$\int_{\Omega}[W(r-r',h)]dr' \neq 1, \tag{3.14}$$

$$\int_{\Omega}(r-r')[W(r-r',h)]dr' \neq 0. \tag{3.15}$$

In order to avoid such truncation at the boundary, remedy, such as introducing ghost or dummy particles at the boundary should be made to resolve such boundary effects. Details of such boundary conditions will be discussed later in this Chapter 3.

3.3.1.1 Types of Kernel

Several types of kernel are described in Liu *et al.* [18] and Monaghan [19, 160]. Some details of these are given below.

Gaussian

Monaghan states that for the correct reconstruction of a physical process a Gaussian function represents the best possible choice [19] and this is seen in his early work [99]. In 2 and 3 dimensions, the function and its derivative used is given in Equations (3.16) and (3.17), respectively. In Monaghan's and Gingold's early paper [99], this function was not described as being limited to a compact support domain, most likely because the number of particles considered was small. The Gaussian kernel gives good results because it approximates the Dirac function correctly.

$$W(\mathbf{r}-\mathbf{r}',h) = W(q,h) = \alpha_D exp(-q^2) \qquad 0 \leq q \leq \infty, \tag{3.16}$$

$$\frac{dW(q,h)}{dr} = \frac{-2q}{h}\alpha_D exp(-q^2) \qquad 0 \leq q \leq \infty, \tag{3.17}$$

where $q = |\mathbf{r}-\mathbf{r}'|/h$, $\frac{dW(q,h)}{dr}$ is its derivative and $|\mathbf{r}-\mathbf{r}'|$ being the scaler distance between particle a and b and α_D is the dimensional factor (normalizer) which is $1/(\pi h^2)$ in $2D$ and $1/(\pi^{3/2}h^3)$ in $3D$ (see Figure 3.3 for the Gaussian kernel).

This kernel suffers from lack of compact support and can be very computationally expensive. Even if compact support is enforced in a similar manner to Lucy's [98] smoothing function, Monaghan *et al.* [161] indicated that a support domain of at least three times the smoothing length, h, is required for a Gaussian kernel to produce good results. This mean that a lot of particles will need to be included in the support domain, thus leading to a high computationally expensive process. However, it is possible to reduce this requirement for a large support domain by using a different kernel with a narrower compact support without drastically reducing accuracy.

Quadratic

In this kernel, the derivative of the kernel always increases as the particles move closer, and always decreases as they move apart. This makes it possible to prevent particles clustering in compression problems without the need for tensile correction. Also the minimum reflection point for the gradient in this kernel occurs at $q = 0.1$ out of 2.0 compared to other kernels, for example, the cubic occurs at $q = 0.75$ out of 2.0. This high range of the quadratic kernel is responsible for the long inter-particles

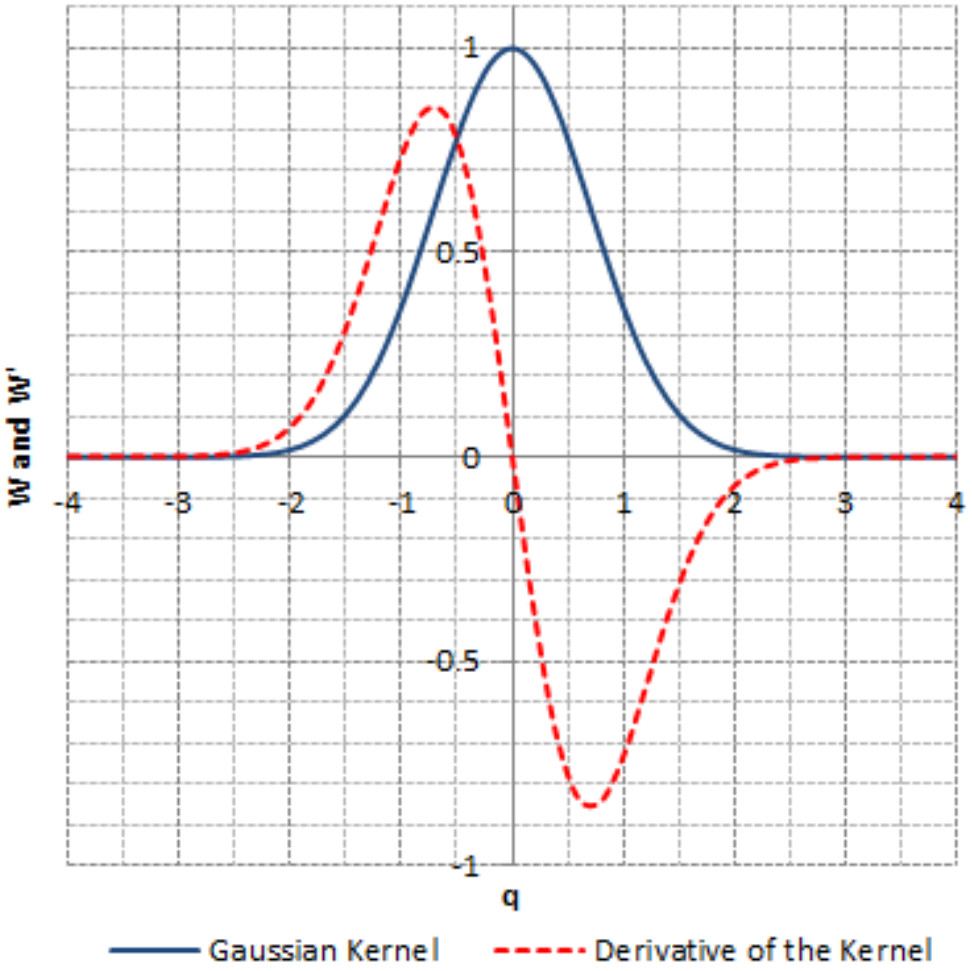

FIGURE 3.3: Gaussian kernel and its derivative divided by the dimensional factor α_D.

repulsion taking place when $q \geq 0.1$, before diminishing return creep in when $q < 0.1$. Johnson *et al.*, [145] used this smoothing function to simulate the high velocity impact problem because its has simple low-order making it computationally cheap and no extremum in the gradient [162]. However, due to its low-order, it is not suitable for simulating physical phenomena where higher-order interpolation are required to capture important physics. This is unlike the B-spline in which its derivative exhibits a maximum value and then decreases for both when the nodes move closer or further apart, thus creating an unrealistic phenomena which leads to compressive instability.

$$W(q,h) = \alpha_D \left[\frac{3}{16}q^2 - \frac{3}{4}q + \frac{3}{4}\right] \qquad 0 \leq q \leq 2, \tag{3.18}$$

$$\frac{dW(q,h)}{dr} = \frac{\alpha_D}{h}\left[\frac{3}{8}q - \frac{3}{4}\right] \qquad 0 \leq q \leq 2, \tag{3.19}$$

where α_D is $2/(\pi h^2)$ in $2D$ and $5/(4\pi h^3)$ in $3D$.

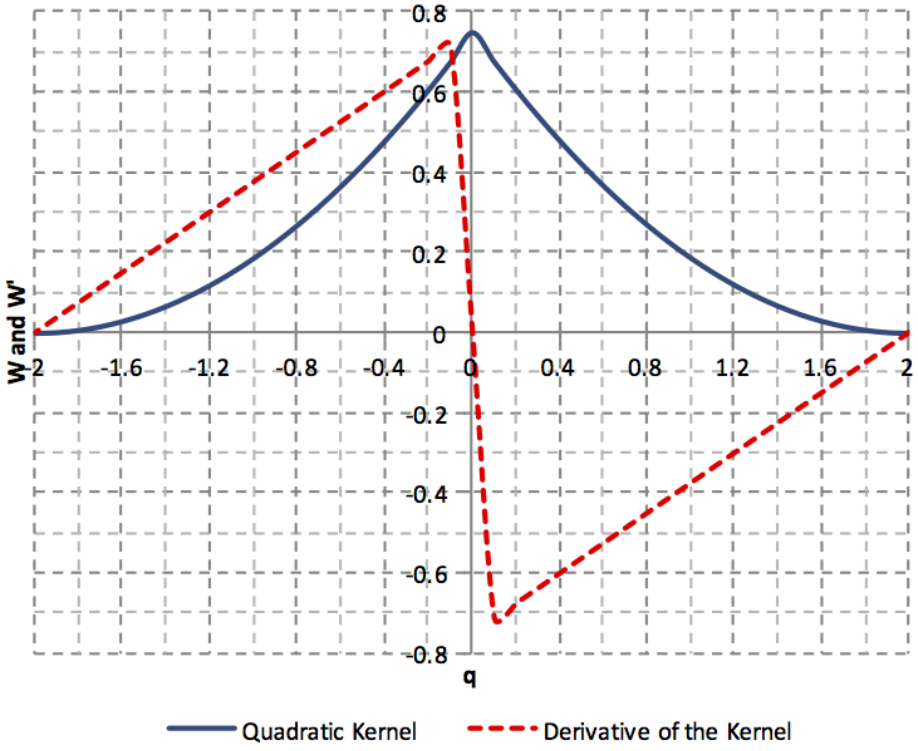

FIGURE 3.4: Quadratic kernel and its derivative divided by the dimensional factor α_D.

Cubic spline

The cubic spline kernel is the most widely used smoothing function, since it resemble the Gaussian kernel, but with a narrower compact support. The main advantages of this kernel is that it has compact support which is equal to zero for $q \geq 2$, hence reducing the numerical computations required. However, it suffers from some form of attraction at some region of the compact support.

$$W(q,h) = \alpha_D \begin{cases} 1 - \frac{3}{2}q^2 + \frac{3}{4}q^3, & \text{if } 0 \leq q < 1, \\ \frac{1}{4}(2-q)^3, & \text{if } 1 \leq q < 2, \\ 0 & \text{if } q \geq 2, \end{cases} \tag{3.20}$$

$$\frac{dW(q,h)}{dr} = \frac{\alpha_D}{h} \begin{cases} -3q + \frac{9}{4}q^2, & \text{if } 0 \leq q < 1, \\ -\frac{3}{4}(2-q)^3, & \text{if } 1 \leq q < 2, \\ 0 & \text{if } q \geq 2, \end{cases} \tag{3.21}$$

where α_D is $10/(7\pi h^2)$ in $2D$ and $1/(\pi h^3)$ in $3D$.

As can be seen, the minimum reflection point for the gradient in the Cubic kernel occurs at $q = 0.75$ compared to other kernels, for example, the Wendland kernel where the minimum reflection point is $q = 0.5$. From the SPH discretised Navier-Stokes equation (see Equation), the pressure gradient term is influence by ∇W and the wider positive range is delineated by the dash-red line of the Wendland kernel (between 0.5 and 2.0) as shown in Figure; while for other kernels, for example, the cubic kernel has a range between 0.75 and 2.0. This allows inter-particles repulsion to occur over a wider range (when $q \geq 0.5$) before diminishing returns after the inflection point (when $q < 0.5$).

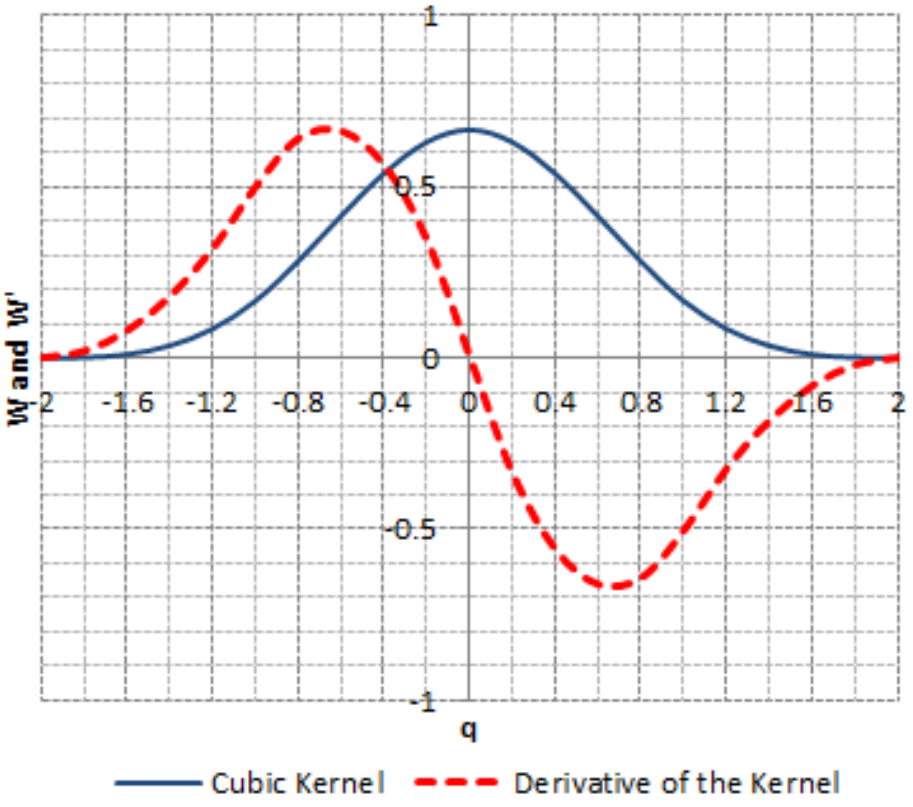

FIGURE 3.5: Cubic Spline kernel and its derivative divided by the dimensional factor α_D.

Quintic (Wendland, 1995)

The results from Panizzo *et al.*, [163], shows that the best compromise between accuracy and computation cost in term of time is obtained by using the Wendland kernel. In general, kernels with higher-order will always gives higher-order interpolation necessary to capture important physical phenomena, thus leading to greater stability and accuracy of the SPH scheme [164].

$$W(q,h) = \alpha_D \left(1 - \frac{q}{2}\right)^4 (2q+1) \qquad 0 \leq q \leq 2, \tag{3.22}$$

$$\frac{dW(q,h)}{dr} = -5q\frac{\alpha_D}{h}\left(1 - \frac{q}{2}\right)^3 \qquad 0 \leq q \leq 2, \tag{3.23}$$

where α_D is $7/(4\pi h^2)$ in $2D$ and $7/(8\pi h^3)$ in $3D$.

Interestingly, the gradient of the kernel has a minimum reflective point at $q = 0.5$ out of 2.0, thus allowing it to have a wide range of inter-particle repulsion necessary to prevent tensile instability. Tensile instability (clumping) is the process whereby two or more particles join together, thus resulting in instability of the SPH scheme.

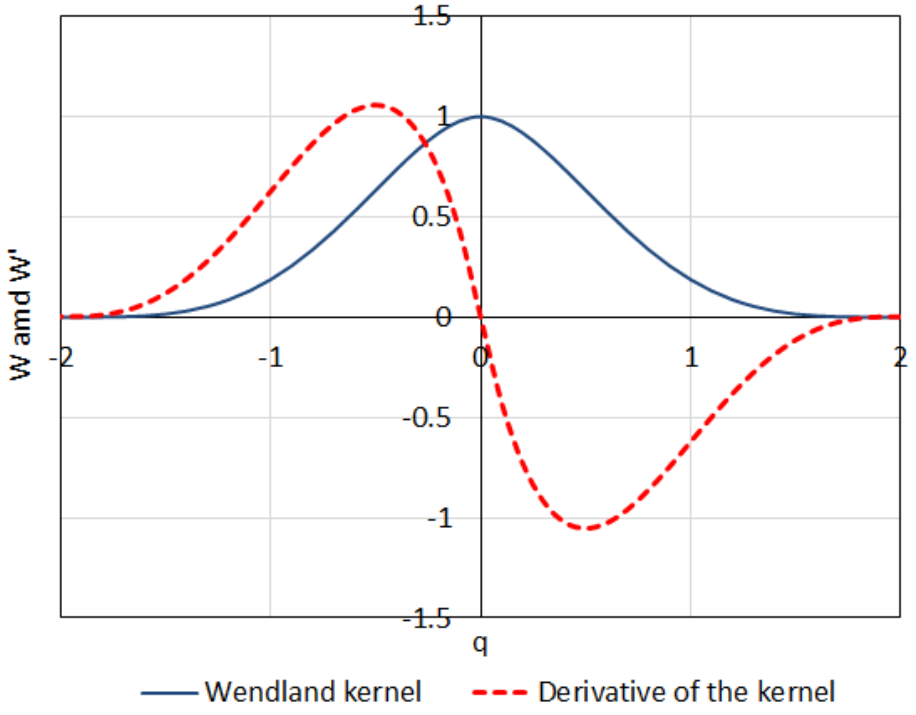

FIGURE 3.6: Quintic (Wendland) kernel and its derivative divided by the dimensional factor α_D.

Bell-shaped

This kernel function was used by Lucy [98]. It has a narrow compact support, hence making it computational less expensive to use. It is however less accurate, since the number of complete neighbour particles are few, thereby violating the unity condition of the kernel.

$$W(q,h) = \alpha_D \begin{cases} (1+3q)(1-q)^3, & \text{if } 0 \leq q < 1, \\ 0 & \text{if } q \geq 1, \end{cases} \tag{3.24}$$

$$\frac{dW(q,h)}{dr} = \frac{\alpha_D}{h} \begin{cases} -12(1-q)^2, & \text{if } 0 \leq q < 1, \\ 0 & \text{if } q \geq 1, \end{cases} \tag{3.25}$$

where α_D is $5/(\pi h^2)$ in $2D$ and $105/(16\pi h^3)$ in $3D$.

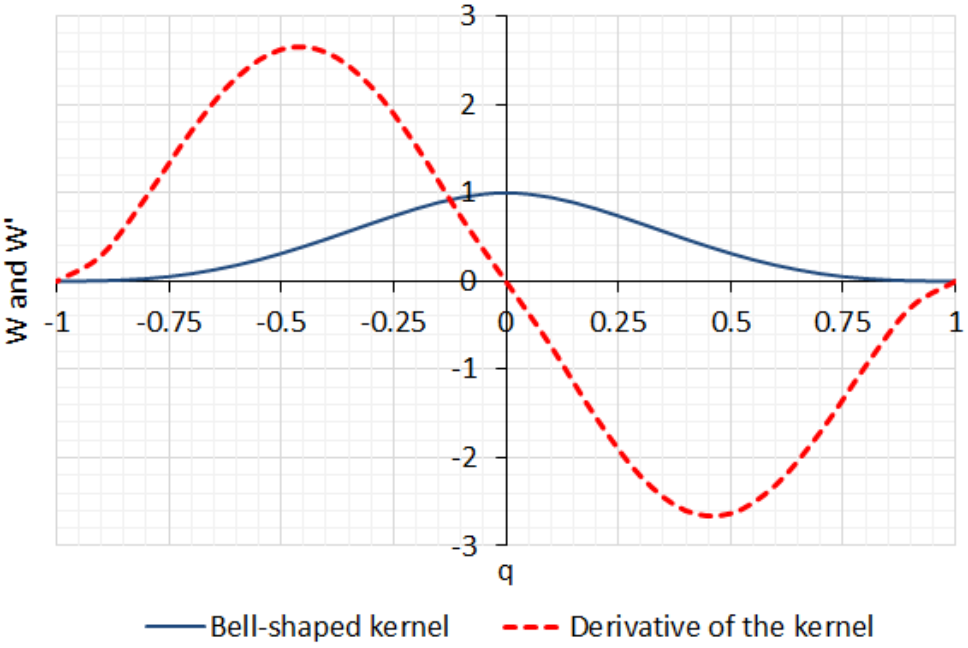

FIGURE 3.7: Bell-shaped kernel and its derivative divided by the dimensional factor α_D.

Quartic

This kernel function was introduced by Morris [164, 165] in his paper. This kernel has a higher order spline, thus making it more stable, but with higher computational

effort because of its region of contributing neighbour are larger (compact support is $2.5h$).

$$W(q,h) = \alpha_D \begin{cases} (2.5-q)^4 - 5(1.5-q)^4 + 10(0.5-q)^4, & \text{if } 0 \leq q < 0.5, \\ (2.5-q)^4 - 5(1.5-q)^4, & \text{if } 0.5 \leq q < 1.5, \\ (2.5-q)^4, & \text{if } 1.5 \leq q < 2.5, \\ 0 & \text{if } q \geq 2.5, \end{cases} \tag{3.26}$$

$$\frac{dW(q,h)}{dr} = \frac{\alpha_D}{h} \begin{cases} -4(2.5-q)^3 + 20(1.5-q)^3 - 40(0.5-q)^3, & \text{if } 0 \leq q < 0.5, \\ -4(2.5-q)^3 + 20(1.5-q)^3, & \text{if } 0.5 \leq q < 1.5, \\ -4(2.5-q)^3, & \text{if } 1.5 \leq q < 2.5, \\ 0 & \text{if } q \geq 2.5, \end{cases} \tag{3.27}$$

where α_D is $96/(1199\pi h^2)$ in $2D$ and $1/(20\pi h^3)$ in $3D$.

Quintic

This kernel function was also introduced by Morris [164, 165]. This kernel has a more higher order splines than the quartic kernel, thus making its much more stable, but with much more higher computational effort because of its region of contributing neighbour are much more larger (compact support is $3h$).

$$W(q,h) = \alpha_D \begin{cases} (3-q)^5 - 6(2-q)^5 + 15(1-q)^5, & \text{if } 0 \leq q < 1, \\ (3-q)^5 - 6(2-q)^5, & \text{if } 1 \leq q < 2, \\ (3-q)^5, & \text{if } 2 \leq q < 3, \\ 0 & \text{if } q \geq 3, \end{cases} \tag{3.28}$$

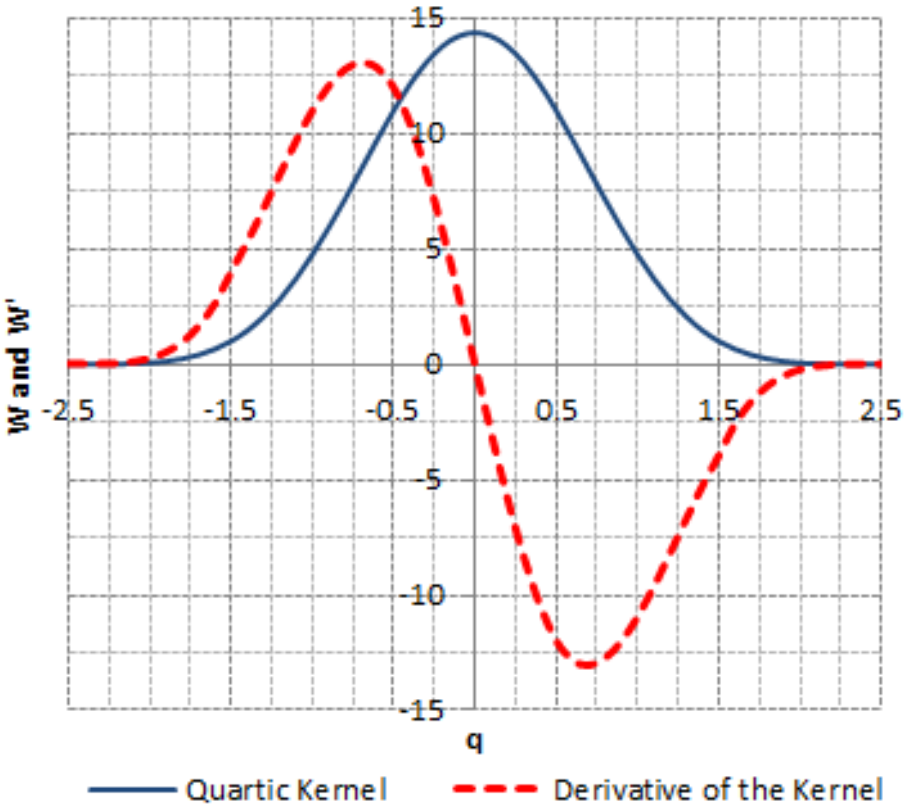

FIGURE 3.8: Quartic kernel and its derivative divided by the dimensional factor α_D.

$$\frac{dW(q,h)}{dr} = \frac{\alpha_D}{h}\begin{cases} -5(3-q)^4 + 30(2-q)^4 - 75(1-q)^4, & \text{if } 0 \leq q < 1, \\ -5(3-q)^4 + 30(2-q)^4, & \text{if } 1 \leq q < 2, \\ -5(3-q)^4, & \text{if } 2 \leq q < 3, \\ 0 & \text{if } q \geq 3, \end{cases} \tag{3.29}$$

where α_D is $7/(478\pi h^2)$ in $2D$ and $3/(359\pi h^3)$ in $3D$.

Poly6, Spiky and Viscosity

These are special kernel functions designed for specific purposes. The poly6 kernel, is used for calculating any other physical quantities except pressure and viscosity properties. This is due to the fact that particles tend to cluster when they come close because its gradient approaches zero at the center, thus making the repulsion

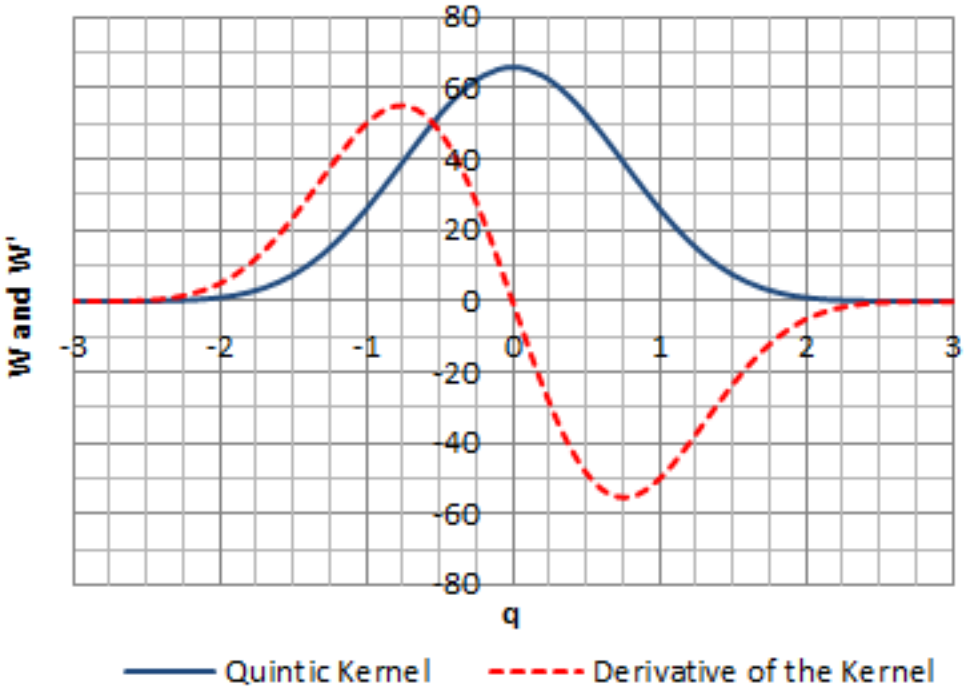

FIGURE 3.9: Quintic kernel and its derivative divided by the dimensional factor α_D.

to vanished. For the spiky kernel function, it is used to calculate the pressure quantity because it able to repel the particles as they come close, since the gradient do not approaches zero at the center, while the viscosity kernel is used to calculate the viscosity quantity because its always has a positive component. The poly6 kernel is described by the following functions:

$$W(q,h) = \alpha_D \begin{cases} (1-q^2)^3, & \text{if } 0 \leq q < 1, \\ 0 & \text{if } q \geq 1, \end{cases} \tag{3.30}$$

$$\frac{dW(q,h)}{dr} = \frac{\alpha_D}{h} \begin{cases} -6q(1-q^2)^2, & \text{if } 0 \leq q < 1, \\ 0 & \text{if } q \geq 1, \end{cases} \tag{3.31}$$

where α_D is $4/(\pi h^2)$ in $2D$ and $315/(64\pi h^3)$ in $3D$.

The spiky kernel function is given by:

$$W(q,h) = \alpha_D \begin{cases} (1-q)^3, & \text{if } 0 \leq q < 1, \\ 0 & \text{if } q \geq 1, \end{cases} \tag{3.32}$$

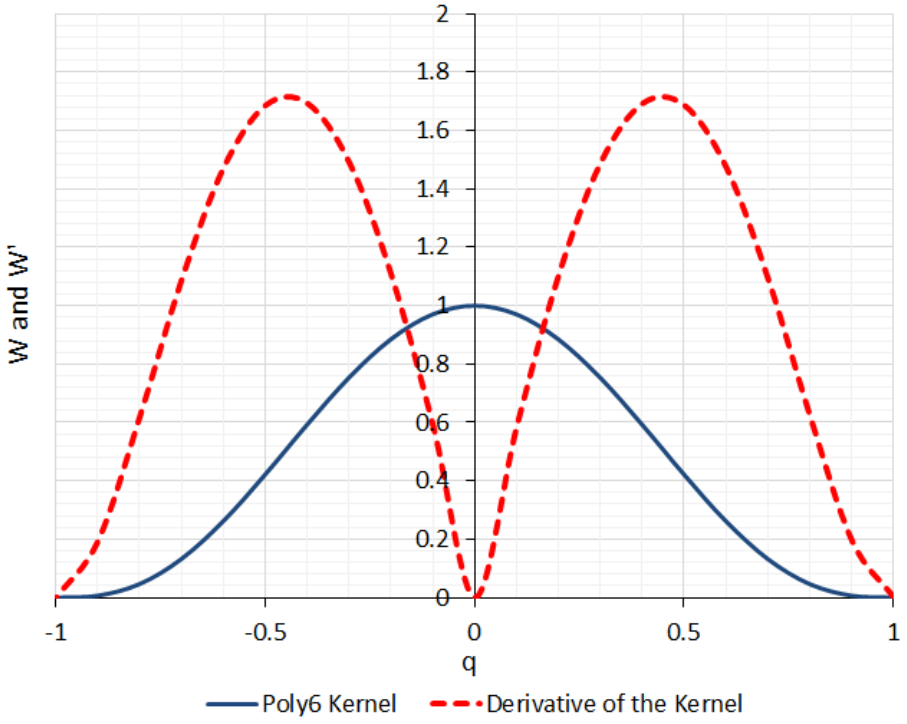

FIGURE 3.10: Poly6 kernel and its derivative divided by the dimensional factor α_D.

$$\frac{dW(q,h)}{dr} = \frac{\alpha_D}{h}\begin{cases} -3(1-q)^2, & \text{if } 0 \leq q < 1, \\ 0 & \text{if } q \geq 1, \end{cases} \tag{3.33}$$

where α_D is $\frac{10}{\pi h^2}$ in $2D$ and $\frac{15}{\pi h^3}$ in $3D$.

The viscosity kernel function is given by:

$$W(q,h) = \alpha_D \begin{cases} -\frac{q^3}{2} + q^2 + \frac{1}{2q} - 1, & \text{if } 0 \leq q < 1, \\ 0 & \text{if } q \geq 1, \end{cases} \tag{3.34}$$

$$\frac{dW(q,h)}{dr} = \frac{\alpha_D}{h}\begin{cases} \left(-\frac{3q}{2} + 2q + \frac{-1}{2q^2}\right) & \text{if } 0 \leq q < 1, \\ 0 & \text{if } q \geq 1, \end{cases} \tag{3.35}$$

where α_D is $\frac{10}{3\pi h^2}$ in $2D$ and $\frac{15}{2\pi h^3}$ in $3D$.

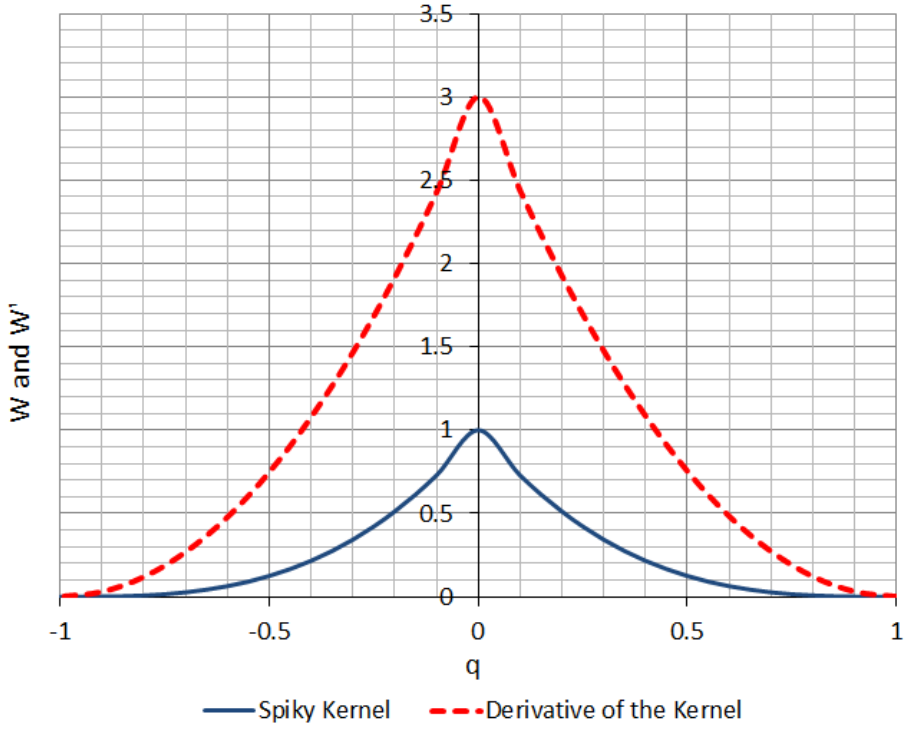

FIGURE 3.11: Spiky kernel and its derivative divided by the dimensional factor α_D.

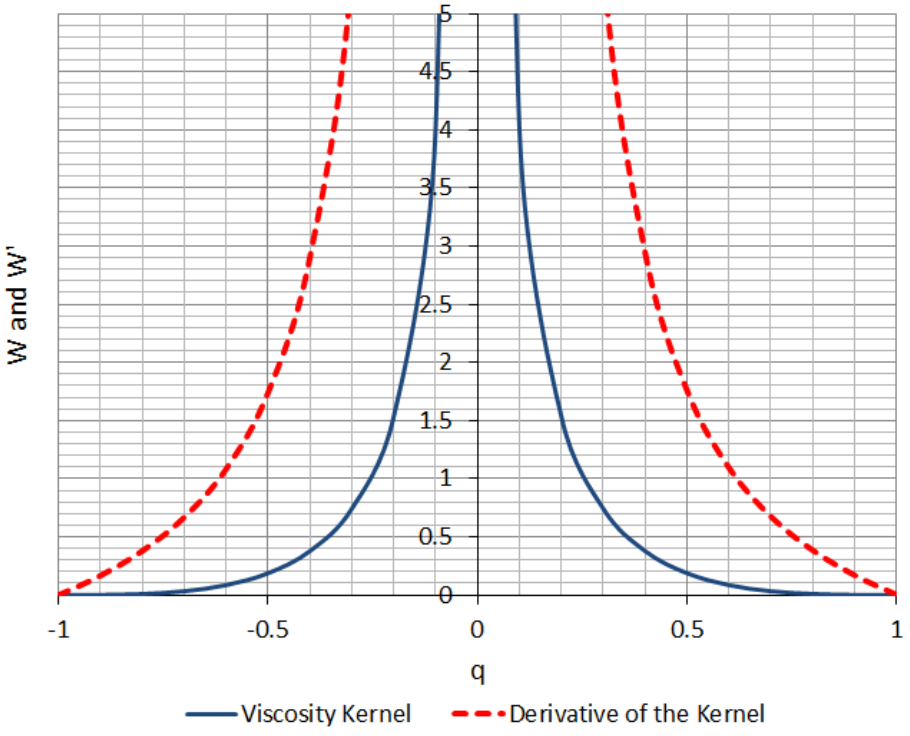

FIGURE 3.12: Viscosity kernel and its derivative divided by the dimensional factor α_D.

3.3.2 Integral representation of spatial derivative of a function

The gradient or spatial derivative of a function can be estimated in a similar way by substituting $\nabla f(r)$ for $f(r)$ in the kernel approximation Equation (3.4) to have the following equation:

$$< \nabla f(r) >= \int_{\Omega} \nabla f(r')W(r - r', h)dr', \tag{3.36}$$

where $\nabla f(r)$ represent the gradient of an arbitrary scaler function $f(r)$.

Now, applying the following identity:

$$[\nabla f(r')W(r - r', h)] = \nabla f(r')W(r - r', h) - f(r')\nabla W(r - r', h), \tag{3.37}$$

and also using the divergence theorem to convert it into an integral over the surface, S, of the domain of the integration Ω, the derivative estimate becomes:

$$< \nabla f(r) >= \int_{S} f(r')W(r - r', h)\vec{n}dS - \int_{\Omega} f(r')\nabla W(r - r', h)dr'. \tag{3.38}$$

Since the integration is taken across the support domain and the smoothing function is defined as being compactly supported when the support domain is located within the computational domain (see Figure 3.13), the surface integral term "$\int_S f(r')W(r - r', h)\vec{n}dS$" in the above equation will equate to zero. If the support domain overlaps with the computational domain, i.e. the smoothing function W is truncated by the computational domain (see Figure 3.2), then this surface integral is no longer equal to zero. When this happen, modification should be made to remedy the boundary effects of the surface integral (see Subsection 3.3.1 for details on how this is done). In the case of the support domain defined within the computational domain, the above Equation (3.38) simplifies to:

$$< \nabla f(r) >= -\int_{\Omega} f(r')\nabla W(r - r', h)dr'. \tag{3.39}$$

This Equation (3.39) is very useful, because it gives the ability to estimate the spatial derivative of a function from the gradient of the smoothing function, W, instead of the gradient of the function, $f(r)$ itself.

The same process can be applied to a vector function via the divergence operator $(\nabla\cdot)$. This is described mathematically as follows:

$$< \nabla \cdot \boldsymbol{f}(r) >= \int_{\Omega} \nabla \cdot \boldsymbol{f}(r') W(r - r', h) dr', \tag{3.40}$$

where $\nabla \cdot \boldsymbol{f}(r)$ represent the divergence of an arbitrary vector function $\boldsymbol{f}(r)$ and applying the identity:

$$[\nabla \cdot \boldsymbol{f}(r') W(r - r', h)] = \nabla \cdot \boldsymbol{f}(r') W(r - r', h) - \boldsymbol{f}(r') \cdot \nabla W(r - r', h), \tag{3.41}$$

the divergence is estimated as:

$$< \nabla \cdot \boldsymbol{f}(r) >= \int_{S} \boldsymbol{f}(r') W(r - r', h) \cdot \vec{n} dS - \int_{\Omega} \boldsymbol{f}(r') \cdot \nabla W(r - r', h) dr', \tag{3.42}$$

which simplifies to:

$$< \nabla \cdot \boldsymbol{f}(r) >= - \int_{\Omega} \boldsymbol{f}(r') \cdot \nabla W(r - r', h) dr'. \tag{3.43}$$

The next step in developing an SPH model is to convert this kernel approximation into a discrete form called the particle approximation.

3.3.3 Particle Approximation

The entire system in SPH method is represented by a finite number of particles that carry individual masses and occupy individual spaces. The previous session discusses SPH method when applied to continuous set of equations. In order to have a discrete set of equations that can be solved by interpolating the field variables of interest (see

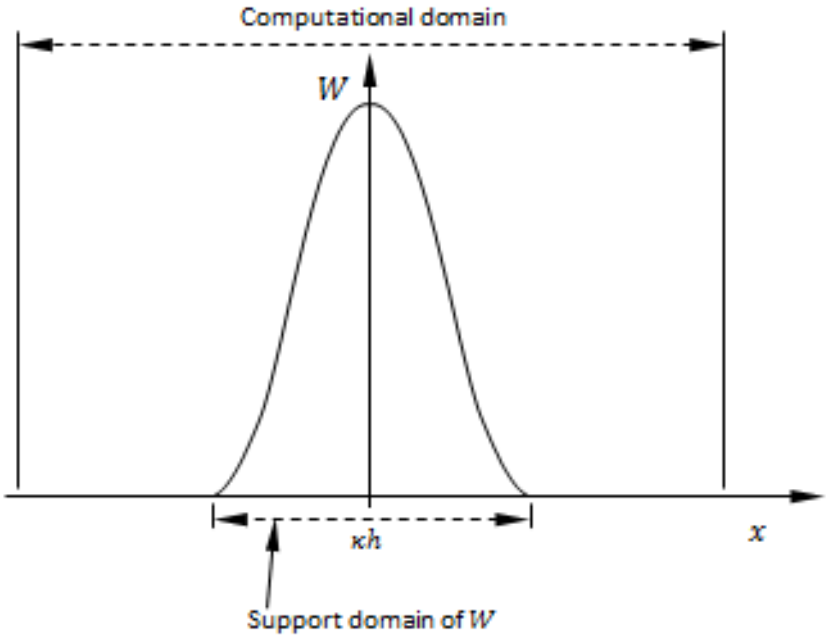

FIGURE 3.13: Support domain of smoothing function W and computational domain

Figure 3.14), the smoothing function must be used to replace the Dirac delta function in Equation (3.1) to give Equation (3.4). This discretized process of summation over the particles is commonly referred to as particle approximation in SPH literature.

If the infinitesimal volume dr' in the above integration Equation (3.4) at the location of particle j is replaced by the finite volume of the particle, ΔV_j, then the mass, m_j, of the particles is given by:

$$m_j = \Delta V_j \rho_j. \tag{3.44}$$

where ρ_j is the density of particle $j(= 1, 2, 3, ...N)$ in which N is the total number of neighbouring particles within the support domain of particle i. Now, the continuous SPH integral representation Equation (3.4) can be written in the following form of the discretized particle approximation as:

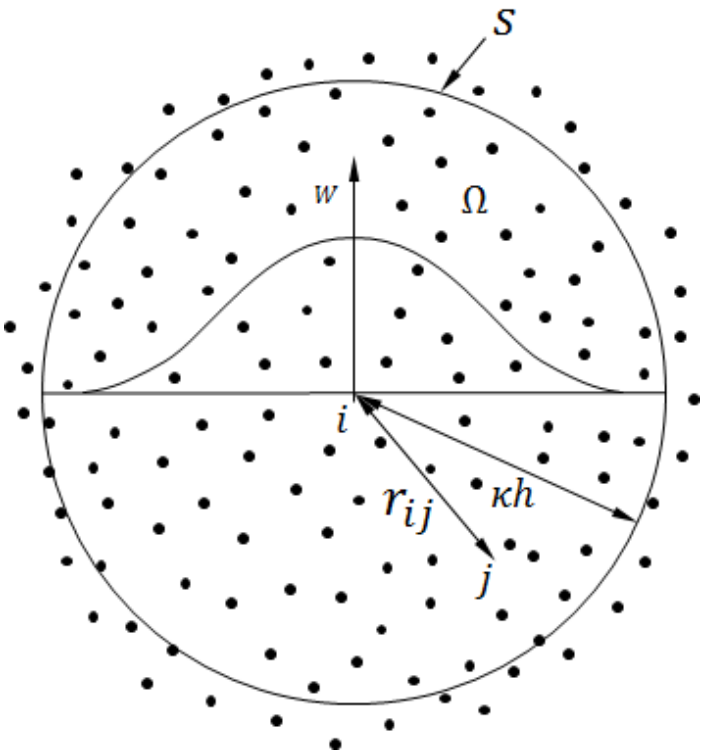

FIGURE 3.14: Particle approximations using particles within the support domain of the smoothing function W for particle i

$$
\begin{aligned}
f(r_i) &= \int_\Omega f(r')W(r_i - r', h)dr' && \text{continuous form} \\
&\approx \sum_{j=1}^{N} f(r_j)W(r_i - r_j, h)\Delta V_j && \text{discretized form} \quad (3.45) \\
&\approx \sum_{j=1}^{N} f(r_j)W(r_i - r_j, h)\frac{1}{\rho_j}(\rho_j \Delta V_j) \\
&\approx \sum_{j=1}^{N} f(r_j)W(r_i - r_j, h)\frac{1}{\rho_j}(m_j), \\
\textit{or} & \\
f(r_i) &\approx \sum_{j=1}^{N} \frac{m_j}{\rho_j} f(r_j)W(r_i - r_j, h). && (3.46)
\end{aligned}
$$

So, the particle approximation for a function at particle i in SPH notation can be written as:

$$< f(r_i) >= \sum_{j=1}^{N} \frac{m_j}{\rho_j} f(r_j) W_{ij}. \tag{3.47}$$

where $W_{ij} = W(r_i - r_j, h)$.

Following the same argument, the particle approximation for the spatial derivation of the function Equation (3.39) in discretized form would be:

$$< \nabla f(r_i) > \approx - \sum_{j=1}^{N} \frac{m_j}{\rho_j} f(r_j) \nabla W(r_i - r_j, h), \tag{3.48}$$

where $\nabla W(r_i - r_j, h)$ in the above Equation (3.48) is taken with respect to the particle j. The particle approximation for a function at particle i in discretized form can finally be written as:

$$< \nabla f(r_i) >= \sum_{j=1}^{N} \frac{m_j}{\rho_j} f(r_j) \nabla_i W_{ij}, \tag{3.49}$$

$$\nabla_i W_{ij} = \frac{\vec{r}_i - \vec{r}_j}{|\vec{r}_{ij}|} \frac{\partial W_{ij}}{\partial r_{ij}} = \frac{\vec{r}_{ij}}{|\vec{r}_{ij}|} \frac{\partial W_{ij}}{\partial r_{ij}}. \quad where \quad \vec{r}_i - \vec{r}_j \quad \text{is replace by} \quad \vec{r}_{ij}, \tag{3.50}$$

where $\vec{r}_{ij}$ is the separation within the vector form (separation) and $|\vec{r}_{ij}|$ the scalar form (magnitude) respectively. The negative sign in Equation (3.48) is removed in Equation (3.49) because, $\nabla_i W_{ij}$ is taken with respect to particle i.

The summation in Equations (3.47) and (3.49) are taken over all the neighbour particles within the support domain. Using particle approximation has a significant and detrimental effect on the accuracy of the basic SPH method. This approximation has the same requirements for accuracy as the kernel approximation and the discrete formulations of the normalization and symmetric conditions (M_0 and M_1) as shown in Equation (3.13).

The fundamental issue affecting the accuracy of the particle approximation stems from the switch to a discrete summation rather than a continuous integration across the support domain for both the continuous integral representations of a function

and also its derivatives. Even if a smoothing function meets the symmetric criterion for an interior region in the kernel approximation, it will not always be met in the particle approximation unless the particles are sufficiently ordered (see Figure 3.15 (a) for regular order). The issue of stability at boundary regions due to truncation of the smoothing function (see Subsection 3.3.1) still exists and suffers from the same root cause as in the kernel approximation where the normalization and symmetric criteria are not met due to truncation of the smoothing function support domain as shown in Figure 3.15 (b). In addition, the symmetric criterion is not met when the particles are not evenly spaced or have instead become disordered. It can be seen clearly from Figure 3.15 (c) that the first moment taken across the discrete particles will not equate to zero.

It can be seen that from Equations (3.47) and (3.49) that density and mass are already included in the equations. This make it possible to apply this particle approximation to hydrodynamic problems where density is the main field variable that is use to calculate other fluid properties such as pressure [166]. With this approximation, the SPH method becomes simple and straightforward for simulating fluid dynamic flow problems.

3.3.3.1 Different Derivatives of SPH Formulations

SPH formulation can be obtained for partial differential equations with the above mentioned technique using particle and kernel approximations. The most prominent approach was described by Monaghan [19], who used Equations (3.47) and (3.49) directly. Monaghan suggested to put the density within the gradient operator as follows:

$$\nabla f = \frac{1}{\rho}[\nabla(\rho f) - f\nabla\rho], \tag{3.51}$$

or

$$\nabla f = \rho\left[\nabla\left(\frac{f}{\rho}\right) + \frac{f}{\rho^2}\nabla\rho\right]. \tag{3.52}$$

Now, Equation (3.51) can be rewrites as:

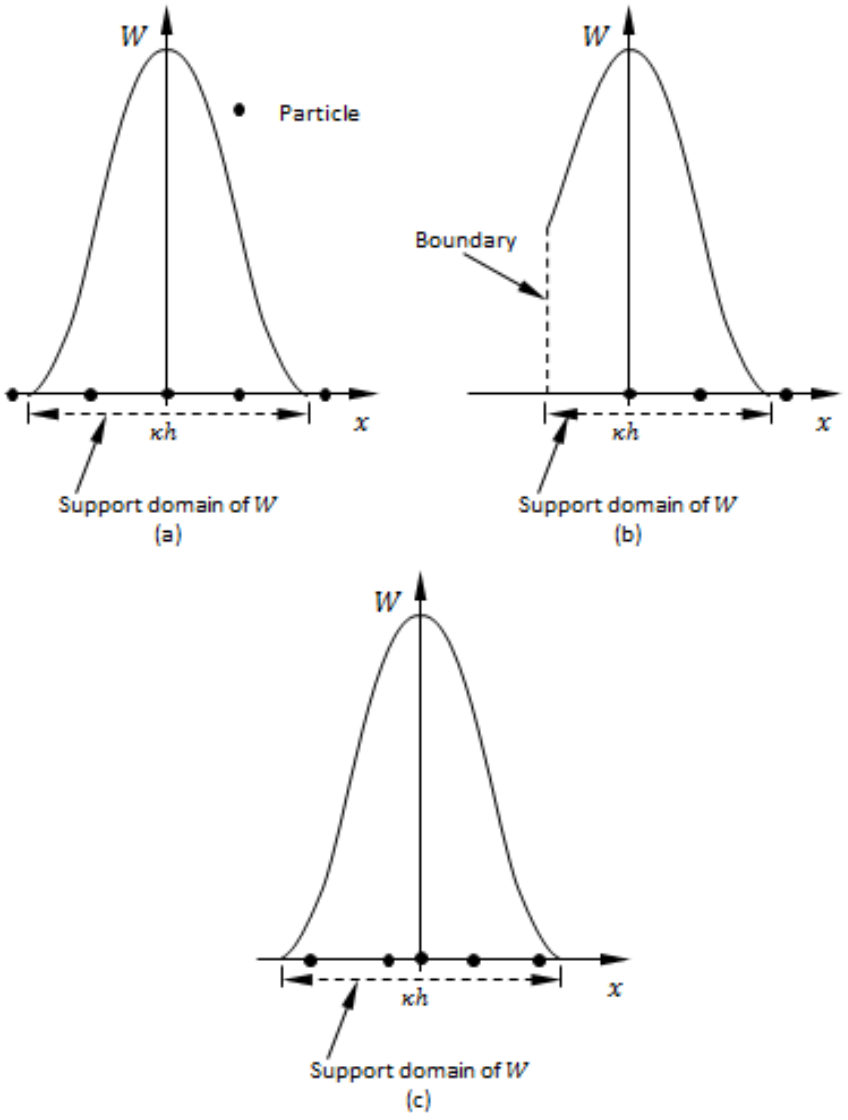

FIGURE 3.15: How boundaries and particle disorder affect the accuracy of the SPH particle representation.

$$
\begin{aligned}
(\nabla f)_i &= \frac{1}{\rho_i}[\nabla(\rho f) - f\nabla\rho]_i, \\
&\doteq \frac{1}{\rho_i}\nabla\int_\Omega (\rho f)W(r-r',h)dr' - \frac{f}{\rho_i}\int_\Omega (\nabla\rho)W(r-r',h)dr', \\
&\doteq \frac{1}{\rho_i}\sum_{j=1}^{N}\frac{m_j}{\rho_j}(\rho f)_j\nabla W(r_i-r_j,h) - \frac{f_i}{\rho_i}\sum_{j=1}^{N}\frac{m_j}{\rho_j}\rho_j\nabla W(r_i-r_j,h), \\
&\doteq \frac{1}{\rho_i}\sum_{j=1}^{N} m_j f_j\nabla W_{ij} - \frac{1}{\rho_i}\sum_{j=1}^{N} m_j f_i\nabla W_{ij}, \\
&\doteq -\frac{1}{\rho_i}\sum_{j=1}^{N} m_j f_{ij}\nabla_i W_{ij}, \qquad (3.53)
\end{aligned}
$$

where $f_{ij} = f_i - f_j$ and $W_{ij} = W(r_i - r_j, h)$.

Similarly, using the same logic, Equation (3.52) can be rewrites as follows:

$$\begin{aligned}
(\nabla f)_i &= \rho_i \left[\nabla \left(\frac{f}{\rho} \right) + \frac{f}{\rho^2} \nabla \rho \right]_i, \\
&\doteq \rho_i \nabla \int_\Omega \left(\frac{f}{\rho} \right) W(r - r', h) dr' + \rho_i \frac{f}{\rho_i^2} \int_\Omega (\nabla \rho) W(r - r', h) dr', \\
&\doteq \rho_i \sum_{j=1}^{N} \frac{m_j}{\rho_j} \left(\frac{f}{\rho} \right)_j \nabla W(r_i - r_j, h) + \frac{f_i}{\rho_i} \sum_{j=1}^{N} \frac{m_j}{\rho_j} \rho_j \nabla W(r_i - r_j, h), \\
&\doteq \rho_i \left(\sum_{j=1}^{N} \frac{m_j}{\rho_j^2} f_j \nabla W_{ij} + \frac{f_i}{\rho_i^2} \sum_{j=1}^{N} m_j \nabla W_{ij} \right), \\
&\doteq \rho_i \sum_{j=1}^{N} m_j \left(\frac{f_j}{\rho_j^2} + \frac{f_i}{\rho_i^2} \right) \nabla_i W_{ij}. \qquad (3.54)
\end{aligned}$$

From Equations (3.53) and (3.54), it can be seen that they are symmetric and anti-symmetric respectively when i and j are interchanged. Equation (3.54) is often used for pressure gradient calculation in physical simulation and because of its antisymmetric nature and the particle function values appear in pairs, momentum is conserved [19]. This Equation (3.54) is used in this thesis for computing the momentum due to pressure because it obey Newton's third Law, that is $< \nabla f >_{ij} = - < \nabla f >_{ji}$ [18].

Alternatively, Bonet and Lot [167] suggested the following form for Equation (3.54):

$$(\nabla f)_i = \sum_{j=1}^{N} \frac{m_j}{\rho_j} (f_j + f_i) \nabla_i W_{ij}, \qquad (3.55)$$

which has stability properties that is independent of the background pressure, but lack momentum conservation [164].

3.3.4 SPH discretization of Navier-Stokes equations

The Navier-Stokes equations (N-S) are formulated based on the assumption that the fluid, at the scale of interest, is a continuum, which mean that it is not made up of discrete particles but rather a continuous substance. Another necessary assumption

is that, all the fields of interest like velocity, density, temperature and so on are differentiable, at least weakly [168]. This section highlight the derived SPH approximation to the N-S equations. The N-S formulation for the conservation of mass, momentum and energy in Lagrangian form are written respectively as follow:

$$\frac{D\rho}{Dt} = \rho\nabla\cdot\vec{\mathbf{v}}, \tag{3.56}$$

$$\frac{D\vec{\mathbf{v}}}{Dt} = -\frac{1}{\rho}\nabla p + \frac{1}{\rho}\nabla\cdot\tau + \frac{\vec{\mathbf{F}}}{\rho}, \tag{3.57}$$

$$\frac{De}{Dt} = -\frac{p}{\rho}\nabla\cdot\vec{\mathbf{v}} + \frac{1}{\rho}\tau:\nabla\cdot\vec{\mathbf{v}} - \frac{1}{\rho}\nabla\cdot\vec{\mathbf{q}}, \tag{3.58}$$

where $\vec{\mathbf{v}}$ is the particle velocity, p is the pressure, ρ is the particle density, t is the time $\vec{\mathbf{F}}$ is the body force, τ is the viscous stress tensor and $\vec{\mathbf{q}}$ is the heat flux. The viscous stress tensor is expressed as:

$$\tau = 2\mu\epsilon - \frac{2}{3}\mu(\nabla\cdot\vec{\mathbf{v}})\boldsymbol{I}, \tag{3.59}$$

where μ is the viscosity, $\boldsymbol{I}$ is the unit tensor, ϵ is the change in deformation tensor and

$$\epsilon = \frac{1}{2}[\nabla\cdot\vec{\mathbf{v}} + (\nabla\cdot\vec{\mathbf{v}})^T]. \tag{3.60}$$

3.3.4.1 Particle Approximation of Density

There are two ways to approximate particle density. The first method is the summation density approach. For a given particle i, the density with the summation density approach can be estimated by directly replacing $f(x)$ in Equation (3.47) with density, ρ:

$$\begin{aligned} \rho_i &= \sum_{j=1}^{N} \frac{m_j}{\rho_j} \rho_j W_{ij}, \\ \rho_i &= \sum_{j=1}^{N} m_j W_{ij}, \end{aligned} \tag{3.61}$$

W_{ij} has a unit which is the inverse of volume and is closely related to the smoothing length, h.

The second method is the continuity density approach. In SPH literature, different operations can be perform on the equation of conservation of mass, Equation (3.56) in order to have different form of density approximation equations. One possible technique is to applied the particle approximation only to the velocity divergence part, by replacing the field function, f, in Equation (3.49) with velocity, $\vec{\mathbf{v}}$, to have:

$$\nabla \cdot \vec{\mathbf{v}} \approx \sum_{j=1}^{N} \frac{m_j}{\rho_j} \vec{\mathbf{v}}_{ij} \cdot \nabla_i W_{ij}, \tag{3.62}$$

where $\vec{\mathbf{v}}_{ij} = \vec{\mathbf{v}}_i - \vec{\mathbf{v}}_j$ is the relative velocity of particle i with respect to particle j.

Now, substituting Equation (3.62) into Equation (3.56), the standard continuity density approach gives:

$$\frac{D\rho}{Dt} \approx \rho_i \sum_{j=1}^{N} \frac{m_j}{\rho_j} \vec{\mathbf{v}}_{ij} \cdot \nabla_i W_{ij}. \tag{3.63}$$

Alternatively, the particle approximation can be done directly on the velocity divergence part, by replacing the field function, f, in Equation (3.53) with velocity, $\vec{\mathbf{v}}$, to have:

$$\nabla \cdot \vec{\mathbf{v}} \approx \frac{1}{\rho_i} \sum_{j=1}^{N} m_j \vec{\mathbf{v}}_{ij} \cdot \nabla_i W_{ij}. \tag{3.64}$$

Now, substituting Equation (3.64) into Equation (3.56), the modified continuity density approach gives:

$$\frac{D\rho}{Dt} \approx \sum_{j=1}^{N} m_j \vec{\mathbf{v}}_{ij} \cdot \nabla_i W_{ij}, \tag{3.65}$$

where $\frac{D\rho}{Dt}$ in Equation (3.63) and Equation (3.65) represent the rate of change in density. The modified continuity density approach Equation (3.65) is used in almost all the simulations in this thesis, because is able to treat densities underestimation at the free surface even when there is deficiency of particle in such locations [169].

For either summation density or continuity density approach, there are advantages and disadvantages. The summation density approach conserved mass exactly [19] while the continuity density approach does not. However the former is prone to edge effect when it being applied to particles at the edge of the fluid domain and will smooth out the density of the concerned particle and this will lead to fake or incorrect results. Another name for edge effect is boundary particles deficiency, which do not only occur near boundary edge, but also near the material interface, if particles from different materials are not allowed to take part in the summation.

To improve the accuracy of the summation density approach, the modified summation density approach was proposed by Randles and Libersky [115], Chen *et al.* [170], and Chen and Beraun [171] to renormalized the density, ρ, as follows:

$$\rho_i = \frac{\sum_{j=1}^{N} m_j W_{ij}}{\sum_{j=1}^{N} \left(\frac{m_j}{\rho_j}\right) W_{ij}}. \tag{3.66}$$

Although these approach improve the accuracy near the free boundaries and the materials interfaces, it still suffers from density discontinuity when the summation is taken only over particles from the same material. Summation density approach yield better results when simulating general fluid phenomena, whereas the continuity density approach is preferred when simulating event with strong discontinuity e.g. explosion or high velocity impact.

Ferrari *et al.* [172] extended the continuity density approach by proposing the stabilized continuity density approach. This new formulation which has been implemented

by Mahdavi and Talebbeydokhti [173], is easy and has the capacity to remove spurious oscillations within the flow field. Therefore, following Ferrari *et al.* [172], the stabilized continuity density approach take the form given as:

$$\frac{D\rho}{Dt} \approx \sum_{j=1}^{N} m_j \vec{\mathbf{v}}_{ij} \cdot \nabla_i W_{ij} + \sum_{j=1}^{N} c_{ij} \frac{m_j}{\rho_j} (\rho_j - \rho_i) \vec{\mathbf{n}}_{ij} \cdot \nabla_i W_{ij}, \tag{3.67}$$

where $\vec{\mathbf{n}}_{ij} = \dfrac{\vec{r}_{ji}}{|\vec{r}_{ji}|}$ and $c_{ij} = max(c_i, c_j)$ corresponds to the highest celerity among the two interacting neighbouring particles.

$$c_i = c_o \sqrt{\left(\frac{\rho_i}{\rho_j}\right)^{\gamma-1}}, \tag{3.68}$$

where $\vec{r}_{ji}$ is as defined previously, c_o is the sound of speed, $\gamma = 7$ and ρ_0 is the reference density, will all be defined in details in Chapter 4.

3.3.4.2 Particle Approximation of Momentum

From the N-S formulation for the conservation of momentum, Equation (3.57), the discretised form of the acceleration due to pressure gradient can be written as:

$$\begin{aligned} \left(\frac{D\vec{\mathbf{v}}}{Dt}\right)_p &= \left(-\frac{1}{\rho}\nabla p\right)_i, \\ &= -\frac{1}{\rho}\sum_{j=1}^{N} \frac{m_j}{\rho_j}(p_j - p_i) \cdot \nabla_i W_{ij}. \end{aligned} \tag{3.69}$$

Because different transformation can lead to different form of acceleration due to the pressure gradient equations, it is very important to ensure that linear and angular momentum are conserved exactly during the discretisation of the pressure gradient terms in the acceleration due to the pressure gradient term. As it can be seen from Equation (3.69), the force acting between particles is zero for constant pressure, but angular and linear momentum are not conserved exactly, despite its great stability. To overcome this problem, Monaghan [107] suggested another way of discretisation that

ensure exact conservation of momentum. Using his approach and applying Equation (3.54) to the pressure gradient part on the right hand side of the momentum Equation (3.57), by replacing the field function, f, in Equation (3.54) with pressure, p, gives:

$$\begin{aligned}(\nabla p)_i &\doteq \rho_i \sum_{j=1}^{N} m_j \left(\frac{p_j}{\rho_j^2} + \frac{p_i}{\rho_i^2}\right) \cdot \nabla_i W_{ij}, \\ \left(\frac{D\vec{\mathbf{v}}}{Dt}\right)_p &\doteq -\sum_{j=1}^{N} m_j \left(\frac{p_j}{\rho_j^2} + \frac{p_i}{\rho_i^2}\right) \cdot \nabla_i W_{ij}. \end{aligned} \tag{3.70}$$

This anti-symmetric Equation (3.70) reduces the errors arising from particle inconsistency problem and is very popular in literature [158]. According to Bonet and Lok [167] suggestion, the following derivative of SPH formulation for the particle approximation of momentum due to pressure gradient is also obtain by replacing the field function, f, in Equation (3.55) with pressure, p, to give:

$$\begin{aligned}(\nabla p)_i &= \sum_{j=1}^{N} \frac{m_j}{\rho_j}(p_j + p_i) \cdot \nabla_i W_{ij}, \\ \left(\frac{D\vec{\mathbf{v}}}{Dt}\right)_p &\doteq -\sum_{j=1}^{N} \frac{m_j}{\rho_i \rho_j}(p_j + p_i) \cdot \nabla_i W_{ij}, \\ \left(\frac{D\vec{\mathbf{v}}}{Dt}\right)_p &\doteq -\sum_{j=1}^{N} m_j \left(\frac{p_i + p_j}{\rho_i \rho_j}\right) \cdot \nabla_i W_{ij}. \end{aligned} \tag{3.71}$$

In a similar way, applying the SPH particle approximation technique to the viscous stress tensor term on the right hand side of the momentum Equation (3.57), gives:

$$\begin{aligned}\left(\frac{D\vec{\mathbf{v}}}{Dt}\right)_\tau &= \left(\frac{1}{\rho}\nabla \cdot \tau\right)_i, \\ &= \sum_{j=1}^{N} m_j \left(\frac{\tau_j}{\rho_j^2} + \frac{\tau_i}{\rho_i^2}\right) \cdot \nabla_i W_{ij}. \end{aligned} \tag{3.72}$$

Now, combining this two terms of pressure and viscous stress tensor into the particle approximation of momentum, the acceleration yields:

$$\frac{D\vec{\mathbf{v}}}{Dt} = -\sum_{j=1}^{N} m_j \left(\frac{p_j}{\rho_j^2} + \frac{p_i}{\rho_i^2}\right) \cdot \nabla_i W_{ij} + \sum_{j=1}^{N} m_j \left(\frac{\tau_j}{\rho_j^2} + \frac{\tau_i}{\rho_i^2}\right) \cdot \nabla_i W_{ij} + \frac{\vec{\mathbf{F}}}{\rho_i}. \quad (3.73)$$

In SPH literature [174], the particle approximation of the viscous stress tensor τ is given as follows:

$$\tau_i = -2\sum_{j=1}^{N} \frac{m_j}{\rho_j} \mu_i \vec{\mathbf{v}}_{ij} \cdot \nabla_i W_{ij} + \left(\frac{2}{3}\sum_{j=1}^{N} \frac{m_j}{\rho_j} \mu_i \vec{\mathbf{v}}_{ij} \cdot \nabla_i W_{ij}\right) \boldsymbol{I}. \quad (3.74)$$

For a fluid such as water and air which are Newtonian, the momentum Equation (3.57) can be rewritten as:

$$\frac{D\vec{\mathbf{v}}}{Dt} = -\frac{1}{\rho}\nabla p + \frac{\mu}{\rho}\nabla^2 \cdot \vec{\mathbf{v}} + \frac{\vec{\mathbf{F}}}{\rho}. \quad (3.75)$$

This momentum Equation (3.75) for Newtonian fluid are very suitable for modelling low velocity fluid flows. Monaghan [175] approximated the viscous term of this Equation (3.75) by using the following approach:

$$\begin{aligned} \left(\frac{D\vec{\mathbf{v}}}{Dt}\right)_{\mu} &= \left(\frac{\mu}{\rho}\nabla^2 \cdot \vec{\mathbf{v}}\right)_i, \\ &= \sum_{j=1}^{N} m_j \left(\frac{\mu_i + \mu_j}{\rho_i \rho_j}\right) \vec{\mathbf{v}}_{ij} \left(\frac{1}{|\vec{\mathbf{r}}_{ij}|} \frac{dW_{ij}}{dr_{ij}}\right). \end{aligned} \quad (3.76)$$

The combine momentum due to pressure gradient term of Equation (3.70) and viscous term of Equation (3.76) form the momentum equation used throughout the simulation in this thesis. This momentum equation is given as:

$$\frac{D\vec{\mathbf{v}}}{Dt} = -\sum_{j=1}^{N} m_j \left(\frac{p_j}{\rho_j^2} + \frac{p_i}{\rho_i^2}\right) \cdot \nabla_i W_{ij} + \sum_{j=1}^{N} m_j \left(\frac{\mu_i + \mu_j}{\rho_i \rho_j}\right) \vec{\mathbf{v}}_{ij} \left(\frac{1}{|\vec{\mathbf{r}}_{ij}|} \frac{dW_{ij}}{dr_{ij}}\right) + \frac{\vec{\mathbf{F}}}{\rho_i}. \tag{3.77}$$

Monaghan and Gingold [176] and Monaghan [175] also proposed the artificial viscosity term given as:

$$\Pi_{ij} = -\upsilon \left(\frac{\vec{\mathbf{v}}_{ij} \cdot \vec{\mathbf{r}}_{ij}}{|\vec{\mathbf{r}}_{ij}^2| + \epsilon \bar{h}_{ij}^2}\right), \tag{3.78}$$

where Π_{ij} denotes the viscous term, $\epsilon \sim 0.01$ is introduced to prevent singularity when $|\vec{\mathbf{r}}_{ij}|$ is zero and υ is given as:

$$\upsilon = \alpha \frac{\bar{h}_{ij} \bar{c}_{ij}}{\bar{\rho}_{ij}}, \tag{3.79}$$

where for example $\bar{\rho}_{ij} = (\rho_i + \rho_j)/2$, α (viscosity coefficient) ~ 0.5 and $\bar{c}_{ij}$ is the average speed of sound. This artificial viscosity Π_{ij} is Galilean invariant and disappear for rigid rotation. Also it is capable of producing a repulsive force between two particles when they approach each other while making them to attract each other when they recede from each other.

3.3.4.3 Particle Approximation of Energy

For the particle approximation of energy, the continuity density approach is used for the formulation in order to get the derivative of SPH formulation for pressure work. Now, the pressure work component of the energy Equation (3.58) can be approximated according to Equation (3.53) as:

$$\left(-\frac{p}{\rho}\nabla\cdot\vec{\mathbf{v}}\right)_i = \frac{p_i}{\rho_i^2}\sum_{j=1}^{N} m_j\vec{\mathbf{v}}_{ij}\cdot\nabla_i W_{ij}. \tag{3.80}$$

The pressure work can also be rewritten according to Equation (3.51) as:

$$-\frac{p}{\rho}\nabla\cdot\vec{\mathbf{v}} = -\nabla\cdot\left(\frac{p}{\rho}\vec{\mathbf{v}}\right) + \vec{\mathbf{v}}\cdot\nabla\left(\frac{p}{\rho}\right). \tag{3.81}$$

Equation (3.54) can be use to expressed the SPH formulation of Equation (3.81) as follows:

$$\left(-\frac{p}{\rho}\nabla\cdot\vec{\mathbf{v}}\right)_i = \sum_{j=1}^{N} m_j\frac{p_j}{\rho_j^2}\vec{\mathbf{v}}_{ij}\cdot\nabla_i W_{ij}. \tag{3.82}$$

In order to have the symmetric SPH formulation for the internal energy equation due to compression, it is necessary to take the average of Equations (3.80) and (3.82), which resulted in:

$$\left(-\frac{p}{\rho}\nabla\cdot\vec{\mathbf{v}}\right)_i = \frac{1}{2}\sum_{j=1}^{N} m_j\left(\frac{p_i}{\rho_i^2}+\frac{p_j}{\rho_j^2}\right)\vec{\mathbf{v}}_{ij}\cdot\nabla_i W_{ij}. \tag{3.83}$$

From the standard formulation of SPH, the discretised form of the viscous dissipation term in the internal energy equation can be expressed as:

$$\left(\frac{1}{\rho}\tau:\nabla\vec{\mathbf{v}}\right)_i = -\sum_{j=1}^{N} m_j\frac{\tau_i}{\rho_i^2}:\vec{\mathbf{v}}_{ij}\cdot\nabla_i W_{ij}. \tag{3.84}$$

Expressing this Equation (3.84) in another form according to Equation (3.52) gives:

$$\begin{aligned}\left(\frac{1}{\rho}\tau:\nabla\vec{\mathbf{v}}\right)_i &= \nabla\cdot\left(\frac{\tau_i}{\rho_i}\vec{\mathbf{v}}_i\right)-\vec{\mathbf{v}}_i\cdot\left(\nabla\frac{\tau_i}{\rho_i}\right),\\ &= -\sum_{j=1}^{N} m_j\frac{\tau_j}{\rho_j^2}:\vec{\mathbf{v}}_{ij}\cdot\nabla_i W_{ij}.\end{aligned} \tag{3.85}$$

Similarly, in order to maintain symmetry of the SPH formulation of the internal energy due to the viscous dissipation term, the average of Equations (3.84) and (3.85) is expressed as:

$$\left(\frac{1}{\rho}\tau:\nabla\vec{\mathbf{v}}\right)_i = -\frac{1}{2}\sum_{j=1}^{N} m_j\left(\frac{\tau_i}{\rho_i^2}+\frac{\tau_j}{\rho_j^2}\right):\vec{\mathbf{v}}_{ij}\cdot\nabla_i W_{ij}. \tag{3.86}$$

For the conduction term of the internal energy, the SPH formulation can be expressed as:

$$\begin{aligned}\left(-\frac{1}{\rho}\nabla\cdot\vec{\mathbf{q}}\right)_i &= -\nabla\cdot\left(\frac{\vec{\mathbf{q}}_j}{\rho_j}\right)-\frac{\vec{\mathbf{q}}_i}{\rho_i^2}\cdot\nabla\rho_i,\\ &= -\sum_{j=1}^{N} m_j\left(\frac{\vec{\mathbf{q}}_j}{\rho_j^2}\right)\cdot\nabla_i W_{ij}-\frac{\vec{\mathbf{q}}_i}{\rho_i^2}\cdot\sum_{j=1}^{N} m_j\nabla_i W_{ij},\\ &= -\sum_{j=1}^{N} m_j\left(\frac{\vec{\mathbf{q}}_i}{\rho_i^2}+\frac{\vec{\mathbf{q}}_j}{\rho_j^2}\right)\cdot\nabla_i W_{ij}.\end{aligned} \tag{3.87}$$

The conduction term $\vec{\mathbf{q}}$ is based on Fourier's law and is given as follows:

$$\begin{aligned}\vec{\mathbf{q}}_i &= -k_i\nabla T_i,\\ &= \frac{1}{\rho_i}\sum_{j=1}^{N} m_j T_{ij}\nabla_i W_{ij},\end{aligned} \tag{3.88}$$

where $T_{ij}=T_i-T_j$ is the temperature difference. Therefore, the SPH formulation for the internal energy is given as:

$$\frac{De_i}{Dt} = \frac{1}{2}\sum_{j=1}^{N} m_j \left(\frac{p_i}{\rho_i^2} + \frac{p_j}{\rho_j^2}\right) \vec{\mathbf{v}}_{ij} \cdot \nabla_i W_{ij} - \frac{1}{2}\sum_{j=1}^{N} m_j \left(\frac{\tau_i}{\rho_i^2} + \frac{\tau_j}{\rho_j^2}\right) : \vec{\mathbf{v}}_{ij} \cdot \nabla_i W_{ij} - \sum_{j=1}^{N} m_j \left(\frac{\vec{\mathbf{q}}_i}{\rho_i^2} + \frac{\vec{\mathbf{q}}_j}{\rho_j^2}\right) \cdot \nabla_i W_{ij}. \tag{3.89}$$

where $\vec{\mathbf{F}}$ represent the body force. This body force could be the effect of gravity or any other external forces, with the exception of surface tension force.

3.4 The equation of state (EOS)

The N-S momentum Equation (3.57) is generally made up of four unknown parameters with just three equations. In order to solve the given problem, there must be at least four equations, in others words the number of unknown parameter must be at least equal the number of equation for the given problem to have a solution. Due to this reason, an extra equation, called equation of state is introduced to close the problem. This equation of state can be in the form of algebraic or differential formulation, which can be solved either as weakly compressible SPH (WCSPH) or incompressible SPH (ISPH) respectively. Generally, from practical point of view, fluid (liquid) are consider to be weakly compressible in the standard SPH form, and this enable the equation of state to be use to establish fluid pressure. There are different form of equation of state used to establish the fluid pressure and are given as:

1. Monaghan [107] and Batchelor [177] suggested using the algebraic Tait's equation as the EOS to establish the fluid pressure for the WCSPH, where pressure depends on the density (ρ) and reference pressure constant, b, and is expressed as:

$$p = b\left[\left(\frac{\rho}{\rho_0}\right)^{\gamma} - 1\right]. \tag{3.90}$$

where γ is the polytrophic constant that can varies within $\gamma = 1$ to 7, and for the particular case of water $\gamma = 7$ [178], ρ_0 is the reference density and b is the reference pressure constant, which is given as:

$$b = \left(\frac{\rho_0 c_o^2}{\gamma}\right). \tag{3.91}$$

where c_o is the speed of sound that control the compressibility of the fluid. In compressible flow, the speed of sound should be chosen very carefully, because it plays an important role in the simulation in tense of fluctuation in density. A small time step is needed for numerical stability based on Courant-Fredrick-Levy (CFL) condition if the real speed of sound is used (e.g. 1480 ms^{-1} in water at standard pressure and temperature) and this might be very expensive in terms of computational time and cost. However, Monaghan [107] demonstrated that the sound speed (c_o) should be chosen as ten to one hundred times greater than the maximum speed of the fluid flow in order to curtail the fluctuation in density to within 1%.

From Equation (3.90), it is observed that a little change in density will lead to a large fluctuation in pressure. So, to have good results, the density change should not be more than 1% according to literature [107]. The subtraction of unity in the Tait's equation of state is to ensure that there is zero pressure at the interface for example at the free surface. Another form of algebraic equation of state is the one by Tartakovsky and Meakin [152], which uses the Van der Waals EOS to establish the fluid pressure, where pressure depends on the density, ρ, mass (m) and three other constant parameters which need to be tuned.

2. The differential form of equation of state that is used in ISPH involves solving pressure Poisson's equation [179] given as:

$$\nabla \cdot \left(-\frac{1}{\rho}\nabla p\right)_i = \frac{1}{\Delta t}\nabla \cdot \vec{\mathbf{v}}_i^*, \tag{3.92}$$

where $\vec{\mathbf{v}}_i^*$ is the intermediate particles velocity which is calculated by having the solution taken one time step while neglecting the pressure. To get the velocity and incompressible pressure fields, the Navier-Stokes equations will need to be divided into two sections following the projection method [104, 180]. The first part have the viscous and body forces, while the second part contain the pressure force. Between these parts, the pressure Poisson's Equation (3.92) need

to be solved, from which the incompressible pressure field can now be calculated.

Solving the pressure Poisson's Equation (3.92) is very expensive due to the computational time required to solve the intermediate particles velocity, intermediate particles position, final velocity field, and finally the incompressible pressure fields. Apart from the expensive computation time required in the pressure Poisson's equation, there are also issues of instability at the free-surface which have been reported [180, 181]. Due to this free-surface instability, correction will need to be carried out, which also requires more computational time. Hence, on the overall, this approach can be extremely slow, making it difficult for use in real life application.

Based on the above mentions facts, the Tait's equation of state is used here in this thesis primarily because it is easier to solve than the pressure Poisson's equation. Although, there is fluctuation in density when using the Tait's equation, this can be controlled by chosen a suitable sound speed.

3.5 The smoothing length

In the SPH methodology, smoothing length is considered to be an important parameter as it defines the radius (catchment area) within which the particles interact with each other. Generally, the support domain is make up of multiple of smoothing length, which is given as:

$$r = \kappa h, \tag{3.93}$$

where r represent the radius (*range*) while the values of κ is fixed and depends on the choice of smoothing kernel used. Generally, $\kappa = 2$, and for particle at a distance greater than two smoothing length $2h$, there will be no influence on this particle (see Figure 3.16). In other words, the smoothing kernel is zero when the distance from the particle of interest to the neighbour particle is greater than or equal to $2h$. This is further illustrated in Figure 3.17, where it can be seen that the circle fades away with distance from the particle (p) of interest.

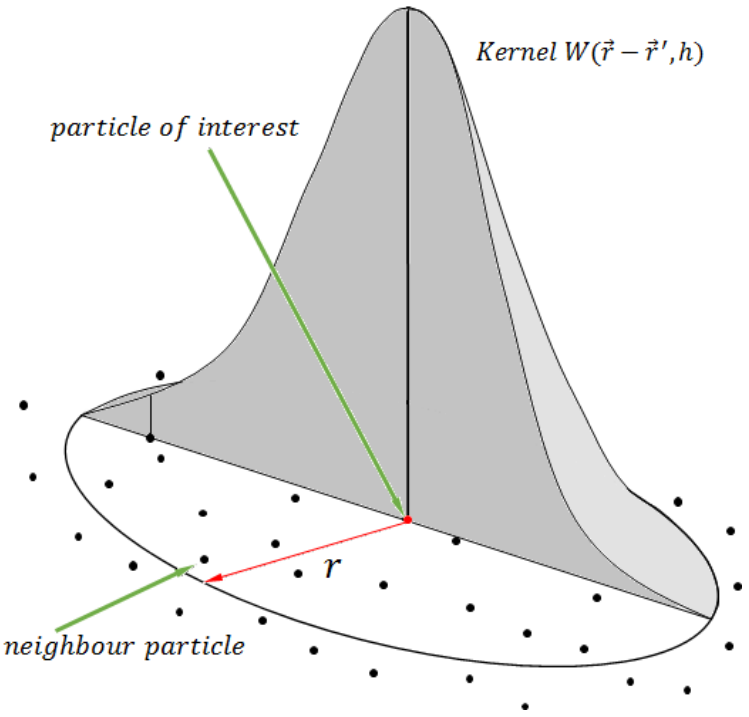

FIGURE 3.16: Support domain of influence with the search radius from the particle of interest to neighbour particles.

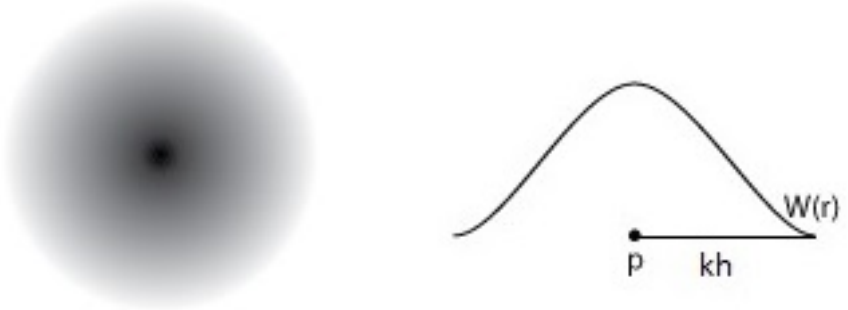

FIGURE 3.17: Fading domain of influence as the smoothing kernel decreases from the center p.

3.6 The Neighbour Range Search (NRS)

In SPH, the dynamic interactions between particles require information about its neighbouring particles within its support domain. Typically the criterion for finding neighbours is a radius check with those particles falling within the κh of the Kernel. The NRS algorithm is seen to be one of the major computational cost of the solver due to its frequent use. The common types of NRS algorithms are brute force, Kd-tree, cell search, quad and oct-trees and hash tables.

3.6.1 Brute Force Search (BFs)

Brute Force also known as linear NRS or All-pair Search Method is a trivial method to search a query in a database. It completely compares each particle i of interest with every particle j in the domain and then select only those particle j within the search range (κh). This method has the advantage of not requiring any pre-processing, but suffers from long computational time, complexity of order $O(N^2)$, where N is the number of particles in the domain, and is only suitable for problems at small scales (see Figure 3.18).

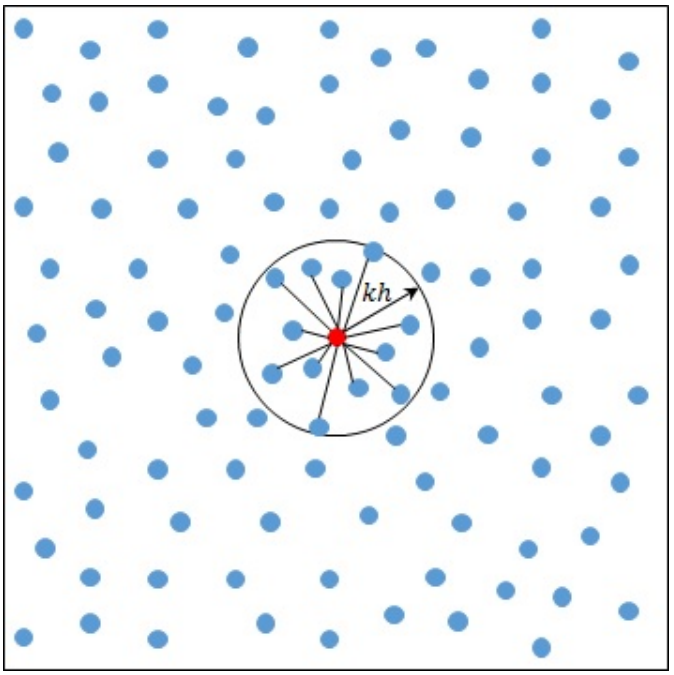

FIGURE 3.18: Showing the particle of interest (*red*) comparing with every neighbour particles (*blue*) in the domain, and then selecting those within the search range.

3.6.2 Kd-Tree Search

The kd-tree which is a generalized simple binary tree used for sorting and searching, was designed specially to take advantages of coordinate information in the form of vector spaces, by using it to partition the search space. For each non-leaf node, an object of the database (pivot) and a split coordinate is chosen. The space is partitioned according to the value of the splitting coordinate of the pivot (splitting value). All the objects with a value in the splitting coordinate smaller than the splitting value go to the left sub-tree; the objects with a value in the splitting coordinate bigger

than the splitting value go to the right sub-tree, while the pivot is stored as the root (see Figure 3.19). This approach was used in this thesis for the solver as the search algorithms.

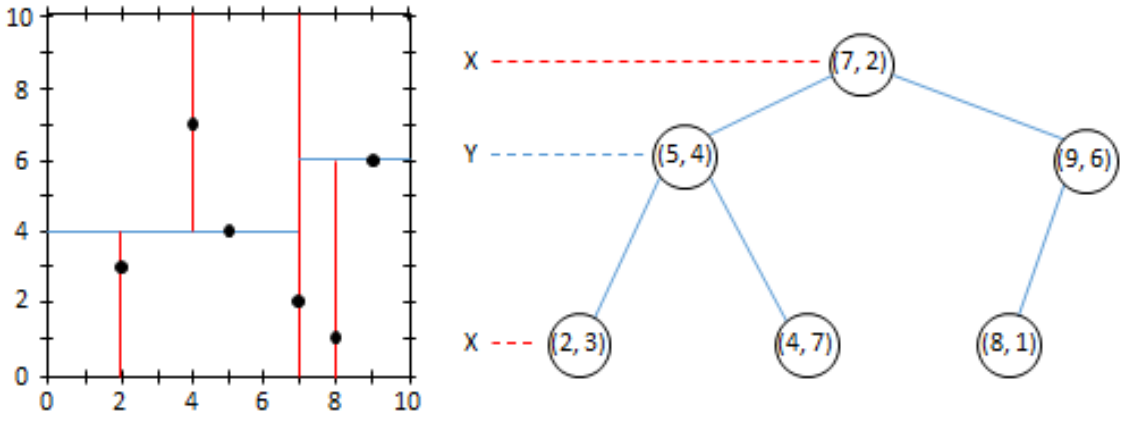

FIGURE 3.19: Kd-tree x-y plane splitting.

Kd-trees are not suitable for efficiently finding the nearest neighbour in high dimensional spaces because it causes the algorithms to visit many more branches than in lower dimensional spaces. So if the number of points is only slightly higher than the number of dimensions, the algorithms is merely better than a linear search (brute force search). Although the algorithms can be improved, it is the only data structure that allows easy multi-key search with an expected efficiency of $O(\log N)$ and build time of $KN(\log N)$ [182]. As noted, the computational trade off of building the tree is worthwhile since for the single generation of the Kd-Tree structure, savings are expected for each subsequent calculation.

3.6.3 Cell Search Approach

The Cell Search method is a simple but effective NRS which uses a specified subregion to partition the domain, usually twice the smoothing length but depends on the kernel, and to assign each particle to the physical cell it resides by using its coordinate position. This simplification allows for a truncated linear nearest neighbour search within a required set of neighbour cells to the particle of interest's parent cell (see Figure 3.20).

Depending on the ratio of search range to cell size, the number of neighbours cells for a full neighbour list can range from 9, 25 cells and 27, 125 cells for $2D$ and $3D$ problems respectively. The approach is very easy to implement, but sensitive to

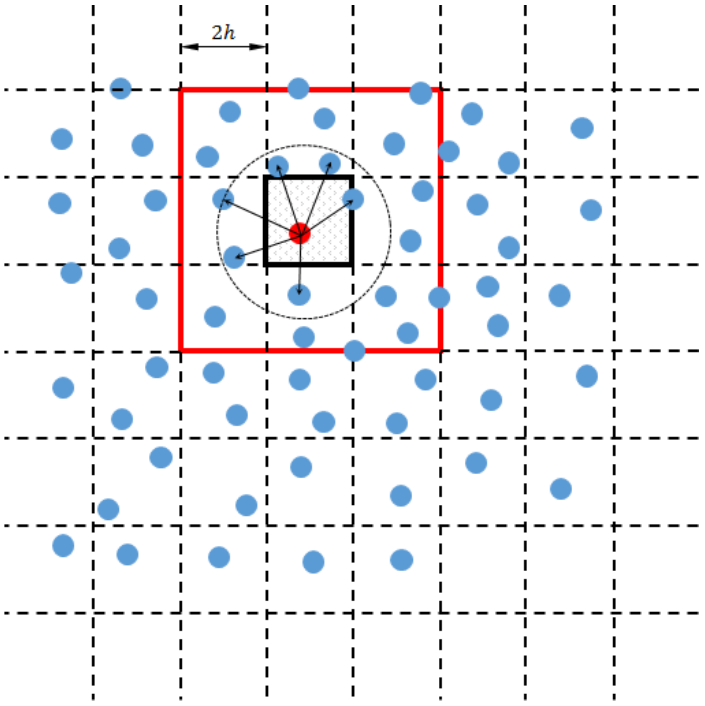

FIGURE 3.20: Cells are based on regular spatial divisions.

issues like numerical round off and truncation errors if not handle properly and with a complexity of order $O(N)$ if the number of particles within the cell is reasonably small.

3.6.4 Quad and Oct Trees

The Quad and Oct tree are the two main categories of pyramids with the Quad and Oct tree the equivalent of pyramid in two and three dimensions respectively. The quad-tree, which has linked lists of four children to each parent is useful to divide a plane into four subdomains by bisecting both the x and y axes at mid-points on a plot containing all the particles. After which the particles present in each subdomain are allocated a location in the tree depending on which quadrant they reside. The parent domain is the node which spans the subdomains. For example, a point incident on the point where both the x and y split lines intersect would clearly be the best candidate. If there is no such a good choice, points intersecting one split line or being closest to one are chosen. If there is more than one particle in each cell, the sub-domain is quartered again. This continues until each cell contains at most one particle not withstanding those on intersect boundaries. Applications for quad-trees include collision detection (tracking moving pixels) and resolution scanning (since the plane divides evenly for both x and y resulting in a n^2 spatial partition). In three

dimensions the quad-tree is modified so that each parent has eight children and as a consequence it is renamed the Oct-tree. This works by bisecting all three dimensions so that the resulting eight octant's are bounded by the planes which are implied by the splits. For example the x split for a point x_i alone would project a plane with solution $x = x_i$, splitting the volume containing all particles along x_i. The Oct-trees and Quad-trees are potentially faster at throwing away points than Kd-Tree since for an evenly distributed set of points and for each transition down the quad-tree, three quarters of the points are thrown away while for the Oct-tree seven eighths. Even at that, the computational time for building these algorithms is high; hence Kd-tree is preferred due to its superior flexibility.

3.6.5 Hash Tables

Hash tables are widely used for information querying due to their speed. The hash table works by taking data, referred to as 'keys' and assigning a value called an index to them. This is done by using a hash function which transforms between key and index. The choice of function is critical since the most appropriate function for the data set will aim to distribute a unique set of indexes to the data. It is however unavoidable by design to ensure that this happens as frequently the same data will be assigned to the same table entries. The indexes identify slots on a table, thus data with similar indexes will have associations with the same slot. Such instances are called collisions and slow the query time. One example of the hash table search is to consider the collisions of three dimensional objects. Hashing is used for particles with uniform smoothing lengths hence the NRS of a particle in a cubic cell of length $2h$, are located in the same cell and the 26 adjacent cells. The unique three dimensional indexes of the cells are used as addresses of a hash table using a hash function. The particles within each cell thus share the same index with every other particle in their cell. Finally a list of the most promising NRS method efficiencies are compared in Table 3.1.

TABLE 3.1: Table of efficiencies for the main NRS methods.

	Linear	**Cell**	**Kd-Tree**	**Hash-Table**
Overhead	N/A	O(N)	O(dNlogN)	N/A
Average	$O(N^d)$	$O(N^d)$	O(logN)	$O(1)$
Worst	$O(N^d)$	$O(N^d)$	$O(N^d)$	O(N)

3.7 Boundary conditions for solid wall modelling

Generally, in fluid flow modelling, the need to model boundaries or solid wall as well as the fluid particles is very important. In most SPH literature, the solid wall is treated as SPH particles fixed in their located at constant interval (this interval is usually equal the diameter of the particle). In this thesis, the most commonly used approaches for modelling solid wall also refers to as wall or edge particles (see Figure 3.21) in SPH will be discussed.

As the fluid particles move close to the edge as shown in Figure 3.22, the number of neighbour particles significantly decreases within the support domain due to lack of complete neighbour particles list. For this reason, the forces are no longer balanced due to the truncation of neighbour particles list and this will lead to the fluid particles leaving the fluid domain or unphysical behaviour of the fluid particles. Based on the above mentioned reason, so many researchers have proposed several approaches to handle this issue depending on the nature of the problem. Some of these approaches will be discussed in the next session.

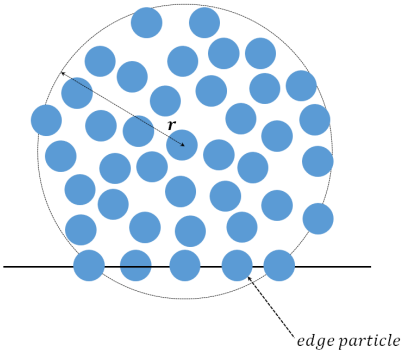

FIGURE 3.21: Showing SPH edge particles.

3.7.1 Dummy particles approach

One of the most popular ways to handle the above mentioned issues is to introduce dummy particles at the other side of the edge particles. This help to resolve the deficiencies in neighbour particles of the fluid particles that are close or near the edge of the domain. Traditionally, the number of layers depend on the support domain of the kernel, which in most cases vary between two and three layers. The dummy particles are stationary and equal spacing, but are spread in layers at the other side of the edge of the domain as shown in Figure 3.23. The duty of this dummy particle

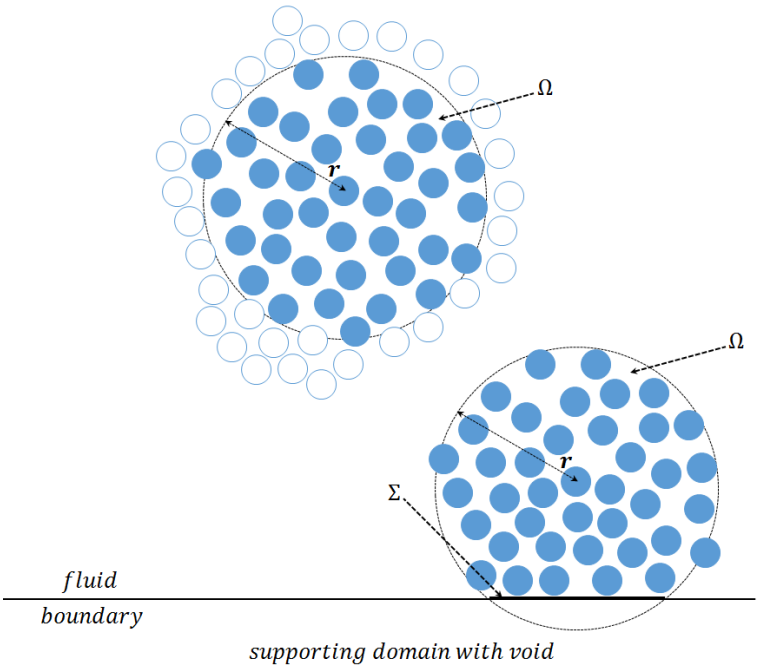

FIGURE 3.22: Showing fluid particles with a void in the supporting domain close to the edge boundary.

is to maintain the complete neighbour particle list of the fluid particles that are near the edge of the domain, but its position must always remain constant (stationary) over time, thus making computational cost less expensive especially for 2D. Also, the approach is straightforward and simple to implement. Based on the above mentioned fact, the approach is used in most of the validation test, see Chapter 4 of this thesis.

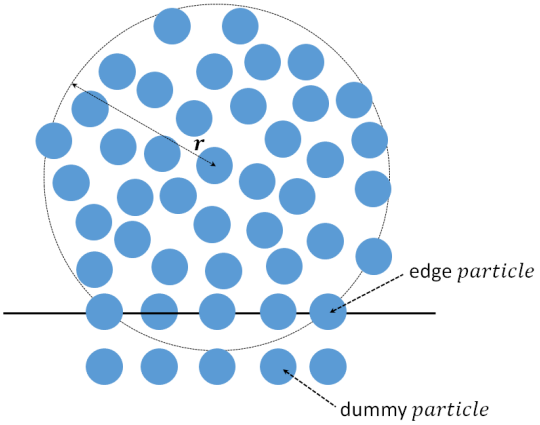

FIGURE 3.23: Showing dummy particles to avoid deficiencies in the supporting domain close to the edge particles.

3.7.2 Mirror particles approach

The mirror particles approach is another well known method of resolving neighbour particles deficiency of the fluid particles that are near the edge of the domain. The mirror particle approach is similar to the dummy particle approach, but differs by having the same physical properties as the fluid particle near the wall or edge particle that is reflected. For each fluid particles (objects) that are close to the edge particles, the mirror particles (images) are created with symmetric parameters of the fluid particles with the black solid line serving as the mirror line (see Figure 3.24). Also for the fluid particles to be mirrored, the fluid particles must be at a certain set distance from the reference line (black solid line) as shown in the Figure 3.24.

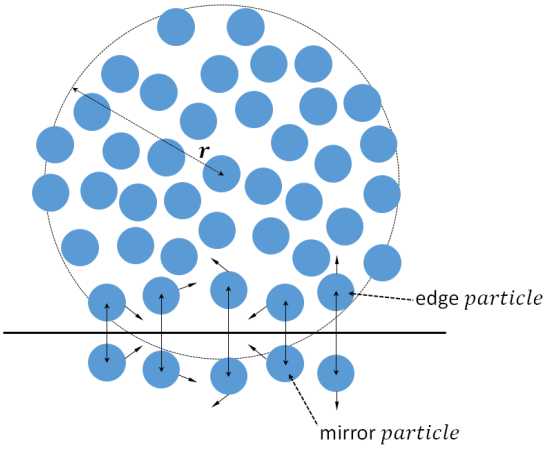

FIGURE 3.24: Showing mirror particles with symmetric parameters of the corresponding fluid particles close to the wall with velocity direction indicated.

It is easy to handle the non-slip condition without difficulties with the mirror particle approach by making the velocity of the mirror particles the same as that of the fluid particles in terms of magnitude, but with opposite directions [100]. But with the dummy particle approach, it is much easier to handle the non-slip condition naturally, because the dummy particles are stationary. The mirror and dummy particle approach are similar in implementation and application, but with the dummy particle approach much easier to implement than the mirror particle approach. They both are computational expensive and take more memory space especially for three-dimensional problems.

3.7.3 Repulsive boundaries approach

In both cases, in order to prevent penetration of the fluid particle into the wall, Monaghan [183] suggested an extra repulsive force between the fluid particles and solid wall particles to keep the fluid particles within the fluid domain. This extra repulsive force is then included in the momentum Equation (3.57). The most popularly used repulsive force is the Lennard-Jones molecular model, which is force per unit mass and in Lennard-Jones representation, is given as follows:

$$f_i(\vec{\mathbf{r}}) \quad = D\left[\left(\frac{r_0}{|\vec{\mathbf{r}}_{ij}|}\right)^{a_1} - \left(\frac{r_0}{|\vec{\mathbf{r}}_{ij}|}\right)^{a_2}\right]\frac{\vec{\mathbf{r}}_{ij}}{|\vec{\mathbf{r}}_{ij}|^2}, \tag{3.94}$$

where $a_1 = 12$, $a_2 = 6$ and D are the constant parameters, with r_0 as the initial particle spacing (dx), and D is assumed to be the multiplication of 120 times the initial particle spacing r_0 and the acceleration due to gravity, g, [34].

3.7.4 Periodic boundary approach

In addition to the above mentioned approaches, periodic boundary plays an important aspect, especially when fluid flow that are assumed to be continuous (infinite), for example fluid flow in a pipe. To model this infinitely long fluid flow domain, a section of it is taken and periodic boundary conditions are imposed. With this approach, computational time and cost are reduced, because only the section taken need to be model instead of the entire domain. Typical examples of this approach are the Poiseuille and Couette flows whose details are given in Chapter 4. Infinitely long plate and fluid flow can be modelled by imagining vertical boundaries (dotted line) that are in x-direction which permits the fluid particles to relate with the fluid particles at the adjacent boundary and permit the fluid particles to flow through the boundary (see Figure 3.25).

As an example, all particle that are $2h$ from this dotted line, has neighbour list comprising of those from the right side (right shaded circle) and those from the left side (opposite left shaded circle) [184].

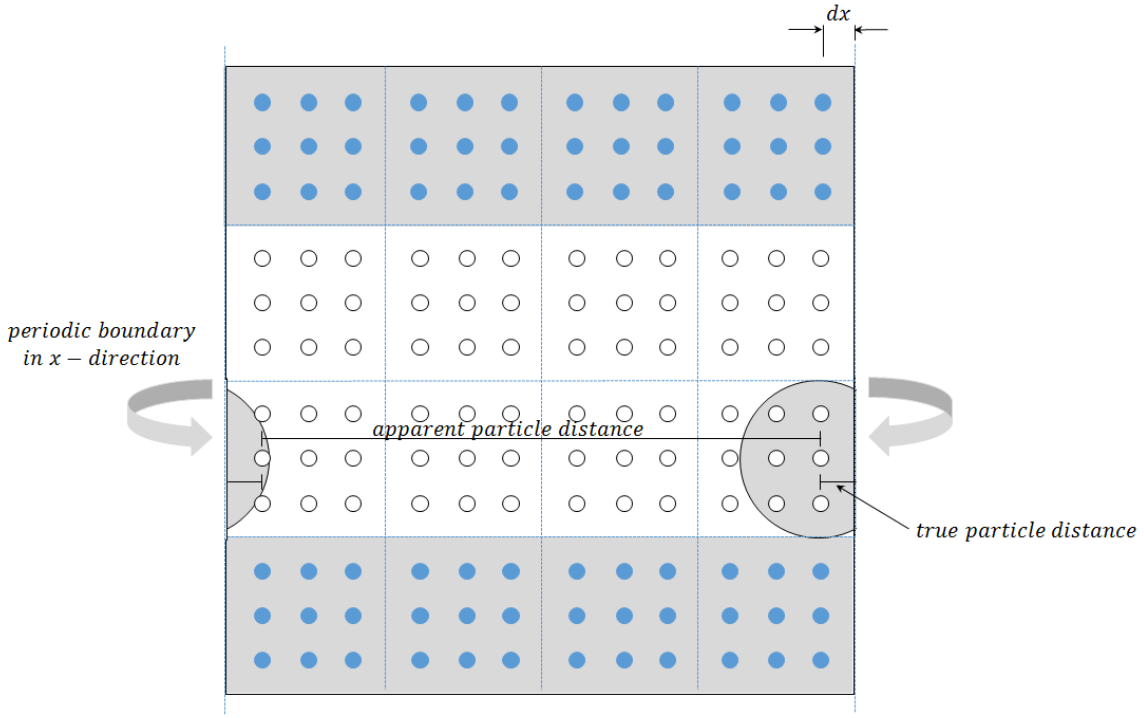

FIGURE 3.25: Periodic boundary condition where the particle at one end interact with particle at the other end in the x-direction.

3.8 The particle position

Instead of moving the particle with Equation (3.99), Monaghan [183] proposed moving the particles with the well-know extended SPH (XSPH), given by:

$$\frac{d\vec{\mathbf{r}}_i}{dt} = \vec{\mathbf{v}}_i + \epsilon \sum_{j=1}^{N} \frac{m_j}{\rho_{ij}} \vec{\mathbf{v}}_{ji} W_{ij}, \tag{3.95}$$

where $\rho_{ij} = 0.5(\rho_i + \rho_j)$ and ϵ is a constant, whose range is between 0 and 1. Its value is usually $\epsilon = 0.5$ in most cases found in literature [183].

The XSPH method make the particle move with a velocity which is close to the average velocity of the neighbour particles in the supporting domain by keeping the particles more orderly and this helps to prevent clustering and fluid particle from penetrating the solid wall, especially in some cases where the is absence of viscosity. Another major interesting features of XSPH is that once pressure and viscosity are set to zero, it is possible to simulate the Burgers equation with large Reynolds number effectively.

The XSPH is used in this thesis as shown in Chapter 4 for Couette and Poiseuille flow problem only by updating the particle position with this scheme.

3.9 Time Integration Schemes

Numerical integration can be broadly divided into explicit and implicit methods. In computer simulation of physical processes, explicit and implicit methods are used for obtaining numerical solutions of time-dependent ordinary and partial differential equations. Explicit methods find the numerical approximation to a function given a set of initial values or better put calculate the state of a system at a later time from the state of the system at the current time. It is more precise, but with high computational cost due to its small time step restriction. The implicit methods solve for the position at a given time based on a function of the current and next value or better put find a solution by solving an equation involving both the current state of the system and the later state of the system. Although, its computational cost is lower, it suffers from spurious current due to the appearance of non-physical velocities.

In mathematically representation, if $Y(t)$ is the current system state and $Y(t + \Delta t)$ is the state at the later time (Δt is a small time step), then, for an explicit method

$$Y(t + \Delta t) = F(Y(t)), \tag{3.96}$$

while in the case of the implicit method, it solves:

$$G(Y(t), Y(t + dt)) = 0, \quad \text{in order to find Y}(t + \Delta t). \tag{3.97}$$

It is clear from the above that implicit methods require extra computation cost and they can be much harder to implement. Implicit methods are used because many problems arising in practice are stiff, for which the use of an explicit method requires impractically small time steps Δt to keep the error in the result bounded [185].

3.9.1 Criteria for choosing Time Integration Schemes

Some basic criteria for choosing time integration schemes are as follows:

- **Accuracy:** The accuracy of a numerical solution is the degree of closeness between the simulated results and the theoretical or experimental results (actual or true value)
- **Stability:** A numerical method is said to be stable if a small error at any stage does not lead to a larger accumulation of error.
- **Convergence:** The solution of the numerical scheme converges towards the real solution of the PDE for Δt, $\Delta x \to 0$. Stability is the necessary and sufficient condition for convergence.
- **Consistency:** If as the limit of time step become smaller (infinitesimal), the algebraic approximation tend toward the differential equation its try to describe, then the method is consistent.
- **Efficiency:** A numerical solution is said to be efficient if time, effort or cost is well used for the intended task or purpose to produce specific outcome with minimum amount of waste.

3.9.2 Types of Time Integration Schemes

Several approaches for the time integration scheme used to update the SPH equations in time exist. In most SPH literature, a second-order scheme is used and some of these approaches will be discussed in this section. For convenience, it will be necessary to rewrite the density Equation (3.65), momentum Equation (3.77), energy Equation (3.89) and position Equation (3.95) as follows:

$$\frac{D\rho_i}{Dt} = \dot{\rho}_i, \tag{3.98}$$

$$\frac{D\vec{\mathbf{r}}}{Dt} = \vec{\mathbf{v}}_i, \tag{3.99}$$

$$\frac{D\vec{\mathbf{v}}_i}{Dt} = \dot{\vec{\mathbf{v}}}_i, \tag{3.100}$$

$$\frac{D\vec{\mathbf{e}}_i}{Dt} = \dot{\vec{\mathbf{e}}}_i. \tag{3.101}$$

3.9.2.1 Euler's Method

The object of Euler's method is to obtain approximations to the well-posed initial-value problem. Let $y = y(t)$ be the desired solution to some first-order differential equation:

$$\frac{dy}{dt} = f(t, y) \quad a \leq t \leq b, \quad y(a) = \alpha, \tag{3.102}$$

and let t_i be some value for t on the interval of interest, where $(t_i,\ y(t_i))$, is a point on the graph of $y = y(t)$, so the nearby points on this graph can be approximated by corresponding points on the straight line tangent (line L_i) at point $(t_i,\ y(t_i))$ in Figure 3.26 below.

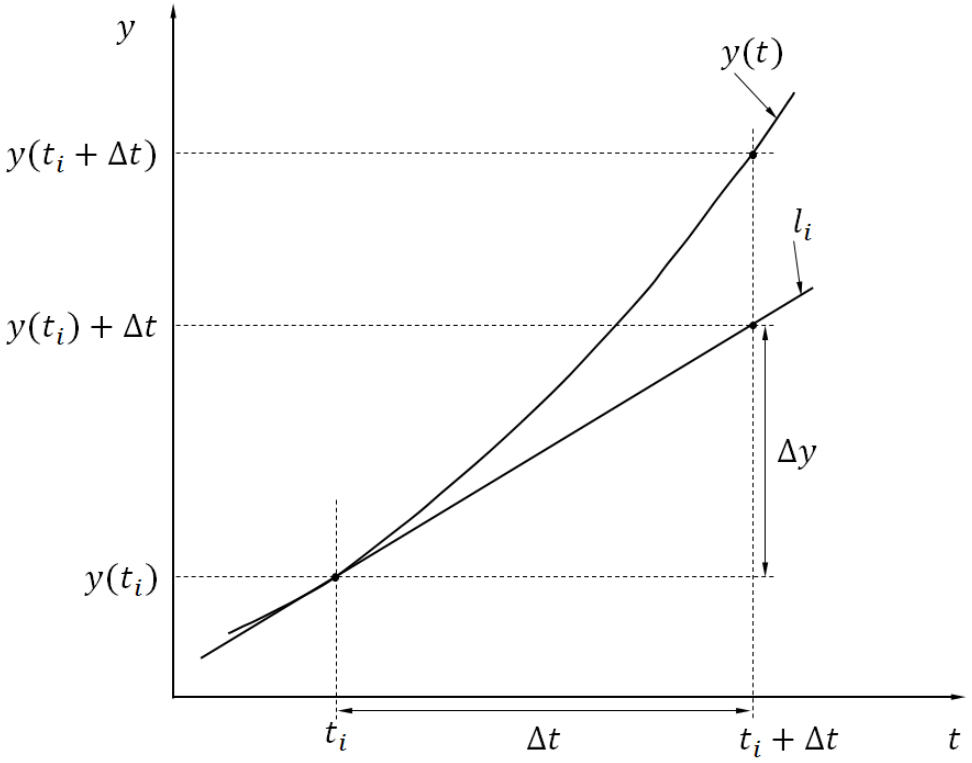

FIGURE 3.26: A single tangent line approximation for the Euler Method

The slope of the approximating line, $= \frac{dy}{dt}$ at $(t_i, y(t_i)) = f(t_i, y(t_i))$. Now let Δt be any positive distance in the t direction. Using the tangent line approximation (again, see Figure 3.26), it shows that:

$$y(t_i + \Delta t) \approx y(t_i) + \Delta y, \tag{3.103}$$

where

$$\frac{\Delta y}{\Delta t} = \textit{ slope of the approximating line } = f(t_i, y(t_i)),$$

therefore

$$\Delta y = \Delta t f(t_i, y(t_i)),$$

and Equation (3.103) becomes:

$$y(t_i + \Delta t) \approx y(t_i) + \Delta t f(t_i, y(t_i)). \tag{3.104}$$

Equation (3.104) is the fundamental approximation underlying each basic step of Euler's method. However, the value of $y(t_i)$ will usually only be known by some approximation y_i . With this approximation, it gives:

$$y(t_i) + \Delta t f(t_i, y(t_i)) \approx y_i + \Delta t f(t_i, y_i), \tag{3.105}$$

which when combined with Equation (3.104), yields the approximation that will actually be used in Euler's method, as:

$$y(t_i + \Delta t) \approx y_i + \Delta t f(t_i, y_i). \tag{3.106}$$

The change, Δt, in the above approximations is called the step size. Choosing a good value for the step size is important as this improves the accuracy of the method. The method is the most basic and simplest, but least accurate time stepping method since it employs only the first order derivative of a time dependent function to predict its value at some later time [186]. Thus it is an example of a first order Runge-Kutta

method (RK0). However, unlike the leapfrog method which you will see in the next session, the gradient is not taken from the midpoint but rather from the initial starting point which is evaluated at t_i here. Thus the expected error is given by comparing the equivalent Taylor expansion around t_i with the Eulerian approximation and given that the time progress by unity to t_{i+1} is defined by $y_{i+1} = \Delta t \cdot f(t_i, y(t_i))$ where, Δt, is the change in time, then:

$$y_{i+1} = y_i + \Delta t \cdot y'(t_i) + \frac{\Delta t^2}{2} \cdot y''(t_i) + ... + \frac{\Delta t^n}{n!} y^n(t_i), \tag{3.107}$$

which diverges from the exact solution at the leading second order term $O(\Delta t^2)$. Thus for a quadratic function, the error imposed is proportional to Δt^2. It may not be practicable to use this method if second order terms are to be retained, however all other methods are modification of the Euler method.

3.9.2.2 Euler Cromer Method

The Euler Cromer Method was developed by Tom Cromer in 1980s as a modify version of Euler's method. It is a symplectic integrator scheme design for specific set of ODEs and is more accurate than Euler's method, even though it has a first order accuracy, for ideal two-body problem. In the method, new points based on the slopes are calculated at the current location exactly like the Euler's method, but it updates the velocity before it updates the position, and this makes it to preserved the energy of the solution. The equations for this method are below:

$$\begin{aligned} v_{i+1} &= v_i + \dot{v}(t_i, y_i)\Delta t, \\ y_{i+1} &= y_i + v(t_i, v_{i+1})\Delta t. \end{aligned} \tag{3.108}$$

3.9.2.3 Predictor-Correction Scheme

From mathematics, especially numerical analysis, the predictor-corrector scheme belongs to a group of algorithms that proceeds in two steps. This method involves a combination of implicit and explicit technique, in order to have a convergence characteristics that is much better. The first step involves the use an of explicit method

for the predictor step and an implicit method for the corrector step. Although, it has a second order accuracy, the step size need to be relatively small just to have good approximation, hence making the method more of an explicit method. More also, the method is computationally expensive due to the number of iterations required to get convergence. In this technique, the evolution is predicted in time at first by the equations below as:

$$\vec{\mathbf{v}}_i^{n+1/2} = \vec{\mathbf{v}}_i^n + \frac{\Delta t}{2}\dot{\vec{\mathbf{v}}}_i^n, \tag{3.109}$$

$$\rho_i^{n+1/2} = \rho_i^n + \frac{\Delta t}{2}\dot{\rho}_i^n, \tag{3.110}$$

$$\vec{\mathbf{r}}_i^{n+1/2} = \vec{\mathbf{r}}_i^n + \frac{\Delta t}{2}\vec{\mathbf{v}}_i^n, \tag{3.111}$$

$$e_i^{n+1/2} = e_i^n + \frac{\Delta t}{2}\dot{e}_i^n. \tag{3.112}$$

By taking into account the pressure $p_i^{n+1/2}$ which depend on the density $\rho_i^{n+1/2}$ according to Equation (3.90), the next step is to correct the above Equations (3.109)-(3.112) at the half step using the equations below:

$$\vec{\mathbf{v}}_i^{n+1/2} = \vec{\mathbf{v}}_i^n + \frac{\Delta t}{2}\dot{\vec{\mathbf{v}}}_i^{n+1/2}, \tag{3.113}$$

$$\rho_i^{n+1/2} = \rho_i^n + \frac{\Delta t}{2}\dot{\rho}_i^{n+1/2}, \tag{3.114}$$

$$\vec{\mathbf{r}}_i^{n+1/2} = \vec{\mathbf{r}}_i^n + \frac{\Delta t}{2}\vec{\mathbf{v}}_i^{n+1/2}, \tag{3.115}$$

$$e_i^{n+1/2} = e_i^n + \frac{\Delta t}{2}\dot{e}_i^{n+1/2}. \tag{3.116}$$

Finally, the equation for the velocity, density, position and energy at the end of the time step at pressure p_i^{n+1} is calculated at density ρ_i^{n+1} according to Equation (3.90)

as follows:

$$\vec{\mathbf{v}}_i^{n+1} = 2\vec{\mathbf{v}}_i^{n+1/2} - \vec{\mathbf{v}}_i^{n}, \tag{3.117}$$

$$\rho_i^{n+1} = 2\rho_i^{n+1/2} - \rho_i^{n}, \tag{3.118}$$

$$\vec{\mathbf{r}}_i^{n+1} = 2\vec{\mathbf{r}}_i^{n+1/2} - \vec{\mathbf{r}}_i^{n}, \tag{3.119}$$

$$e_i^{n+1} = 2e_i^{n+1/2} - e_i^{n}. \tag{3.120}$$

According to Monaghan [183], this technique conserves both linear and angular momentum. But in Monaghan's approach, he uses the values at the half time step instead of at the end of the time step and was able to save time, although his approach had a small margin of error.

3.9.2.4 Verlet Scheme

The Verlet integration is a numerical technique used to integrate Newton's equations of motion [187]. In fluid dynamics, the Verlet algorithm is derive from the basic Verlet method [187] and is more popular in time integration scheme than any other scheme. This algorithm is used in this thesis because it offers greater stability, time-reversibility and area preservation than the much simpler Euler method. It is also less computational expensive than the predictor-corrector scheme while its global error is third-order in position and second-order in velocity. For this scheme, the variables are given as:

$$\vec{\mathbf{v}}_i^{n+1} = \vec{\mathbf{v}}_i^{n-1} + 2\Delta t\dot{\vec{\mathbf{v}}}_i^{n}, \tag{3.121}$$

$$\rho_i^{n+1} = \rho_i^{n-1} + 2\Delta t\dot{\rho}_i^{n}, \tag{3.122}$$

$$\vec{\mathbf{r}}_i^{n+1} = \vec{\mathbf{r}}_i^{n} + \Delta t\vec{\mathbf{v}}_i^{n} + 0.5\Delta t^2\dot{\vec{\mathbf{v}}}_i^{n}, \tag{3.123}$$

$$e_i^{n+1} = e_i^{n-1} + 2\Delta t\dot{e}_i^{n}. \tag{3.124}$$

Because the Verlet algorithm is not self-starting, a different algorithm (basic Euler scheme) is used to ensure that the scheme for odd and even steps are coupled. In other to achieve this, an M time step (generally, M is suggested to be 50) is used to evaluate the following variable according to:

$$\vec{\mathbf{v}}_i^{n+1} = \vec{\mathbf{v}}_i^n + \Delta t \dot{\vec{\mathbf{v}}}_i^n, \tag{3.125}$$

$$\rho_i^{n+1} = \rho_i^n + \Delta t \dot{\rho}_i^n, \tag{3.126}$$

$$\vec{\mathbf{r}}_i^{n+1} = \vec{\mathbf{r}}_i^n + \Delta t \vec{\mathbf{v}}_i^n + 0.5 \Delta t^2 \dot{\vec{\mathbf{v}}}_i^n, \tag{3.127}$$

$$e_i^{n+1} = e_i^n + \Delta t \dot{e}_i^n. \tag{3.128}$$

With the above equations, the divergent in the time integration is overcome, since the equations are no-longer de-coupled.

3.9.2.5 Leap Frog Method (LFM)

The Leap Frog Method is built on Euler's method and is commonly the preferred method compared to Euler. It updates $y(t)$ for time steps of Δt by calculating gradients at the half way points $(i + \frac{\Delta t}{2})$ and using a linear prediction on the updated $y(t + \Delta t)$. This is represented by:

$$y(t_{i+h}) = y(t_i) + v(t_{i+\frac{\Delta t}{2}}) \Delta t, \tag{3.129}$$

with the velocity also being predicted by using the velocity gradients calculated from the intermediate points of $y(t_{i+\frac{\Delta t}{2}})$:

$$v(t_{i+\frac{\Delta t}{2}}) = v(t_{i-\frac{\Delta t}{2}}) + \dot{v}(t_i)\Delta t. \tag{3.130}$$

A more useful form for the velocity is given by truncating the Taylor series expansion of $v(t_{i+\frac{\Delta t}{2}})$ so that quantities at t_i may be used:

$$v(t_{i+\frac{\Delta t}{2}}) = v(t_i) + \dot{v}(t_i)\frac{\Delta t}{2} + O(\Delta t^2). \tag{3.131}$$

Thus Equations (3.129) and (3.131) are alternately used to update each other. Since the LFM is second order, it is more accurate than the linear method for most cases but requiring the same order of calculation thereby minimizing storage. Another important aspect of the LFM is that it is time reversible since to advance in time by Δt, the mid-point gradient is used, thus:

$$y(t_i) = y(t_{i+\Delta t}) - v(t_{i+\frac{\Delta t}{2}})\Delta t, \tag{3.132}$$

which is obviously just Equations (3.129) re-written, confirming the symmetry. The LFM is a variant of the Verlet method which calculates the updated position via the mutually time reversed equations of a Taylor expansion:

$$y(i+\Delta t) = y(i) + \frac{\partial y(i)}{\partial t}\Delta t + \frac{\partial^2 y(i)}{\partial t^2}\frac{\Delta t^2}{2} + \frac{\partial^3 y(i)}{\partial t^3}\frac{\Delta t^3}{6} + O(\Delta t^4), \tag{3.133}$$

$$y(i-\Delta t) = y(i) - \frac{\partial y(i)}{\partial t}\Delta t + \frac{\partial^2 y(i)}{\partial t^2}\frac{\Delta t^2}{2} - \frac{\partial^3 y(i)}{\partial t^3}\frac{\Delta t^3}{6} + O(\Delta t^4), \tag{3.134}$$

which when combined gives:

$$y(i+\Delta t) = 2y(i) - y(i-\Delta t) + \frac{\partial^2 y(i)}{\partial t^2}\Delta t^2 + O(\Delta t^4), \tag{3.135}$$

and is accurate to the fourth order of the time step Δt with the added advantage of low computing cost. However the problem of not explicitly knowing the velocities $v(\Delta t)$ means that various quantities such as the kinetic energy are not known. Note

that the position is just a function of the acceleration and position of the particles as is expected from Newton's second law.

3.9.2.6 Adaptive Time Stepping

The time reversibility of either the LFM or the Verlet scheme is very useful for many symmetric application and for preserving energy conservation. However, introducing a variable time step which is deemed necessary for efficiency and accuracy, requires information from rates in one direction of time. Thus an adaptive time step finding algorithm may find alternate solutions depending on the direction of time flow. This in turn would cause diverging numerical solution to the problem at hand.

Hut *et al.* [188, 189] removed this restriction by using a modified LFM that does away with the half integer time steps in favour of using a Taylor expansion approximation of the velocity at the whole integer time steps and using a function $\xi(\vec{r_i}, \vec{v_i})$ which depends on the system information at the beginning and end points thus removing dependence on the beginning point alone, while also depending on velocities or positions of the system.

Courant-Friedrichs-Lewy Condition and other limits

The CFL condition is the major drawback of the explicit time stepping approach, as it requires Δt to be small. This makes the leapfrog technique very suitable for problem involving small time steps, however for problem with large time scale, explicit leapfrog technique is handicaped [190]. Explicit methods uses the present and past values to predict future values making it easy to code but susceptible to numerical instability while Implicit methods are generally harder to implement than explicit methods, but they have much better stability properties. An example is the Crank–Nicolson scheme [191, 192]. It is implicit in time and can be written as an implicit Runge–Kutta method, and it is based on the trapezoidal rule, and unconditionally stable with respect to the choice of Δt, although the cost of iteratively solving implicit equations is acceptable for small number of particles, but not for large scale system.

The Courant-Friedrichs-Lewy (CFL) condition is a necessary but not sufficient condition for stability while solving certain partial differential equations (usually hyperbolic PDEs) numerically. It arises in the numerical analysis of explicit time integration

schemes, as a consequence, the time step must be less than a certain time; otherwise the simulation will produce incorrect results. The dimensionless parameter, c, called the Courant number, is a stability criterion which establishes a link between the speed of the propagation of information and that of the system [193] and which is given by:

$$|c|^2 = \frac{\omega^2}{k^2 c_o^2}, \tag{3.136}$$

where ω^2 is the dispersion relation for the sound wave, k is the wavenumber and c_o is the reference speed of sound. For an ideal system, the magnitude of $|c|$ should be close to unity, in order to have a realistic propagation of the sound wave [164].

For a one-dimensional case, the CFL is given by:

$$c = u\frac{\Delta t}{\Delta x} \leq c_{max}, \tag{3.137}$$

where u is the magnitude of the velocity (whose dimension is length/time), Δt is the time step (whose dimension is time) and Δx is the length interval (whose dimension is length).

In the two-dimensional case, the CFL condition becomes:

$$c = u_x\frac{\Delta t}{\Delta x} + u_y\frac{\Delta t}{\Delta y} \leq c_{max}, \tag{3.138}$$

with obvious meaning of the symbols involved. By analogy with the two-dimensional case, the general CFL condition for an n-dimensional case is:

$$c = \Delta t \sum_{i=1}^{n} \frac{u_{x_i}}{\Delta x_i} \leq c_{max}. \tag{3.139}$$

For liquid media the parameter c is defined by the ratio of the signal distance, characterised by the speed of information, c_o which replace the parameter u in Equation (3.137). In SPH, Δx is scaled according to the smoothing length h. This means:

$$\Delta t_{1_{cfl}} \leq \frac{h}{c_o}, \tag{3.140}$$

where c_o is the reference speed of sound associated with the problem. Following Monaghan [107], c_o, should be chosen to be 10 to 100 times greater than the maximum speed (where $\vec{\mathbf{v}}_{max}$ represent the maximum speed in the system), just to curtail the fluctuation in density to within 1%. The CFL condition does not guarantee stability, since the violation of the condition is by definition un-stable.

Monaghan [19] uses a viscous update form of the CFL condition with the following:

$$\Delta t_{2_{visc}} = min_i \left(\frac{h_i}{c_o + 0.6(\alpha c_o + \beta max_{ij}(\mu_{ij}))} \right), \tag{3.141}$$

where α and β are weighting parameters, while Cleary and Monaghan [194] reported that for a pure conduction problems, the time step for an explicit scheme must satisfy:

$$\Delta t_2 \leq 0.15 \frac{h^2}{\nu}, \tag{3.142}$$

in order to have a stable solution, where ν represent the kinematic viscosity.

For the acceleration update form of the CFL condition,

$$\Delta t_{3_{acc}} = min_i \left(\sqrt{\frac{h}{|\vec{\mathbf{f}}_a|}} \right), \tag{3.143}$$

where $\vec{\mathbf{f}}_a$ is the force per unit mass; which represent the acceleration due to pressure, viscosity, surface tension terms or a combination of them.

To ensure that the force exerted on the particles are combined correctly, a convenient time step is chosen as:

$$\Delta t = \frac{1}{4} min_i \left(\Delta t_{1_{cfl}}, \Delta t_{2_{visc}}, \Delta t_{3_{acc}} \right), \tag{3.144}$$

so that the total energy can be conserved within 0.5% over 400 time steps. Also, the choice of the coefficients in the time step can varies slightly depending on the model parameters of the problem at hand [19].

$$\Delta t = min_i \left(0.4\Delta t_{1_{cfl}}, 0.25\Delta t_{2_{visc}}, 0.3\Delta t_{3_{acc}}\right). \tag{3.145}$$

3.10 The SPH algorithm and Code Structure

This section discusses the SPH algorithm and Code Structure in details. This SPH solver developed for all the fluid problems that will be discussed in this thesis's were done using C++ code written from scratch.

3.10.1 The SPH algorithm

The SPH algorithm start with the defining the domain, which is then populated with particles carrying material properties such as mass, position, pressure, velocity, density, viscosity, acceleration etc. These particles are then inserted into the kd-tree search algorithm (see section 3.6.2) by using their particles position information, from which the neighbour list for each particle are computed by using Equation (3.93) for the search range and then storing the neighbour list in a variable (nn). The next task is initialising the kernel function (see section 3.3.1.1) and then determining the density, either by using the summation density approach given by Equation (3.61) or the continuity density approach given by Equation (3.65) depending on the problem. In this thesis Equation (3.65) was used for most of the problem case as will be seen in Chapter 4. Once, the density is known, the next stage is the computational update of pressure, momentum, velocity, and position by using Equation (3.90), (3.77), (3.121 and 3.125) and (3.123) respectively. Furthermore, the particle density is updated using Equation (3.122) and (3.126) if the continuity density approach is adopted for the simulation, follow by the time update, why the output files generated depending on the write interval. The above process is repeated starting by insertion the updated particle position into the kd-tree search algorithm until the set end time is reached and the programme terminate.

3.10.2 Code Structure

Figure 3.27 show the schematic flow chart for the working of the code structure where all the necessary major step by step approach are presented in a chronological order. Now, the SPH solver can be use for simulating either one (1), two (2) or three (3) dimensional space problems. The switch from one to two or from two to three-dimensions is made possible by a vector class created at the initial stage for this purpose in the common.h file. However, for the purpose of this thesis, only the two-dimensional case is presented here.

Once the dimension, boundary conditions and domain of the problem are determine, then the next task is to populate the domain with particles (create) carrying properties such as position, density, type (fluid or solid particle), pressure, velocity, acceleration, mass, smoothing length e.t.c in the generate.cpp file. This generated particles are fluid particles if the particle type is zero (0) and solid particles if the particle type is one (1) and are space (dx) apart.

The next step is to setup the loop for either to end or continue the program using the current simulation time t to compare against the end time t_{end}, after which all the variable are clear, follow by inserting the new particle position into the kd-tree and then doing NN search (see the kdtree.h file), density, EOS, acceleration, velocity and position update. This flow chart illustrate the step by step approach on how the programme is developed from scratch by testing first the pressure terms of the momentum equation, then the viscosity terms and finally the body force (gravity). Later the surface tension terms is introduce in order to handle the aspect of droplet which will be discussed in details in Chapter 5. Finally, the output files produced (with extension .vtu) are then visualised using paraview simulation package to see the particles behaviour during the simulation. From the paraview simulation, one can tell if the generated results are in good agreement with analytical results by making a comparison through the use of graph representation or by quality observation. Table 3.2 shows a brief overview of the source and header file description use in the code structure with details of the C++ code describe in Appendix (B). Also, Table 3.3 shows here the main variables used in the code structure where D and I is used here to represent double and integer precision respectively.

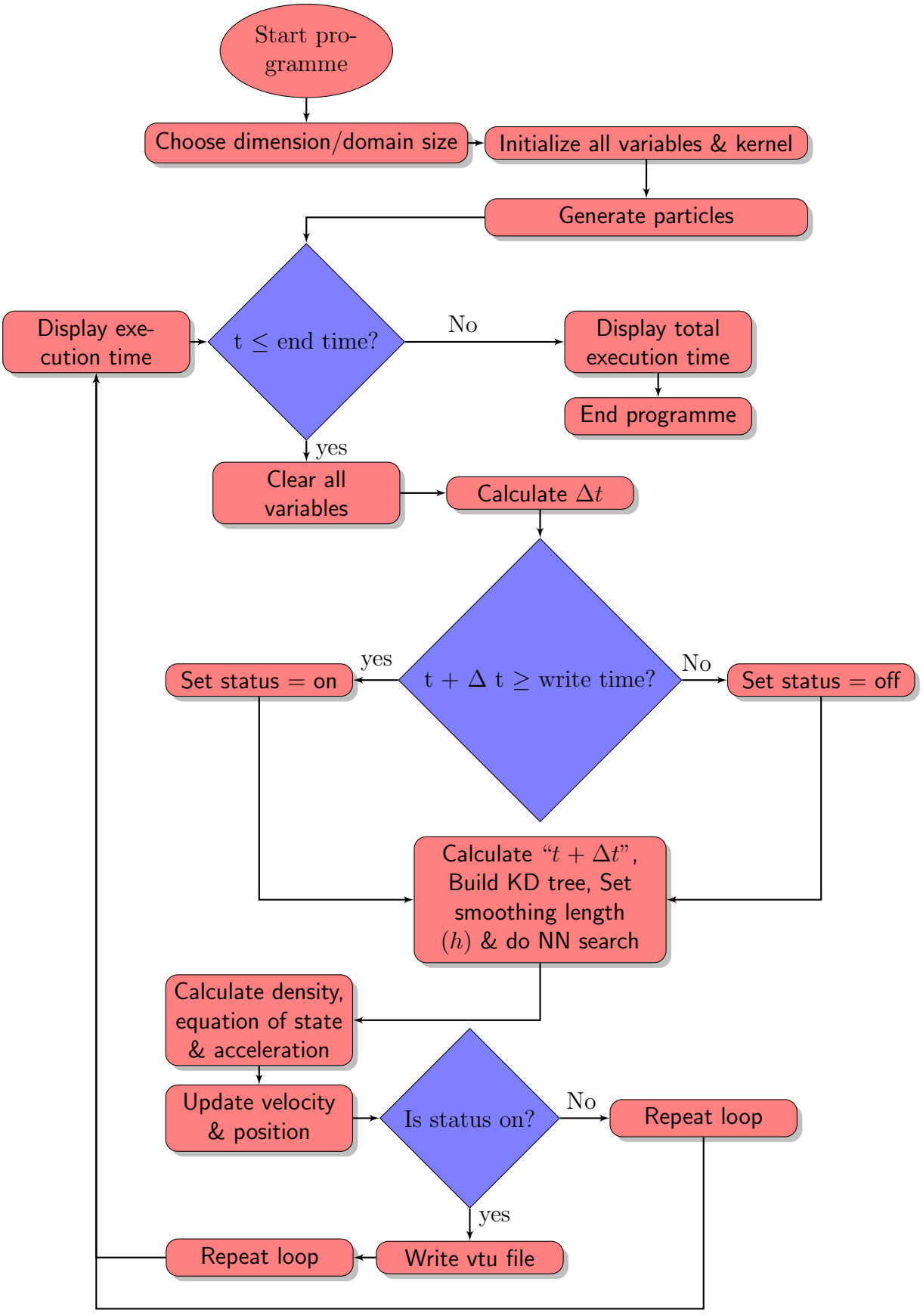

FIGURE 3.27: Schematic flow chart of the solver code.

TABLE 3.2: The source and header file used in the code.

File name	**Description of file**
main.cpp	This is the entry to the programme used for executing the code
common.h	This define all the constants used during the execution of the programme, such as Gravity, CFL constants, speed of sound, reference density, etc
generator (.cpp and .h)	Generating the particles within the problem domain
kdtress.h	This search for neighbour particle for each interested particles
c_parameter (.cpp and .h)	Define the domain size, kernel and density type, write interval output, time end etc
c_particle (.cpp and .h)	This is where all the computation are perform
data (.cpp and .h)	This is the part that linked the solver to the c_particle
init (.cpp and .h)	This is where the kernel to be use in the code is initialised
kernel (.cpp and .h)	This is where all the kernel function and their derivative are define
progress (.cpp and .h)	This shows the time, time step and percentage progress
init (.cpp and .h)	This is where the kernel to be use in the code is initialised
kernel (.cpp and .h)	This is where all the kernel function and their derivative are define
solver (.cpp and .h)	In this section, the loop is terminated or continue for the total set time
timer (.cpp and .h)	This is where the current time is obtained
utilities (.cpp and .h)	This is where the display shown by the progress is computed
vector.h	This is where all the vector class are defined for 1D, 2D or 3D, for example addition, subtraction, division, dot and cross product e.t.c

TABLE 3.3: The SPH variable and description used in the code.

Variable name, Unit	**Descriptions of variable**	**Type**
m, (kg)	Mass of particle	D
dx, (m)	Initial particle spacing	D
t, (s)	Time of simulation	D
dt, (s)	Time steps during the simulation	D
ρ, (kg/m^3)	Density of particle	D
p, (N/m^2)	Pressure of particle	D
c_0, (m/s)	Speed of sound	D
mu, (m/s)	Particle viscosity	D
h, (m)	Smoothing length	D
idx, ( )	Particle index	I
vel, (m/s)	Particle velocity	D
vel_prime, (m/s^2)	Particle acceleration	D
$VARIABLE\_H\_ETA$, ( )	The expansion ratio	D
$TAITS\_GAMMA$, ( )		D
$type$, ( )	Particle type	I
p_num_X, ( )	Number of particle in X direction	I
p_num_Y, ( )	Number of particle in Y direction	I

Chapter 4

Solver Validation Test

"We shall not cease from exploration. And the end of all our exploring will be to arrive where we started and know the place for the first time."

T.S. Eliot, (1888-1965).

4.1 Validation Test

All analysis presented in the present thesis are conducted in 2-dimensions, although it is readily extendable for 3-dimensional problems, to explore the develop proof-of-concept models to ensure that they are accurate as these has immersed practical applications to industrial problems such as those in solidification and deposition of molten materials, anisotropic wettability on striped surfaces for fluid control and transport, printing processes and dip-coating [195]. Cunjing [195] argued that in fact, 2-dimensional solutions has generated a lot of interest recently, with results suggesting that the physics of 2D and 3D problems are almost indistinguishable in problems such as wettability of drops on soft solids, motion of long bubbles in channels and liquid spreading. However, 3D solutions remains very relevant in droplet mixing and coalescence applications due to the surface tension effects acting in all three spatial directions. Here, the developed SPH solver is tested against known 2D classical problems in order to test its capabilities on accuracy, efficiency and stability properties.

4.1.1 Test case 1: Determination of suitable choice values for expansion ratio η

The first test for the developed SPH solver is to investigate that the right number of particle neighbours are captured during the neighbour search operation for $1D$, $2D$ and $3D$. From literature [157], the kernel function contribution to a particle of interest for a full neighbour list sum approximately to one (unity), see Equation (3.7). In order to demonstrate this, a 100×100 system of particles were generated at equal-spacing of ($dx = 1.0$ mm) while the value of η were varied from 1 to 2.5 with increment of 0.1. For each values of η, the corresponding smoothing length $h = \eta \times dx$, were evaluated. To illustrate this graphically, only the one of $2D$ is presented as shown in Figure 4.1, where the kernel summation $\sum W_{ij}$ is plotted against varying h. From this graph, it is seen that the kernel function contribution to a particle of interest for a full neighbour list sum approximately to one (unity) within η ranges of 1.2 to 1.3 and 1.9 to 2.5. Between η ranges of 1.3 to 1.9, the neighbour contribution to a particle of interest is significant, hence the kernel summation $\sum W_{ij}$ is larger than one (unity). Now, for computational cost, the η range between 1.2 to 1.3 is consider the best choice and this agrees with literature [196]. As for η range between 1.9 to 2.5, the graph pattern remains almost constant, even with increasing contribution from the neighbours to the particle of interest, however the neighbour contribution are almost insignificant, thus making this choice of range computation expensive to carry out.

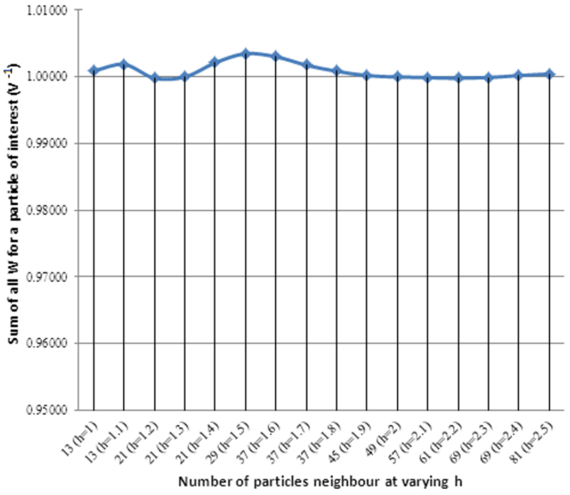

FIGURE 4.1: Graph of $\sum W_{ij}$ versus No of particles neighbour at varying h.

4.2 Test case 2: Particle bounce

Consider the case of a particle bounce problem on a flat stationary surface in a perfectly elastic system. The aim of the test is to ensure that for an inviscid system, the SPH methodology preserves momentum and therefore conservation of mass, as the interaction between the bouncing particle and the boundary is made possible only by the pressure gradient change. The movement of a single SPH particle initially at rest is modelled while falling under the influence of gravity and upon hitting a solid wall of either five (5) or six (6) SPH dynamics boundary particles rebounds to the same height. In spite of the simplicity of the test, it shown that the bouncing particle can be kept re-bouncing infinitely by the repulsive force of solid wall boundary particles without mechanical energy losses in the system. This was made possible by the weakly compressible equation of state (EOS) Equation (3.90) and the cubic kernel Equation (3.20).

The initial set-up of boundary particle positions are in the first instant uniformly distributed and in the second instant in a staggered arrangement inside a box (1.0m×1.0m). For either arrangement, the particles positions are shown in Figure 4.2 (a) and (b), where the shaded circle represent the falling particle and donut represents the dynamic boundary particles. The separation between the dynamic boundary particles for the normal arrangement in X and Y directions is $dx = dy = 0.1$m while for the staggered arrangement is $dx = 0.1$m in X and $dy/2 = 0.05$m in Y-direction and $h = \eta \times dx$ which represent the smoothing length is applied to all the particles with the expansion ratio, $\eta = 1.3$, chosen for this test case.

The initial conditions and properties of all the particles are listed in Table 4.1 with the bouncing particle located at a height of (0.1, 0.6) directly above the middle for both arrangements respectively, where it is allowed to fall under gravity of $-9.81m/s^2$ along the Y-axis for an entire test period of 2 seconds. At this height, the bouncing particle do not feel the interaction of the bottom particles until it comes close enough to the search range of $r = \kappa h$, determine by the chosen kernel function in this case, for a cubic kernel, $\kappa = 2$. Throughout the simulation, the values of both κ and h remain constant. The maximum reference sound speed, c_o was chosen such that is was 50 times the maximum impact velocity to limit the particles compressibility [107]. With this sound speed, c_o, the density variations was reduced significantly to 0.88% and 0.92% as seen in Figure 4.3 (a) and (b) arrangements respectively.

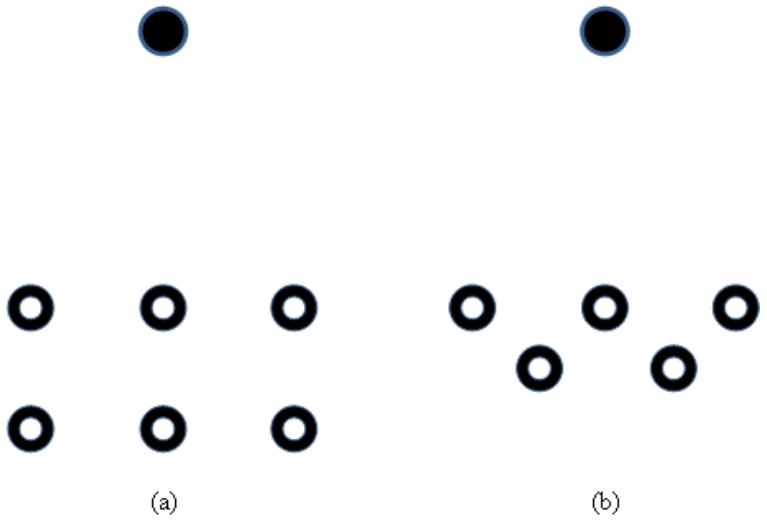

FIGURE 4.2: Sketch of particles initial positions for (a) Uniformly distributed (Normal) (b) Staggered, arrangement respectively.

TABLE 4.1: Initials conditions and properties of particles (test case 1).

Properties, symbols (Units)	**Fluid particle value**	**Wall particle value**
Mass, m (kg)	10 for normal, 5 for staggered	10 for normal, 5 for staggered
Density, ρ (kg/m^3)	1000.0	1000.0
Sound speed, c_o (m/s)	221.47	221.47
Smoothing length, h (m)	1.3× dx	1.3× dx
Separation, $dx = dy$ (m)	0.5 from top wall particle for both normal and staggered arrangement	0.1 in both dx and dy for normal while 0.1 in dx and 0.05 in dy for staggered arrangement respectively

By using the smoothing length and continuum density function Equations (3.65), this test case was able to establish the conservation of momentum and the particle keep re-bouncing indefinitely, each time returning back to its initial height and maintaining its initial density without experiencing any significant acceleration in the X-direction.

In SPH, mass is invariant but particle volume and initial density are not, which make the initial density very necessary in this simulation. This test case results agreed strongly with similar approach carried out by Crespo *et al.* [196]. A plot of height of bouncing particle against time is shown in Figure 4.4 (a) and (b) for

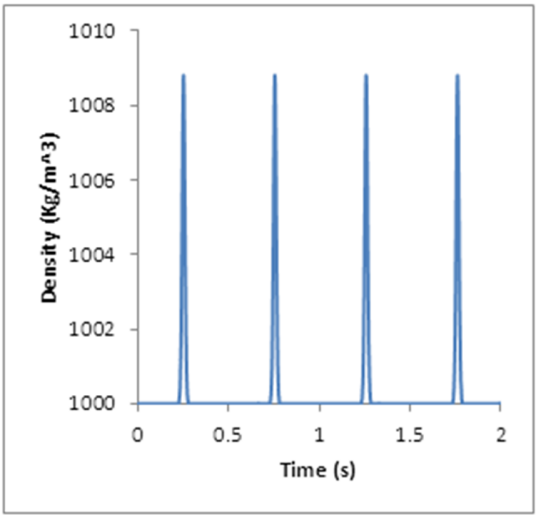

(a)

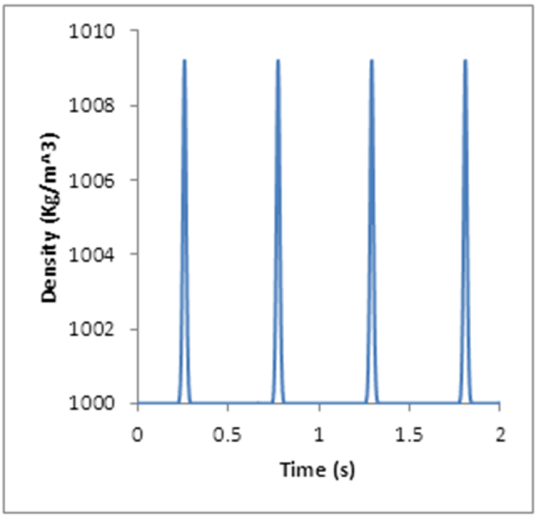

(b)

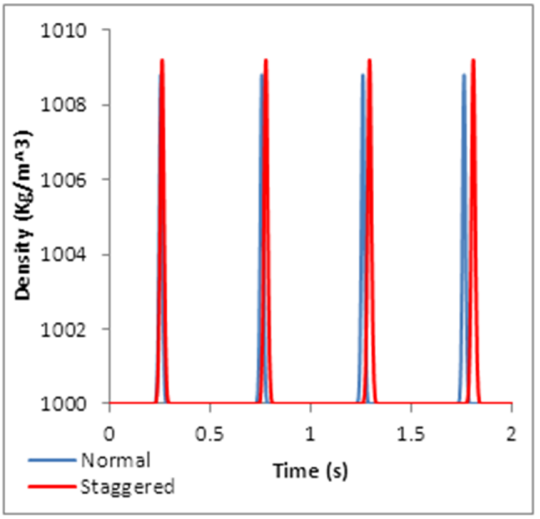

(c)

FIGURE 4.3: Density fluctuation for (a) Uniformly distributed (Normal) (b) Staggered (c) combine, setup.

both arrangements. As can be seen, there is no noticeable or appreciable variations between the maximum attained and initial release height for the entire period of simulation. However a maximum height error of 0.49% and 4.11% were observed for normal and staggered arrangements respectively, at the final point of re-bounce, hence the difference in their point of rebounce as shown in Figure 4.4 (c). This may be due to lack of impact shock resistance in the staggered (because it is more compact or dense) than the normal arrangement, hence the bouncing particle returned earlier in the normal arrangement which account for the the difference in the return point.

A plot of velocity in $Y-$axis against time is shown in Figure 4.5 for both arrangements, again there is a regular pattern of rebounce, but with a time lag noticed. In addition, there is a slight velocity fluctuation which is believe to be caused by the time integration scheme used. The Verlet time integration scheme was used and because it not self starting, the leap frog technique was used to start the integration scheme. A switch of every fifty time steps was adapted and this removed any velocity oscillations.

As seen previously, when a particle is not within the full support domain of a kernel, it experiences this error, which fade away as seen in Figure 4.5 where the velocity return to the expected path, immediately the period of fluctuation is over, thus making the error insignificant. Figure 4.6 plots the velocity in $Y-$direction against the height for a complete cycle. As can be seen, the velocity against height plot is in close agreement with the other profile, this further re-affine momentum conservation.

4.3 Test case 3: Couette flow

This test case is to verified the accuracy of the developed SPH solver for a viscous system where viscous dissipation is important. Couette flow is a flow between two infinite parallel plates located at $L = 10^{-3}$m apart in which the bottom plate is at rest and the top plate is moving with a constant velocity, $V_0 = 1.25 \times 10^{-5}ms^{-1}$, parallel to the X-axis. The simulation is setup such that the fluid and plates has s periodic boundary in the X-direction so that the flow is infinitely continuous. The use of periodic boundary conditions also helped to reduce the computational time of the solver by bounding the problem (see Violeau [100] and Zhu *et al.* [197]). A schematic representation is shown in Figure 4.7 for the initial particle arrangement with 10×50 particles use to populate the domain. Fluid flow parameters are summarized in Table 4.2, which gives the resulting Reynolds number, $Re = 1.25 \times 10^{-2}$.

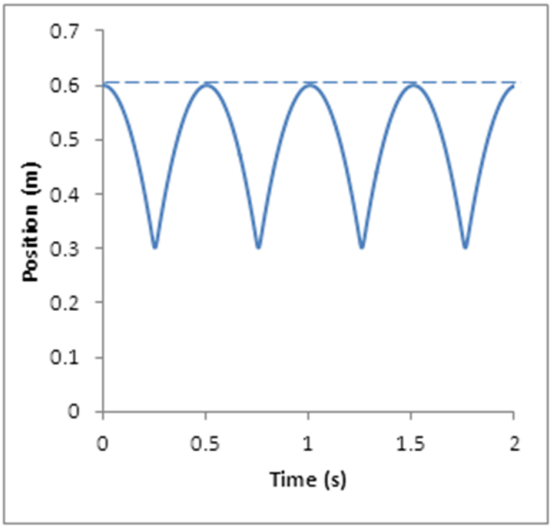

(a)

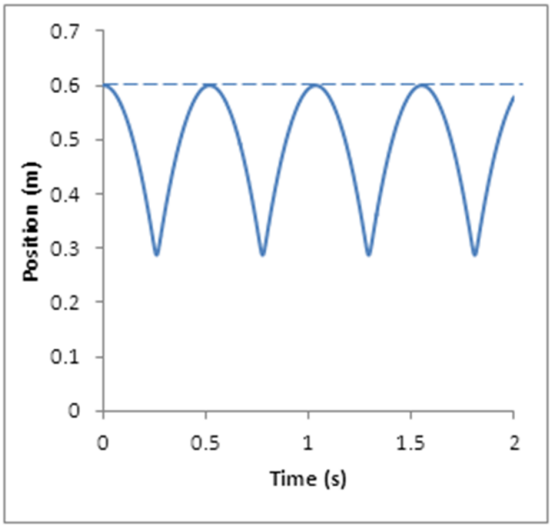

(b)

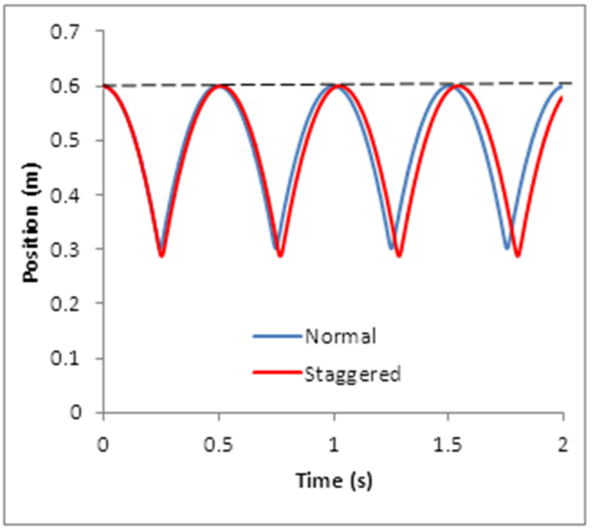

(c)

FIGURE 4.4: Maximum height attained for (a) Uniformly distributed (Normal) (b) Staggered (c) combine, setup.

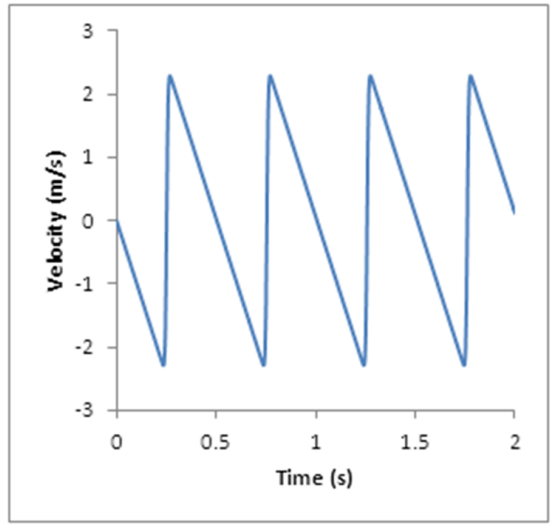

(a)

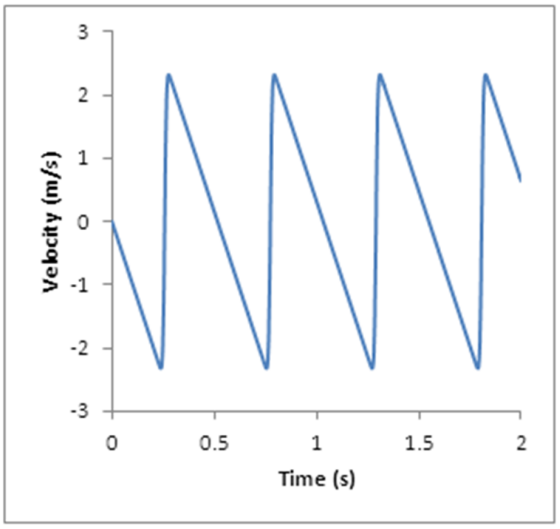

(b)

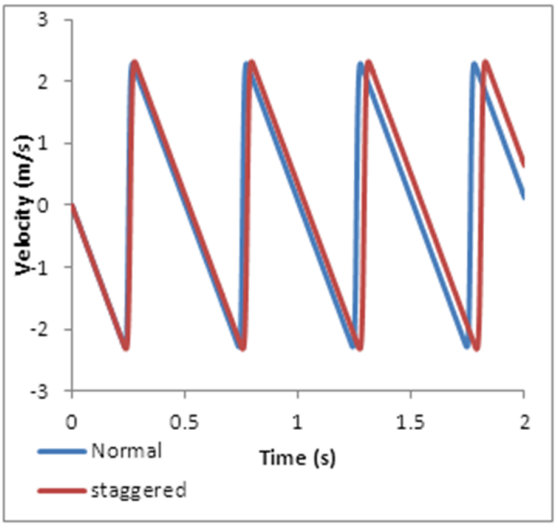

(c)

FIGURE 4.5: Plot of Velocity versus Time for (a) Uniformly distributed (Normal) (b) Staggered (c) combine, setup.

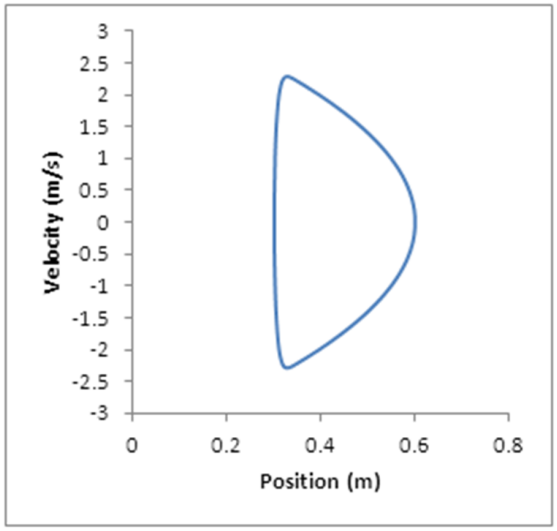

(a)

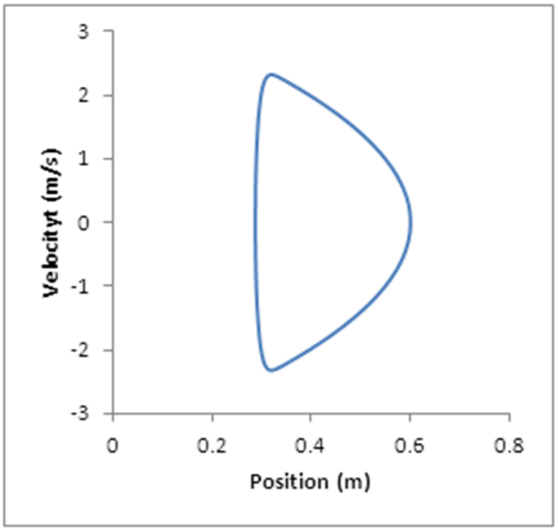

(b)

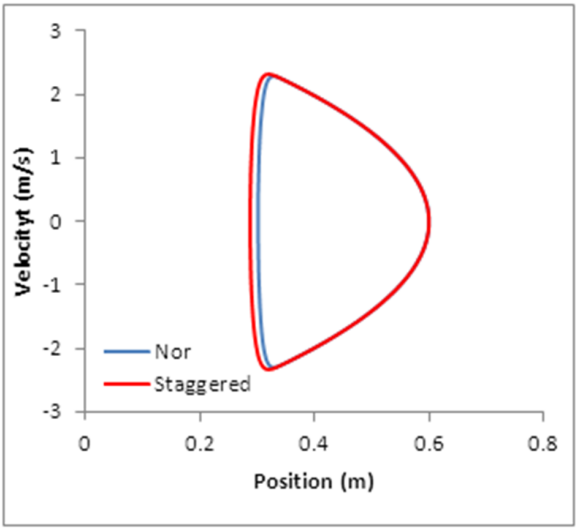

(c)

FIGURE 4.6: Plot of Velocity versus Position for (a) Uniformly distributed (Normal) (b) Staggered (c) combine, setup.

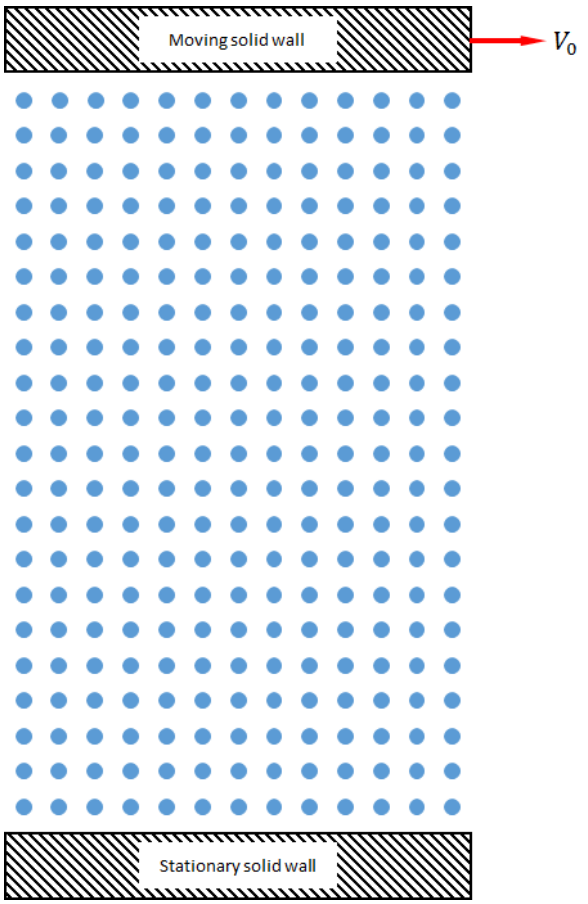

FIGURE 4.7: A virtual arrangement of the particles initial positions setup for couette flow).

TABLE 4.2: Initials conditions and properties of particles (test case 3).

Properties, symbols (units)	**Fluid**	**bottom plate**	**top plate**
Mass, m (kg)	4.0×10^{-7}	4.0×10^{-7}	4.0×10^{-7}
Density, ρ (kg/m^3)	1000.0	1000.0	1000.0
Pressure, p (Pa)	0	0	0
Acceleration, $\vec{\mathbf{a}}$ (m/s^2)	0	0	0
Dynamics viscosity, μ (Pas)	10^{-3}	10^{-3}	10^{-3}
Velocity, $\vec{\mathbf{v}}$ (m/s)	0	0	$V_0 = 1.25 \times 10^{-5} ms^{-1}$
Sound speed, c_o (m/s)	221.47	221.47	221.47
Smoothing length, $h(m)$	1.3× dx	1.3× dx	1.3× dx
Separation, $dx = dy$ (m)	2.0×10^{-5}	2.0×10^{-5}	2.0×10^{-5}

The analytical solution for this fluid flow time−dependant behaviour following the derivation given by Morris *et al.* [101] is:

$$V_x(y,t) = \frac{V_0}{L}y + \sum_{n=1}^{\infty} \frac{2V_0}{n\pi}(-1)^n \sin\left(\frac{n\pi}{L}y\right) \exp\left(-\nu\frac{n^2\pi^2}{L^2}t\right), \tag{4.1}$$

where V_x is the velocity of the fluid in X-direction, L is the distance between the top and bottom plates, y is the particles positions, n (varies from 1 to 100) is the assumed control parameter for infinity summation, while all other parameters are as define previously in Table 4.2.

A comparison of the SPH and analytical solutions was carried out. Figure 4.8 shows the velocity against distance profile at various times resulting from Equation (4.1) and the SPH solver, with dots and solid lines represent the latter and former solutions, respectively. From the simulation, the maximum error recorded at steady state was approximately 1.6% without any velocity correction for the boundary particles, in order to implement the no-slip condition, when the SPH and analytical results are compared. These results are in strong agreement with those presented by Morris *et al.* [101] with maximum error of 0.5%, but with velocity correction for the boundary particles, which they implemented by giving it an artificial velocity, just to simulate the no-slip boundary condition, especially at the steady state when $t = \infty$, but for the purpose of simulation it is taken to be 2s in this test case. The author believe that with velocity correction for the boundary particles, the computational cost will be high, thus in conclusion, there is no need for velocity correction.

4.4 Test case 4: Poiseiulle Flow

This test case is another standard test to verify the developed SPH algorithms for viscous force in 2D. In the present case, Poiseuille flow, a flow between two infinite parallel plates located at $L = 10^{-3}$m apart in which both plates are at rest while the fluid which was at rest initially is driven with a body force of $F = 10^{-4}\mathrm{m}s^{-2}$ parallel to the x-axis. Just like in Couette flow, the simulation is setup such that the fluid flow is defined periodically in the X-direction. A virtual representation is shown in Figure 4.9 for the initial particles arrangement with 10×50 fluid particles used. The parameters summarized in Table 4.3, are used, which gives a Reynolds number $Re = 1.25 \times 10^{-2}$.

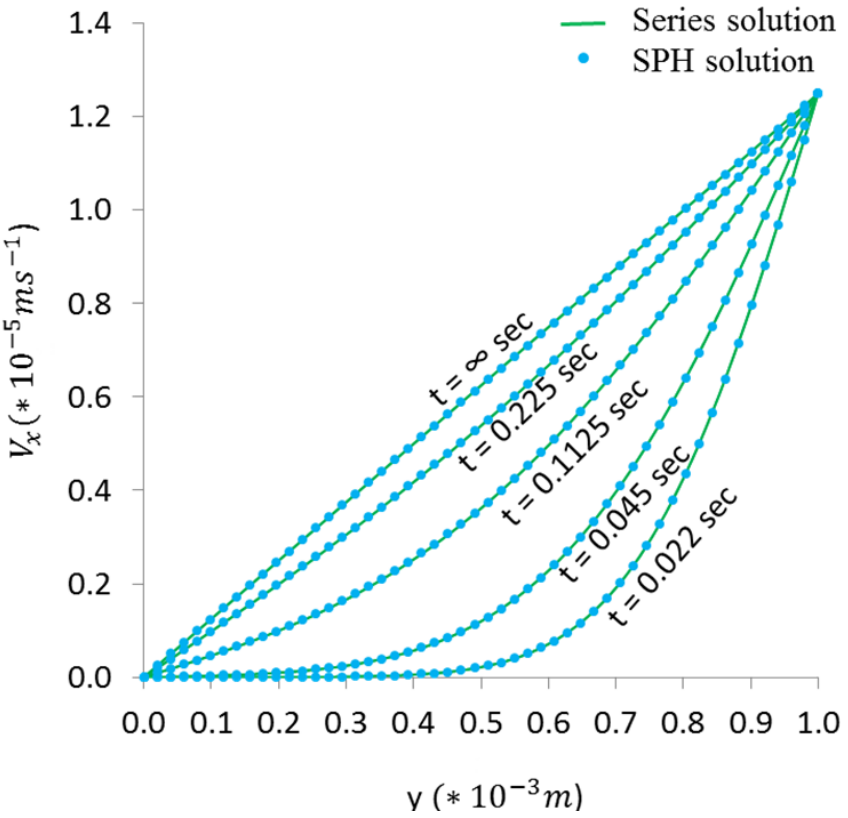

FIGURE 4.8: Comparison of SPH and Series Solution for Couette Flow ($Re = 1.25 \times 10^{-2}$).

The analytical solution for this fluid flow time−dependant behaviour is given by:

$$V_x(y,t) = \frac{F}{2\nu}y(L-y) - \sum_{n=0}^{\infty} \frac{4FL^2}{\nu\pi^3(2n+1)^3} \sin\left(\frac{\pi y}{L}(2n+1)\right) \exp\left(-\frac{(2n+1)^2\pi^2\nu}{L^2}t\right), \tag{4.2}$$

where F is the body force, while all other parameters are as define previously in Couette flow problem and Equation (4.1). The fluid parameters in the present case gives a maximum velocity of 1.25×10^{-5} at the centre of the channel.

A comparison of the SPH and the analytical solution was carried out. Figure 4.10, shows the velocity against particle position profile at various times resulting from Equation (4.2) and the SPH solver; the dots and solid lines represent the SPH and analytical solutions, respectively. From the results, the maximum error recorded at steady state was 1.6% without velocity correction when the former and latter results

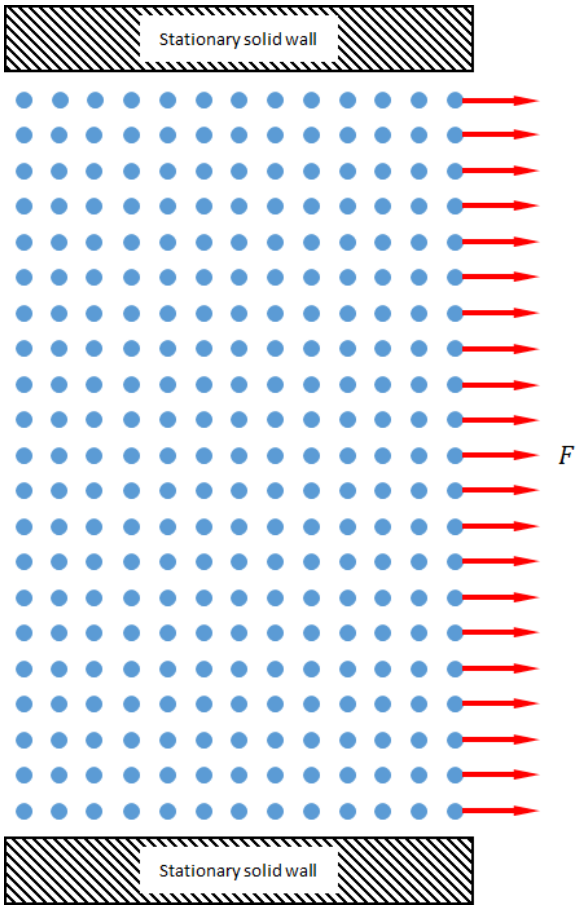

FIGURE 4.9: A virtual arrangement of the particles initial positions setup for poiseuille flow.

are compared. These results are in strong agreement with literature Morris *et al.* [101], where they had 0.7% maximum error with velocity correction. Again, as stated previously in Couette flow problem, more computational time will be required to accomplish the task, this the author believe is unnecessary and thus in conclusion, there is no need for velocity correction.

4.5 Test case 5: Lid Driven Cavity Flow

The Lid driven cavity is another prominent, challenging and classical benchmarking test for viscous flows which is much used to validate the accuracy of numerical models, see Adami *et al.* [198] and Leroy *et al.* [199] . The system is made up of a closed square box of size $L = 1$mm, which is filled with fluid (water) while the top plate (upper boundary or upper wall) is moving with a constant horizontal speed of $U_{max} = 1$m/s, driving the fluid as a result of viscosity (details of this can be seen in

TABLE 4.3: Initials conditions and properties of particles (test case 4).

Properties, symbols (units)	**Fluid**	**bottom plate**	**top plate**
Mass, m (kg)	4.0×10^{-7}	4.0×10^{-7}	4.0×10^{-7}
Density, ρ (kg/m^3)	1000.0	1000.0	1000.0
Pressure, p (Pa)	0	0	0
Acceleration, $\vec{\mathbf{a}}$ (m/s^2)	0	0	0
Body Force, $\vec{\mathbf{f}}$ (ms^{-2})	10^{-4}	0	0
Dynamics viscosity, μ (Pas)	10^{-3}	10^{-3}	10^{-3}
Velocity, $\vec{\mathbf{v}}$ (m/s)	0	0	0
Sound speed, c_o (m/s)	$50.0 \times \vec{\mathbf{V}}_0$	$50.0 \times \vec{\mathbf{V}}_0$	$50.0 \times \vec{\mathbf{V}}_0$
Smoothing length, $h(m)$	$1.3\times\ dx$	$1.3\times\ dx$	$1.3\times\ dx$
Separation, $dx = dy$ (m)	2.0×10^{-5}	2.0×10^{-5}	2.0×10^{-5}

Rogers [200]). This continuous moving lid causes the fluid to rotate clockwise within the square cavity box, which becomes less or more complex depending on the Re number of the flow. Figure 4.11 shows the 2D geometry of the square cavity with lid (cover plate) for the simulation.

Three Reynolds numbers $Re = 100$, $Re = 1000$, and $Re = 10000$ were employed using the fluid parameters presented in Table 4.4. These Reynolds numbers were each simulated with resolutions 50×50, 100×100, and 200×200 respectively, while the fluid particles are initially uniformly spaced $dx = dy$. The initial system were all set from rest and a cubic kernel with smoothing length $h = 1.3 \times dx$ is adopted. For the simulation, a sound speed of $100 \times U_{max}$ and excess repulsive pressure from Equation (3.94) were employed to prevent particles clustering. The square box wall is modelled using three layers of stationary particles with the same properties as that of the fluid particles while the lid wall has the same fluid properties but moving at constant lateral speed.

As there is no known analytical solution for this test case, steady-state solution were compared against the results of Ghai *et al.* [201], who modelled this flow with multi-grid finite-difference scheme on a 257×257 mesh. Figure 4.12 (a) and Figure 4.12 (b) show the velocity field of the SPH along with those in Adami *et al.*[198]. They are in close agreement for the case when $Re = 100$ even at low resolutions of 50×50 and

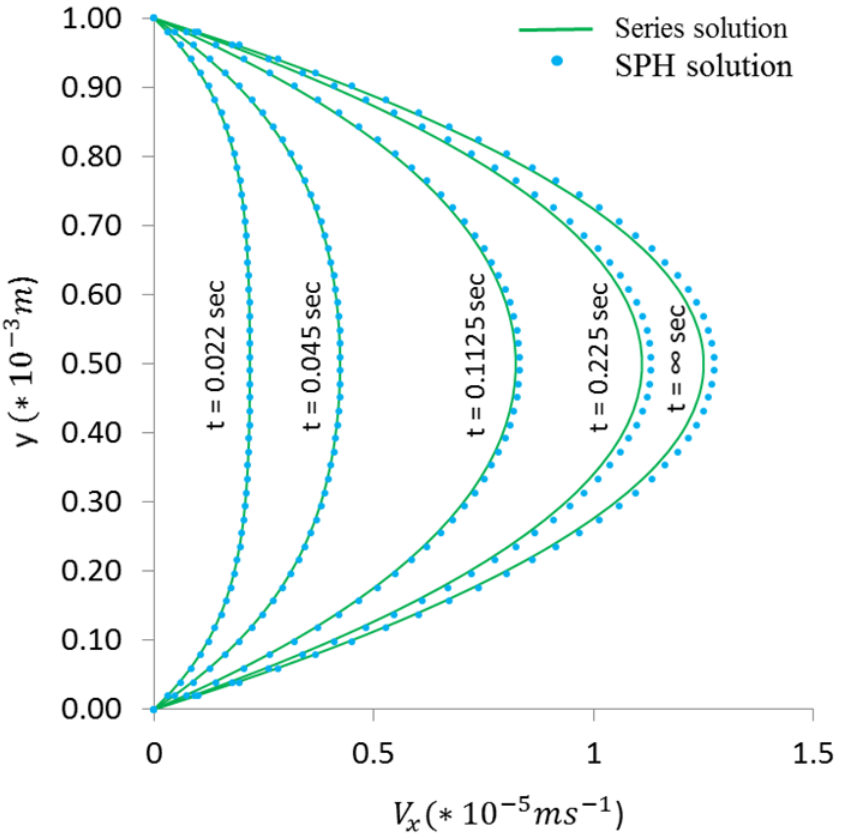

FIGURE 4.10: Comparison of SPH and Series Solution for Poiseuille Flow ($Re = 1.25 \times 10^{-2}$).

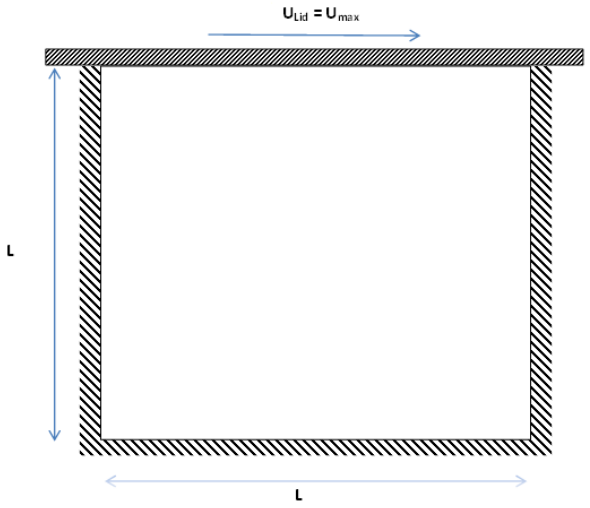

FIGURE 4.11: The 2D geometry of Lid Driven Cavity flow setup.

TABLE 4.4: Initials conditions and properties of particles in Lid Driven Cavity Flow (test case 5).

Properties, symbols (Units)	**Fluid**	**Lid Plate**	**Tank Wall**
Mass, m (kg)	$\rho \times dx \times dy$	$\rho \times dx \times dy$	$\rho \times dx \times dy$
Density, ρ (kg/m^3)	1000.0	1000.0	1000.0
Pressure, p (Pa)	0	0	0
Acceleration, $\vec{\mathbf{a}}$ (m/s^2)	0	0	0
Dynamics viscosity, μ (Pas)	10^{-3}	10^{-3}	10^{-3}
Velocity, $\vec{\mathbf{v}}$ (m/s)	0	$U_{Lid} = U_{max}$	0
Sound speed, c_o (ms^{-1})	$100 \times U_{Lid}$	$100 \times U_{Lid}$	$100 \times U_{Lid}$
Smoothing length, h (m)	$1.3\times$ dx	$1.3\times$ dx	$1.3\times$ dx
Separation, $dx = dy$ (m) (Depends on resolutions used)	$1/resolution$	$1/resolution$	$1/resolution$

100×100.

The colour-map shows the velocity magnitude ranging from zero (blue) to U_{max} (red). Since the fluid particle rotate clockwise, the particle close to the bottom of the cavity moves slower and because of shear force of the lid movement, a single core vortex emerge between the moving lid and the center of cavity. Furthermore, Figure 4.12 (c) shows the comparison of the reference results from Ghai *et al.* [201], where vertical velocity ($V_y(x)$ with symbol colour □) and horizontal velocity ($V_x(y)$ with symbol colour ◯) components plotted against the horizontal and vertical centerline of the cavity, respectively. The SPH results for 50×50 and 100×100 resolutions for $V_x(y)$ and $V_y(x)$ were represented by dot and dash line.

Figures 4.13 and 4.14 show the results for $Re = 1000$ and $Re = 10000$. From these Figures, the intensity of the core vortex increases as the Reynolds number increases. At $Re = 1000$, the velocity profiles along the centerline correspond qualitatively to the reference results only at 200×200 resolution. As, can be notice from Figures 4.13 (c), the SPH solutions are becoming noisy at $Re = 1000$ when the resolution increases from 50×50 to 200×200, which may be due to the beginning of transition from lamina to turbulent flow.

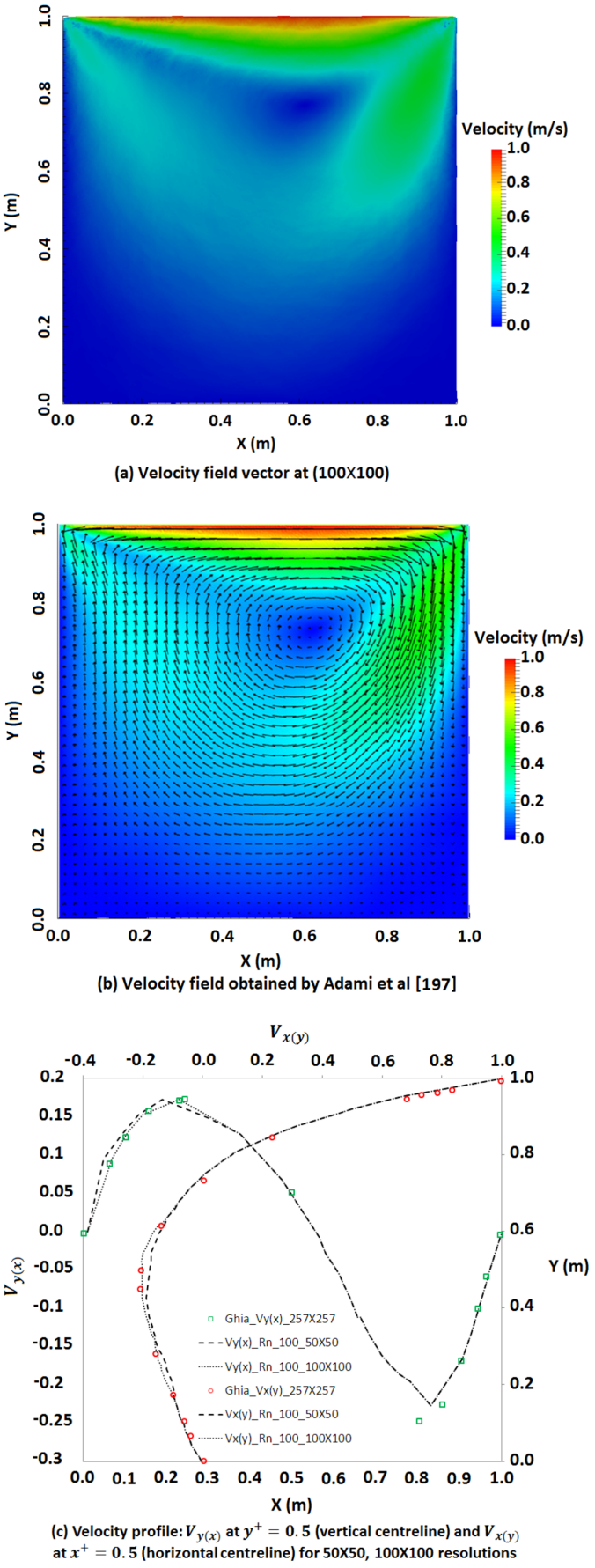

FIGURE 4.12: 2D results of the lid driven cavity flow simulation at $Re = 100$.

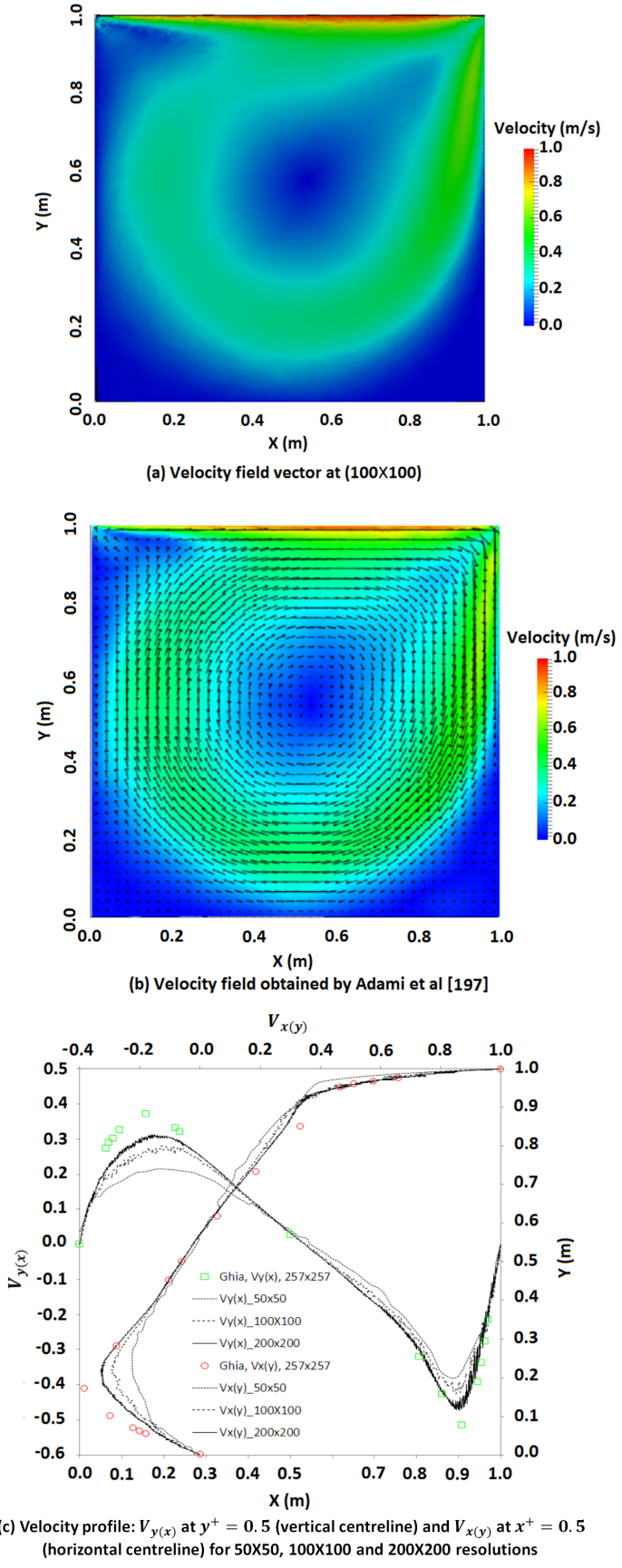

FIGURE 4.13: 2D results of the lid driven cavity flow simulation at $Re = 1000$.

At $Re = 10000$, a much higher resolution is required for more convergence to the reference results as shown in Figure 4.14, but because of computational time 200×200 resolution is the maximum used, with the core vortex almost centered within the cavity. With $Re = 10000$, it is notice that the SPH solutions are now fully developed into more turbulent flow, even at lower resolutions with more noisy. The author argues that, even though the developed SPH solver was for lamina viscous dominated flows, it was able to gives good qualitative agreement with reference results, which is acceptable as shown in Figure 4.14 (c) especially at 200×200 resolution and that changing the SPH solver to account for turbulent flow is beyond the scope of this thesis.

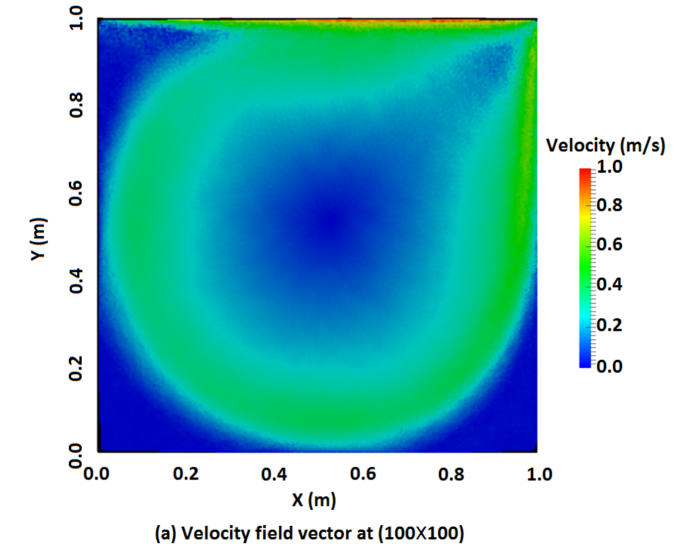

(a) Velocity field vector at (100X100)

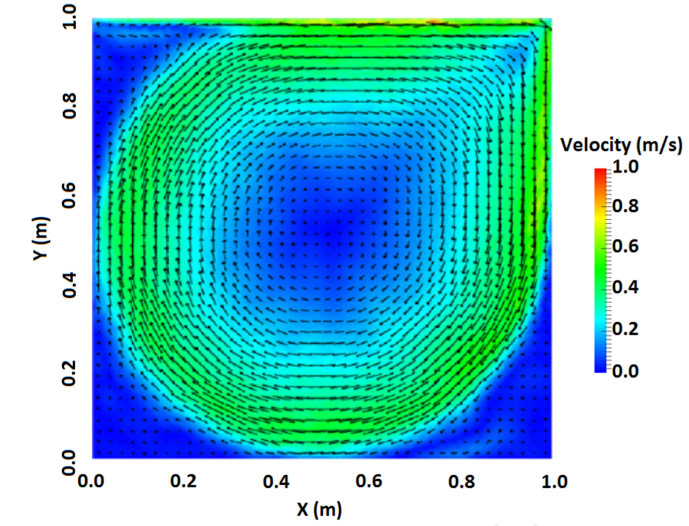

(b) Velocity field obtained by Adami et al [197]

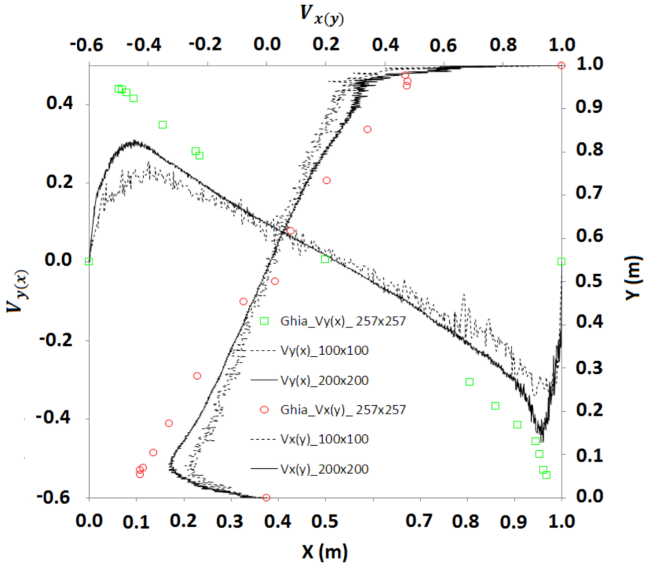

(c) Velocity profile: $V_{y(x)}$ at $y^+ = 0.5$ (vertical centreline) and $V_{x(y)}$ at $x^+ = 0.5$ (horizontal centreline) for 100X100 and 200X200 resolutions

FIGURE 4.14: 2D results of the lid driven cavity flow simulation at $Re = 10000$.

4.6 Test case 6: Dam Break

Consider the case of a dam break problem defined schematically in Figure 4.15. However, unlike previous test cases such as Coeutte flow, Poiseuille flow and lid-driven cavity, where the fluid near the boundary do not suffer from density deficiency because of the way these problems are well defined such that there are no free-surfaces and therefore the fluid particles maintains a full kernel support, the dam break problem explores how the developed SPH solver treats the free-surface as it evolves and deforms dynamically with time. The assembly is made up of a column of $2D$ water of height $2m$ and width $1m$ that collapse due to gravity in a tank of height $3m$ and width $4m$ internal dimension. This mimics the experiment setup carried out by Koshizuka and Oka [202] and which were also used by Violeau and Issa [203] and further by Crespo *et al.* [196] to verified SPH accuracy. Here, 2,418 particles were used for the boundary particles (tank walls) while 20,000 particles were used for the fluid water column. A smoothing length of $h = 1.3dx$, viscosity term (Equation (3.76) for real and Equation (3.78) for artificial viscosity respectively) were considered, while also using two kernels, namely cubic and Wendland kernel for the simulation in order to demonstrate which kernel is able to handle tensile instability naturally with these viscosity. Table 4.5 describe the particles properties employed for the simulation.

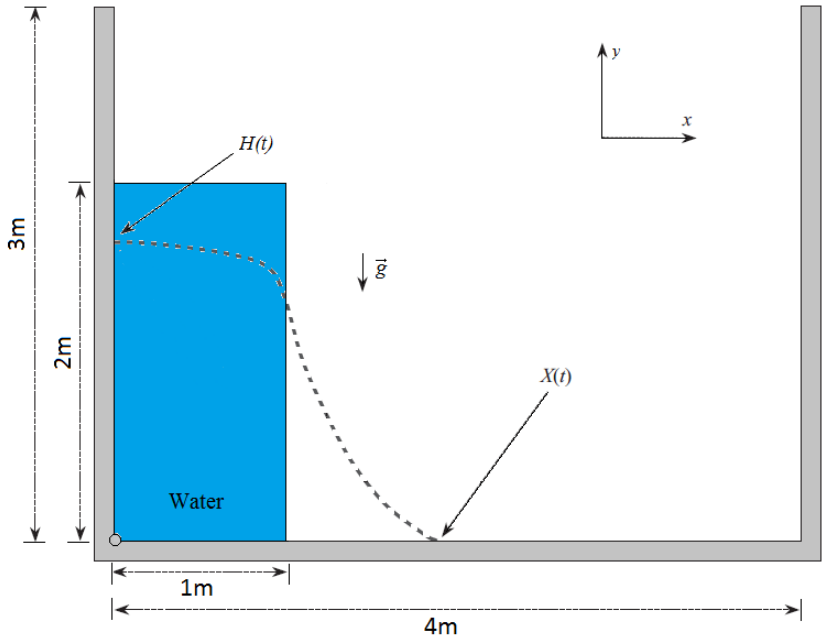

FIGURE 4.15: 2D geometry of initial setup of the water column (blue colour area) and the tank (ash colour area), with the evolution of the water column collapse by the dashed line.

TABLE 4.5: Initials properties of particles for the Dam Break Flow (test case 6).

Properties, symbols (Units)	**Fluid**	**Tank wall**
Mass, m (kg)	$\rho \times dx \times dy$	$\rho \times dx \times dy$
Density, ρ (kg/m^3)	1000.0	1000.0
Pressure, p (Pa)	0	0
Acceleration, $\vec{\mathbf{a}}$ (m/s^2)	-9.81	0
Dynamics viscosity, μ (Pas)	10^{-3}	10^{-3}
Velocity, $\vec{\mathbf{v}}$ (m/s)	0	0
Sound speed, c_o (ms^{-1})	$100 \times U_{max}$	$100 \times U_{max}$
Smoothing length, h (m)	$1.3\times$ dx	$1.3\times$ dx
Separation, $dx = dy$ (m)	0.01	0.01

Apart from the initial geometrical constraints of the water column, the movement of the fluid particles within the tank depends on the interaction between the fluid and solid boundary. So, to generate a realistic simulation of the water height decrease near the left tank wall and an accurate water velocity near the dam toe (right of water column toe), proper solid boundary treatment is needed to be carried out. To do this, the solid boundary wall is modelled with three (3) or four (4) layers of particles depending on the search range of the kernel used. Basically, for a search range of $2h$ and $3h$, particles layers of three (3) and four (4) are usually recommended respectively. This approach, prevents fluid penetration into the wall boundaries and eventually escapes the system especially on the right tank wall which suffers this problem the greatest as the energetic water collides with it.

The simulation was carried out with the modified continuity density Equation (3.65) while using the cubic (with and without artificial viscosity, Equation (3.78) and Equation (3.76)) and Wendland kernel. In the case where the Wendland kernel is used, there was no need for the use of the stabilized continuity density Equation (3.67), repulsive force Equation (3.94) or XSPH Equation (3.95), to be applied in order to have a smoothed particle distribution, as there was no tensile instability occurring throughout the simulation as shown in Figure 4.16 (a); the big square box represent the exploded view.

This is evident from the joint work of Macia *et al.* [156], who concluded that Wendland kernel has the capability to replicate dissipation mechanism more accurately, couple with its soft repulsive force thereby preventing pairing instability of particles otherwise

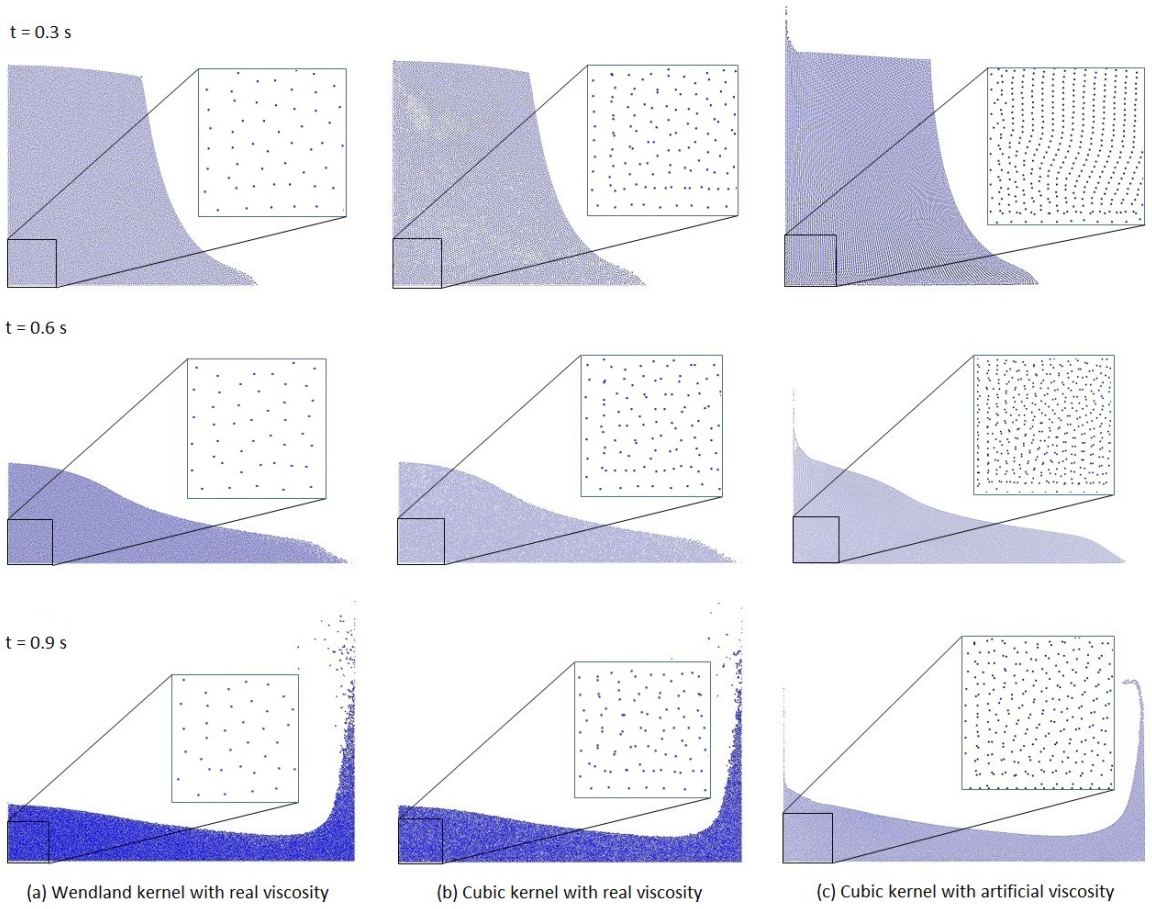

FIGURE 4.16: Shows the evolution of particle distribution at various instant of time with the difference kernels and viscosity terms.

known as particle clustering or clumping. This was further collaborated by Dehnen and Aly [204] who concluded that Wendland kernel has the potential to avoid pairing instability despite having vanishing derivatives at the origin. With these attributes of the Wendland kernel, the simulation is smoother and more realistic in describing the free-surface compared to when cubic kernel with real and artificial viscosity as shown in Figure 4.16 (b) and (c). It is clear that, the Wendland kernel is a better kernel candidate for treating free-surfaces compare to any other kernels [204]. Furthermore, Figure 4.17 (a), (b) and (c) shows the evolution of water column height (h) against the dam toe (x) for the various cases with the difference kernels and viscosity models used.

In Figure 4.18, the velocity magnitude is shown at different instants in time while the colour bar is the same for all snapshots using only the Wendland kernels. For this particular simulation, the smoothing length was increase to $h = 1.9dx$ in order to have a smoother distribution. This is evident when both Figure 4.17 (a) and Figure 4.18 at $t = 0.9s$ are compared. At $t = 0.64s$, the maximum dam break velocity near the

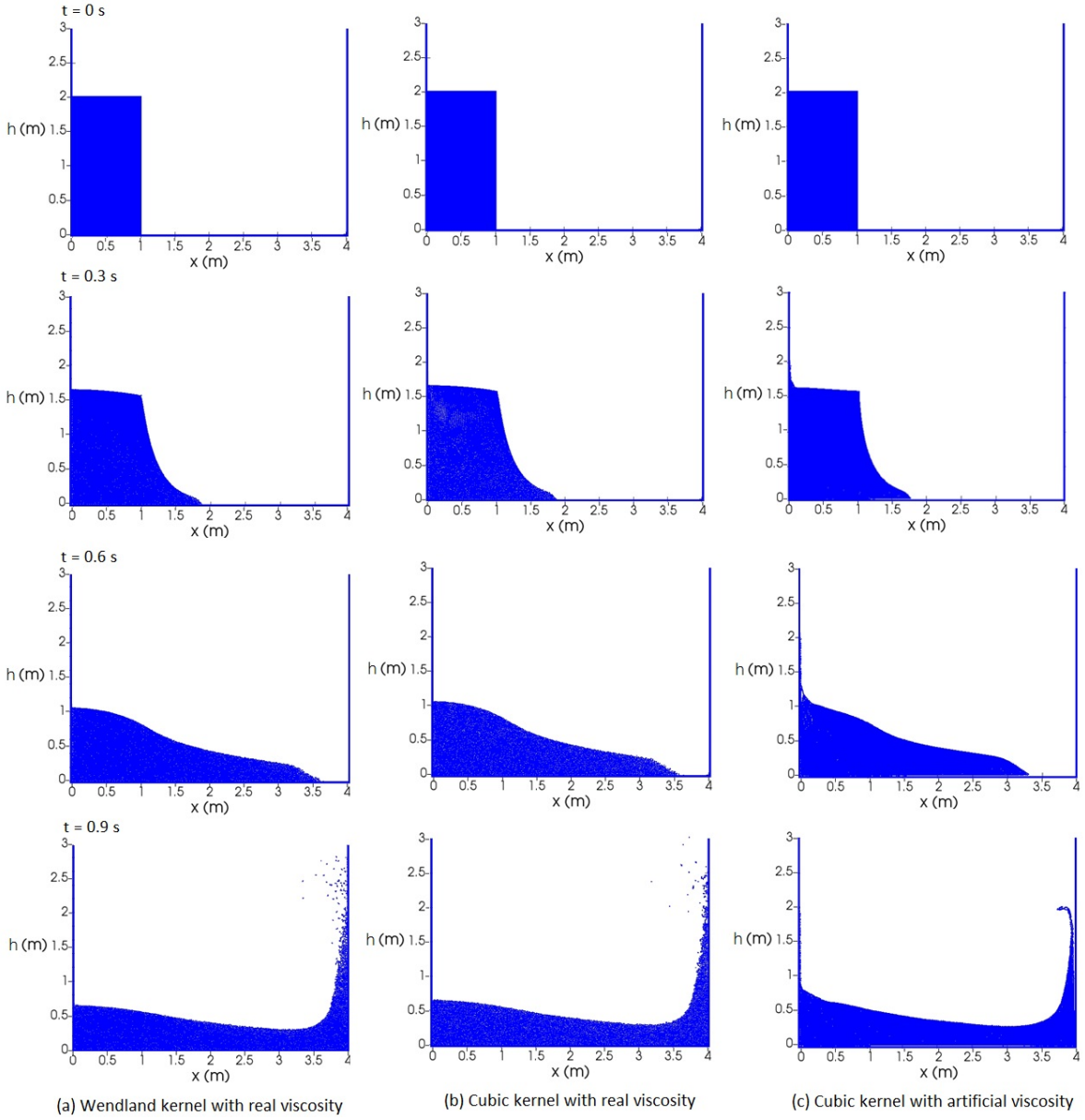

FIGURE 4.17: (a) Plot of height h (m) against dam toe x (m), at various instant of time t (s) for Wendland kernel with real viscosity, and Cubic kernel both with real and artificial viscosity respectively.

toe is observed just before it collides with the right wall. Also at $t = 0.66s$, the wave front collides with the right wall, at $t = 0.68s$, it begins to climb the right wall, while at $t = 1.5s$, it starts to fall back into the bulk fluid. As the dam toe advances, this proves the proper manner of the boundary conditions, while there is a corresponding water height decrease near the left wall which is observed during the whole dam break simulation.

To show that the simulation captures real-life physics, the result from the simulation with the difference kernels and viscosity terms were compared with experiment. This

is shown in Figure 4.19, where it can be seen that there is a very good agreement with experiment especially with the Wendland kernel because of its smoothed and orderly distributed particles.

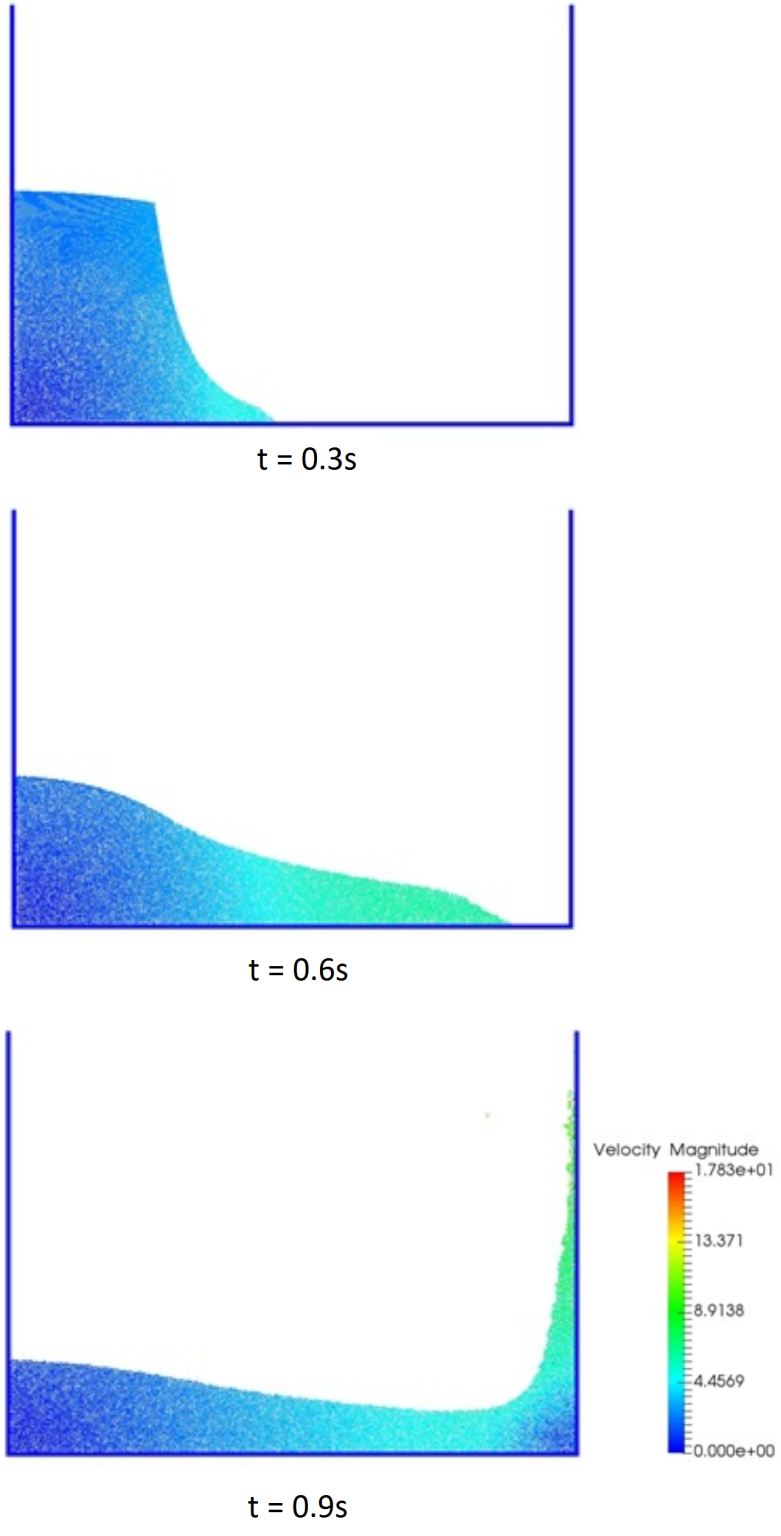

FIGURE 4.18: (a) Snapshot of the velocity v (ms^{-1}) evolution with time t (s).

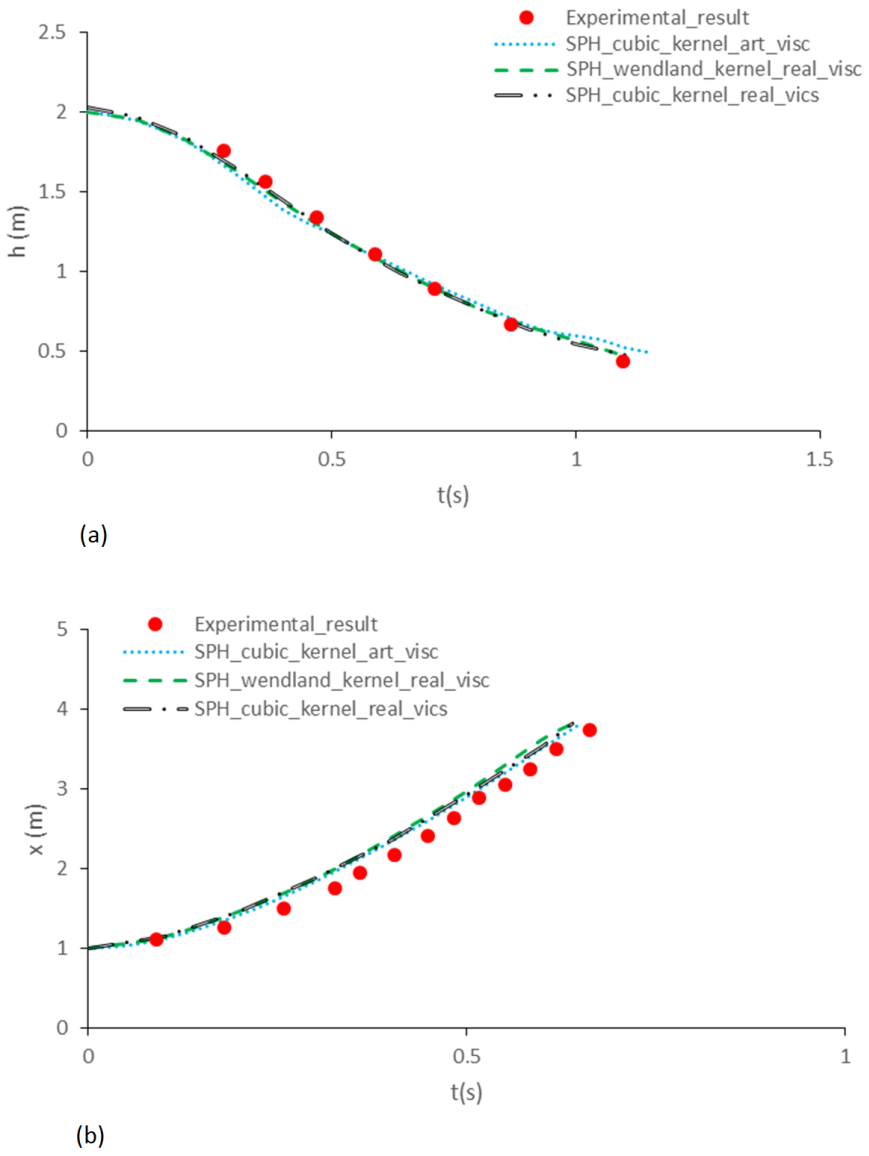

FIGURE 4.19: (a) Plot of height h (m) evolution, while (b) Plot of dam toe x (m), respectively against time t (s) for cubic kernel with or without artificial viscosity and Wendland kernel, all compared with Experiment result by Koshizuka and Oka [202].

To illustrate this good agreement, the R-squared value which is the statistical measure of how close the average of h and x values are fitted to the regression line will be use for the analysis. From the error bar of Figure 4.20 (a) and (b), these R-squared values are 0.9768 and 0.9696 respectively. For a model to be useful or valid, the R-squared value need to be close to unity and this is evident from Figure 4.20 (a) and (b) of the R-squared values of the trend (regression) lines with the data set spread over the mean (average).

To further shows that there is a valid agreement, the root mean square error (RMSE),

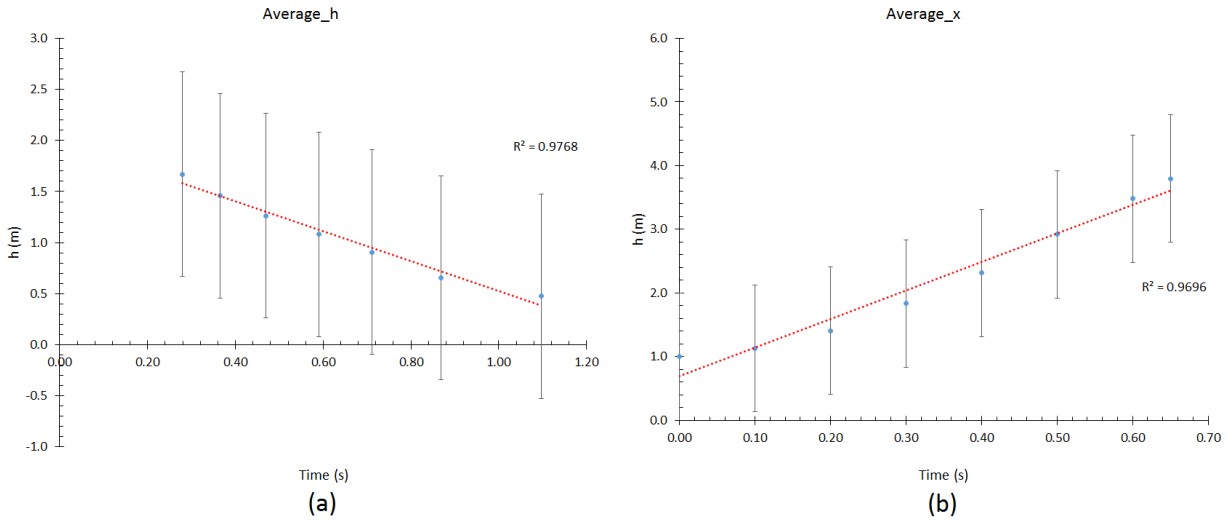

FIGURE 4.20: (a) The average height (h) evolution with time t (s) (b) The average toe (x) evolution with time t (s).

which is a measure of the difference between actual values observed and the predicted values is used to analyse the various models. Mathematically, the RMSE is given as:

$$RMSE = \sqrt{\frac{\sum_{i=1}^{n}(X_{obs,i} - X_{model,i})^2}{n}}, \tag{4.3}$$

where X_{obs} is experiment (observed) values and X_{model} are the difference modelled values at time/place i.

Now, using Equation (4.3) to analyse the various models which are SPH-cubic-kernel-art-visc, SPH-wendland-kernel-art-visc and SPH-cubic-kernel-real-visc for the height, their corresponding RMSE are 10%, 8% and 8% respectively for the predicted height (h) whereas for the toe (x), the predicted values are 13%, 18% and 15% respectively of the unlikely event. These values shows that the confident level is high, as all the predictions are above 80% of likely event, thus showing a valid agreement with experiment.

Chapter 5

Surface Tension Effect

"The simplification of anything is always sensational."

G.K. Chesterton, (1874-1936).

5.1 Surface Tension

Surface tension plays a vital role in interfacial flows that is especially important at the micro-scale and is observed ubiquitously in processes such as droplet formation, coalescence and in capillary dominated flows. Its effects are caused by the cohesion of fluid particles especially at characteristic length scale that is sufficiently small, and because it is considered as an external force, it is not included in the Navier-Stokes description which is only based on conservation laws. General, surface tension is necessary for realistic fluid motion because it pulls the fluid together, to minimise surface area to volume ratio; thus allowing, for example, small insects to walk on water surfaces, and enable tiny heavy objects that are much denser to float on water. However, surface tension occurs only on the free-surface of the liquid and modelling it requires dynamic tracking of this interface caused by the cohesion of the fluid at the free-surface where the cohesive forces of the liquid are asymmetric (see Figure 5.1).

In general, just like the liquid has inherent surface tension, so is also every material surface with a specific surface tension. For reliable adhesion between the fluid (liquid) and solid (material surface) with long-term stability of coating, gluing, spreading or

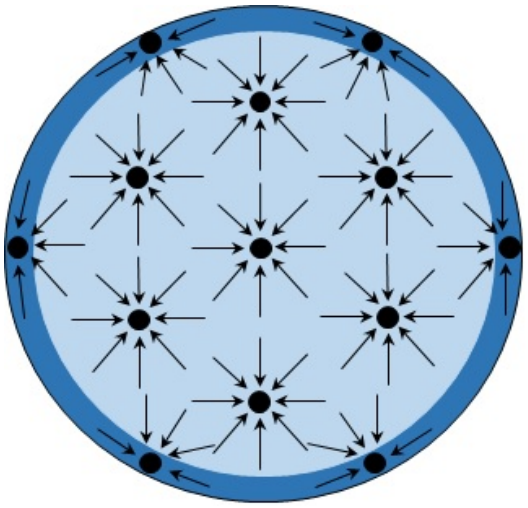

FIGURE 5.1: Real life behaviours of fluid particles near the free-surface under surface tension.

printing, the surface tension of the material surface should be greater than that of the liquid. In many applications, it is important that the adhesive and surface properties are optimally aligned. Details of this adhesion (wettability) will be given later in Chapter 6.

Now, generally, there have been a few different approaches to model surface tension in SPH like Brackbill *et al.* [150], Nugent and Posch [151] and Tartakovsky and Meakin [152]. However, the two most accepted approaches which are the continuous surface force (CFS) method and the inter-particle interaction force (IIF) method, will be discussed in details in this Chapter with emphasis on the CSF method by Brackbill *et al.* [150] that the present work considers as one of the best surface tension model developed for wettability (spreading).

Firstly, in the IIF method, the SPH particles are treated as real physical particles, while the inter-particle interaction force is introduced between all SPH particles. As a result of this additional force, the particle within the fluid repel and attract each other depending on the relative distances between them and for internal fluid particles, it should result in a net force of zero. However, for fluid particles located near the free-surface, the summed forces from asymmetric adjacent fluid particles generates a net pull normal to the free-surface towards the centre of the fluid and this mimics the effects of surface tension [152, 205, 206]. Tartakovsky and Meakin [152] used the following Equation (5.1) as the inter-particle interaction force which is given by:

$$\vec{\mathbf{F}}_{ij} = \begin{cases} s_{ij} cos\left(\dfrac{1.5\pi}{3h}|\vec{\mathbf{r}}_{ij}|\right)\dfrac{\vec{\mathbf{r}}_{ij}}{|\vec{\mathbf{r}}_{ij}|}, & |\vec{\mathbf{r}}_{ij}| \leq 3h, \\ 0, & |\vec{\mathbf{r}}_{ij}| > 3h, \end{cases} \tag{5.1}$$

where s_{ij} could be fluid-fluid (s_{ff}) or solid-fluid (s_{sf}) representation of the strength of the force between particles either to repel or attract and it is also used to control the wettability (spreading) of the fluid on the substrate.

The above force can now be converted to acceleration due to surface tension by simply dividing it with particle mass and then introduce it into the momentum Equation (3.77). On a final note, the momentum equation becomes:

$$\begin{aligned} \frac{D\vec{\mathbf{v}}}{Dt} &= -\sum_{j=1}^{N} m_j \left(\frac{p_j}{\rho_j^2} + \frac{p_i}{\rho_i^2}\right) \cdot \nabla_i W_{ij} + \sum_{j=1}^{N} m_j \left(\frac{\mu_i + \mu_j}{\rho_i \rho_j}\right) \vec{\mathbf{v}}_{ij} \left(\frac{1}{|\vec{\mathbf{r}}_{ij}|}\frac{dW_{ij}}{dr_{ij}}\right) \\ &\quad + \vec{\mathbf{F}} + \frac{1}{m_i}\sum_{j=1}^{N} \vec{\mathbf{F}}_{ij}. \end{aligned} \tag{5.2}$$

The attraction and repulsion effects from Equation (5.1) are depicted in Figure 5.2 which shows that as the particles get closer to each other they are repelled (within the range $0 < r_{ij} < 1h$) while as they move far apart they are attracted to each other (within the range $1h < r_{ij} < 3h$). For symmetric particle distributions especially for internal fluid particles the IIF method is balanced. However, because it is practically impossible to have symmetric distribution within the inner fluid particle during simulation, this cause an unbalanced force to exist even within the inner fluid. This unbalanced forces makes surface tension to take place inside the inner fluid. Also at the free surface, this IIF interaction is unbalanced, thereby causing the net force to move toward the fluid and give rise to a surface tension effect. Tartakovsky and Panchenko [207] gave a second variation for the inter-particle interaction force as:

$$\vec{\mathbf{F}}^{*}_{ij} = \begin{cases} s_{ij} cos\left(\dfrac{1.5\pi}{3h}|\vec{\mathbf{r}}_{ij}|\right)\dfrac{\vec{\mathbf{r}}_{ij}}{|\vec{\mathbf{r}}_{ij}|}W_{ij}, & |\vec{\mathbf{r}}_{ij}| \leq 3h, \\ 0, & |\vec{\mathbf{r}}_{ij}| > 3h. \end{cases} \tag{5.3}$$

From Equation (5.3), all parameter remained the same as the one defined in Equation (5.1) except for the introduction of the kernel W_{ij}. Figure 5.2 shows two variations

of the inter-particle interaction force where the first one is from Equation (5.1) but multiplied by the kernel ($W(3h)$) thereby giving rise to Equation (5.3). It is evident from the graph that the introduction of the kernel lead to a reduction in the attractive strength of the surface tension effect as shown by the blue dotted line compared to the red dash line in Figure 5.2. Details of these two surface tension models will be discussed later in Session 5.3 and 5.4 respectively.

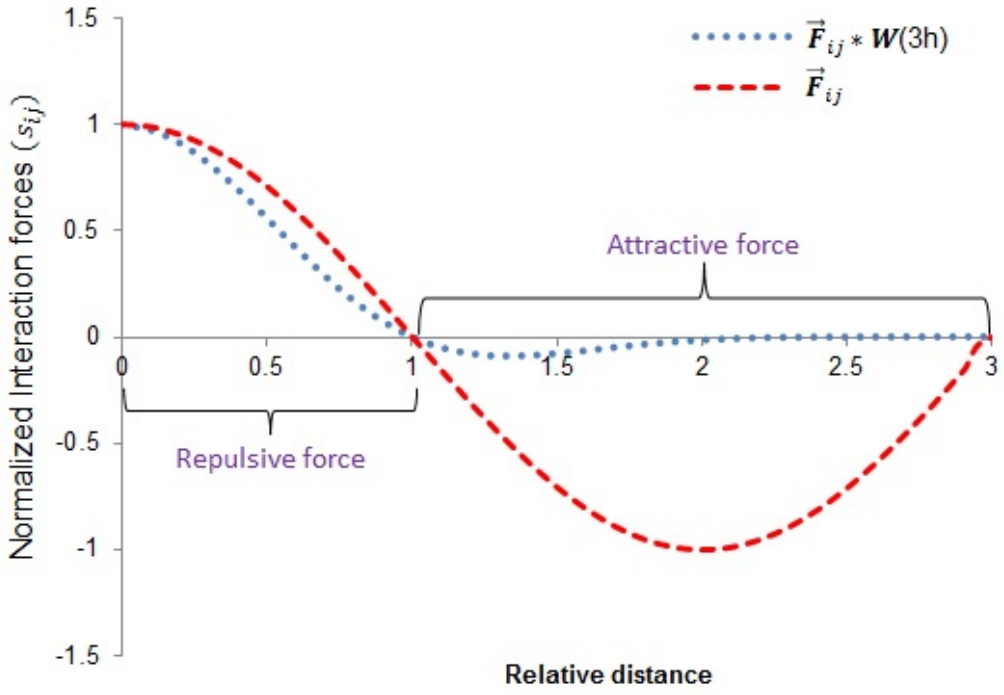

FIGURE 5.2: The inter-particle interaction force for repulsive and attractive forces when particles come close or far from each other respectively for with or without kernel contribution.

The main advantage of the IIF method is that it is straightforward, simple and easy to implement. Other advantages are that the IIF method can be applied to single-phase flow with ease thereby reducing the computational time spent significantly. However, the major disadvantages of the IIF method are that the strength of the force, s_{ij}, which determine the magnitude of the surface tension, are not easily obtainable and need to be tuned each time in order to generate the appropriate surface tension coefficient for the particular fluid of interest. Usually, for practical applications, these surface tension coefficients of difference fluids are given as macroscopic input parameter.

The second method is the CSF method proposed by Brackbill *et al.* [150], where the curvature of the free-surface of the fluid are determine and then surface tension force is apply to it. The major advantage of this method is that it uses the real physical

surface tension property of the fluid in the model. Another obvious advantage is that there is no surface tension occurring at the bulk of the fluid except at the free-surface. This makes the approach ideal for simulating free-surface flow better than any other known approaches, because it is able to predict the actual physics more accurately especially for wettability (spreading). With the CSF method, the surface tension force per unit mass is written as follows:

$$\vec{\mathbf{f}}^{\,surface} = \frac{\sigma\kappa\vec{\mathbf{n}}\delta_{\varepsilon}}{\rho}, \tag{5.4}$$

where σ is the surface tension coefficient which depends on the type of fluid, κ is the surface curvature of the interface, $\vec{\mathbf{n}}$ is the unit surface normal, acting directly inward into the fluid, δ_{ε} is surface delta function which is set to $1/dx$ at the surface with dx representing initial particle spacing.

In Morris [208], the implementation of the CSF method uses a smoothed colour field to locate the free-surface of the fluid and then a surface tension force is applied to it. With SPH, this smoothed colour field is defined as:

$$c_i = \sum_j \frac{m_j}{\rho_j} c_j W(\vec{\mathbf{r}}_i - \vec{\mathbf{r}}_j, h), \tag{5.5}$$

where

$$c_j = \begin{cases} 1, & \text{if } c_j \text{ is fluid,} \\ 0, & \text{otherwise.} \end{cases} \tag{5.6}$$

From Equation (5.5), its shows that the value of the smoothed colour field depends on the full neighbour particles support of the kernel W_{ij}; particles on the free surface will have value less than 1.0 while particles moving away from the free surface toward the bulk of the fluid will have a value approaching unity.

Now the surface normal in its simplex form is given as follows:

$$\vec{\mathbf{n}}_i = \frac{\nabla c_i}{|c_i|}, \tag{5.7}$$

where

$$\nabla c_i = \sum_j \frac{m_j}{\rho_j} c_j \nabla W(\vec{\mathbf{r}}_i - \vec{\mathbf{r}}_j, h).$$

To improve the accuracy [208], the difference between the neighbouring particle colours is taken, thus given the surface normal as follows:

$$\vec{\mathbf{n}}_i = \sum_j \frac{m_j}{\rho_j} (c_j - c_i) \nabla W(\vec{\mathbf{r}}_i - \vec{\mathbf{r}}_j, h). \tag{5.8}$$

The curvature is now calculated by using the divergence of the surface normal as follows:

$$\kappa = -\frac{\nabla \cdot \vec{\mathbf{n}}}{|\vec{\mathbf{n}}|} = -\frac{\nabla^2 c}{|\vec{\mathbf{n}}|}. \tag{5.9}$$

The calculation of curvature in SPH is usually cumbersome because of the large deviations in the curvature as a result of the Laplacian of the colour field. An alternative formulation for tracking the surface of the fluid by Lee *et al.* [209] determine the divergence of the particle position, $\nabla \cdot \vec{\mathbf{r}}$, instead of the colour field and is given as:

$$\nabla \cdot \vec{\mathbf{r}} = \sum_j \frac{m_j}{\rho_j} \vec{\mathbf{r}}_{ij} \nabla_i W(\vec{\mathbf{r}}_{ij}, h). \tag{5.10}$$

This divergence for a two-dimensional problem has a value of 2.0 when a particle has a full kernel support within its domain and less than 2.0 for surface particles. Lee *et al.* [209] used a divergence threshold value of 1.5 for particle located at the free-surface. Adami *et al.* [210], proposed a difference formulation for a two-phase fluid (for example, fluid and air) for calculating the surface curvature using the following approach as:

$$\nabla \phi_i = d \frac{\sum \phi_{ij} \cdot e_{ij} \dfrac{\partial W}{\partial \vec{\mathbf{r}}_{ij}} V_j}{\sum_j |\vec{\mathbf{r}}_{ij}| \left| \dfrac{\partial W}{\partial \vec{\mathbf{r}}_{ij}} \right| V_j}, \tag{5.11}$$

such that

$$\kappa = \nabla \phi_i, \tag{5.12}$$

where $\nabla\phi_i$ is the surface curvature, κ, d is the spatial dimension, $\phi_{ij} = \vec{\mathbf{n}}_i - \vec{\mathbf{n}}_j$, $e_{ij}\dfrac{\partial W}{\partial \vec{\mathbf{r}}_{ij}}$ is the gradient of W_{ij} of the kernel, $\dfrac{\partial W}{\partial \vec{\mathbf{r}}_{ij}}$ is the partial derivatives of the kernel, $\vec{\mathbf{r}}_{ij}$ is the separation distance, and V_j is the volume of particle j.

The present work proposed a modified form of the original Equation (5.11) to support the solution for a single-phase problem by introducing a control parameter, ϵ, such that:

$$\nabla\phi_i \;=\; \epsilon * d\frac{\sum \phi_{ij}\cdot e_{ij}\dfrac{\partial W}{\partial \vec{\mathbf{r}}_{ij}}V_j}{\sum_j |\vec{\mathbf{r}}_{ij}||\dfrac{\partial W}{\partial \vec{\mathbf{r}}_{ij}}|V_j}, \tag{5.13}$$

where $\epsilon = 0.5$ was found to be acceptable since ignoring the air particles, requires that the curvature from Equation (5.11) have to be halved. Mathematically, the curvature, κ, of a droplet can be express as follows:

$$\kappa \;=\; \frac{1}{R}, \tag{5.14}$$

where R is the equilibrium radius of the droplet. This new formulation of curvature proposed in Equation (5.13) will be verified against known theoretical results (5.14) later in Session 5.5. However, to ensure that the surface tension forces are applied to the particles at the free-surface, the following condition are imposed:

$$|\hat{\mathbf{n}}| = \begin{cases} 1, & \text{at the free surface,} \\ 0, & \text{otherwise.} \end{cases} \tag{5.15}$$

where $|\hat{\mathbf{n}}|$ is set to unity for the particles at the free-surface and zero elsewhere. In order to avoid numerical instability, Equation (5.10) is use in conjunction with Equation (5.15) to track particles located at the free-surface.

5.2 Bond number

The bond number indicate the comparative importance of forces occasioned by surface tension and gravity. When its value is high, the system is unaffected by surface tension effect, whereas if it is low (typically less than one or unity) surface tension

effect prevails. For a liquid system that is progressively becoming smaller, the relative dominates of surface tension over gravitational force increases; thus making surface tension effects crucial in micro-scale engineering processes. Bond number is a dimensionless number arising from the ratio of gravitational force to surface tension force and in mathematical representation is given as:

$$B_O = \frac{\rho g L^2}{\sigma}, \tag{5.16}$$

where g is the acceleration due to gravity; ρ, the liquid density; σ, the coefficient of surface tension; and L is the appropriate linear dimension (length scale), e.g., bubble, droplet diameter or length of substrate.

5.3 Simulation Droplet using IIF Method

The simulation of droplet with the IIF method will be conducted in two phases using the different models proposed in Figure 5.2 where the two version of the surface tension forces are given by Equation (5.1) and Equation (5.3).

5.3.1 IIF Method without the kernel contribution (Model 1)

A water droplet with surface tension effect is simulated using IIF method without a kernel contribution (red dash line in Figure 5.2) from Equation (5.1). An initial square droplet shape of size 2.25mm × 2.25mm that is made up of 2025 SPH particles in two dimensions, with initial separation of ($dx = dy = 0.00005m$) is setup, as shown in Figure 5.3 (a). For the strength of the force between fluid and fluid, s_{ff}, this parameter was tuned such that, $s_{ff} = 0.0015$ (reasons see details in Session 5.6) while the maximum reference sound speed, $c_o = 2.0$ is chosen to ensure density variations was curtail significantly. Other details properties of the fluid are presented in Table 5.1.

At the start of the simulation, the SPH particles were all stationary with zero initial velocity ($\vec{\mathbf{v}} = 0ms^{-1}$) and is solved using the quintic kernel only (Equation (3.28)) in every aspect of the solver along with adaptive time stepping, followed by a summation

TABLE 5.1: Initial properties of Droplet using Model 1.

Properties, symbols (Units)	**Fluid values**
Mass, m (kg)	$\rho \times dx \times dy$
Density, ρ (kg/m^3)	1000.0
Pressure, p (Pa)	0
Acceleration (gravity), $\vec{\mathbf{a}}$ (m/s^2)	0
Dynamics viscosity, μ (Pas)	10^{-3}
Sound speed, c_o (ms^{-1})	2.0, which is $(50 \times \vec{\mathbf{v}}_{max})$
Smoothing length, h (m)	$1.3\times$ dx
Strength of the repulsive force, D (-)	0.006
Kernel, W_{ij} (m^{-3})	Quintic

density approach using Equation (3.61) which had being re-normalized using Equation (3.66) every 30 iterations and then the Verlet scheme using Equations (3.121)-(3.128) are used to update the position and velocity. For this simulation, the use of XSPH is not necessary as it is not able to ensure homogeneous distribution of the particles. In the original formulation of IIF method by Tartakovsky [152], Van der Waals equation of state was used to compute the pressure terms, but in this thesis, Tait's equation of state Equation (3.90) is employed instead and this help to eliminate the time spent on tuning the three parameters in the Van der Waals equation of state. Due to the effect of surface tension force, the initial square droplet shape oscillate by evolving through a configuration of diamond front and back for some period before finally getting stabilized into a circular shape at time $0.02s$ after about 3 diamond oscillations as seen in Figure 5.3 (a) - (f), with the presence of unphysical rings at steady-state. This unphysical rings also appears even with initial circular droplet shape (see Figure 5.4 (a) - (c)), generated with a simple algorithms for perfect circle (see Appendix B where the algorithms is in the generator.cpp file). However, comparing the final circular shape of the droplet with the initial square shape, the size ratio's error is 6.9%, which is within acceptable limit of universal standard of 10% maximum error margin especially when experiment are compared against theoretical/numerical results.

Now, to validate that surface tension exist even within the bulk of the fluid, Figure 5.5 (a) and (c) show the initial surface tension effect, though negligible at $t = 0s$, as can be seen by the colour bar and arrows showing the direction of surface tension

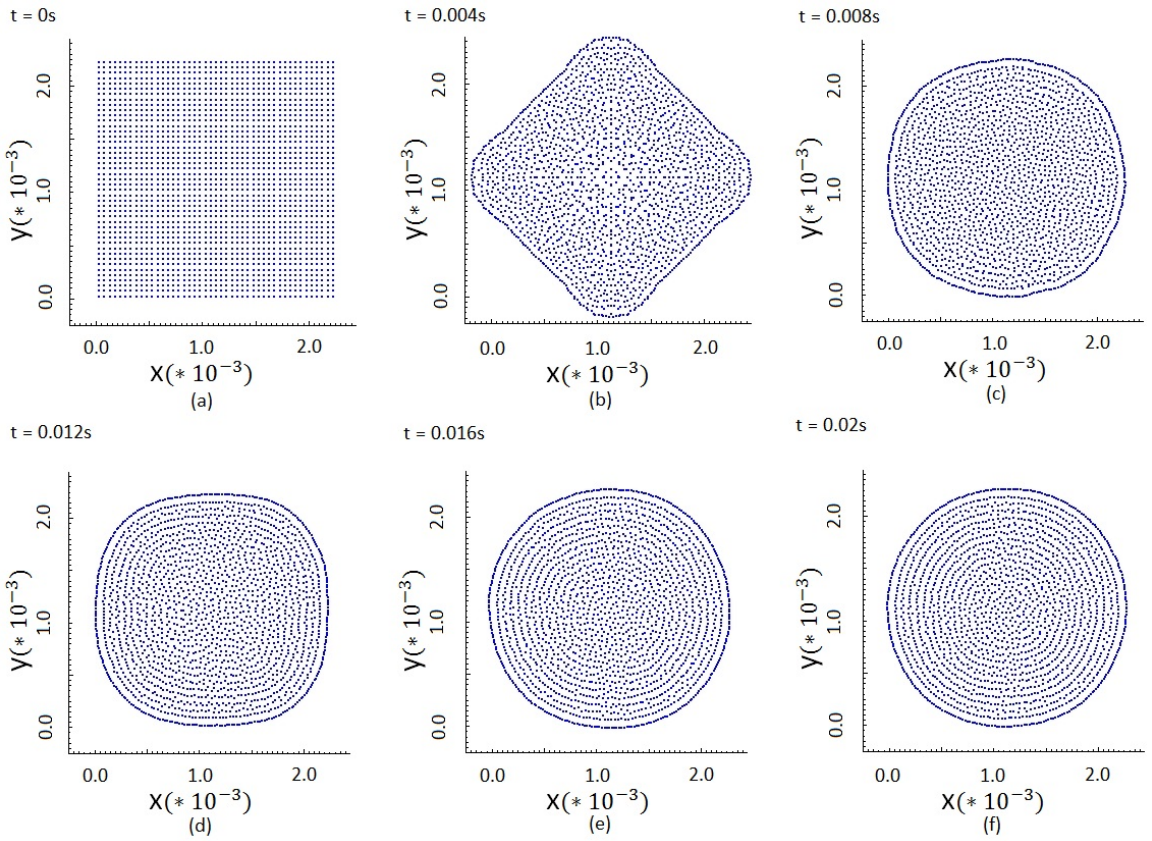

FIGURE 5.3: The evolution of initial square droplet using the inter-particle interaction force ($\vec{\mathbf{F}}_{ij}$) with quintic kernel only.

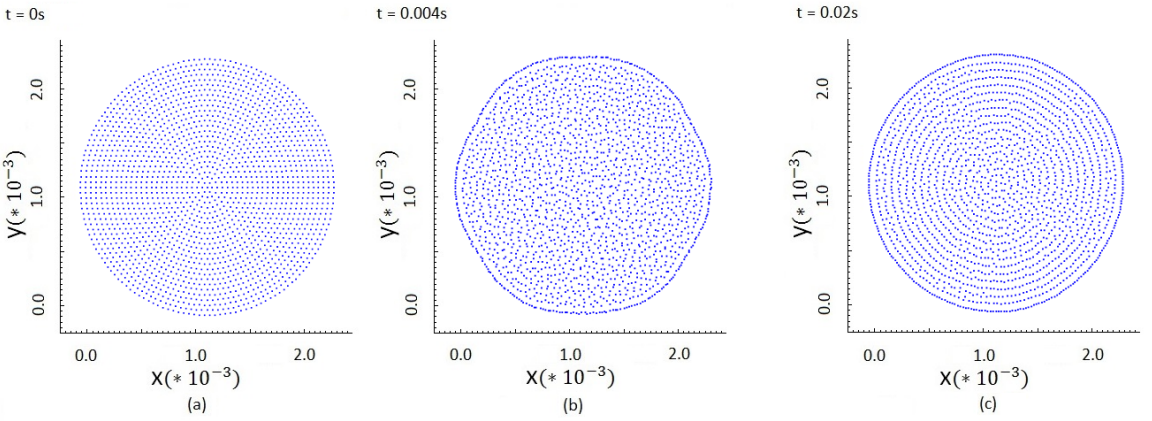

FIGURE 5.4: The evolution of initial circle droplet using the inter-particle interaction force ($\vec{\mathbf{F}}_{ij}$) with quintic kernel only.

vector on the fluid. However, this surface tension effect becomes higher when the simulation is taken over a period of say at $t = 0.02s$ as shown in Figure 5.5 (b) and (d), by the difference particles colours and the direction the surface tension vector act, respectively. From Figure 5.5, it is evident that surface tension effect exist even in the inner part of the fluid, and this is one of the major disadvantage of using the IIF method. However, since there is no approach that is completely perfect, the IIF method is still considered as one of the reliable approach for simulating droplet [207].

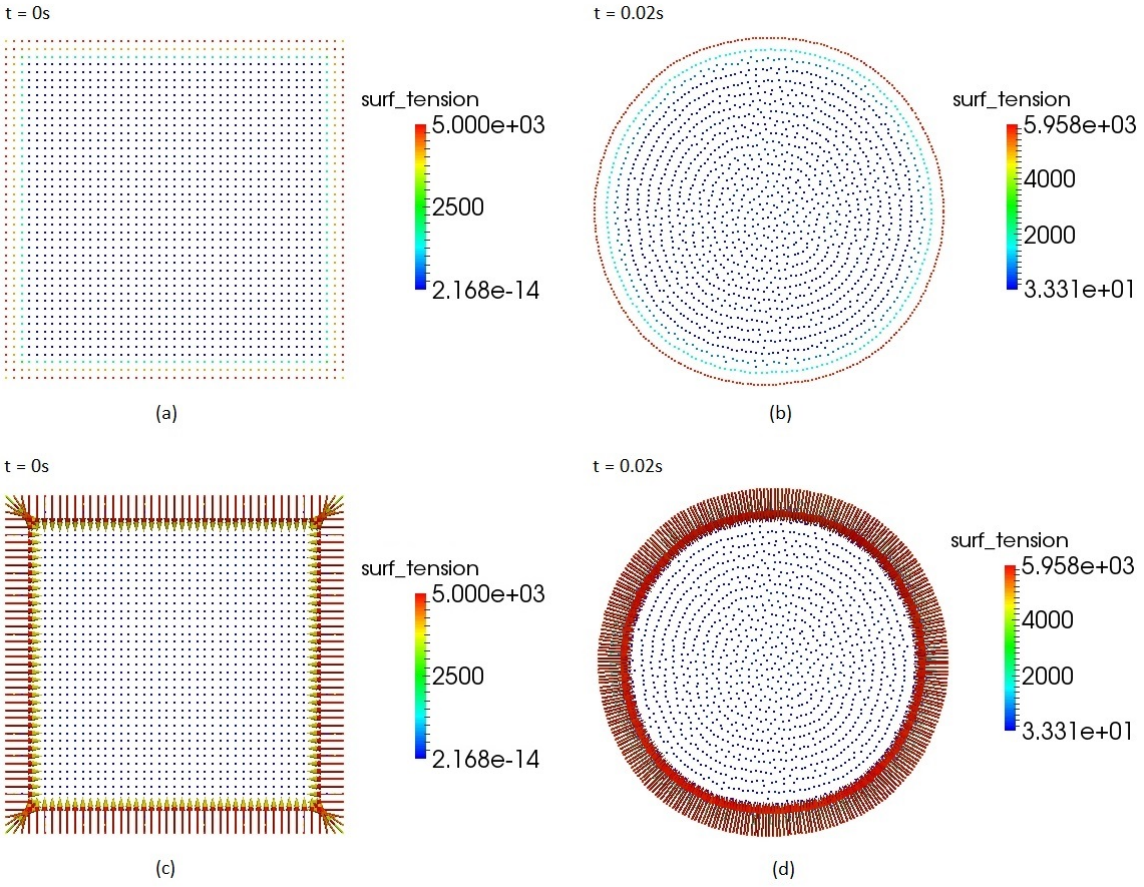

FIGURE 5.5: (a) The initial square shape with negligible surface tension effect (b) Final circular shape with noticeable surface tension effect with the unphysical rings (c) The initial square shape with surface tension vector (d) Final circular shape with surface tension vector with the unphysical rings.

In order to resolve the unphysical rings, two approaches were implemented. For the first implementation, the high velocity impact kernel (quadratic kernel Equation (3.18)) developed by Johnson *et al.* [145] is introduced into the momentum equation due to pressure term. From Figure 3.4, it is obvious that the derivative of this quadratic kernel function increases as the SPH particles come close to each other. This makes the SPH particles to repel each other once they are too close,

hence helping to prevent clustering or tensile instability that produces these unphysical rings (see Figure 5.6). Nevertheless, some gaps are still observed just between the first and second outer layers close to the free surface compare to the internal particles distribution.

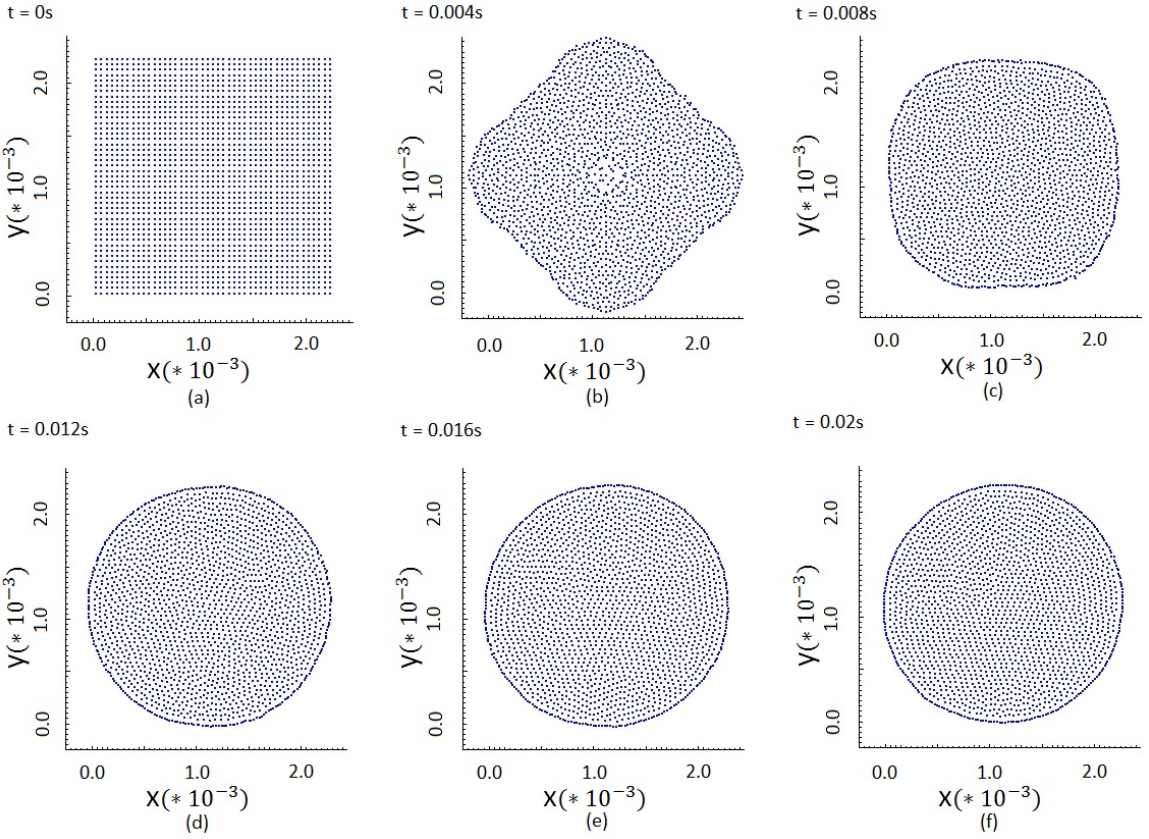

FIGURE 5.6: The evolution of droplet using the inter-particle interaction force ($\vec{\mathbf{F}}_{ij}$) with implementation of quintic and quadratic kernels for resolving the unphysical rings.

Following Model 1, the implementation of the high velocity impact kernel along with the quintic kernel was able to resolves the unphysical ring, however it was noticed that the surface tension in term of acceleration in the bulk of the fluid in this case is higher as evident from the value of $33.31ms^{-2}$ in Figure 5.5 (d) where there is unphysical rings to a value of $43.0ms^{-2}$ in Figure 5.7 (d) where there is no unphysical rings.

Also, in order to resolve the unphysical ring, the repulsive force according to Lennard-Jones (Equation (3.94)) which was originally designed between fluid and solid particles is now applied between fluid-fluid particles and because it is considered as an external force, it is added to the momentum equation during implementation. For more details about the Lennard-Jone equation, see Chapter 3. Due to the present of this repulsive force, there is a fair distribution of the SPH particles during the simulation similar

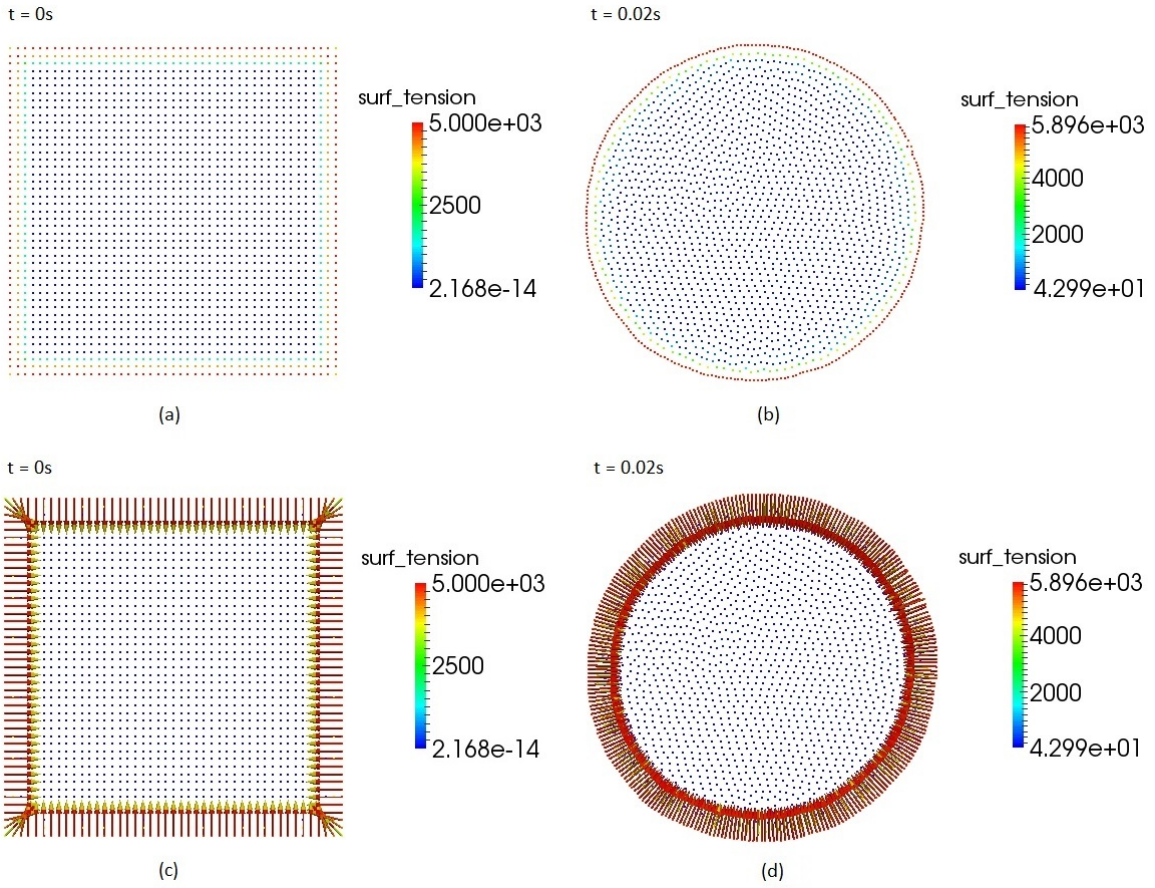

FIGURE 5.7: Implementation of the high velocity impact kernel (a) Initial square shape with negligible surface tension effect (b) Final circular shape with noticeable surface tension effect without the unphysical rings (c) Initial square shape with surface tension direction (d) Final circular shape with surface tension direction without the unphysical rings.

to what happened when the high velocity impact kernel function (quadratic kernel) was used (see Figure 5.8). The results from this modified implementation of the IIF method is almost the same as the previous, but with small little gap noticeable between the second and third outer layers.

To show that surface tension exist (which should not) within the bulk of the fluid using Lennard-Jones force implementation for resolving the unphysical rings, Figure 5.9 (a) and (c), show the initial present of surface tension effect, though negligible at $t = 0$. However, these internal surface tension effect becomes higher over a period of time has lapsed, as shown in Figure 5.9 (b) and (d) where both illustrated the magnitude and direction of these surface tension vectors. From Figure 5.9 (d), it can be seen that surface tension magnitude has a value of $5.6ms^{-2}$ within the fluid, which is much lower when compared to the previous one (Figure 5.7 (d)), hence making this implementation much better.

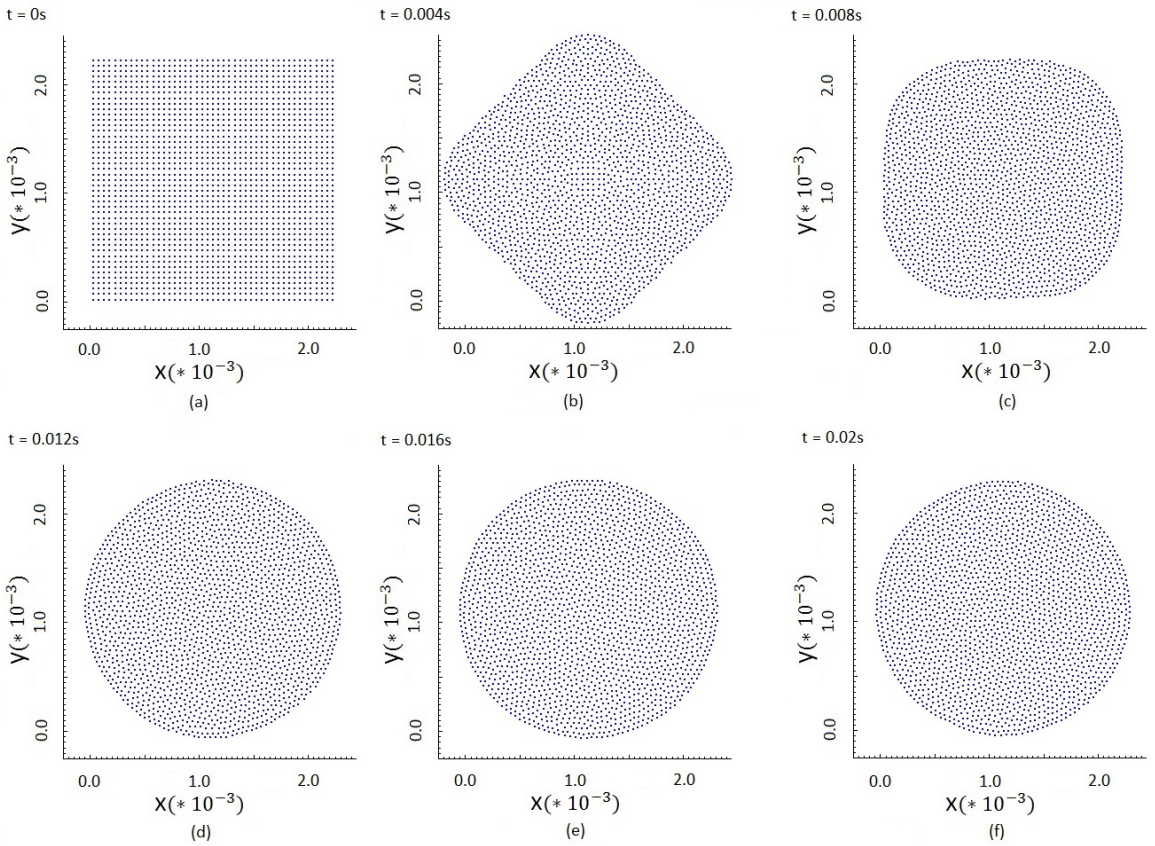

FIGURE 5.8: The evolution of drop using the inter-particle interaction force ($\vec{\mathbf{F}}_{ij}$) with implementation of quintic kernel only and Lennard-Jones force for resolving the unphysical rings.

5.3.2 IIF Method with the kernel contribution (Model 2)

A water droplet is presently simulated using Equation (5.3) which included the modified kernel contribution in the IIF method, (blue dash line in Figure 5.2) for surface tension effect. For this version of the IIF method, all the operating parameter used are the same when compared with the previous one (subsection 5.3.1), except that only the quintic kernel is used along with the surface tension force been multiplied by a kernel function this time. This makes the attractive strength of this surface tension force to become weaker while there is little or no reduction in the repulsive strength when compared with the former approach in section 5.3. Figure 5.10 illustrate the droplet with the same size as the former for a period of 0.02s. Although the SPH particles in this case are more ordered compared to the previous Figure 5.6 or Figure 5.8, this droplet is far too stiff (which the author believe maybe due to the high repulsive strength over the attractive strength) and irregular in shape, with the SPH particle too difficult oscillate, hence making it damp very quickly. Based on the fact that this

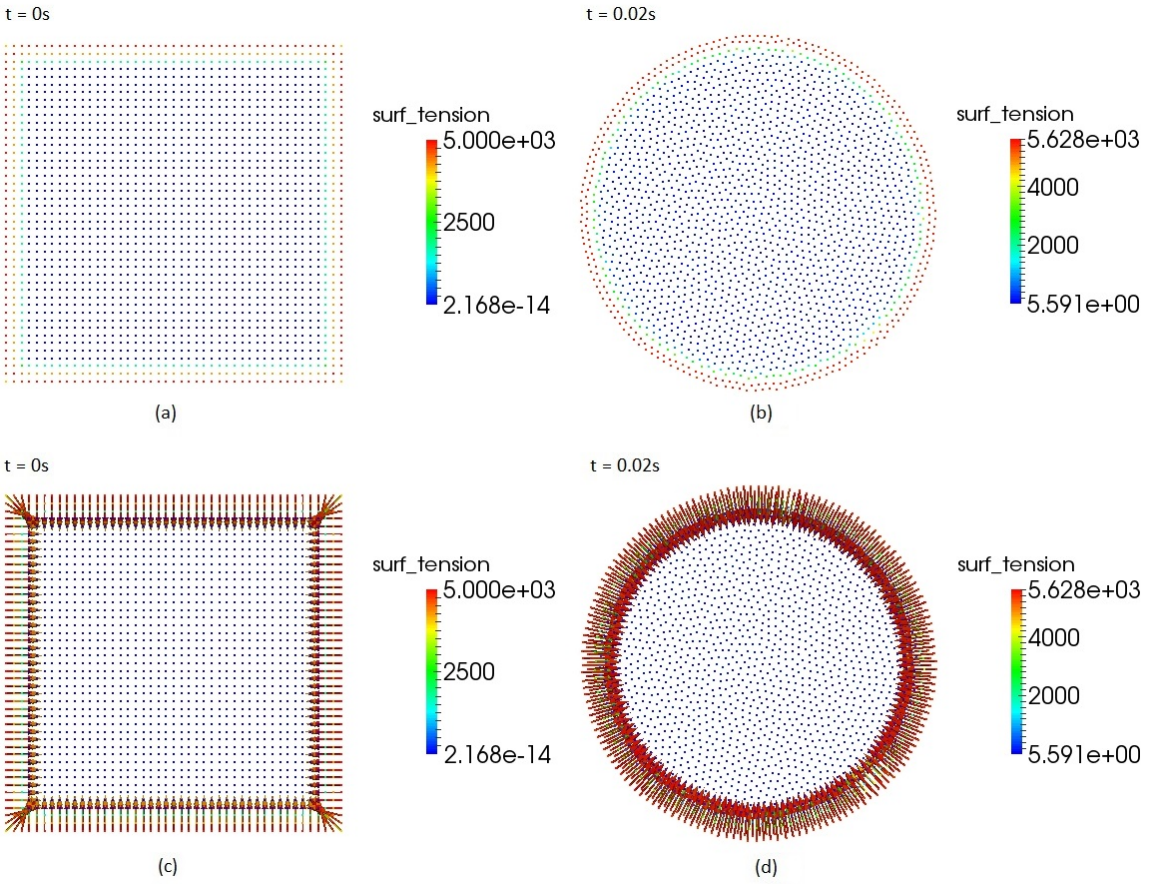

FIGURE 5.9: Implementation of the Lennard-Jones force (a) The initial square shape with negligible surface tension effect (b) Final circular shape with noticeable surface tension effect without the unphysical rings (c) The initial square shape with surface tension direction (d) Final circular shape with surface tension direction without the unphysical rings.

droplet is difficult to oscillate, there was not need to verify if fictitious surface tension forces exist within the bulk of the fluid.

5.4 Simulation Droplet using CSF Method

The simulation of droplet with the CSF method will be investigated in two phases and this will be shown in the next section.

5.4.1 CSF Method with square/repulsive force (Model 3)

In this simulation, 2025 SPH fluid water particles are generated with an initial square shape and with the same operating parameters as that used in Model 1. Table 5.2

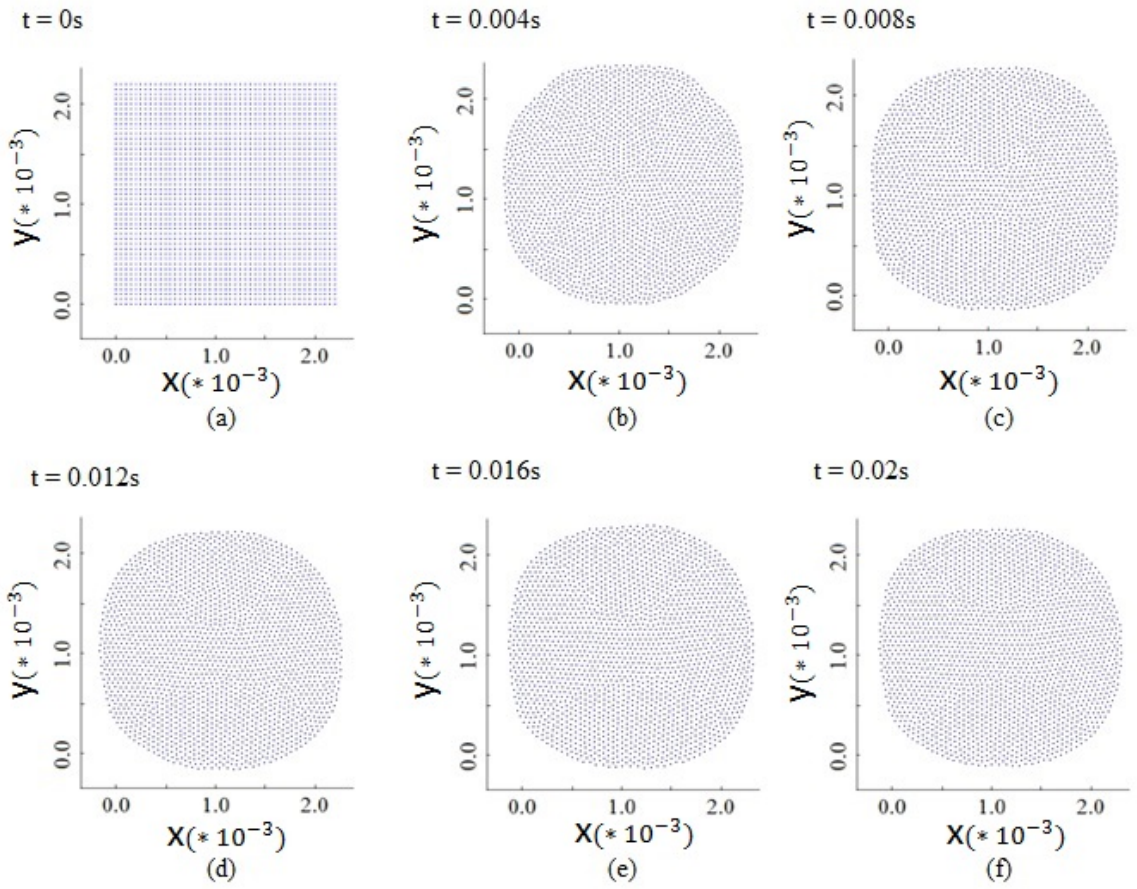

FIGURE 5.10: The evolution of droplet using the inter-particle interaction force ($\vec{\mathbf{F}}^{*}_{ij}$) with quintic only using Model 2

shows some of the important parameters used in this simulation. Here, the continuity density approach were used for density calculation while also using the quintic kernel only. During the simulation, the free-surface particles with threshold value less than 1.5 are tracked using Equation (5.10). The surface normal of these free-surface particles are then normalized to get the unit surface normal ($\vec{\mathbf{n}}$) while the surface normal of the remaining particles are set to zero. For those normalized particles, Equation (5.13) is applied to get the surface curvature (κ) while the remaining particles curvature are set to zero, follow by Equation (5.15) to detect either free-surface or bulk particles and then finally applying Equation (5.4) to compute the surface tension. The main advantage of this approach is that the surface tension coefficient of real fluid properties is used here, unlike the previous Models 1 and 2 where s_{ij} was turned to get the corresponding fluid behaviour.

To prevent tensile instability in this simulation, the repulsive force using Lennard-Jones (Equation (3.94)) were introduced. The major advantage of this CSF method over the previous Models 1 and 2, is that real fluid parameter can be used for the

TABLE 5.2: Initials properties of particles for the Droplet Flow for Model 3.

Properties, symbols (Units)	**Fluid values**
Pressure, p (Pa)	0
Acceleration (gravity), $\vec{\mathbf{a}}$ (m/s^2)	0
Sound speed, c_o $(\mathrm{m}s^{-1})$	5.0
Kernel, W_{ij} (m^{-3})	Quintic only
Surface tension coefficient, σ (N)	0.0728
Strength of the repulsive force, D ( )	0.006

simulation, with the resulting simulation giving a better ordered smoothed distribution (see Figure 5.11 (a) - (f)) when XSPH is applied by using Equation (3.95). The major setback in this approach is that, there are four sharp corners highlighted by the *red circle* ◯ on the droplet in Figure 5.11 (f) at time 0.02s, which come from the four corners of the initial square shape in Figure 5.11 (a) at time 0s. Another setback of this approach is that, the strength of this repulsive force need to be turned depending on resolutions in order to get the correct period of oscillation as will be shown later. Apart from these setbacks, the droplet oscillates well by virtual observation and agreed well with the theoretical result as will be seen later in this Chapter. At time of 0.05s, a well ordered distribution and steady droplet were formed which is much better than Model 1 and 2 when compared. However, the simulation time to get a stable droplet for Model 3 is more than twice that for either Model 1 or 2, thereby making this Model 3 to be computationally expensive than the former.

To validate that surface tension do not exist even within the bulk of the fluid by using Model 3, Figure 5.12 (a) and (c), shows the surface tension effect to be zero for all bulk particles and free-surface particles of the fluid at $t = 0s$, except for those at the four corners in Figure 5.12 (a) and (c). Figures 5.12 (b) and (d) show the surface tension from the CSF approach is applied accurately on all the fluid particles at the free-surface, while all the bulk particles have zero surface tension at $t = 0.02s$. From the above, it is evident that surface tension effect do not exist even within the inner part of the fluid, which make this CSF approach realistic for simulating real world phenomena. However, though the droplet is uniformly distributed, there still exist four sharp corners as shown in Figure 5.12 (d) which is indicated by the red colour and originated from the corners of the initial square shape; this have also been observed in literature [151].

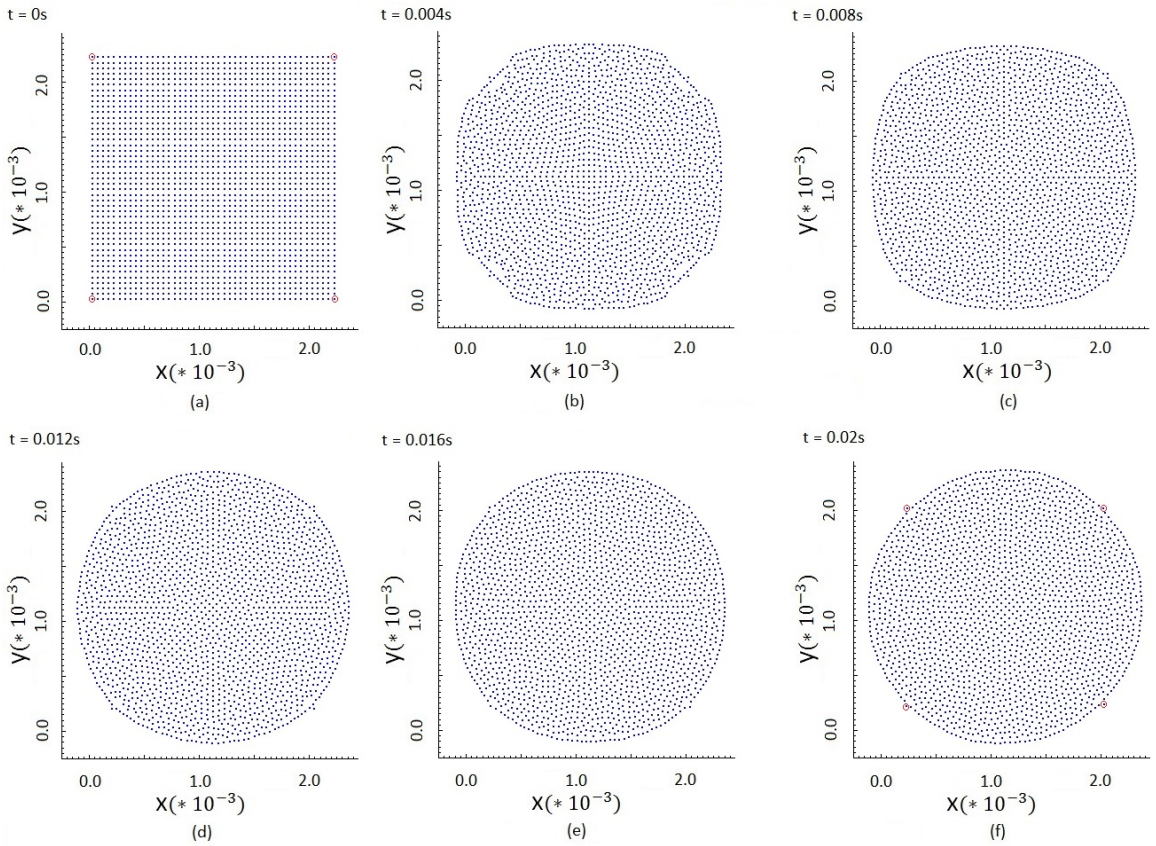

FIGURE 5.11: The evolution of drop using the Continuous Surface Force (CSF) Method with quintic only using Model 3.

5.4.2 CSF Method with square/without repulsive force (Model 4)

In Model 4, there was no need for the Lennard-Jones (Equation (3.94)) repulsive force to be applied. Also, all the operating parameters are the same with Model 3, except that the Wendland kernel is used in place of the quintic kernel while still having the initial droplet shape as a square. From the simulation, the result shows that there is no difference between Model 3 and 4, except that the particles are more orderly distributed in Model 4 as shown in Figure 5.13 (d) with the same appearance of sharp four corners which was also noticed in Model 3. By increasing the droplet resolutions, it is noticed that these sharp four corners reduced as can be seen in Figure 5.14 (d). Increasing the droplet resolutions, makes it computationally expensive, couple with the disadvantages associated with the clustering and circular ring noticed at equilibrium state all around the four corners and quadrants respectively as shown in Figure 5.14 (d).

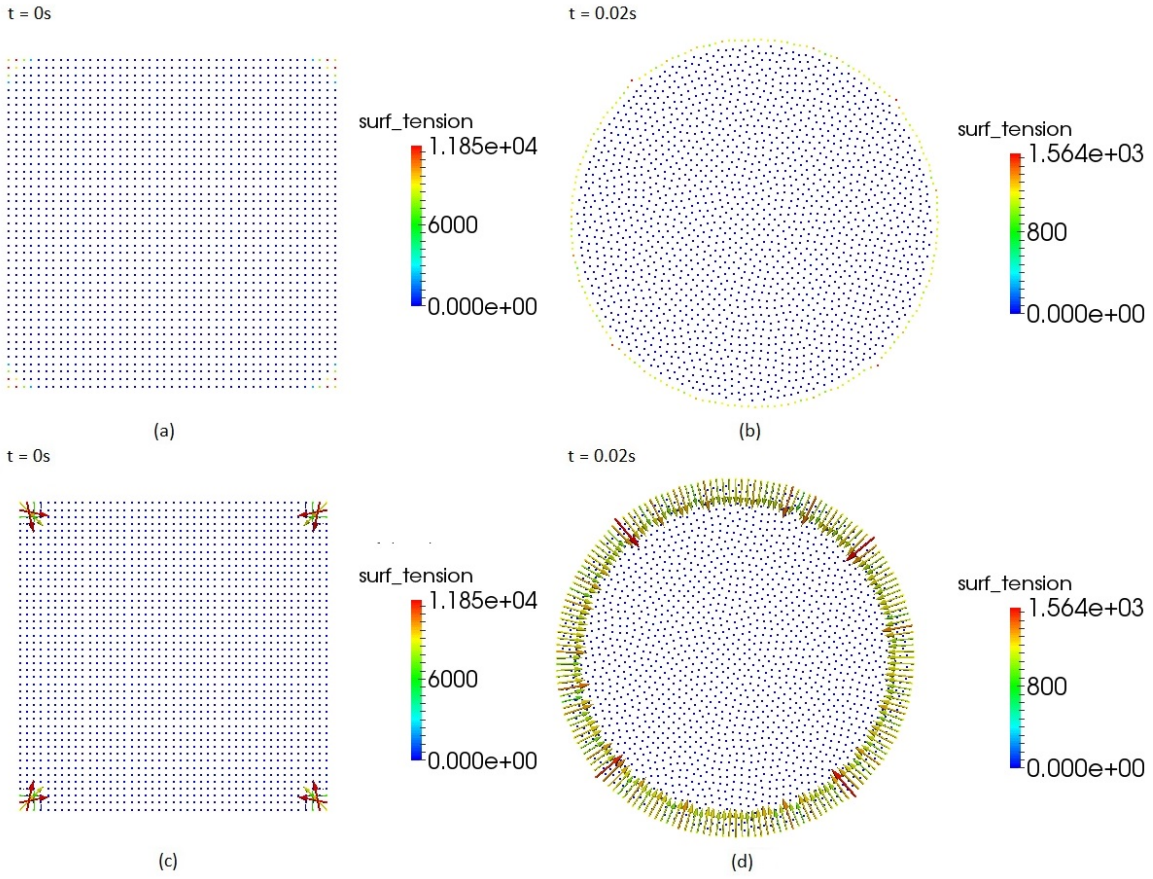

FIGURE 5.12: (a) The initial square shape with zero surface tension effect at the bulk of the fluid and some free-surface particles (b) Final circular shape with very high surface tension effect at the four sharp corners with zero surface tension in the bulk (c) The initial square shape with surface tension direction at the four corners (d) Final circular shape with high surface tension effect at the free-surface and also showing the direction with four sharp corners.

5.4.3 CSF Method with circle/without repulsive force (Model 5)

The shortcoming of Models 3 or 4 is overcome by introducing the Wendland kernel in place of the quintic kernel in addition with initial starting shape of droplet to be a perfect circle. No potential force is applied in this case because this Wendland kernel has the capacity to replicate dissipation mechanisms (soft repulsive force) more accurately both for low and high Reynolds numbers, thereby preventing clustering effects from noisy vorticity fields [156]. This generated initial circle with good particle distribution, made it possible to avoid the four corner edges found in the previous Models 3 and 4. This initial shape of a perfect circle was achieved through the use of a developed algorithms for generating a two-dimensional perfect circle (for details

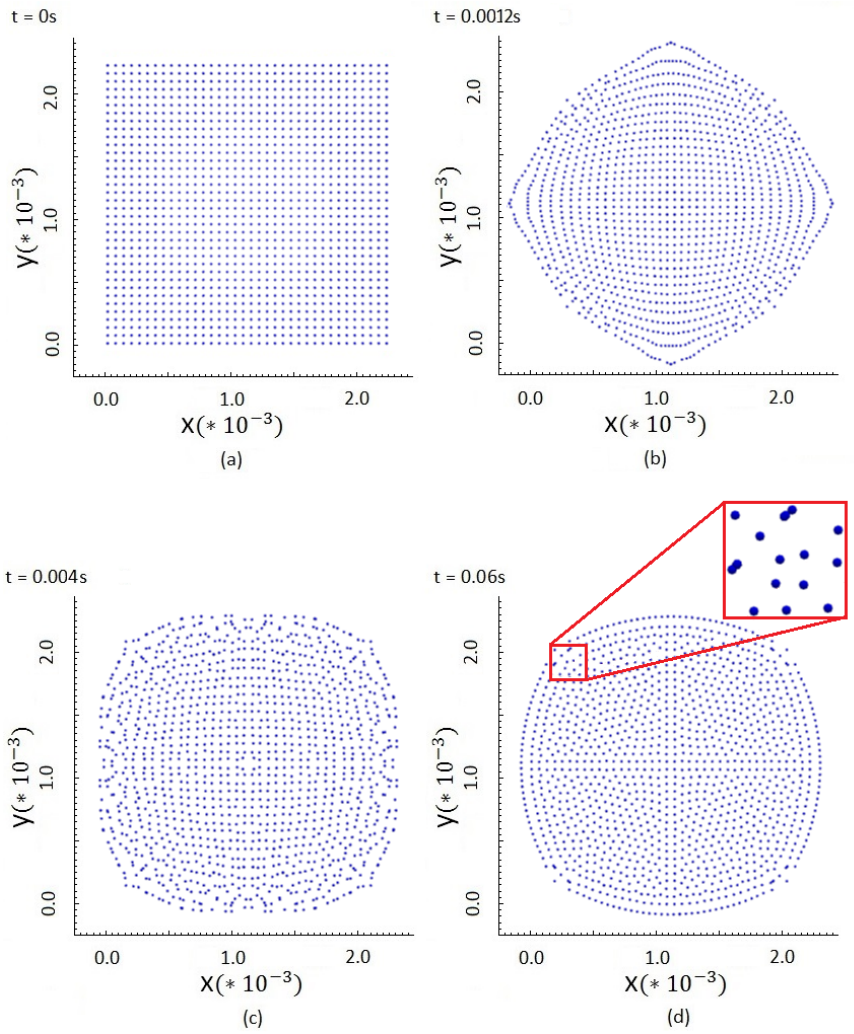

FIGURE 5.13: The evolution of initial square droplet using the Continuous Surface Force (CSF) Method with Wendland only using 2025 particles resolutions.

see Appendix B for the algorithms). Table 5.3 shows parameters used with the fluid being water.

Similar to Model 4, Model 5 uses real fluid parameters for its simulation. Starting the simulation with an initial perfect circle of radius 2.25 mm as shown in Figure 5.15 (a), the surface tension force is implemented using Equation (5.4), where the curvature (κ) is computed with the new modified curvature Equation (5.13) which is going to be validated later in Session 5.5. The error in this discretize calculated curvature of the droplet from (Equation (5.13)) which gave a value of $446.22m^{-1}$ as a result of the simulation compared to the theoretical calculated curvature from Equation (5.14) which gave a value of $444.44m^{-1}$ is 0.4%. With this small error margin, it shows that the proposed discretize curvature is in good agreement with theoretical calculated curvature. The temporal evolution of the droplet is shown in Figure 5.15, where the

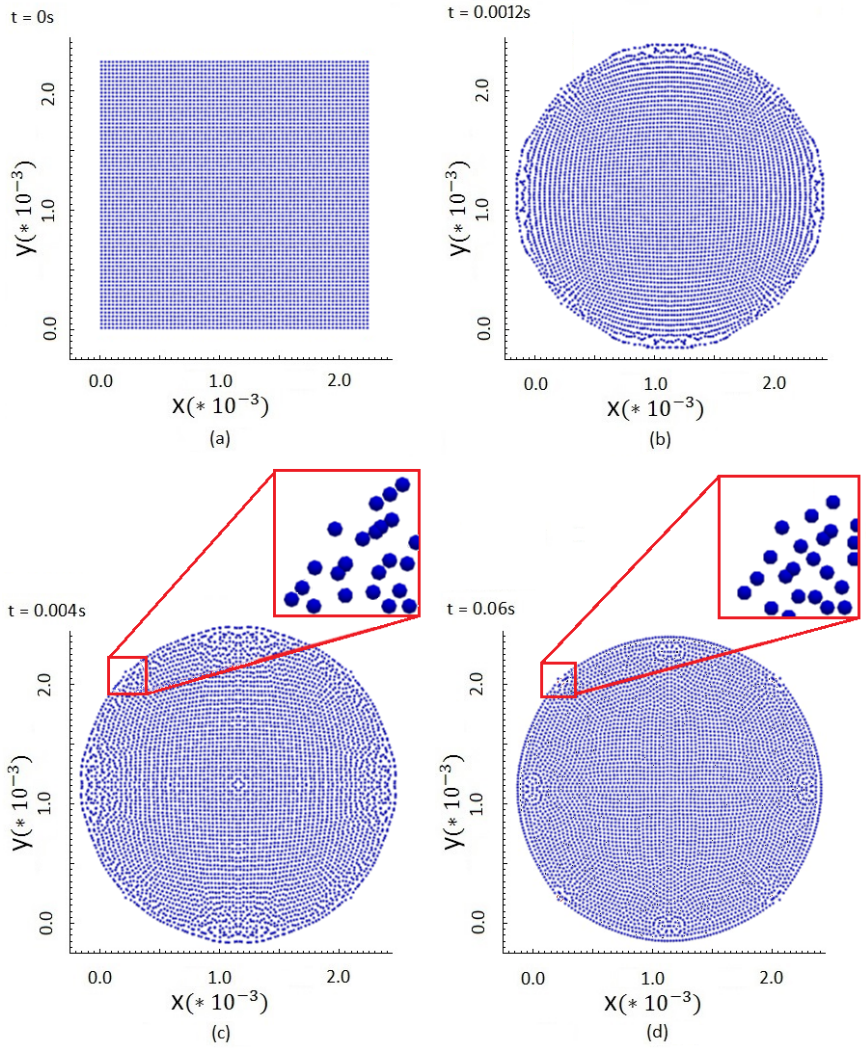

FIGURE 5.14: The evolution of initial square droplet using the Continuous Surface Force (CSF) Method with Wendland only using 4225 particles resolutions.

TABLE 5.3: Initials properties of particles for the Droplet Flow for Model 4.

Properties, symbols (Units)	**Fluid values**
Pressure, p (Pa)	0
Acceleration (gravity), $\vec{\mathbf{a}}$ (m/s^2)	0
Sound speed, c_o $(\mathrm{m}s^{-1})$	5.0
Kernel, W_{ij} (m^{-3})	Wendland only
Surface tension coefficient, σ (N)	0.0728

particles try to rearrange themselves to get to the final equilibrium stage, given by Figure 5.15 (f), at which the droplet experience a little shrinkage as a result of the applied surface tension forces giving rise to the above error.

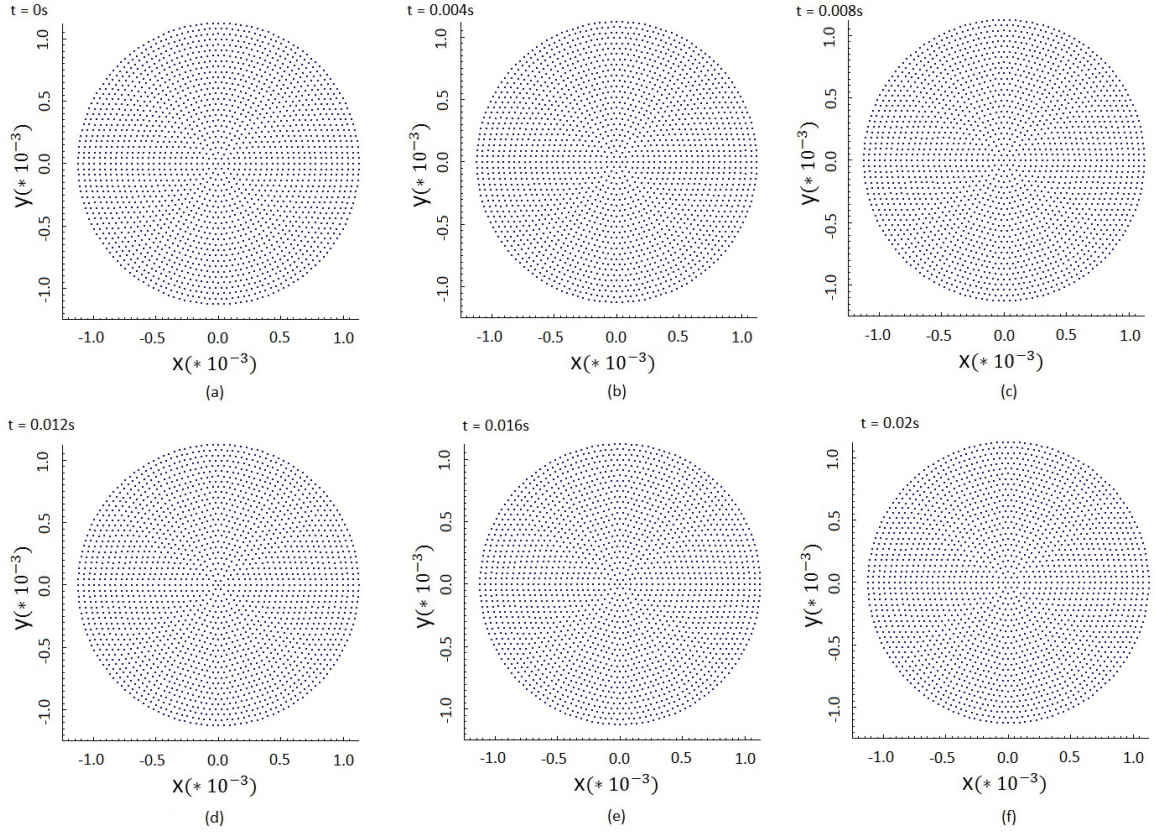

FIGURE 5.15: The evolution of droplet using the Continuous Surface Force (CSF) Method with Wendland only using Model 5 with real fluid properties.

Figure 5.16 (a) to (d) validates that surface tension do not exist within the bulk of the fluid by using Model 5; it shows the surface tension is zero for all bulk particles of the fluid at $t = 0s$ to $t = 0.02s$, except for those particles located adjacent or near the interface. From the above, it is evident that surface tension effect do not exist even within the inner part of the fluid, which make this CSF approach realistic for simulating real world phenomena. Also, the droplet is well uniformly ordered even up to the final equilibrium stage. This approach is highly dependent on the particle distribution that is well ordered with uniformly curvature. So, for complex movement where the curvature varied, it will be difficult for this approach to handle. This is one of the major disadvantage of this approach compared to the former IIF method Model 1, which can be use for different initial droplet shapes.

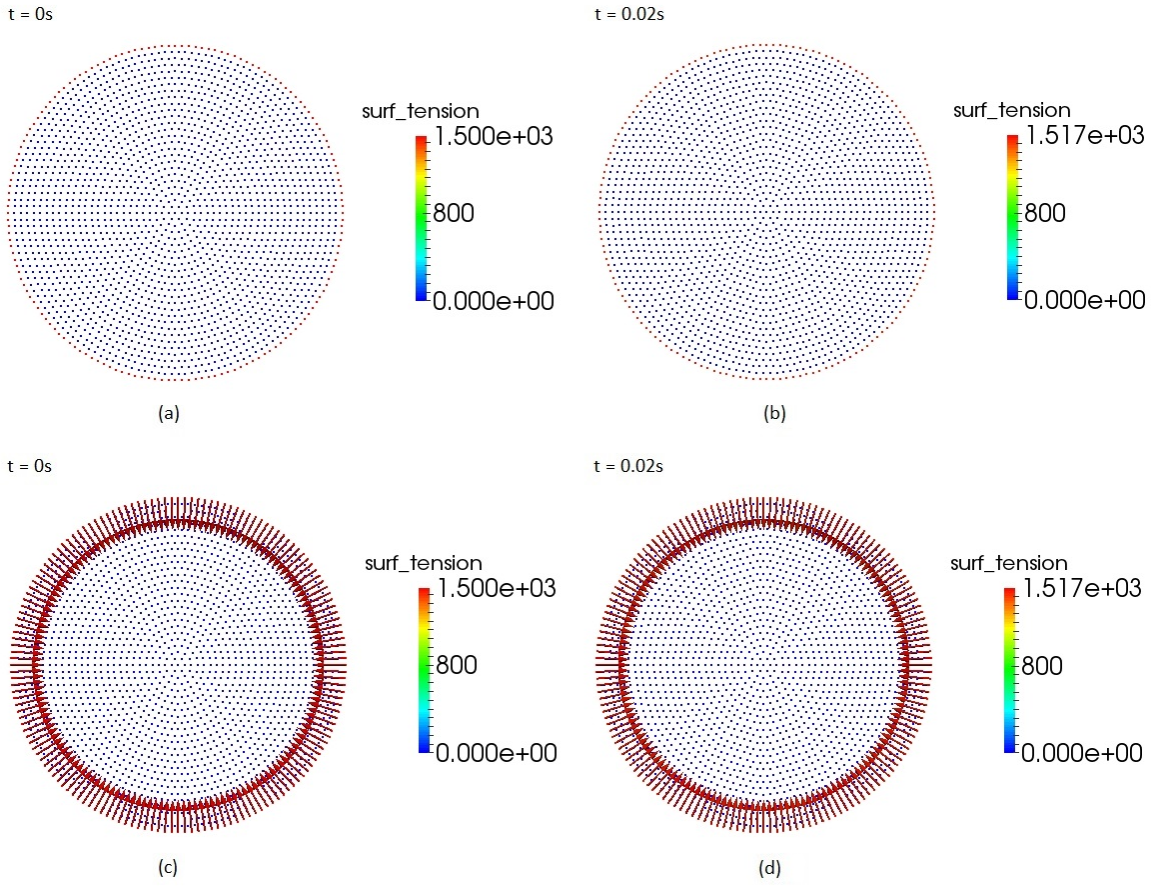

FIGURE 5.16: (a) The initial circle shape with zero surface tension effect at the bulk of the fluid (b) Final circular shape with higher surface tension effect at the interface with zero surface tension in the bulk (c) The initial circle shape with surface tension vector pointing toward the center (d) Final circular shape with higher surface tension vector at the free-surface pointing toward the center.

5.5 Droplet Curvature Validation

To validate the accuracy and validity of our proposed curvature formulation of Equation (5.13) for single-phase fluid flow, a two-dimensional water droplet of size 1mm in radius is considered with initial particle spacing set at 0.1mm, 0.05mm and 0.025mm intervals, giving particle resolutions of 331, 1261 and 4921, respectively. The setup to this simulation is similar to that in Model 5 with all real parameter of water used for the simulation. Figure 5.17 (a) to (c) shows the initial perfect circle shape of the droplet at time $t = 0s$, where it can be seen that the curvature applied only to particles at the free-surface with the unit surface normal vector acting uniformly and normally towards the centre of the droplet as shown in Figure 5.18 for resolution 1261. This interface layer is highlighted by only red particles as can be seen in Figure 5.17

with the curvature, κ value approximately 1000 shown by the colour bar while from the analytical curvature Equation (5.14), κ gives a value of $1000m^{-1}$.

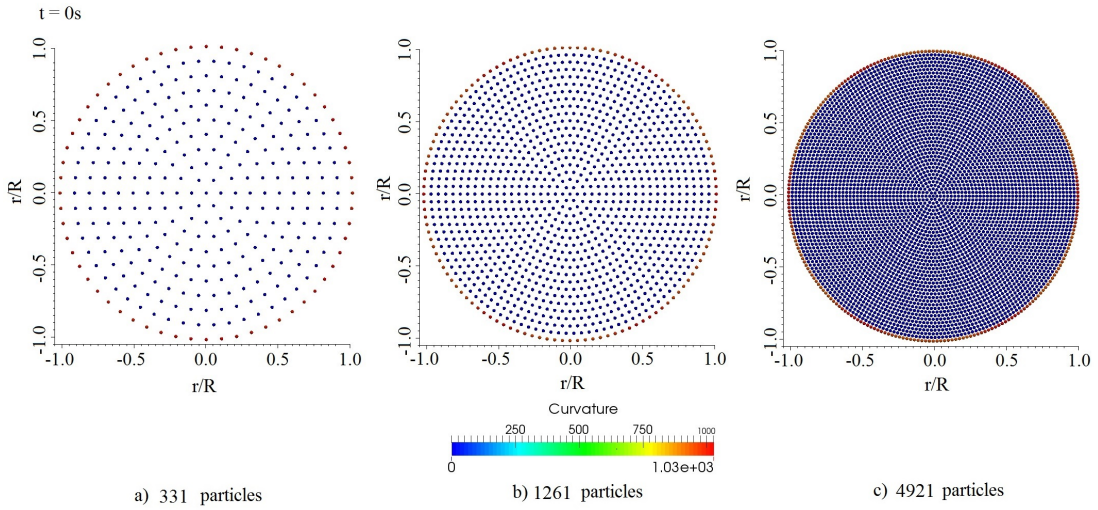

FIGURE 5.17: Snapshots of curvature validation with different resolution.

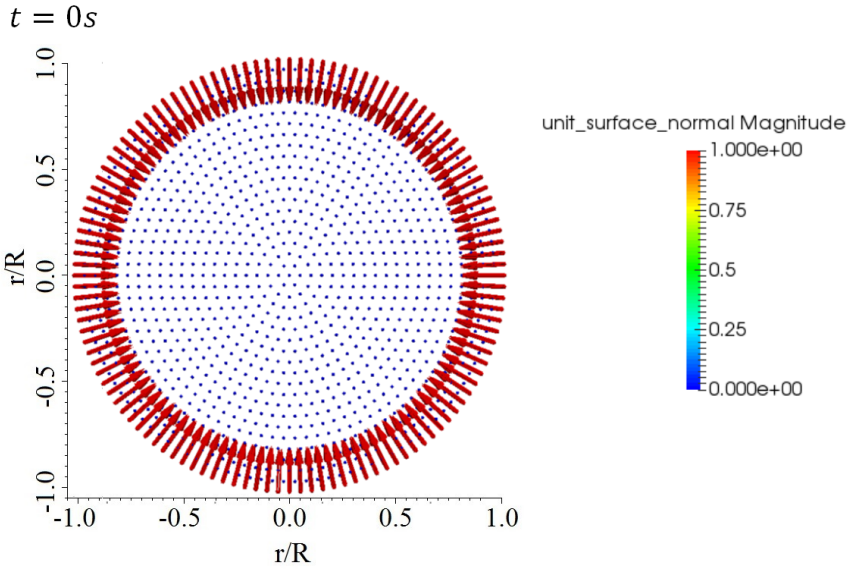

FIGURE 5.18: Snapshots of unit surface normal vector pointing toward the centre using 1261 particles resolution.

To validate these curvature values for the different resolutions, the average curvature of all the fluid particles at the interface calculated from Equation (5.13) were compared with the theoretical result from Equation (5.14). By plotting these average curvature values of the particles at the interface and the one from theoretical against all the particle index for the various resolution, it was observed that as the resolution increase, the accuracy of the curvature also increases [211] as shown in Figure 5.19. From the Figure 5.19, it can be seen that there is a strong agreement between the average

curvature from Equation (5.13) and the one from analytical Equation (5.14) with an error of $5 \times 10^{-5}\%$ which is negligible. A further increase in resolution will result in no change in curvature value, showing that the simulation for this test case have converged.

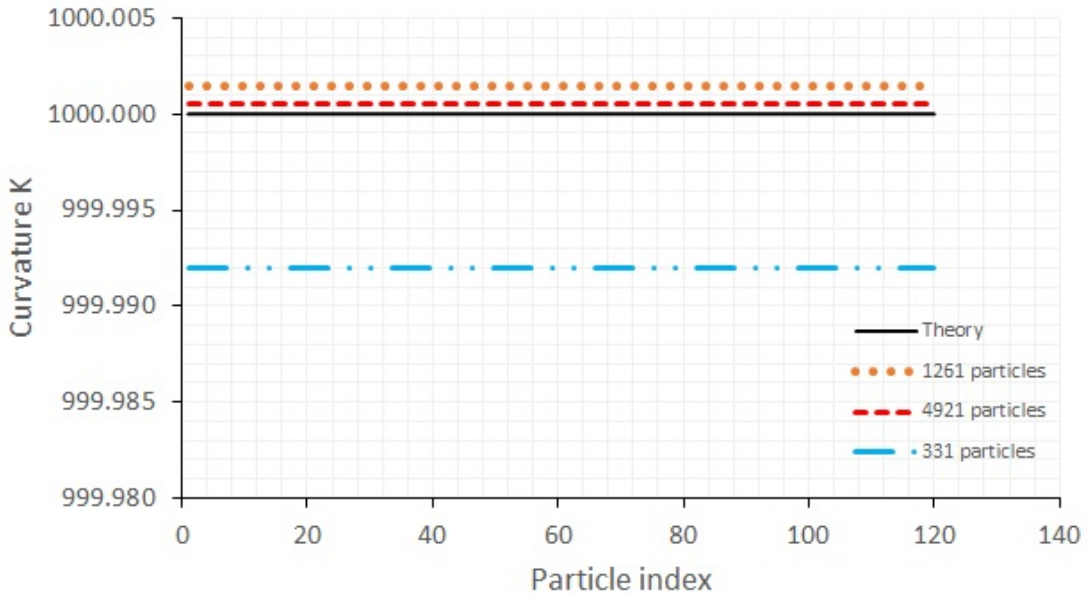

FIGURE 5.19: Plot of curvature against particle index with different resolution.

5.6 Droplet Oscillation

For more than a century now, the oscillation of droplet has fascinated researchers both to gain theoretical understanding [212–217]; and also its scientific applications [218, 219]. The first mathematical formulation for linear droplet oscillation in a vacuum in the case of inviscid fluid (zero viscosity) was done by Rayleigh [220]. However, a more general linear solution model which include the influence of the surrounding medium was given by Lamb [221]. Now, when a liquid drop is forced out of its equilibrium spherical shape, it undergoes shape oscillation, but if it is a gas bubble, it experiences both shape and volume oscillation because of its compressibility [222]. However, if the liquid is free from any other external forces except surface tension forces, then the liquid will remain in an equilibrium spherical shape. This oscillation happens because both the liquid droplet and gas bubble are exposed externally without any restrictions. This session will provide the basic theory and numerical simulation of an oscillation liquid droplet.

In order to describe the deformation of a stable equilibrium drop and its subsequent period of oscillation, the following expressions:

$$\begin{pmatrix} x^* \\ y^* \end{pmatrix} = \sqrt{\frac{2}{\sin\theta}} \begin{bmatrix} x\sin(\theta/2) \\ y\cos(\theta/2) \end{bmatrix}, \tag{5.17}$$

$$T = 2\pi\sqrt{\frac{R^3\rho}{6\sigma}}, \tag{5.18}$$

given by Nugent and Posch [151], where R is the equilibrium radius of the droplet, ρ is the density of liquid droplet, σ is the surface tension, $\theta = \varepsilon\pi$, ε is the eccentricity , x, y, and x^*, y^* are the component of position for each particle before and after the initial deformation respectively. Equation (5.17) will be used to initiate the droplet to undergo elliptic shape deformation while Equation (5.18) will be used to determine the theoretical period of oscillation. This period of oscillation, T, which is the time to complete one full oscillation, is necessary in order to compare if the droplet have the correct behaviour.

5.6.1 Droplet Oscillation with IIF (Model 1)

Using the IIF Method of Model 1 with the repulsive force implementation since it is better Model 2, a two-dimensional water droplet of radius $1.6mm$ is generated with an initial circular shape at rest, with the same operating parameters as in Model 1. However, a particle spacing of $\Delta x = 9.41\times10^{-5}mm$ is used, which delineates a particle count of 919 particles in the first instance and then particle counts of 547 and 1951 particles, as will be seen later. The two-dimensional droplet is allowed some time to attain its equilibrium state and configuration. This is necessary in order to eliminate any initial oscillation setup as a result of particles movement due to the effect of surface tension. Since, there is no gravity, the droplet relaxes to form a circular stable shape due to the present of surface tension. At this equilibrium state, the droplet is squeezed for a short period of time using Equation (5.17) into an elliptic shape with eccentricity of $\varepsilon = 0.55$ utilising an area-preserving and also density-conserving transformation of the particle coordinates [151]. After squeezing it into an elliptic shape and letting it go, the droplet begin to oscillations as shown in Figure 5.20 with the shape evolution in the x and y directions.

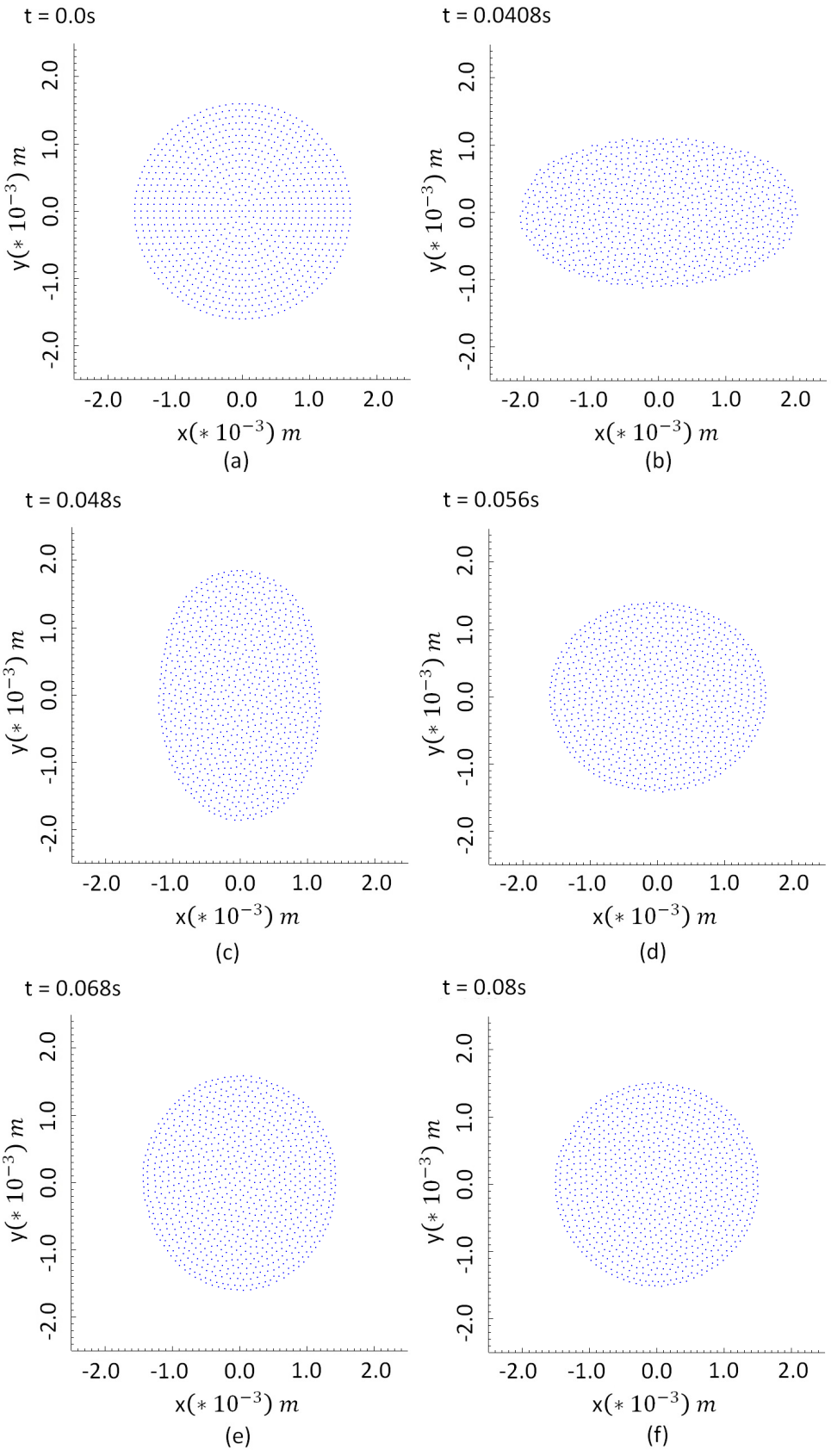

FIGURE 5.20: Evolution of droplet oscillation with resolution of 919 using Model 1.

In order to get the correct period of oscillation, the strength of the force s_{ff} in Equation (5.1) needs to be tuned to a value of 0.008 to have water like behaviour of the same droplet size. By matching the theoretical period of oscillation of water which is, $T = 0.0192$s, when all the necessary parameters are substituted into Equation (5.18) with the numerical oscillation period which was 0.019s as illustrated in Figure 5.21, it can be seen that both the numerical and theoretical oscillation period are in good agreement with an error of 1.05%. To further validate that this numerical period of oscillation result are consistent, two difference particle resolutions of 919 and 1951 were used for the simulation as shown in Figure 5.22. Again there is good agreement between the numerical and theoretical period of oscillation. However, from the results showed in Figure 5.21, the IIF approach damps very quickly and reaches steady state in only 2 oscillations compared to literature where it was reported that a $6.6cm^3$ squeezed droplet will oscillate 82 times under micro-gravity [223]. This is due to the ever-present dissipating internal inter-particle forces within the droplet as stated previously.

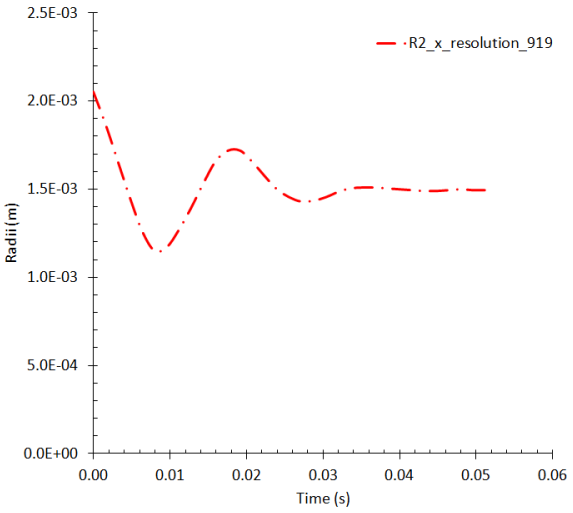

FIGURE 5.21: Droplet oscillation using Model 1 at resolution of 919.

5.6.2 Droplet Oscillation with CSF (Model 5)

In a similar manner, following from the simulation of droplet, using the CSF Method of Model 5, a two-dimensional water droplet of radius $1.6mm$ is generated with an initial circular homogenous shape at rest, using the same operating parameter as in Model 5. Furthermore, a particle spacing of $\Delta x = 9.41 \times 10^{-5}mm$ is used, which delineates a particle count of 919 particles in the first instance and later 547 and 1951 particle

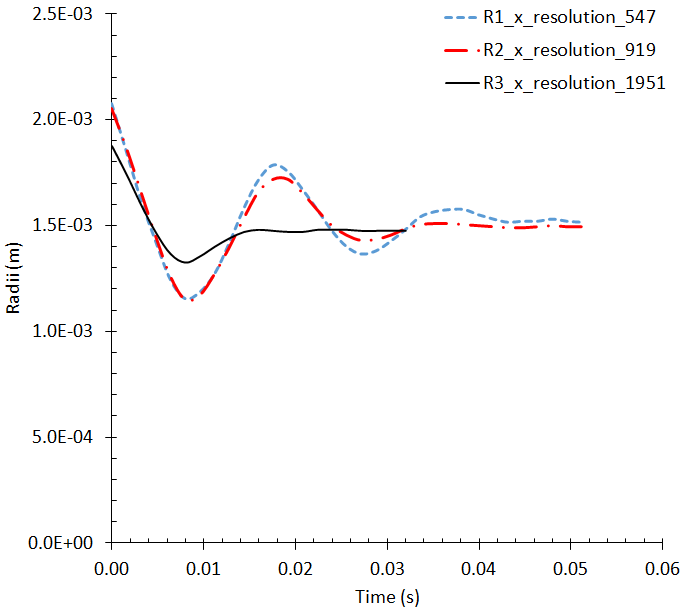

FIGURE 5.22: Droplet oscillation using Model 1 at resolutions of 547, 919, and 1951.

resolutions. The two-dimensional drop is allowed time to attain equilibrium state, just to remove any initial oscillation setup during the formation. Because gravity is absent, the droplet relaxes to form a circular stable shape due to the present of surface tension. At this equilibrium state, the droplet is squeezed for a short period of time using Equation (5.17) into an elliptic shape with eccentricity of $\varepsilon = 0.55$ utilising an area-preserving and also density-conserving transformation of the particle coordinates [151], before letting it go. The droplet begin to oscillate as shown in Figure 5.23 with the shape evolution in the x and y directions. During the oscillation, there appears a void at the sides of the droplet as shown in Figure 5.23 (d) and (f), which is not possible with the IIF Model 1 shown previously. However, these voids disappeared if higher resolutions of particles are used as shown in Figure 5.24. This increase in resolution make the droplet hold better, but does not affect their oscillation behaviour.

Furthermore, this droplet oscillation by CSF Model 5 does not require the turning of parameters, but rather it involves the use of real parameters of the fluid. The numerical period of oscillation is shown in Figure 5.25 and is calculated to be 0.0191s and corresponds to the theoretical period of oscillation of 0.0192s when all the necessary parameters, like surface tension coefficient, σ, density, ρ, and droplet radius, R, are substituted into Equation (5.18). From the above, it can be seen that both the numerical period of oscillation and the theoretical period of oscillation are also in good agreement with an error of 0.5%. Apart from the fact that this error is smaller,

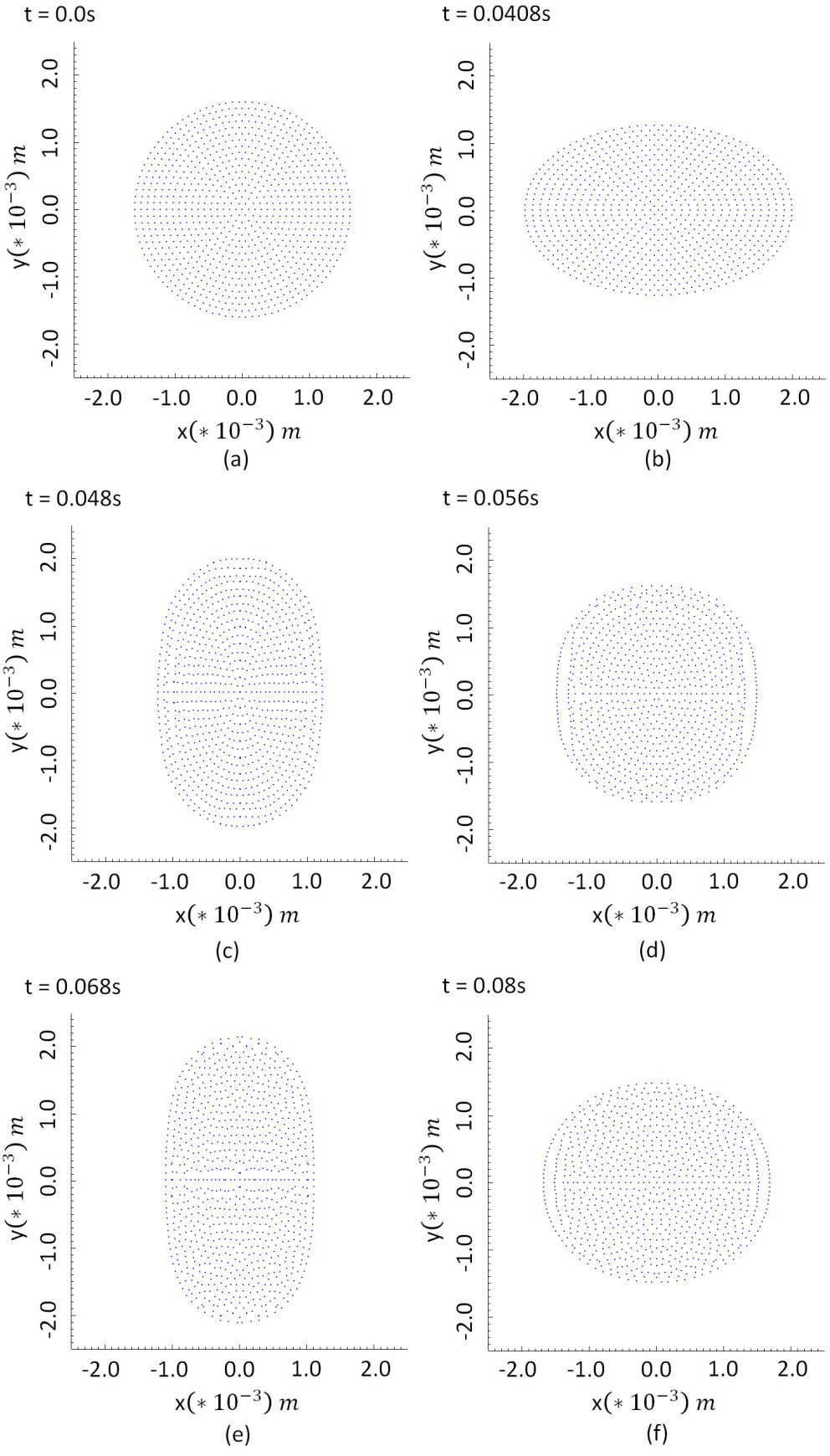

FIGURE 5.23: Evolution of droplet oscillation with resolution of 919 using Model 5.

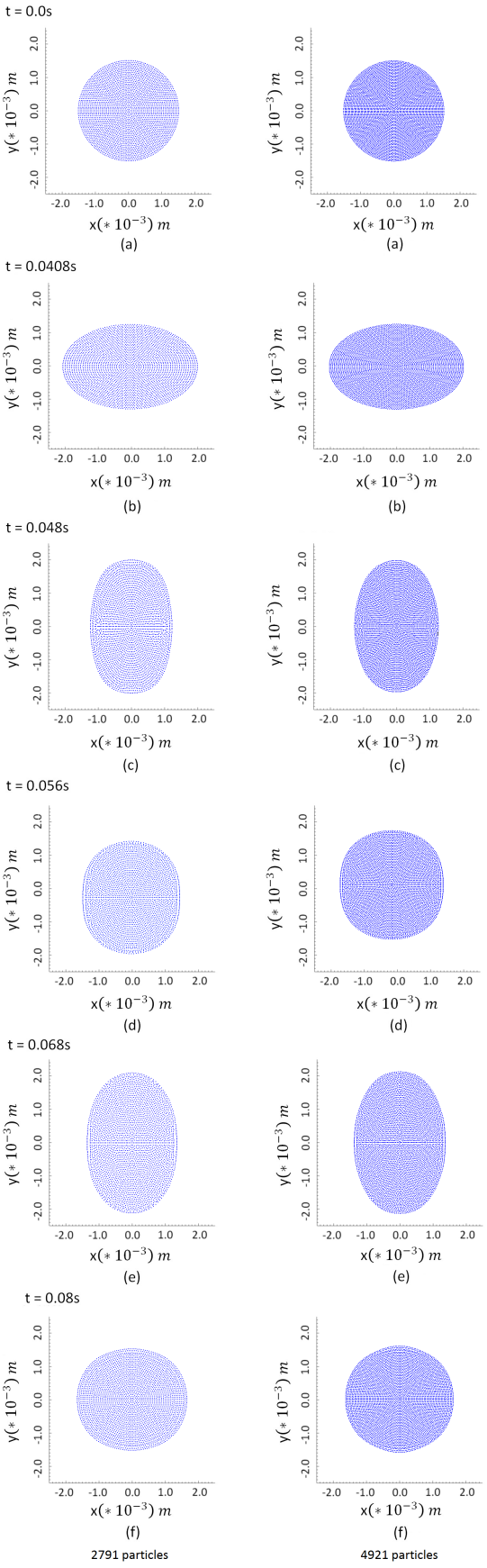

FIGURE 5.24: Evolution of droplet oscillation with resolutions of 2791 and 4921 using Model 5.

the additional major advantage in this case is that any real fluid properties can be used for simulation without time wasting tuning an artificial force s_{ij} for the fluid to behave like water. In order to shows that this result is reliable, three difference resolutions were used as shown in Figure 5.26. The droplet modelled using the proposed CSF approach (Model 5) oscillates far longer and damps out in approximately 60 oscillations (see Figure 5.27). Comparisons with experimental results in Apfel *et al.* [223] reported that a squeezed droplet of $6.6cm^3$ in micro-gravity oscillates as much as 82 times. The results obtained from the modified CSF approach (Model 5) were performed in two-dimensions and one would expect that the surface tension contribution would be smaller and thus the number of oscillations will be fewer compared to three-dimensional ones.

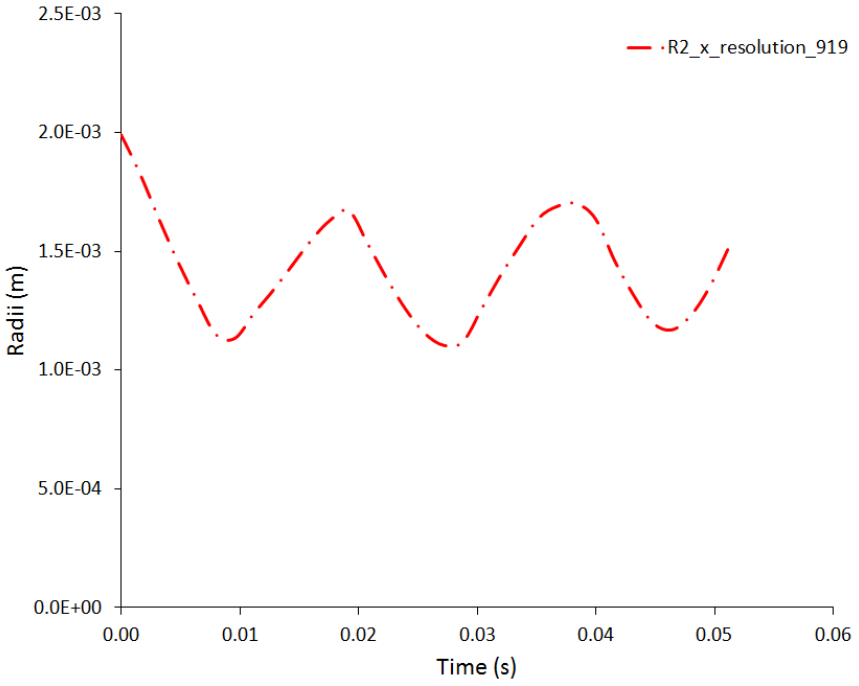

FIGURE 5.25: Droplet oscillation using Model 5 at resolution of 919.

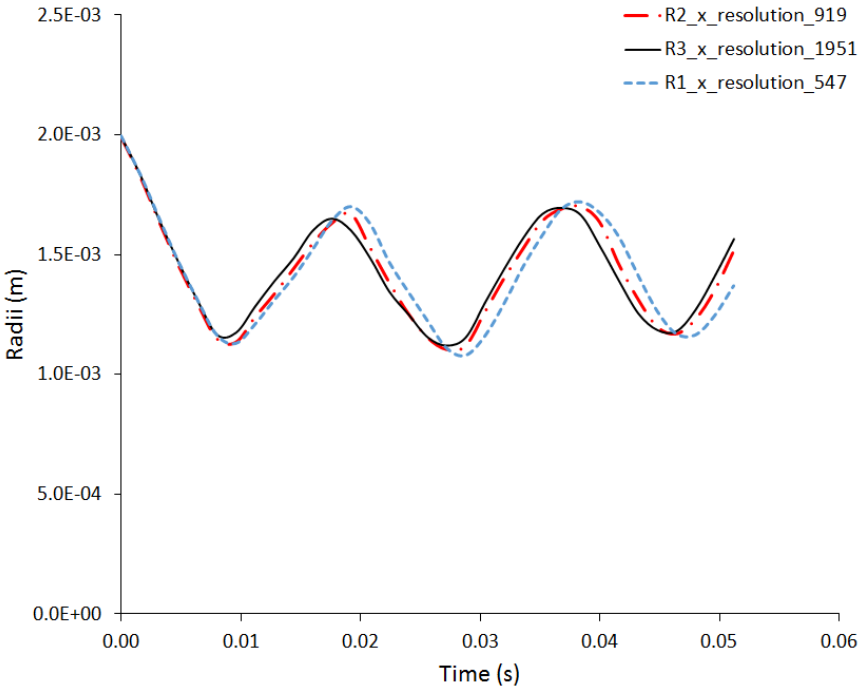

FIGURE 5.26: Droplet oscillation using Model 5 at resolutions of 547, 919, and 1951.

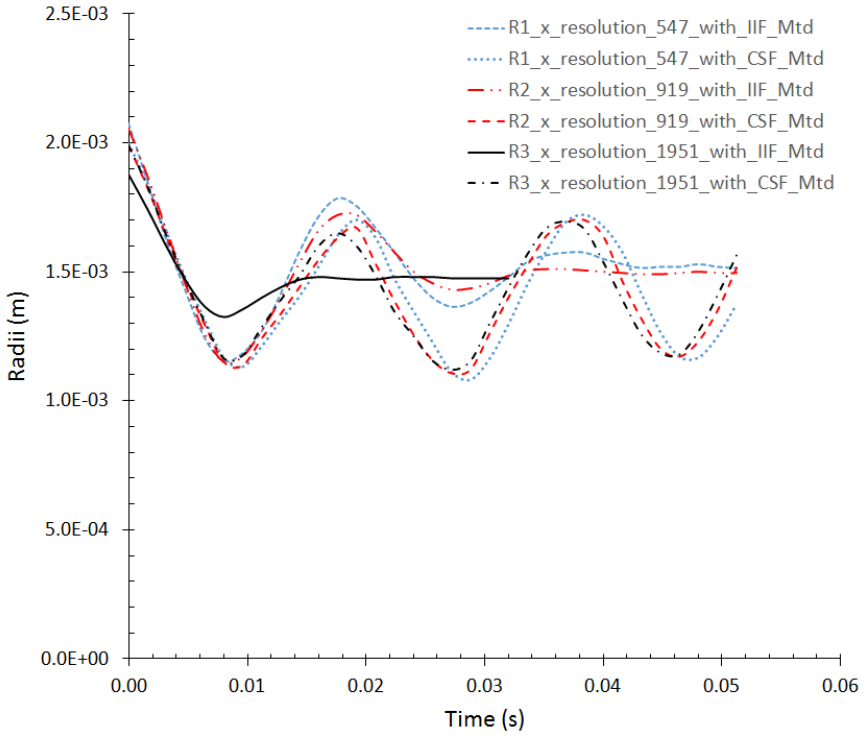

FIGURE 5.27: Droplet oscillation comparison using Model 5 and Model 1 at resolutions of 547, 919, and 1951.

Chapter 6

Droplet Spreading Process

> "It isn't that they can't see the solution. It is that they can't see the problem."
>
> G.K. Chesterton, (1874-1936).

6.1 Contact Angle and Wetting

When a liquid droplet is placed on a solid surface, it will begin to spread to a greater or lesser extent, depending on the intermolecular forces interacting between the gas-liquid-solid interface. If this interaction forces (cohesive forces) within the liquid molecules is less than those forces between the liquid molecules and solid substrate (adhesive forces), then the liquid will spread over the solid surface, even up to a single layer especially if the surface is fully wetting. On the other hand, if these interaction forces within the liquid molecules are greater, then the liquid will contract or remain as a droplet over the solid surface. This is what is called "the wetting process".

The angle between the solid surface line within the liquid and the tangent to the drop surface at the triple point solid/liquid/gas where the phases meet is called "wetting contact angle" or simply put "contact angle" which is represented by θ as shown in Figure 6.1. For $\theta \approx 0°$, the fluid is fully wetting, whereas if the $\theta > 0°$, the fluid is considered as partial wetting. Furthermore, for contact angle less than 90°, the solid surface is considered as hydrophilic surface as shown in the experimental result

in Figure 6.2 (a), whereas if it is greater than 90°, the solid surface is considered as hydrophobic surface as shown also in the experimental result in Figure 6.2 (b). For contact angles up to 120°, the surface is considered as still hydrophobic especially for water droplet, whereas if the contact angle increases up to 150° and more, the surface is considered to be super-hydrophobic. Super-hydrophobic surfaces are possible due to the present of micro or nano-size rough protrusions at the solid surface and this make the droplet to have much bigger contact angle which would not have been possible if the same surface were flat. Natural occurring super-hydrophobic contact angle up to 170° is known to have been possible when water droplet is placed on the lotus leaf (see Figure 6.3). Figure 6.4 (a) and (b) shows a rough visualisation of this criterion.

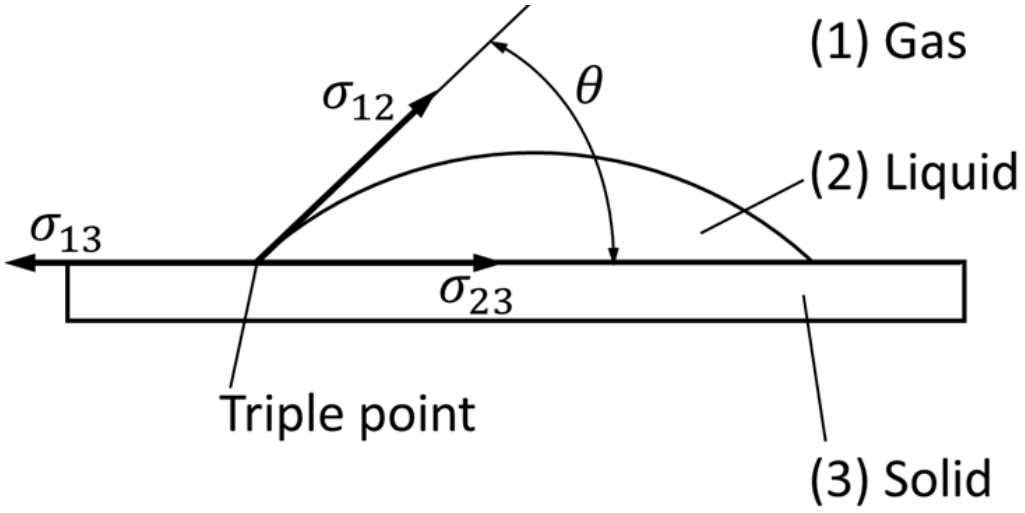

FIGURE 6.1: Showing contact angle along with the triple point.

where the gas, liquid and solid phases are represented by 1, 2 and 3 respectively.

Thomas Young in [226] was the first to describe the forces acting in the line of the three phase contact as represented by Figure 6.1. The mathematical expression that describe this is known as Young's equation and is stated as follows:

$$\sigma_{sv} = \sigma_{sl} + \sigma_{lv}\cos\theta \tag{6.1}$$

where $\sigma_{sv} = \sigma_{13}$ is the solid vapour interface, $\sigma_{sl} = \sigma_{23}$ the solid liquid interface, $\sigma_{lv} = \sigma_{12}$ the liquid vapour interface of the surface free energy respectively and θ the equilibrium contact angle. For all the Models that will be discussed later in this Chapter, the effects of gravity will be ignored because the bond numbers, B_O, are of $O(1)$ (i.e. an order of magnitude unity or less).

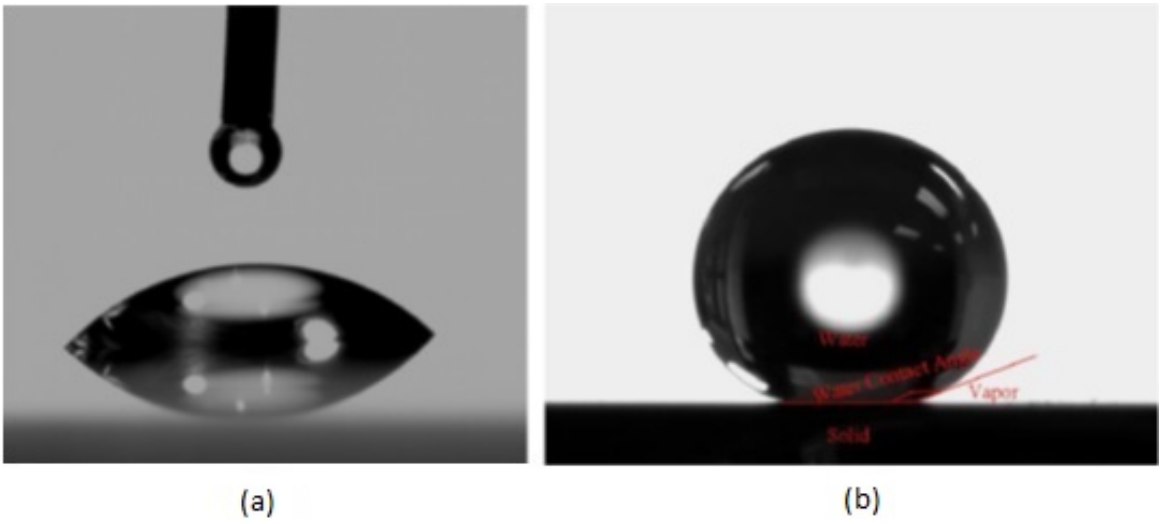

FIGURE 6.2: Photograph of experimental studies on (a) Hydrophilic and (b) Hydrophobic surfaces [224].

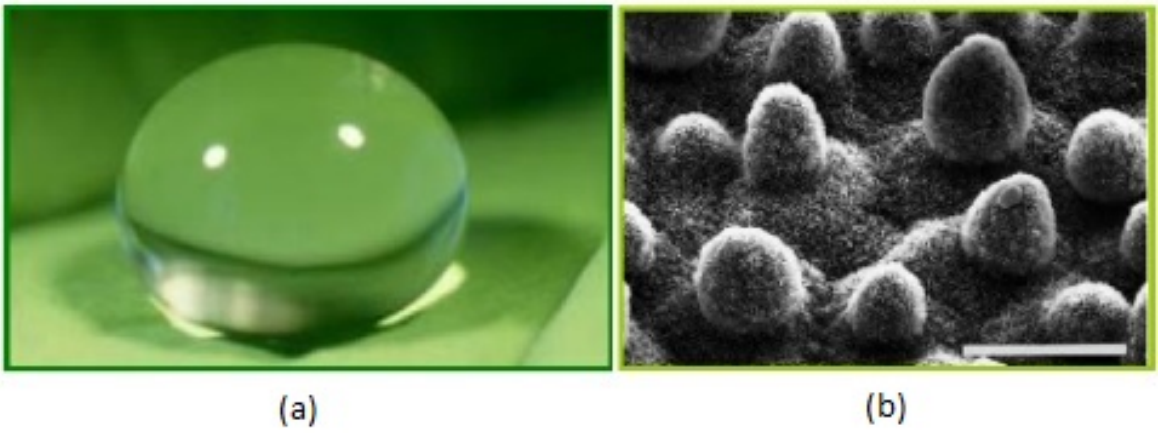

FIGURE 6.3: Super-hydrophobic of contact angle by SEM (a) water droplet on the lotus leaf (b) photo of lotus leaf [224, 225].

6.1.1 Contact Angle with IIF (Model 1)

Using the IIF Method of model 1 with the the repulsive implementation, a two-dimensional water droplet with initial square shape is generated at rest and placed on a solid substrate having four layers, upon which the water droplet is spread. To have a clearer picture and brief description, a schematic representation for the setup is illustrated in Figure 6.5 in which the fluid and substrate are shown before applying the necessary equations. It can be seen from Figure 6.5, that the simulation start with an initial square droplet shape of size 3.0 $mm \times 3.0$ mm made up of 576 particles and solid substrate made up of 479 particles of four layers. The other initial parameters for the setup of this problem is the same as in Model 1, see Section 5.6.1 for details.

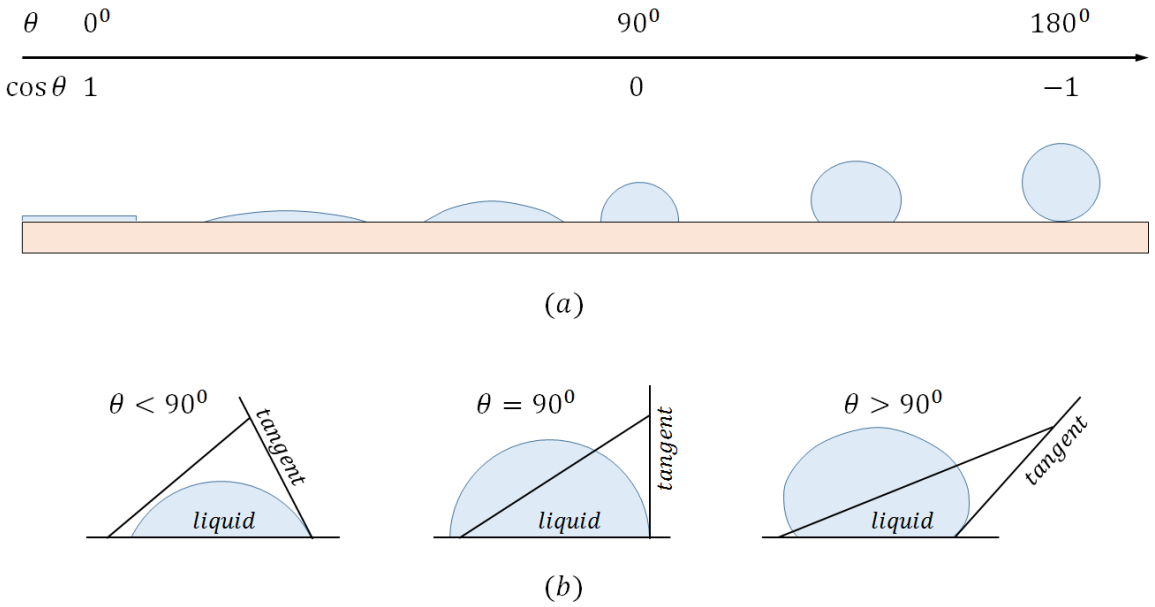

FIGURE 6.4: Rough visualisation of contact angle evolution.

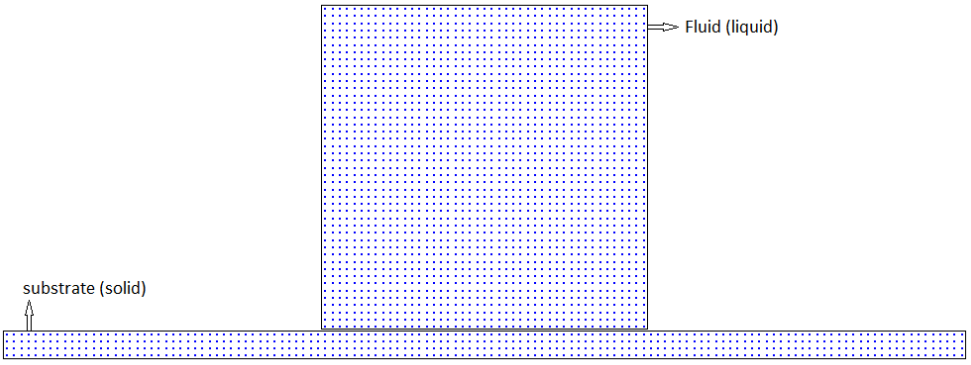

FIGURE 6.5: The schematic representation of the fluid on the substrate before surface tension force is applied.

Tartakovsky and Panchenko [207] and Zhou *et al.* [227] used this approach to successfully control the contact angle for a two-phase problem. As stated in Section 5.1, the method is simple and straightforward, however, it requires the tuning of three parameters.

In our proposed modified IIF method (see Section 5.3.1), the Taits equation of state is used to update the pressure instead of the van der Waals equation of state employed originally by Tartakovsky and Meakin [152].

Following the procedure set out in Model 1 (see Section 5.6.1), the strength of force between the fluid and fluid particles are set to be $s_{ff} = 0.008$, but because there is also the presence of solid substrate, the interaction force strength between the fluid

and solid particles were tuned within the range of $0 \leq s_{sf} \leq 0.008$ in order for the fluid to spread with difference contact angles on the substrate. In this present test case, gravity is ignored because B_o is 1.2, which is of $O(1)$ and thus still within acceptable limit where surface tension is dominant couple with the length scale, l_c, been approximately 3mm.

The simulation begin by letting the two-dimensional droplet spread until it attain its equilibrium state. During the simulation, there were no gravity and because of the tuning of the strength of force between the fluid and solid particles, the droplet relaxes into an equilibrium shape due to the present of surface tension as shown in Figure 6.6. From Figure 6.6, it can be seen that the contact angle is dependent on the interaction strength, s_{sf}, between the fluid and solid particles. However, the contact angle at the equilibrium state is not very accurate, which is believe to be due to low particle resolution. Higher particle resolutions are considered to improve the above mentioned problem.

To carry out convergence study for this problem, different particle resolutions of 576, 961 and 2025 were considered. Figures 6.6 to 6.8 illustrate the equilibrium contact angle (θ) evolution which depend on the interaction force (s_{sf}) between the solid and fluid for fluid particle resolution of 576, 961 and 2025 respectively. In order to have a clear visualisation comparison of these three particle resolutions, Figure 6.9 shows the surface profile of some selected static contact angles at s_{sf} values of 0.001, 0.002, 0.004, 0.0055 and 0.007. It is seen from Figure 6.9 that, there is almost a complete overlap of the surface profiles of these three particle resolutions, except at smaller contact angle where there is a little deviation. A further justification is given in Figure 6.10, which shows the standard deviation error when the mean static contact angle are plotted against the interaction strength s_{sf} for the three particle resolutions, although with a little kick at static contact angle of 100°. Again, it is clear that particle resolution do not affect much the relationship between the static contact angle, θ, and the interaction force, s_{sf}, with almost a linear graph. The proposed IIF method with the Tait's equation of state limit the contact angle to within 23° to 180° compared to Kordilla *et al.* [228] who achieved within 25° to 110° with the Van der Waals equation of state in the present of air particles. The absence of air particles in our proposed model make its computationally less expensive.

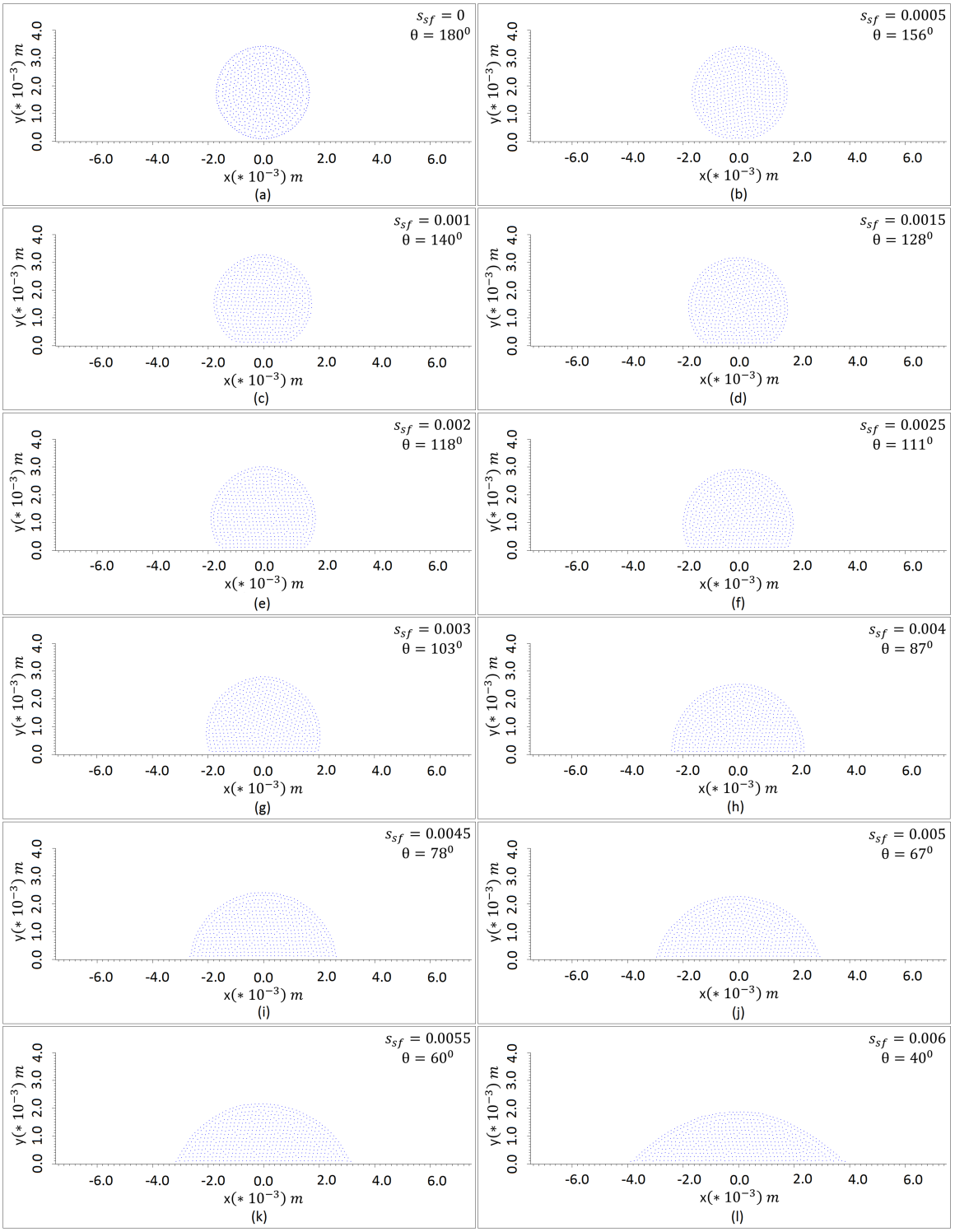

FIGURE 6.6: Evolution of droplet contact angle with 576 particles resolution on the substrate by tuning the strength between solid and fluid (s_{sf}) to take value from 0 to 0.006 so as to have the correspond contact angle as shown in (a) to (l) while the strength between fluid and fluid is made ($s_{ff} = 0.008$).

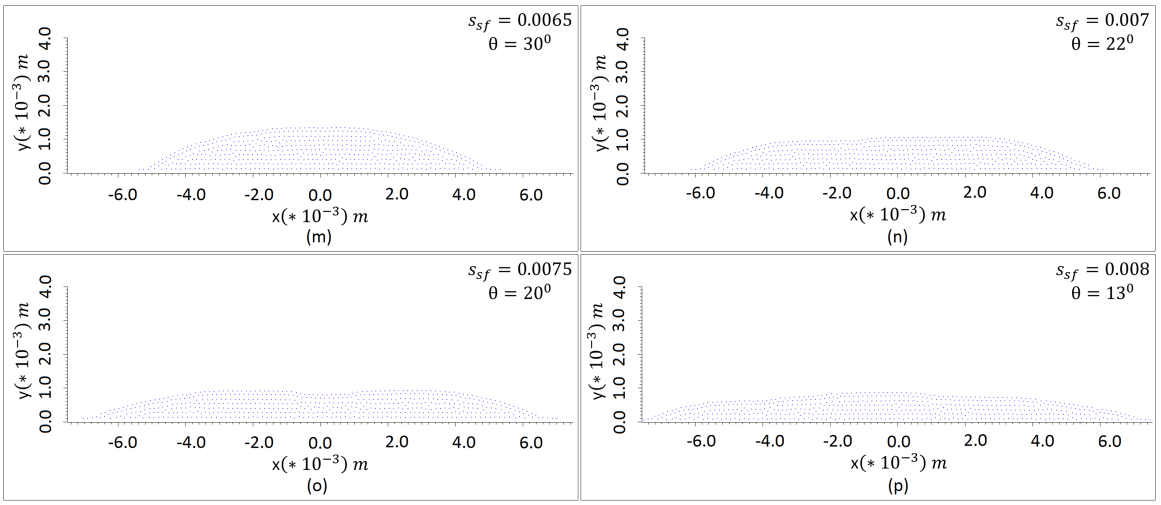

Continuation of Figure 6.6: Evolution of droplet contact angle with 576 particles resolution on the substrate by tuning the strength between solid and fluid (s_{sf}) to take value from 0.0065 to 0.008 so as to have the correspond contact angle as shown in (m) to (p) while the strength between fluid and fluid is made ($s_{ff} = 0.008$).

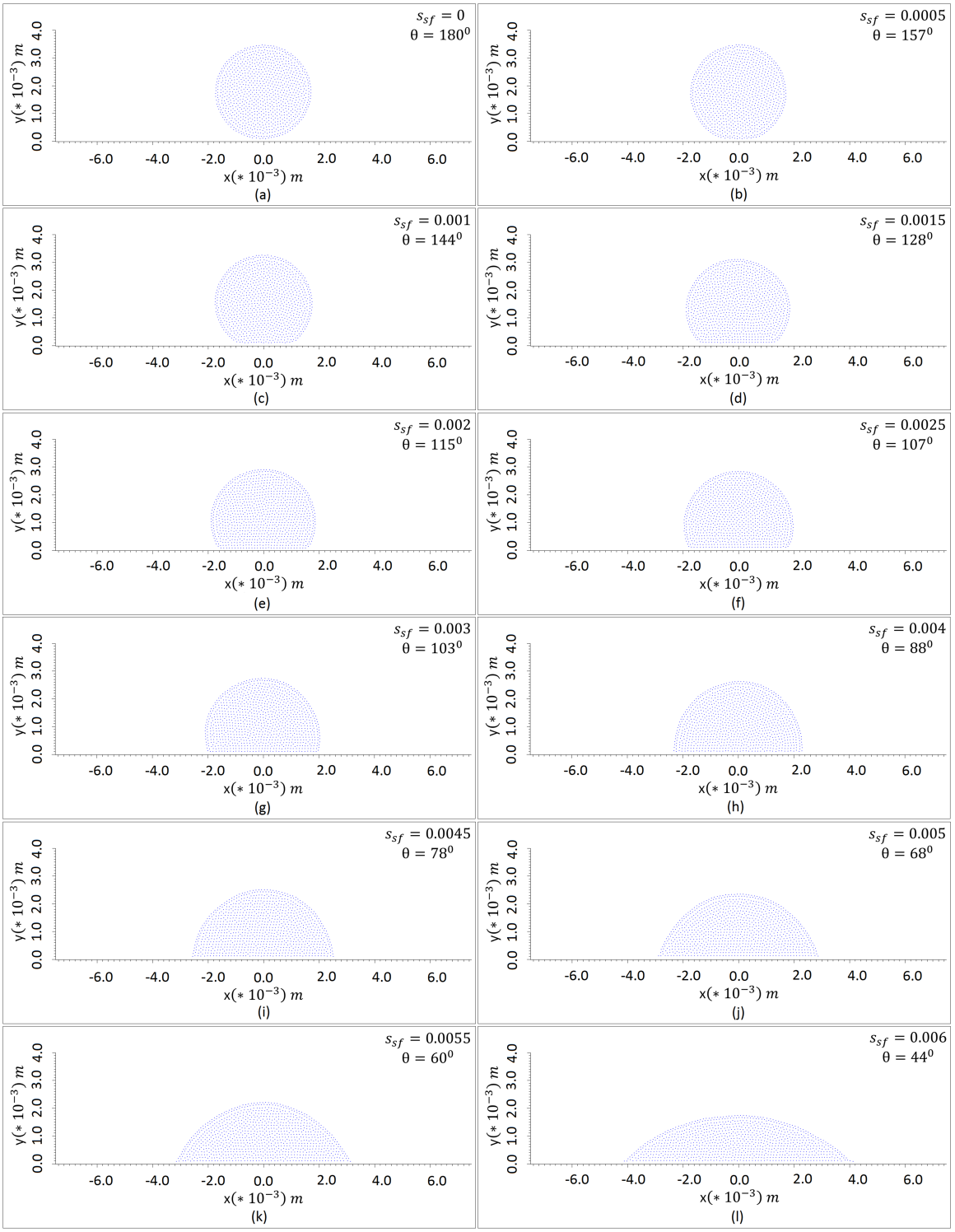

FIGURE 6.7: Evolution of droplet contact angle with 961 particles resolution on the substrate by tuning the strength between solid and fluid (s_{sf}) to take value from 0 to 0.006 so as to have the correspond contact angle as shown in (a) to (l) while the strength between fluid and fluid is made ($s_{ff} = 0.008$).

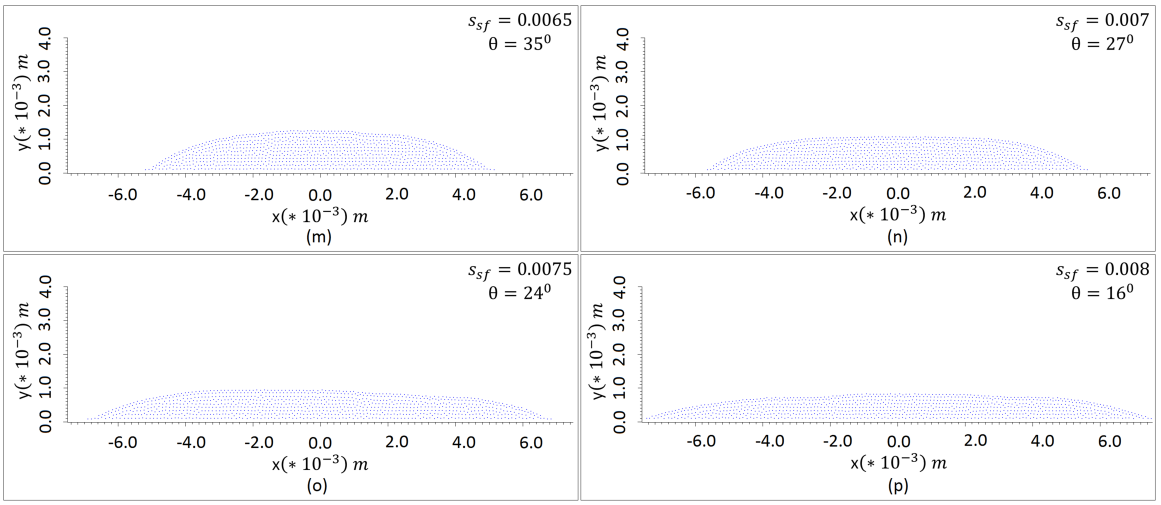

Continuation of Figure 6.7: Evolution of droplet contact angle with 961 particles resolution on the substrate by tuning the strength between solid and fluid (s_{sf}) to take value from 0.0065 to 0.008 so as to have the correspond contact angle as shown in (m) to (p) while the strength between fluid and fluid is made ($s_{ff} = 0.008$).

6.1.2 Contact Angle with CLF Model

The Contact Line Force (CLF) model was used recently by Huber *et al.* [229] to control the contact angle of two-phase problems. This force is applied only to the surface fluid particles that are at a certain small distance (called the distance vector d_i) from the solid substrate (see Figure 6.11 (a)). Furthermore, the modified CSF method Model 5 is then applied to the remaining surface fluid particles far away from this distance vector (see Figure 6.11 (b)). This distance depends on the chosen smoothing length, so if the smoothing length is $2h$, only the first two layer of the fluid particle close to the solid substrate is selected whereas if the smoothing length is $3h$, only the first three layer of the fluid particle close to the solid substrate will be selected. However, it was found that with smoothing length of $2h$, the spreading of the droplet is more stable. This CLF model is straight forward to implement as an external force into the Navier-Stokes equation. These forces is responsible for pulling these fluid particles along the surface of the solid substrate resulting in spreading as shown in Figure 6.11 (a).

The CLF per unit mass for a two phase problem is given by:

$$\mathbf{f_c} = \frac{\sigma\Big[cos(\alpha_s) - cos(\alpha_d)\Big]\hat{\nu}}{\rho}\delta, \tag{6.2}$$

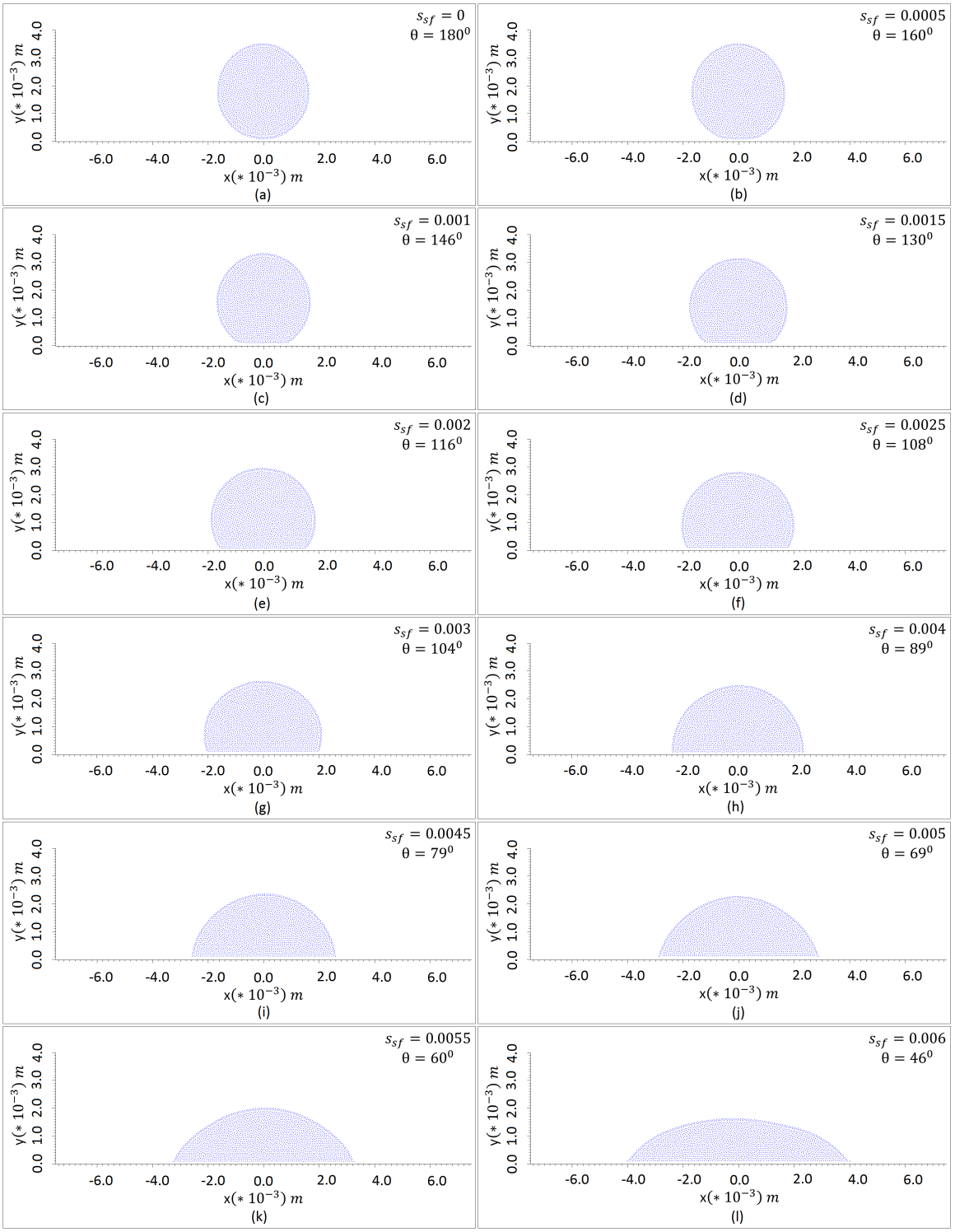

FIGURE 6.8: Evolution of droplet contact angle with 2025 particles resolution on the substrate by tuning the strength between solid and fluid (s_{sf}) to take value from 0 to 0.006 so as to have the correspond contact angle as shown in (a) to (l) while the strength between fluid and fluid is made ($s_{ff} = 0.008$).

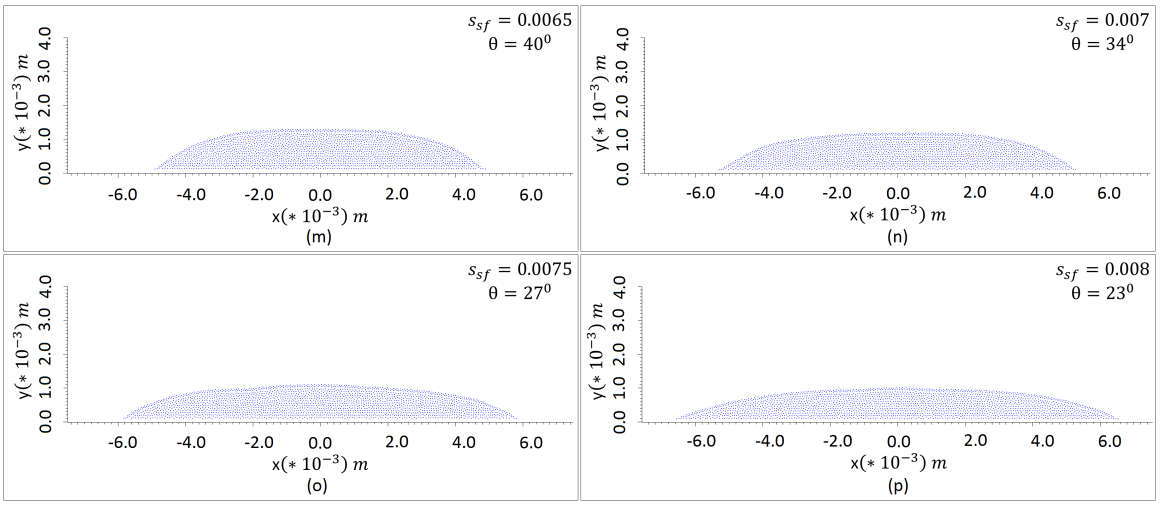

Continuation of Figure 6.8: Evolution of droplet contact angle with 2025 particles resolution on the substrate by tuning the strength between solid and fluid (s_{sf}) to take value from 0.0065 to 0.008 so as to have the correspond contact angle as shown in (m) to (p) while the strength between fluid and fluid is made ($s_{ff} = 0.008$).

where σ is the surface tension coefficient, α_s is the static contact angle, α_d is the dynamic contact angle, $\hat{\nu}$ is the unit vector with direction parallel to the substrate (see Figure 6.12), δ is the volume reformation and ρ is the density.

However, in order to use this CLF model from Equation (6.2) for single-phase problem, the following modified expression is introduce:

$$\mathbf{f_c} = \gamma \frac{\sigma \Big[cos(\alpha_s) - cos(\alpha_d) \Big] \hat{\nu}}{\rho} \delta, \tag{6.3}$$

where $\gamma = 2.0$ is to account for single phase and all other parameters remaining the same as in Equation (6.2), unless otherwise stated.

This modified CLF Equation (6.3) will be used in subsequent sections thereafter. At equilibrium state, $\mathbf{f_c} = 0$, when the dynamic and static contact angles balances each other, otherwise the droplet will evolve (spread) until it is zero. The $\hat{\nu}$ vector at the right side of Equation (6.3) is computed as:

$$\vec{\nu_i} = |\vec{\mathbf{d}}_i|^2 \vec{\mathbf{n}}_i - (\vec{\mathbf{d}}_i \cdot \vec{\mathbf{n}}_i) \vec{\mathbf{d}}_i, \tag{6.4}$$

where $\vec{\mathbf{n}}_i$ is the surface normal and $\vec{\mathbf{d}}_i$ is the distance vector between neighbouring particles. Here, the distance vector is given as:

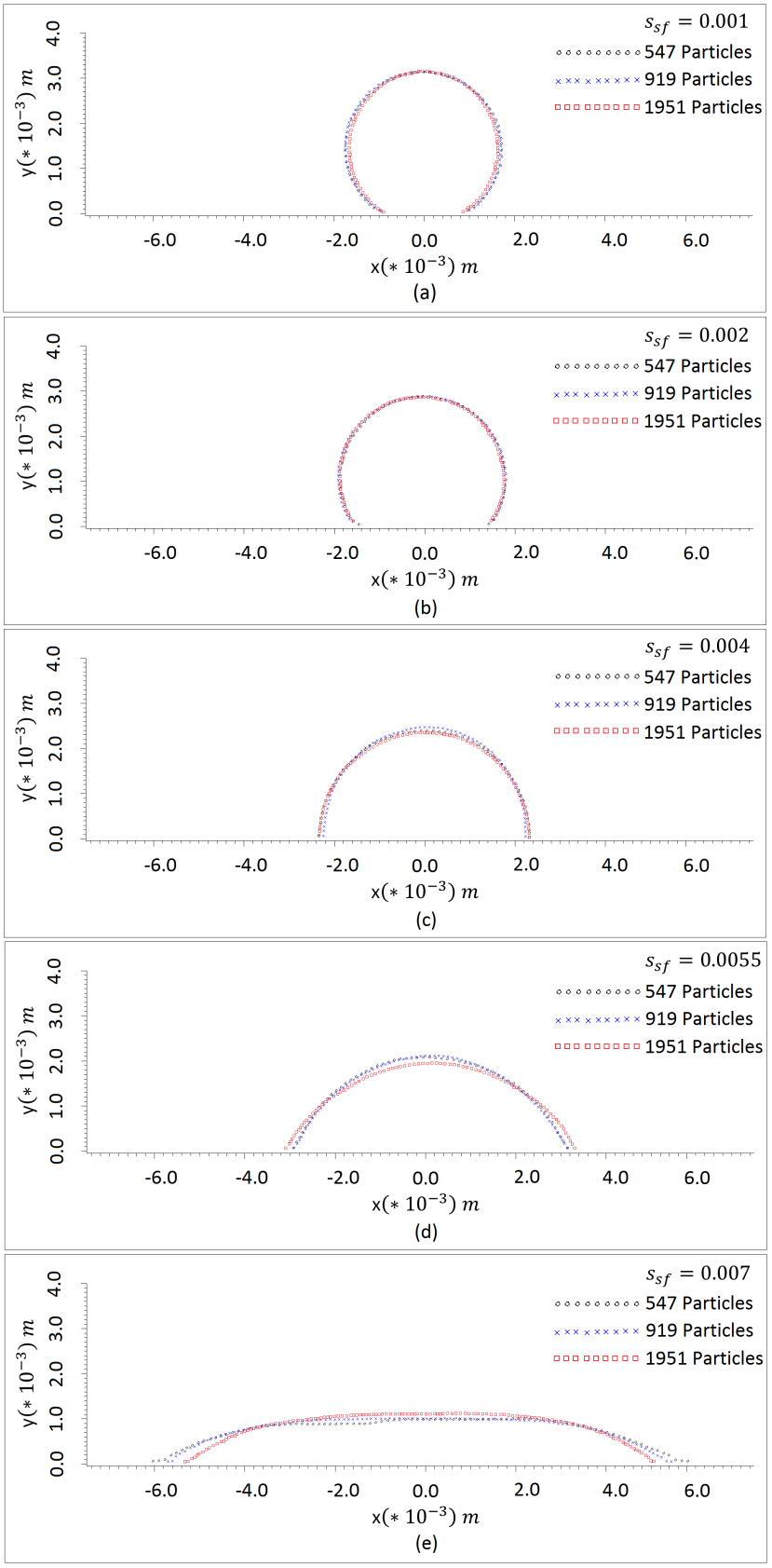

FIGURE 6.9: Evolution of the droplet surface profile of 576, 961 and 2025 particles resolution on the substrate at the various strength force between solid and fluid (s_{sf}) as shown while the strength force between fluid and fluid is ($s_{ff} = 0.008$).

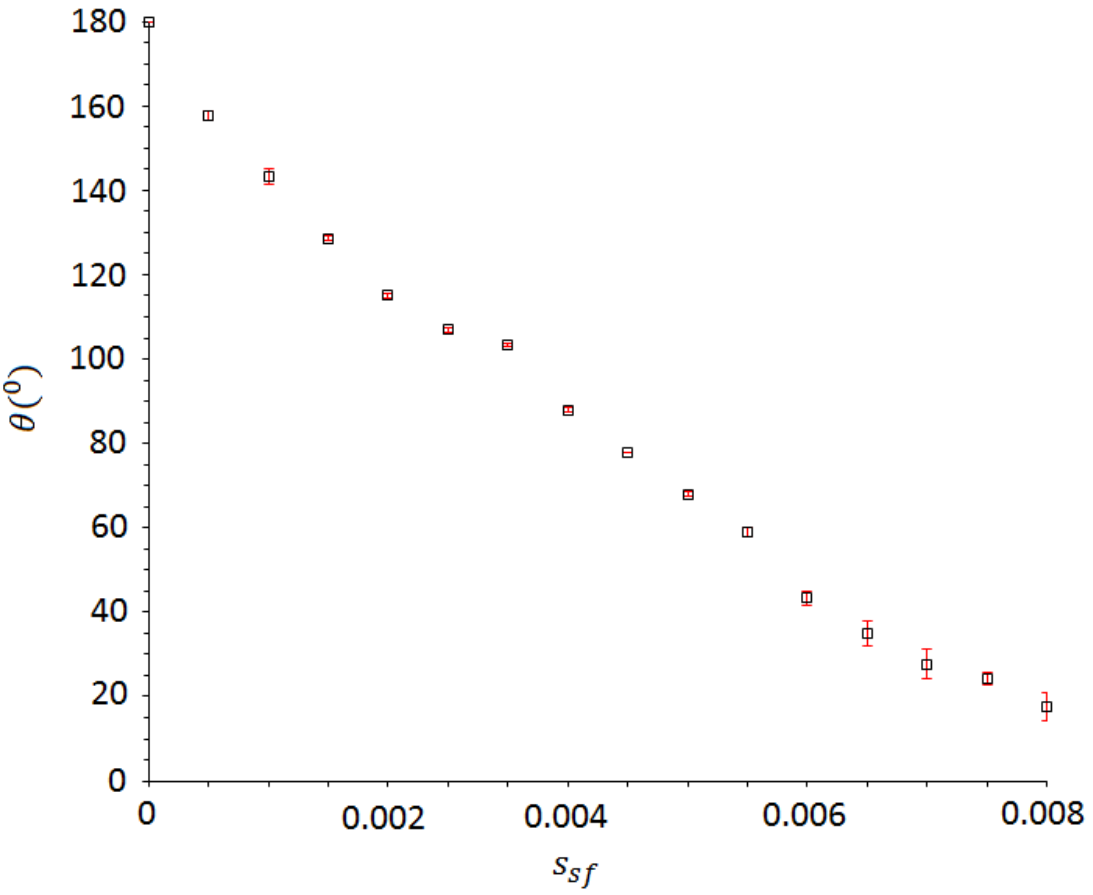

FIGURE 6.10: The mean standard deviation error against the interaction strength for 576, 961 and 2025 particles resolution.

$$\vec{\mathbf{d}}_i = \sum_j V_j \vec{\mathbf{r}}_{ij} W_{ij}, \tag{6.5}$$

where V_j is the volume, $\vec{\mathbf{r}}_{ij}$ is the particle separation and W_{ij} is the smoothing function. The distance vector always point directly into the substrate and its summation is taken only over the solid particles as shown in Figure 6.13.

The static contact angle is defined as an input parameter whereas the dynamic contact angle is determined from the following:

$$cos(\alpha_d) = -\hat{\mathbf{n}}_i \cdot \hat{\mathbf{d}}_i, \tag{6.6}$$

where now $\hat{\mathbf{n}}_i$ is the unit surface normal and $\hat{\mathbf{d}}_i$ is unit distance vector.

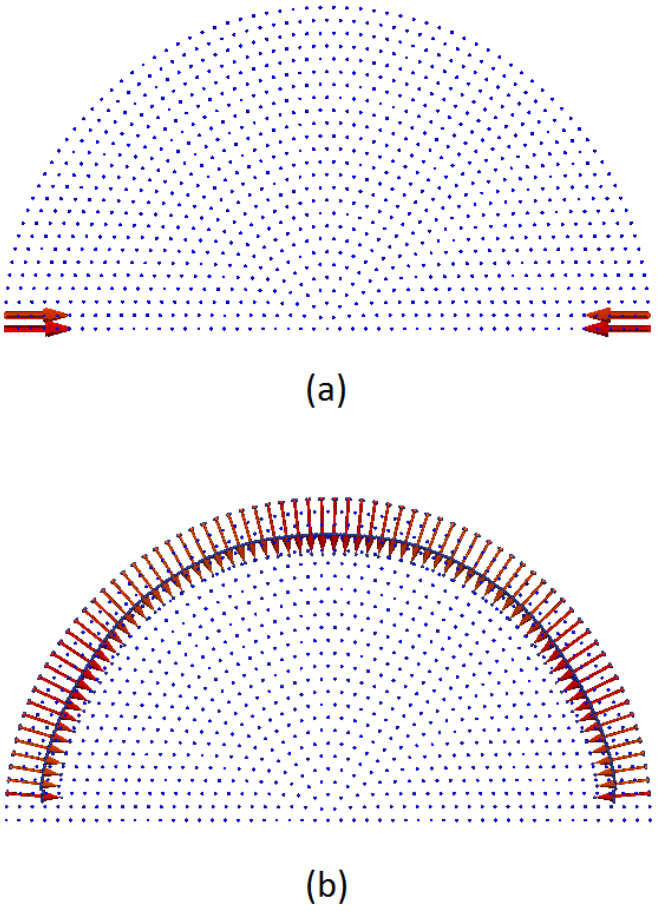

FIGURE 6.11: The descriptive way of how to implement (for simplicity the substrate is not shown here): (a) The modified CLF (b) The modified CSF Model 5.

The main objective of the volume reformation term, δ, in Equation (6.3) is to transform the force per line to the force per unit volume. Following Huber *et al.* [229], they proposed the function δ as:

$$\delta_i = -2\hat{\mathbf{d}}_i \cdot \sum_j V_j(\delta'_j - \delta'_i)\nabla W_{ij}, \tag{6.7}$$

and is similarly implemented here to ensure:

$$\delta'_i = \hat{\nu}_\mathbf{i} \cdot \vec{\mathbf{n}}_i, \tag{6.8}$$

and

$$\delta'_j = \begin{cases} \delta'_i & \text{if } j \in \text{ fluid}, \\ 0 & \text{if } j \in \text{ boundary}. \end{cases} \tag{6.9}$$

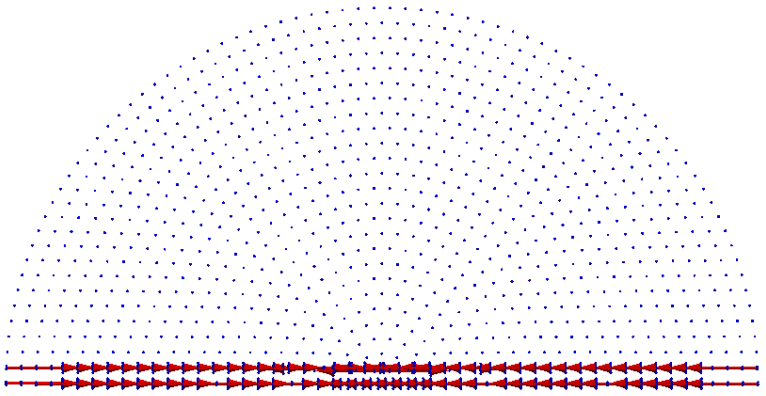

FIGURE 6.12: The descriptive of the unit vector implementation for the fluid particles at a certain close distance to the solid boundary.

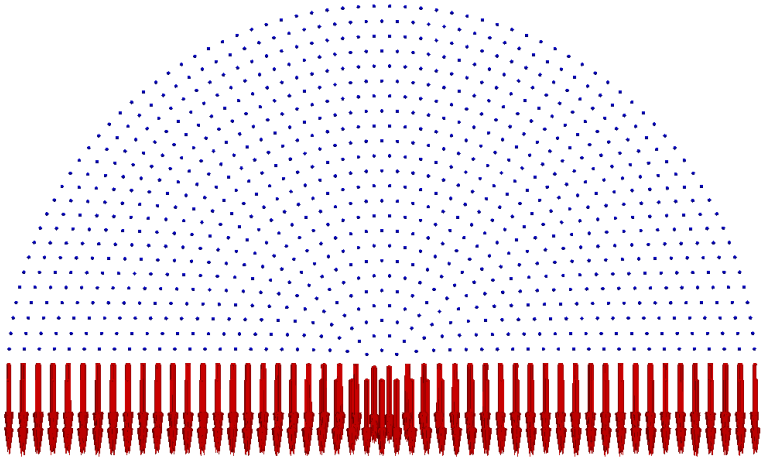

FIGURE 6.13: The descriptive of the distance vector implementation for the fluid particles at small distance from the substrate and where summation is taken only over the solid boundary.

It is be noticed from Equation (6.3) that the static contact angle (α_s) and the coefficient of surface tension (σ) are the only two input parameter needed to control the droplet spreading (contact angle).

6.1.2.1 Droplet spreading using the modified CLF Model

The above proposed CLF model was used to solve droplet spreading with an initial semicircular shape made up of 1420 particles of radius 1.5 mm, placed on a horizontal substrate consisting of 490 particles. The solid substrate is modelled using three dummy layers with the same properties as the fluid particle. The Wendland kernel with search range of $2h$ and smoothing length $h = 1.3dx$ are employed throughout the study with the continuity density approach, Tait equation of state, and all the other

initial parameters shown in Table 6.1. The gravity also in this test case is ignored due to reasons previously given.

Note that, surface tension effect is implemented by using the modified CSF method Model 5 whereas the spreading (contact angle) is implemented using the proposed CLF method Equation (6.3).

TABLE 6.1: Initial parameters of the droplet.

Properties, symbol (unit)	Fluid and Solid Particles
Density, ρ (kg/m^3)	10^3
Pressure, P (Pa)	0
Mass, m (kg)	1.4×10^{-6}
Initial Separation, dx (m)	3.75×10^{-5}
Velocity, $\hat{v}$ (m/s)	0
Viscosity, μ (Ns/m^2)	10^{-3}
Surface tension coefficient, σ (N/m)	0.728

The difficult part of the CLF model implementation is the accurate computation of the dynamic contact angle (α_d). This difficulty is attributed to the fact that the unit surface normal for those surface fluid particles close to the solid substrate computed by default from Equation (6.6) points in the wrong direction, because it involves the summation of all the neighbouring particles as indicated in Figure 6.14 (a) by the shaded green 3/4 of circle.

Based on the starting initial shape of the semicircle drop on the solid substrate, the dynamic contact angle is supposed to be 90° degree, but it is not so from the computations as noticed by the closest surface fluid particle to the solid substrate in the blowout in Figure 6.14 (a). To correct this, a special treatment in the form of correct neighbour list, is given to those surface fluid particles close to the solid substrate as indicated in Figure 6.14 (b) by the shaded green semi-circle. This correction is achieved through the implementation of a simple algorithm developed solely for this purpose (for details of this algorithm see Appendix (C)). This algorithm helped to reconstruct the correct neighbour list especially for surface fluid particle near the solid substrate. Furthermore, conditions such as $\nabla \cdot \vec{\mathbf{r}} < 1.5$ (see Equation (5.10)) and $|\vec{\mathbf{d}}_i| \neq 0$ (see Equation (6.5)) were used to track the surface fluid particles near the solid substrate during the simulation for the adjacent surface and fluid particles. Now, depending on the provided value of static contact angle, the applied CLF force will either drive the

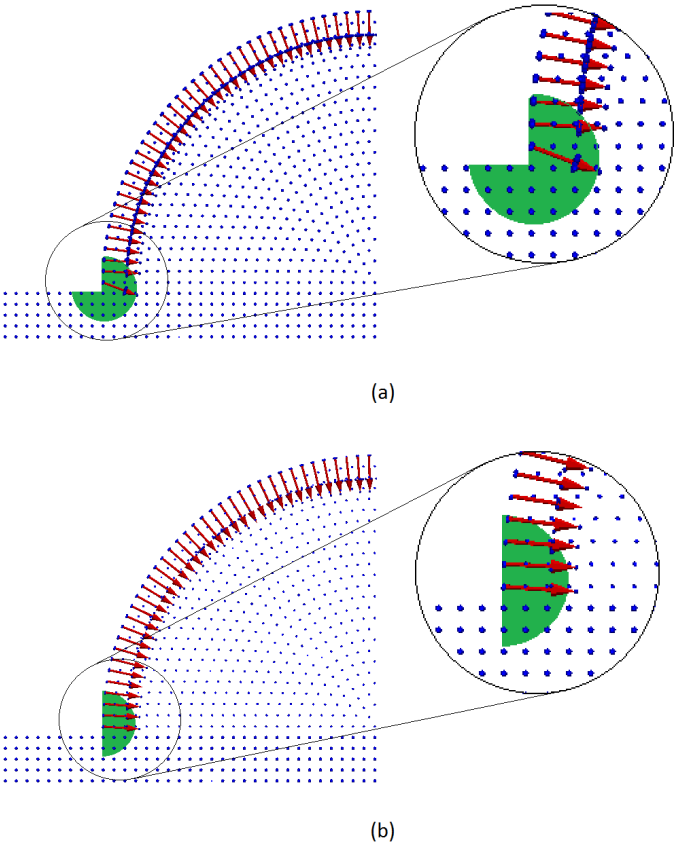

FIGURE 6.14: The descriptive of the unit surface normal implementation for the surface fluid particles at a certain close distance and where summation is taken over all neighbour particles (a) Before correction (b) After correction.

contact line away (see Figure 6.15 (a)) or towards (see Figure 6.15 (b)) the bulk of the fluids.

For either situation, the CLF force will influence the contact line movement until it reaches a stable equilibrium (i.e. $\mathbf{f_c} = 0$ is satisfied). To show the evolution of the various equilibrium contact angles (θ), droplet spreading at various set static contact angle (α_s) are setup at angles 30° to 140° at interval of 10°. Figure 6.16 shows a snapshot of the droplet shape and its spreading after 0.2sec with only 376 fluid particles used. To demonstrate the consistency of this modified CLF model, higher fluid particles resolution of 1001 and 3876 were simulated with the result presented in Figures 6.17 and 6.18, respectively. The contact angle is measured by visual inspection once the simulation has attained stable equilibrium and then the result is printer out and measurement taken. From Figures 6.16, 6.17 and 6.18, it can be seen that the droplet spreading shape is realistic and symmetric on both side with not much different between the equilibrium contact angle and the set static contact

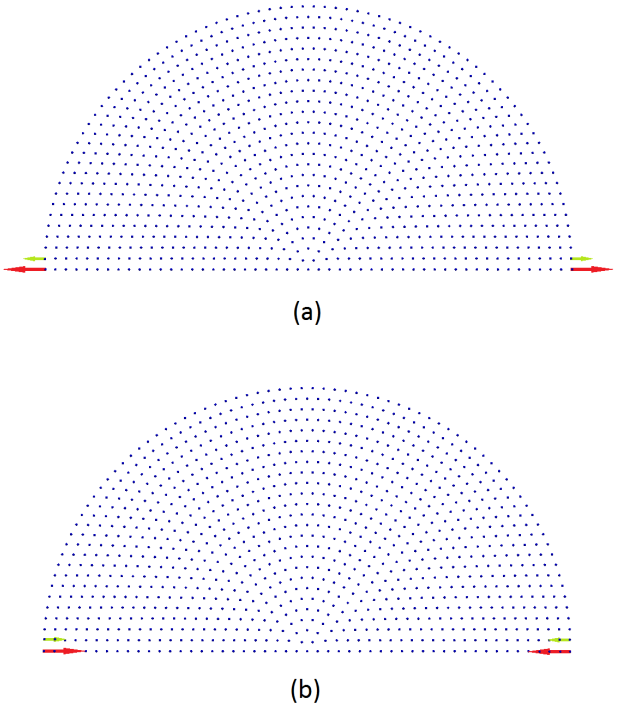

FIGURE 6.15: The descriptive of the CLF force drive direction (a) Static angle smaller than the initial dynamic contact angle (b) Static angle greater than the initial dynamic contact angle.

angles. Figure 6.19 shows the surface profile when these three resolution of particles were compared. The maximum absolute error recorded during the simulation is 10%, shown in Figure 6.20. This error could be due to the single-phase approach adopted compared to Huber *et al.* [229] who has absolute error of 5% in their two-phase CLF model. However, the proposed modified CLF model is more efficient and provides cost savings in terms of computational time and resources compared to its two-phase counter part above.

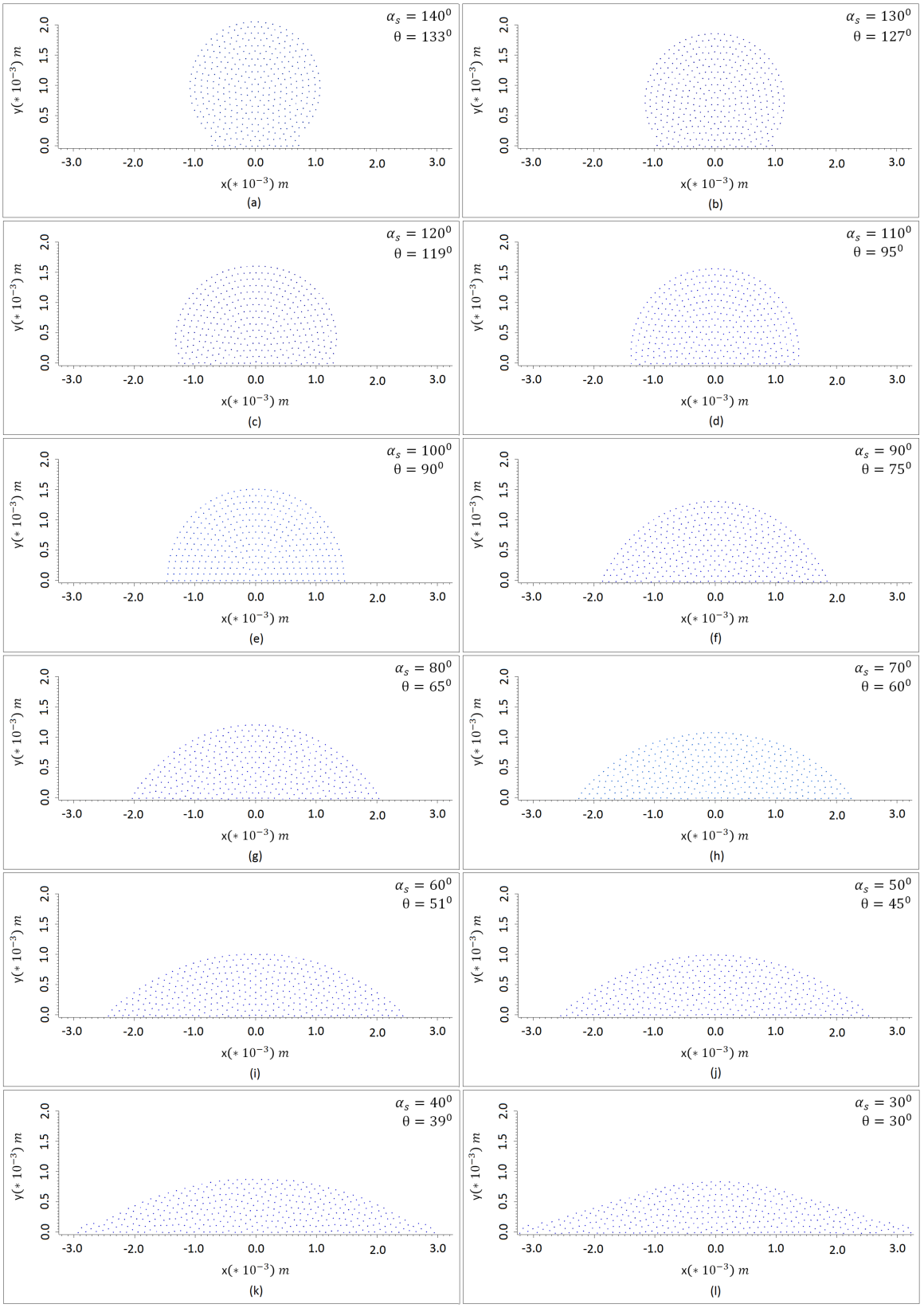

FIGURE 6.16: The droplet evolution of set contact angle (α_s) along with the corresponding visual equilibrium contact angle (θ) for 376 particles resolution.

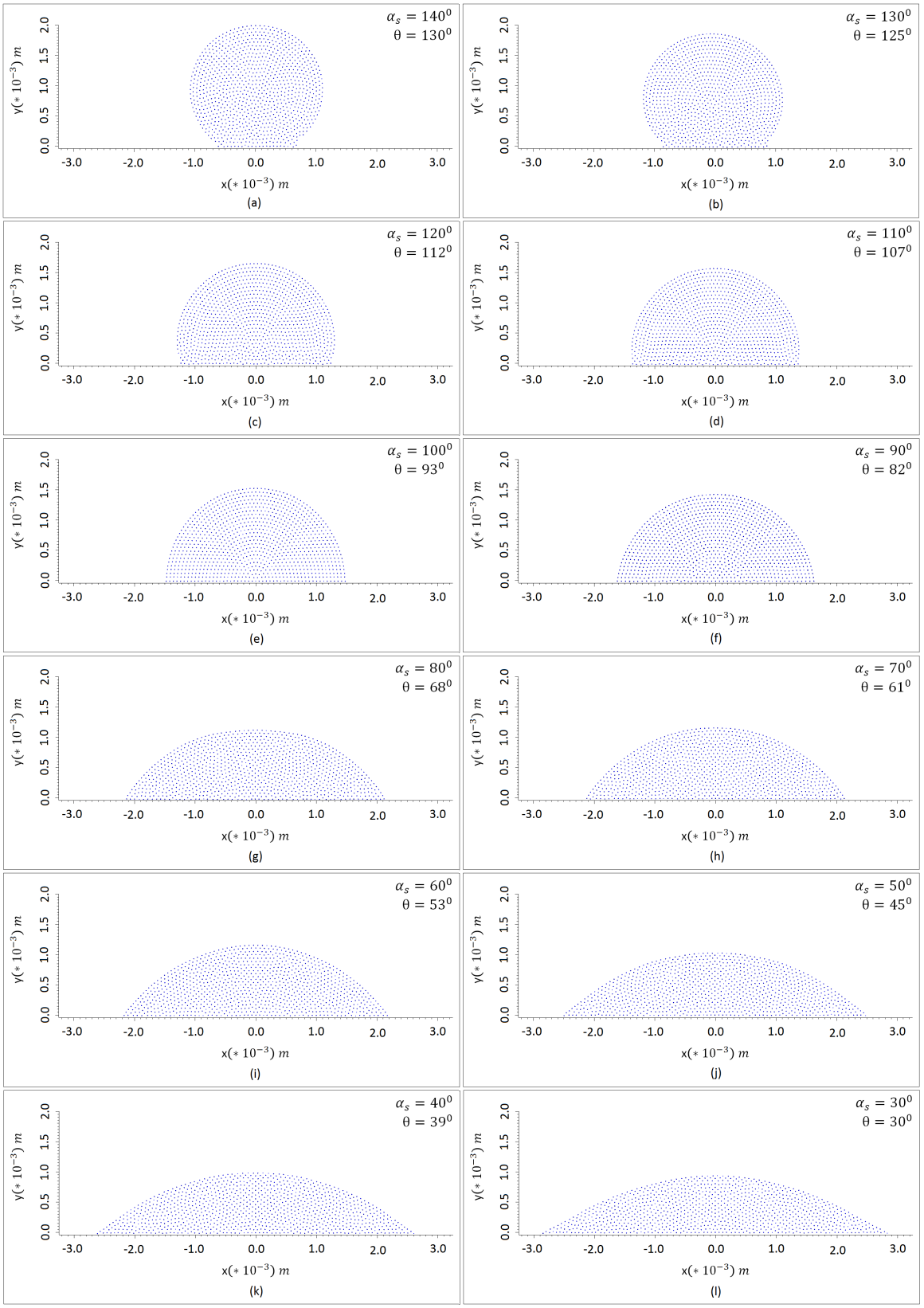

FIGURE 6.17: The droplet evolution of set static contact angle (α_s) along with the corresponding visual equilibrium contact angle (θ) for 1001 particles resolution.

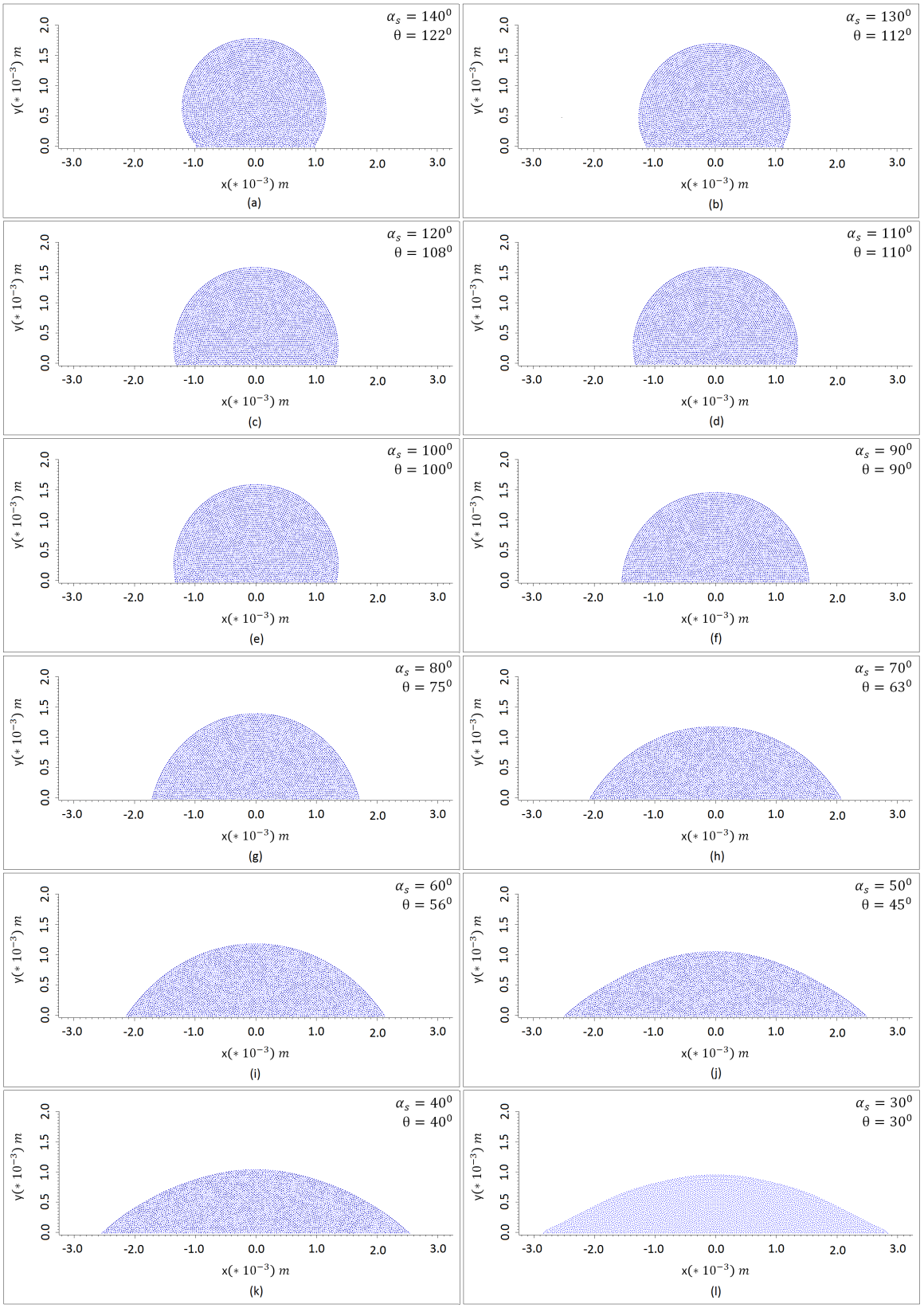

FIGURE 6.18: The droplet evolution of set static contact angle (α_s) along with the corresponding visual equilibrium contact angle (θ) for 3875 particles resolution.

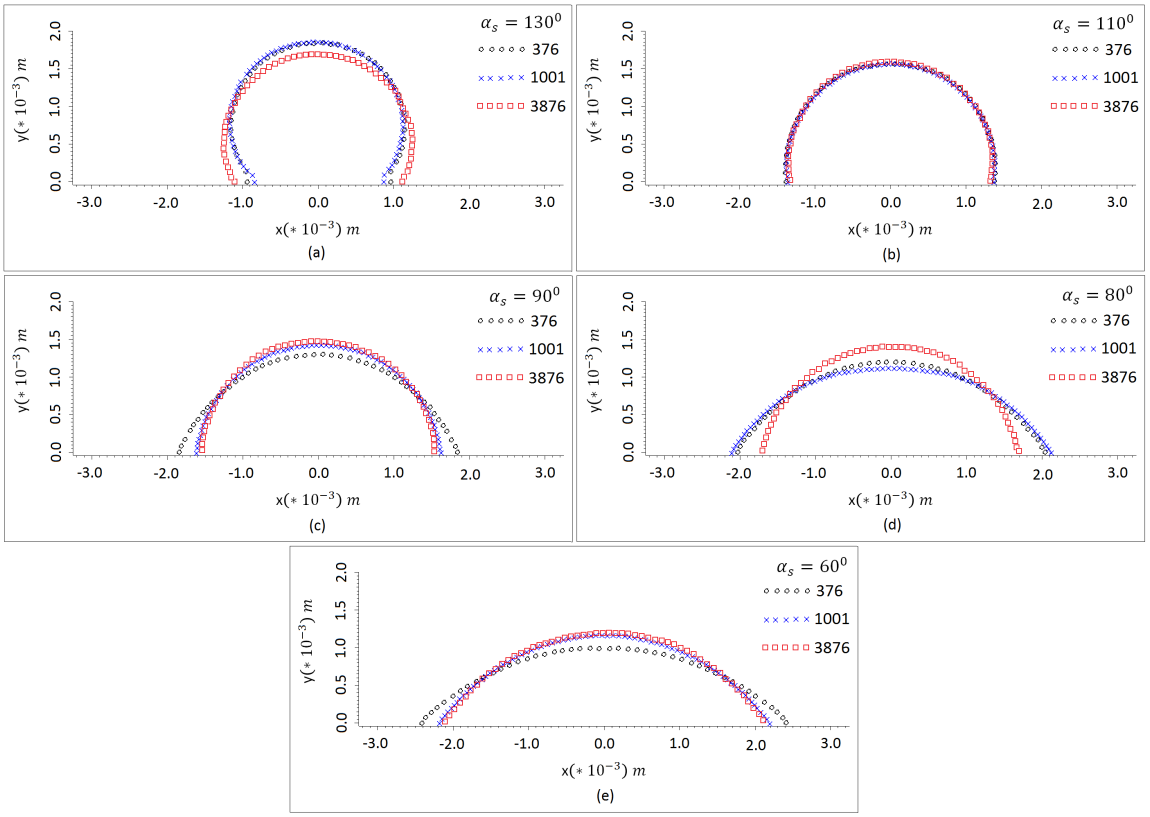

FIGURE 6.19: The droplet surface profile of some selected set static contact angle (α_s) for 376, 1001 and 3876 particles resolution.

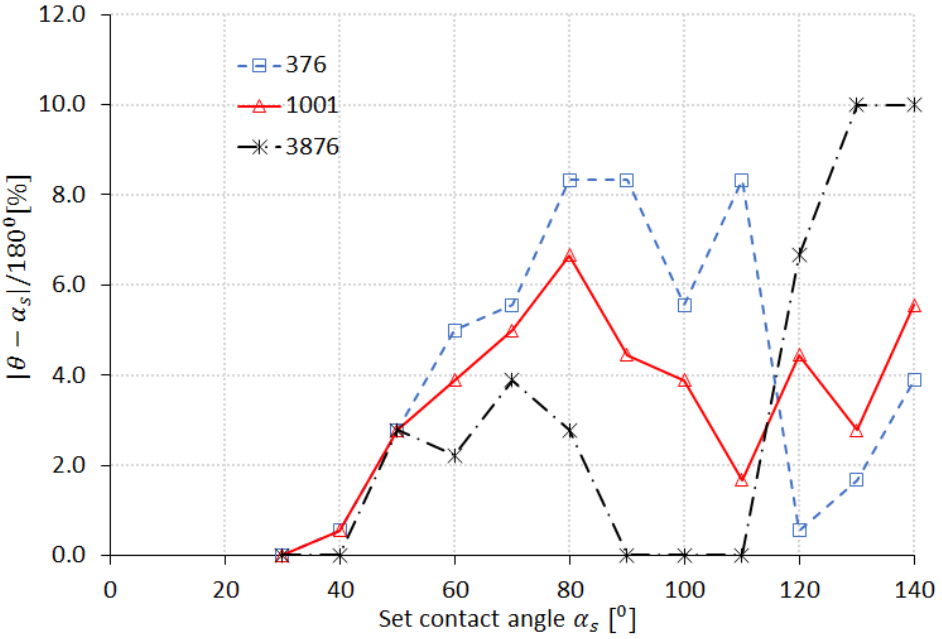

FIGURE 6.20: The droplet absolute error against set static contact angle (α_s) for 376, 1001 and 3876 particles resolution.

6.1.3 Contact Angle with Disjoining Pressure Model

This adopts the method used by Schwartz [83], who investigated thin film flow over heterogeneous substrates using the lubrication approximation (mesh based) approach by controlling the contact angle with a disjoining pressure model. This disjoining pressure model however, is based on the hypothesis that a very thin precursor film paves the way in front of the film to spread as if the surface is pre-wet. The existence of this precursor film has been described experimentally for various vapour/liquid/solid systems when the liquid totally wets the substrate. A more detail experimental review can be found in de Gennes [56]. The asymptotic thickness H* of the precursor film depends largely on the interaction ability of the vapour/liquid/solid systems and it is affected by the stability rules reported in Mitlin [230]. However, a uniform film cannot exist outside of this stability criteria, thus leading to the formation of holes due to de-wetting of the substrate. Deryagin [231] was the first to report that the gradient of the disjoining pressure as a result of the long-range interaction forces is responsible for the movement of the contact lines. Although, the challenges associated with this model is the need to derive the exact form for the disjoining pressure for each particular vapour/liquid/solid systems, however, Teletzke [232] was able to come up with a disjoining pressure term that is applicable to most fluid-solid interactions. By incorporating electrostatic, molecular and structural forces, he discovered that the disjoining pressure can be represented as:

$$\Pi(H) \quad = \quad \sum_{1}^{4} \frac{A_n}{H^n}, \tag{6.10}$$

where the constant A_n is system-dependent.

Following to Sellier [233], the disjoining pressure model that will be used in the present work is given as:

$$\Pi(H) \quad = \quad B\left[\left(\frac{H^*}{H}\right)^n - \left(\frac{H^*}{H}\right)^m\right], \tag{6.11}$$

where B, n and m are positive constant with $n > m > 1$. Note that the first and second components on the right side of Equation (6.11) represent the solid-liquid attraction and solid-liquid repulsion respectively. H^* is the precursor film thickness, which is generally believe to be within the range of 1 to 100nm according to literature [82, 234]. Various values of n and m has been reported in literature, especially in the work of Teletzke [232] and Churaev and Sobolev [235] who used the values (3,

2), while Mitlin and Petviashvili [236] used the values (9,3). Figure 6.21 represent the normalized disjoining pressure with (n, m) having the values (9, 3) and (3, 2) respectively.

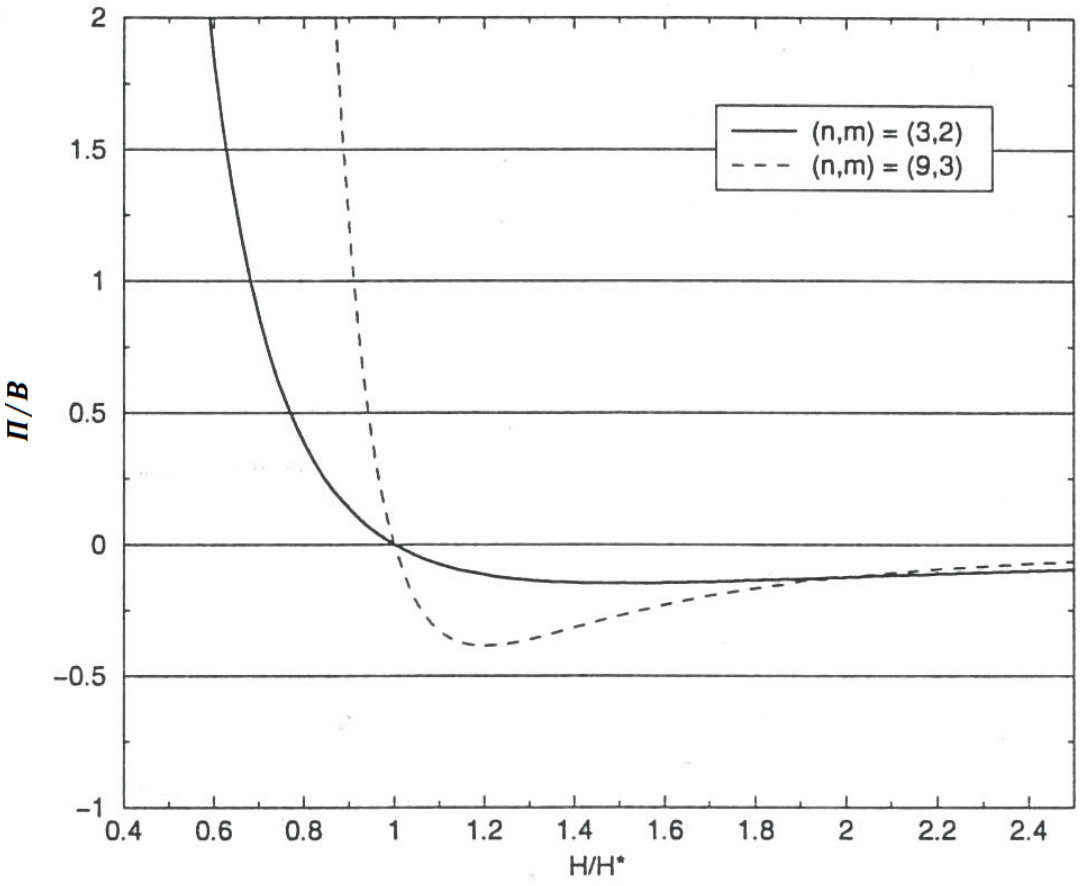

FIGURE 6.21: Normalised Disjoining Pressure for (n, m) = (9, 3) and (n, m) = (3, 2) [233].

Figure 6.21 reveals that at the the precursor film thickness H^*, there is a minimum single stable energy since, if $H^* > H$, the positive pressure will act to restore the film thickness H^*, while if $H^* < H$, the negative pressure will have the same effect.

According to Schwartz's [83] formulation, the constant B is derived from the force balance in the contact line zone when the contact line reaches an equilibrium state. It is further assumed that B will remain constant even during the contact line movement. A detailed derivation of the constant B according to Schwartz's [83] is presented in Appendix D with the final form given as:

$$B = \frac{(n-1)(m-1)}{H^*(n-m)}\sigma(1-cos\alpha_s), \tag{6.12}$$

where α_s is the static contact angle.

In order to implement this disjoining pressure model in the present work, part of the solid substrate in the SPH formulation is assumed to be the precursor film, since, it carries the same properties as the fluid. Now, because the spreading rate of the droplet depends on the precursor film thickness H^*, which is arbitrary [233] and defined as $\varphi \times dx$, this gives the freedom to set part of the solid substrate layers to H^* in the simulation in order to control the spreading rate. For the same reason, the static contact angle is set to say 90° and then tuned the, φ, value until the simulation get to an equilibrium state where the equilibrium contact angle θ is $\approx 90°$ qualitatively and quantitatively through virtual inspection. Once, this H^* has been determine at this particular contact angle, it now serve as a reference that can be use for simulating all other static contact angle. Figure 6.22 shows the schematic representation of the droplet and the solid substrate (precursor film) using this disjoining pressure model in SPH formulation.

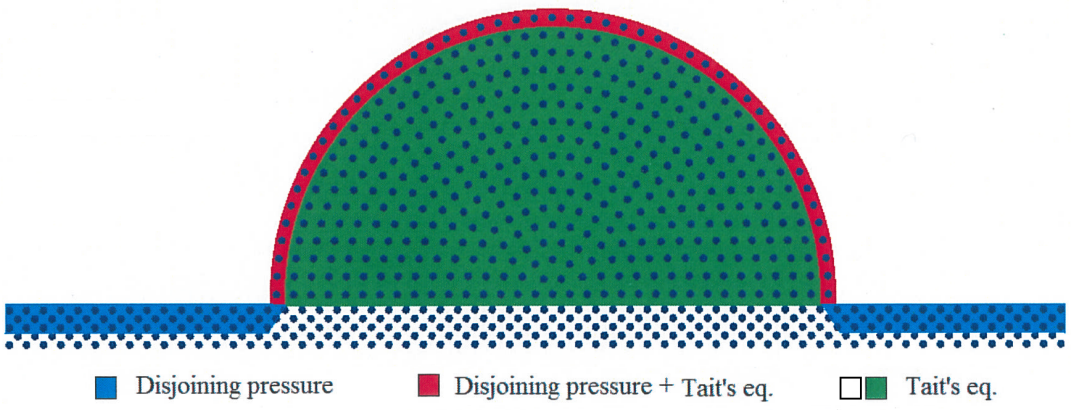

FIGURE 6.22: Schematic representation of the disjoining pressure model when implemented in SPH.

From Figure 6.22, it can be seen that the disjoining pressure can be applied to any number of layers of the solid substrate on both sides of the droplet to initiate the spreading. However, in the SPH simulation, five layers of solid substrate were used due to the fact that it gives better spreading rate and droplet stability (see Figure 6.22 where the disjoining pressure is applied to the solid particles highlighted in blue coloured squares). Furthermore, the disjoining pressure is also applied to all the free-surface fluid particles (see Figure 6.22 highlighted with red coloured squares for the surface fluid particles) while finally applying the Tait's equation to all the fluid particles of the droplet and the remaining solid substrate particles (see Figure 6.22 highlighted with green coloured squares for the bulk fluid particles and white coloured

squares for the remaining solid substrate particles). The solid substrate particles were generated in a staggered form in order to improve accuracy especially at large static contact angle.

6.1.3.1 Droplet spreading using the Disjoining Pressure Model

An initial semi-circular droplet made up of 426 particles with a radius of 1.5 mm is placed on a staggered particle arrangement on a horizontal substrate make up of 490 particles. The solid substrate were modelled with five dummy particles layers with the same properties as the fluid particle. The Wendland kernel with search range of $2h$ and smoothing length $h = 1.3dx$ is used. The continuity density approach and Tait equation of state are used. All other initial parameters are provided in Table 6.2.

During the simulation, surface tension effect were implemented by using the modified CSF method in Model 5 whereas the spreading (contact angle) is implemented using the proposed disjoining pressure model Equation (6.11) in the absent of gravity reason given previously.

TABLE 6.2: Initial parameters of the droplet.

Properties, symbol (unit)	Fluid and Solid Particles
Density, ρ (kg/m^3)	10^3
Pressure, P (Pa)	0
Mass, m (kg)	1.4×10^{-6}
Initial Separation, dx (m)	3.75×10^{-5}
Velocity, $\hat{v}$ (m/s)	0
Viscosity, μ (Ns/m^2)	10^{-3}

Starting from a semi-circular droplet ($\alpha_s = 90°$), several trials were performed to ascertain the required precursor film thickness for the given set of parameters of the above droplet. It was found that using a precursor film thickness set within the neighbourhood of $H^* = 2.8dx$ gives a contact angle (θ) of 90° at stable equilibrium. Once, this is done, the simulation is now carried out for cases with smaller and bigger set static contact angles, shown in Figure 6.23.

As it can be seen from Figure 6.23, there is a noticeable gap between the solid substrate and the droplet, which is more pronounced especially in Figure 6.23 (a) to (c). Also, there is a wide margin between the set static and visual equilibrium contact angle

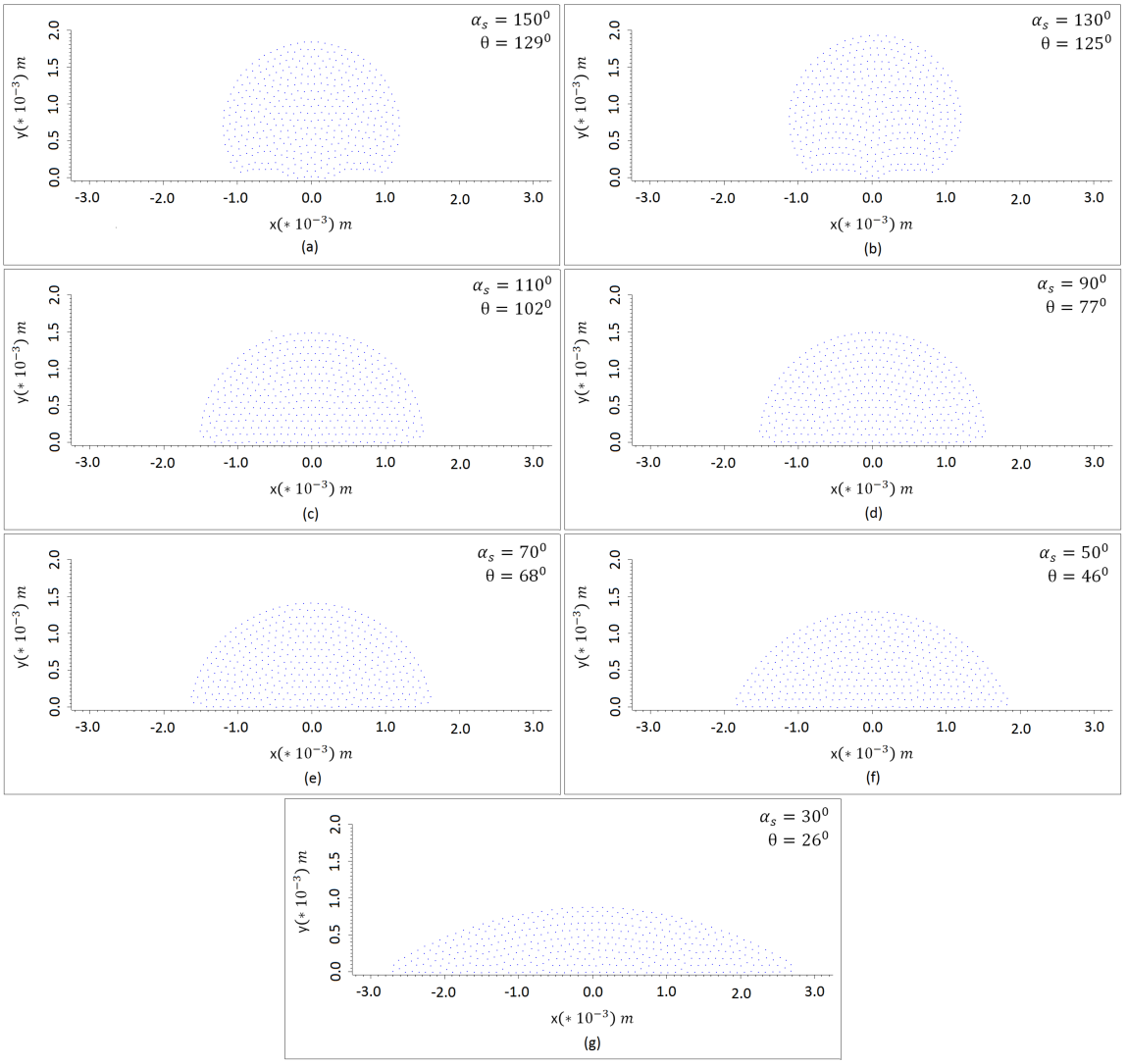

FIGURE 6.23: The droplet evolution of set static contact angle (α_s) along with the corresponding visual equilibrium contact angle (θ) for 426 particles resolution with the precursor film thickness set at $H^* = 2.8dx$.

especially when $\alpha_s > 90°$. To do a convergence study, droplet resolutions of 1001 and 1926 particles were used with the results shown in Figures 6.24 and 6.25. With these higher resolutions, this gap noticed previously is reduce as observed in Figure 6.24 (a) to (c) and Figure 6.25 (a) to (c). However, the precursor film thickness H^* needs to be adjusted to $3.1dx$ and $3.5dx$ for particles resolution of 1001 and 1926 respectively, so as to achieved the set static contact angle to correspond to the equilibrium contact angle. To further illustrate the effect of increasing the particle resolution, Figure 6.26 shows the surface profile of these three particles resolution, where it is clear that higher particle resolution gives better accuracy and hence more smoother equilibrium contact angle.

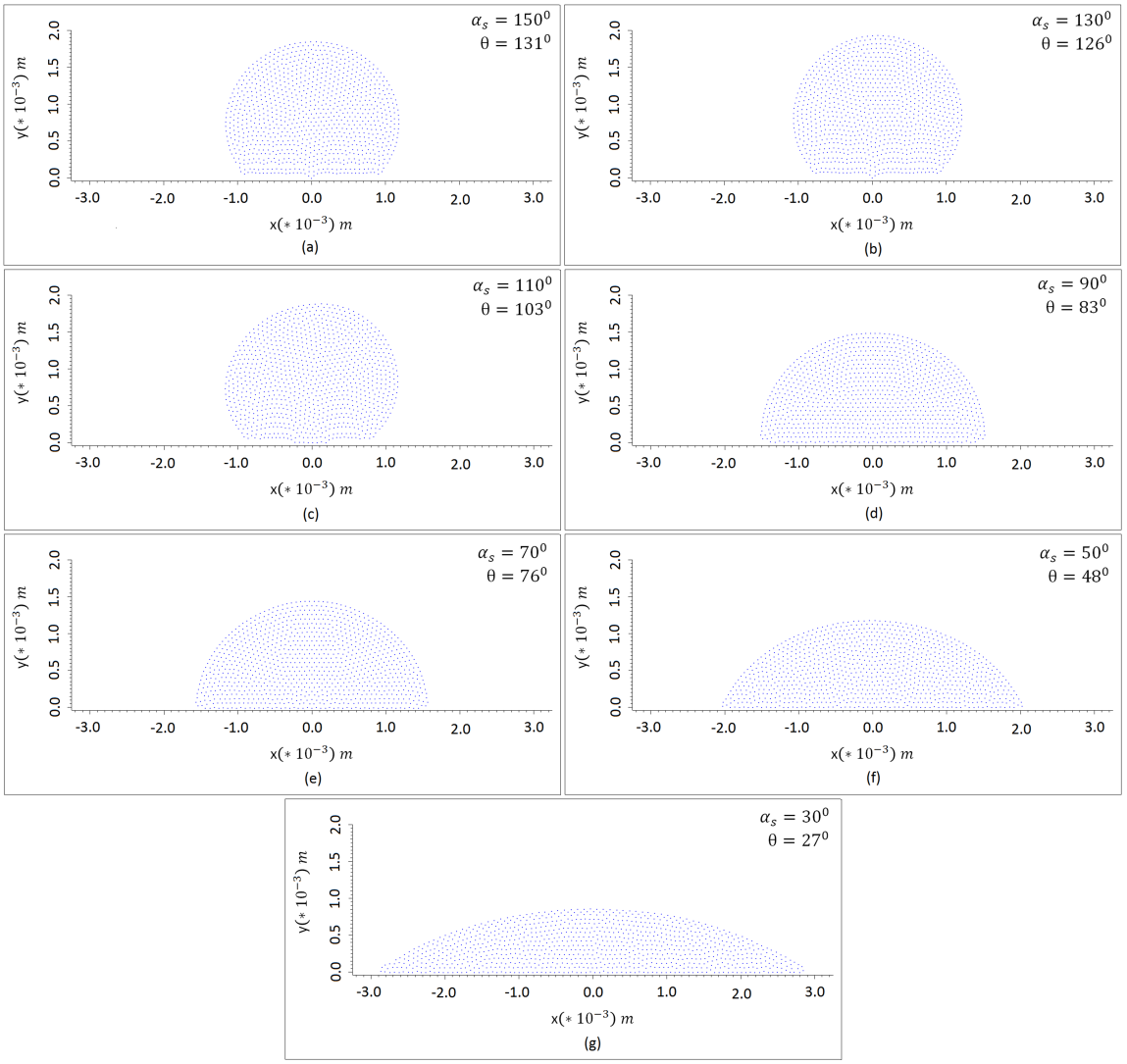

FIGURE 6.24: The droplet evolution of set static contact angle (α_s) along with the corresponding visual equilibrium contact angle (θ) for 1001 particles resolution with the precursor film thickness set at $H^* = 3.1dx$.

Furthermore, as the particle resolution increases, the equilibrium contact angle (θ) also increases toward the set static contact angle (α_s) such that ($\theta \approx \alpha_s$) as shown in Figure 6.26. In general, the proposed disjoining pressure model worked better within the range of 30° to 130° static contact angle, as the droplet equilibrium constant angle is more accurate and stable within these range. The major advantage of this model when it is compared with the lubrication approximation approach, is that it can be used to investigate large contact angles. Other advantages of this model are that, it is relatively easy to implement without the need to track the contact line and correct the surface normal like it is required in the CLF model. To show the relationship between the particle resolution and precursor film thickness, Figure 6.27 shows that the particle resolution is directly proportional to H^*, that is varies linearly.

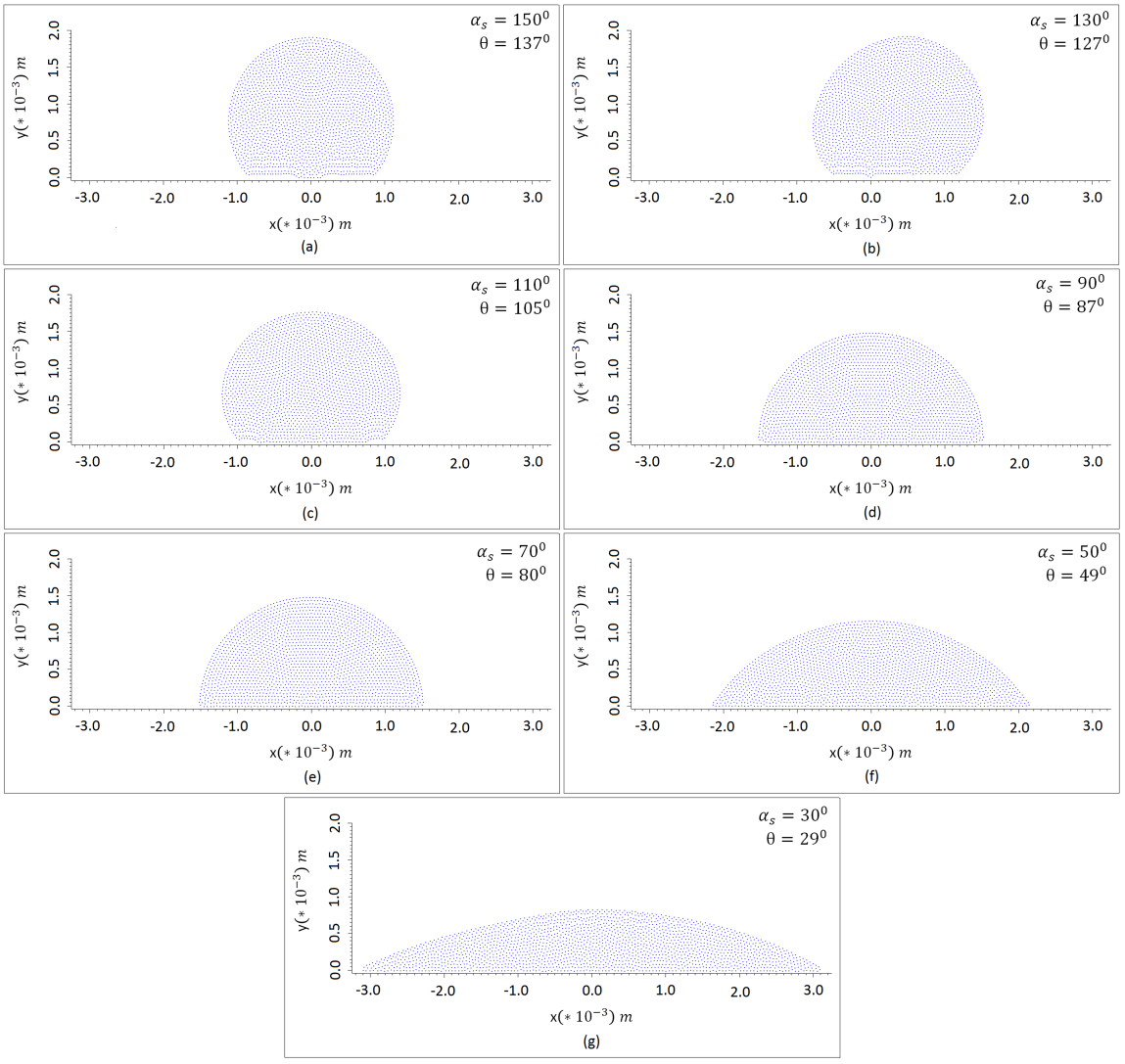

FIGURE 6.25: The droplet evolution of set static contact angle (α_s) along with the corresponding visual equilibrium contact angle (θ) for 1926 particles resolution with the precursor film thickness set at $H^* = 3.5dx$.

6.1.4 Tanner's Law

To investigate the accuracy of these models, the spreading rates from the three approaches are compared with that of Tanner's law [237], given as:

$$H \sim t^{-1/\alpha}, \tag{6.13}$$

where the droplet height (H) is a function of time (t) with the exponential constant $\alpha = 7$ for a two-dimensional problem.

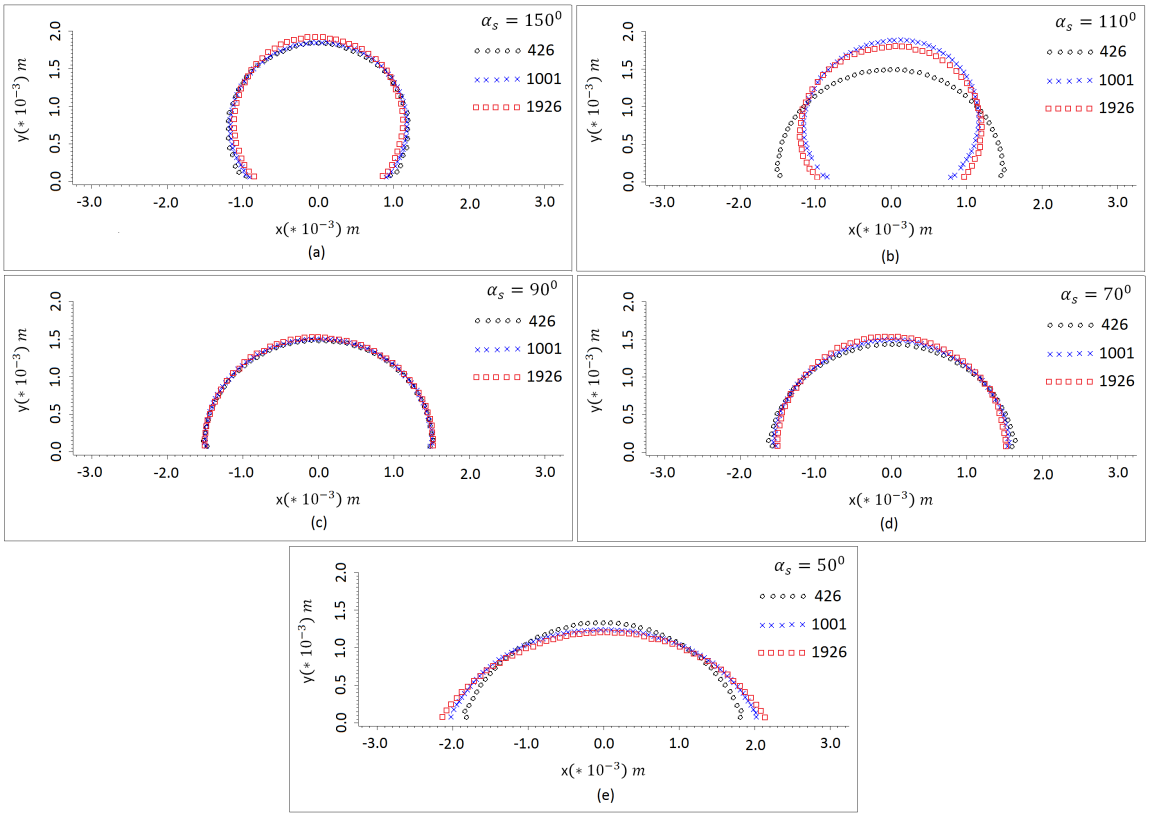

FIGURE 6.26: The droplet surface profile of some selected set static contact angle (α_s) for 426, 1001 and 1926 particles resolution.

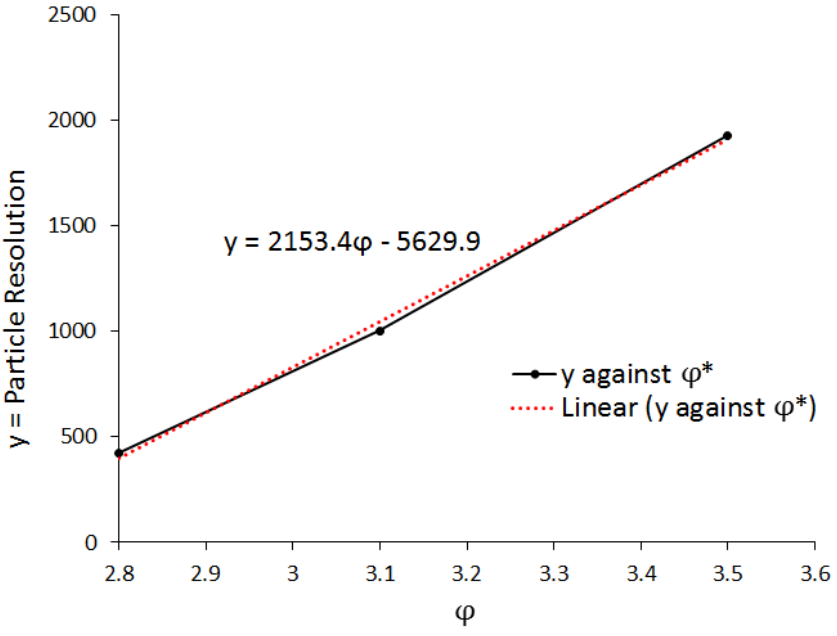

FIGURE 6.27: Showing the relationship between the resolution and the precursor film thickness tuning parameter φ.

Furthermore, an experiment that was validated by Lelah and Marmur's [238] showed that the droplet spreading height as a function of time is given by:

$$H \sim t^{-1/\beta}, \tag{6.14}$$

where the exponential constant parameter is in the range $0.16 \leq 1/\beta \leq 0.32$.

To carryout the simulation, the spreading for the three cases were studied by allowing the droplet to spread from a contact angle of 60° to 30° upon which the height as a function of time is observed. Figures 6.28, 6.29 and 6.30, show the relationship that exist between the height as a function of time with the exponential parameter constant having $1/\alpha = -0.373, -0.131$ and -0.137 for Tartakovsky, CLF and disjoining pressure models, respectively. These exponential parameter constant are in very good agreement with that of Tanner's law especially for the CLF and disjoining pressure models. Although, the IIF model fall outside Tanner's law, but considering the experimental work of Lelah and Marmur's [238], it can still be said to be acceptable. Also it is the only approach among the others that can simulate droplet with larger contact angle and still maintain the stability of the droplet.

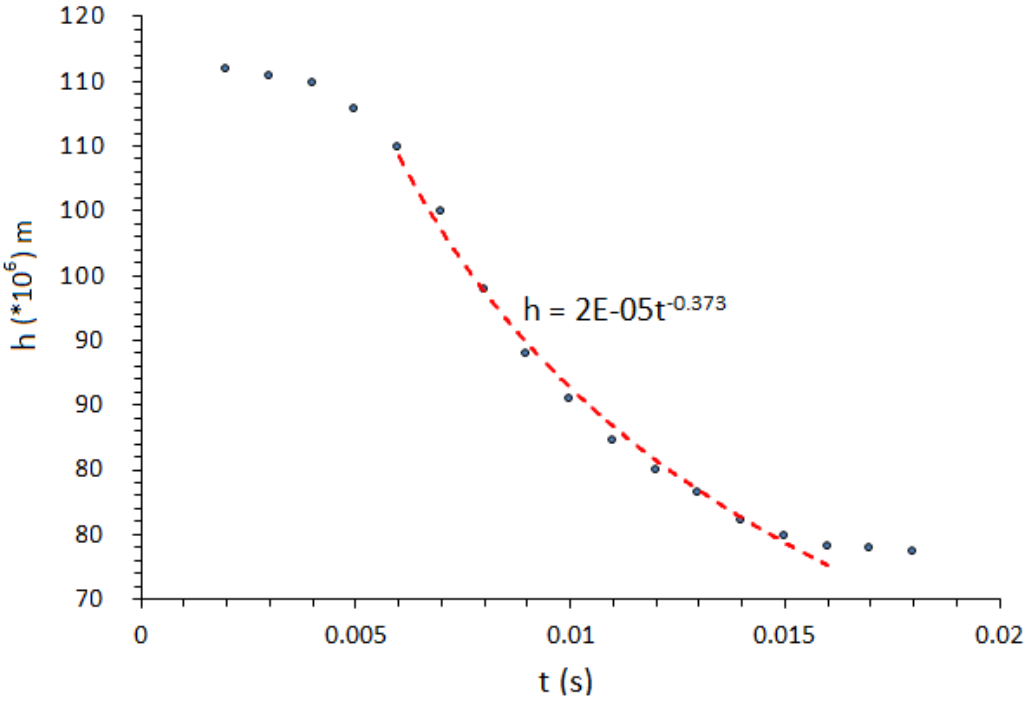

FIGURE 6.28: Showing the relationship between the height (h) as a function of time (t) using the IIF model.

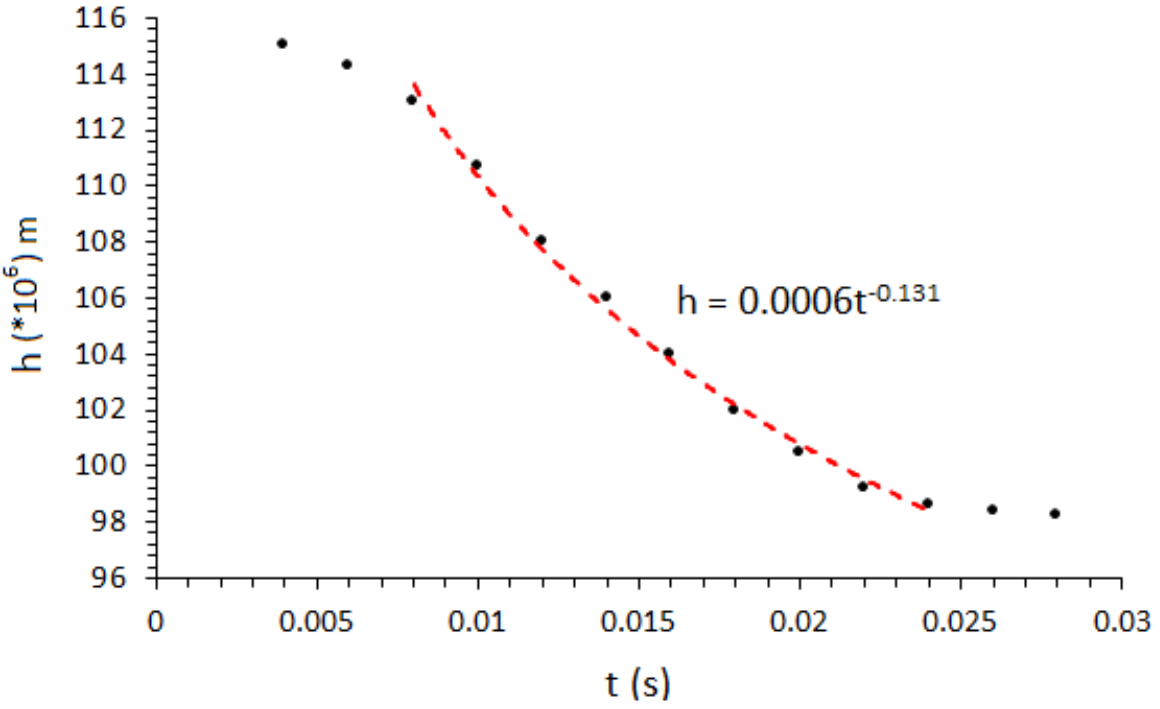

FIGURE 6.29: Showing the relationship between the height (h) as a function of time (t) using the CLF model.

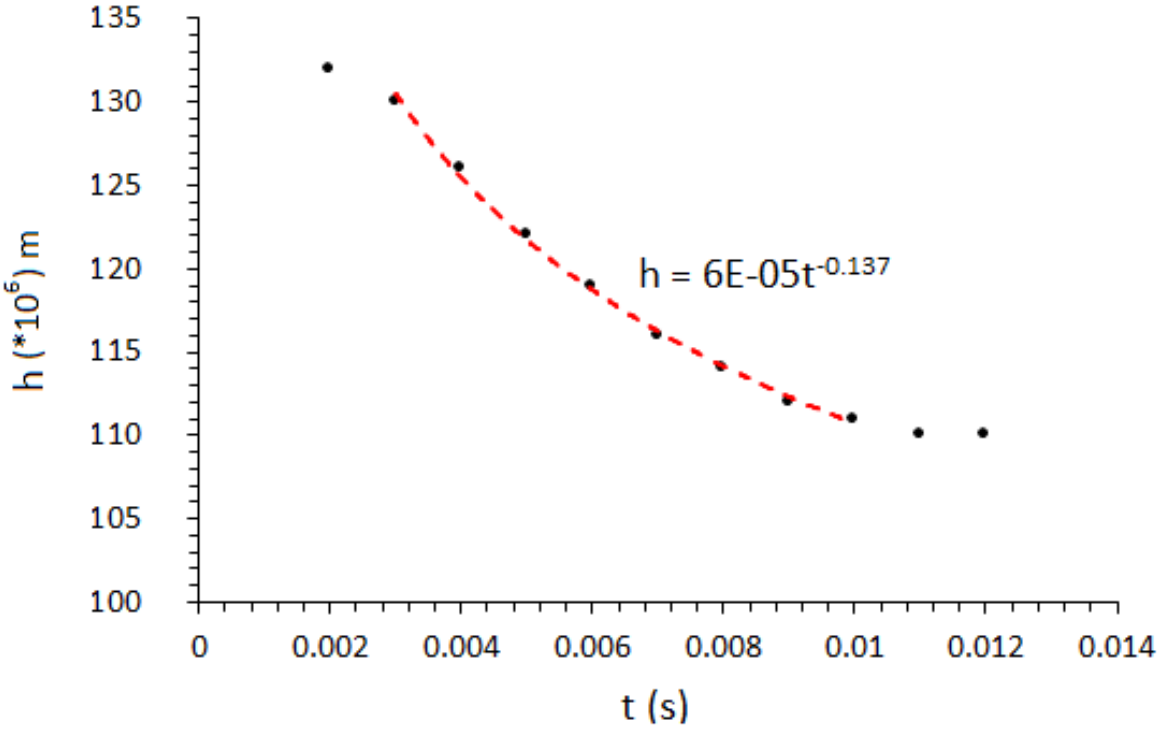

FIGURE 6.30: Showing the relationship between the height (h) as a function of time (t) using the disjoining pressure model.

Chapter 7

Droplet and Thin Film Migration

> "Life is like riding a bicycle. To keep balance, you must keep moving."
>
> Albert Einstein.

7.1 The Phenomenon of Contact Angle Hysteresis

Contact angle hysteresis (θ_{Hys}) which is of great important in surface energy, can be defined as the difference between receding (θ_R) and advancing (θ_A) contact angles, and this difference can be as high as 50° [239]. It has becomes important in recent times in superhydrophobic and self-cleaning surfaces [240, 241], as a small gradient (the angle the substrate need to be tilt in order to move the droplet) causes self-cleaning to occur has the droplet flow down the slope. They are also important in others areas such as coating, adsorption at solid/liquid interface and intrusion of water into porous media. It occurs due to the large range of "metastable" states which are observed when the liquid moves through the surface of a solid at the vapor/liquid/solid interface. Due to the free energy barriers that occur between these metastable states, it is impossible to measure the true equilibrium contact angle in real time. For a "perfect" surface that is wetted by a pure liquid, contact angle hypothesis forecast one and only one thermodynamically stable contact angle [242]. However, there is no perfect surface found in the real world [242], hence to fully characterize any surface, it is imperative

to measure both receding and advancing contact angles and then report the difference as contact angle hysteresis.

7.2 Controlling Contact Angle Hysteresis

The phenomenon shown above is similar to the Marangoni effect [25, 26] and is responsible for the spontaneous mechanical agitation of the droplet. Basically, there are two types of self-agitation, namely thermal and chemical Marangoni convection which have been investigated extensively. Like the chemical Marangoni convection where the variation of interfacial tension under isothermal conditions result in spontaneous mechanical movement due to the reactive liquid droplet placed on the substrate. The motion of this phenomena has been reported theoretically [56, 243] and verified experimentally [244, 245].

Contact angle hysteresis can be studied at difference substrate orientation, which could be horizontal, inclined at varying angles, circular, stair-like. For the purpose of this Chapter, only the horizontal, stair-like and inclined substrate orientation will be presented in order to reproduce comparable qualitative results of an experiment conducted by Sumino *et al.* [1] of the motion of oil droplet on an horizontal and stair-like glass substrate coated with chemical. In the case of the stair-like substrate, the model is new in SPH and aims at showcasing the capabilities of the methodology. Also, to showcase the potential of simulating dynamic interplay of gravity dominated flow, the results from the incline substrate are compared qualitatively against an experiment conducted by Schmuki and Laso [61] who worked on the rivulet flow stability at varying inclination angles.

7.2.1 Droplet movement on a horizontal substrate

The purpose of this section is to study the effect of contact angle hysteresis of droplets on horizontal substrate. In this study, the IIF method was selected to control the contact angle hysteresis due to its simplicity and straightforwardness, couple with the ease of implementation into the solver compared to the CLF and disjoining pressure methods. Also, for the IIF method, there is no need to track the interface particles as this lead to more computational cost/time. Furthermore, tracking the interface particles may give rise to inaccurate results due to the complex movement of the

droplet, thus leading to numerical noise resulting from clustering as is been observed in the case of CSF and CFL methods. In addition, it is possible to simulate bigger stable static contact angle of up to 180° using the IIF method while with the disjoining pressure and CLF methods, stable static contact angle are limited to less than or at maximum 130° (for details see Chapter 6).

For the simulation, a 3mm × 3mm initial square shape droplet was generated on a horizontal substrate with the same static contact angle on both sides in the same manner as the one shown in Figure 6.5, but with a longer substrate while using the same operating physical properties as in sub-section 6.1.1.

For the two-dimensional droplet, the s_{sf} for both advancing and receding strength are set equidistance (symmetric interaction) from the centre of the droplet as shown in Figure 7.1 (a) (substrate not shown), by computing the average particles position. Once this is done, the droplet begin to spread until it reaches its equilibrium state where the static equilibrium contact angle (θ) is maintained (see Figure 7.1 (a)). At this stage in the simulation, the s_{sf} strength at one side of the droplet is varied (asymmetric interaction), thus making the droplet move towards the side with a smaller contact angle as shown in Figure 7.1 (b); the bigger contact angle is called receding angle (θ_R) and the smaller contact angle is called advancing angle (θ_A). This movement is due to the fact there is an unbalanced force which propels the droplet resulting from the difference in surface tension pressure at both sides of the triple point (see Figure 7.1 (b)).

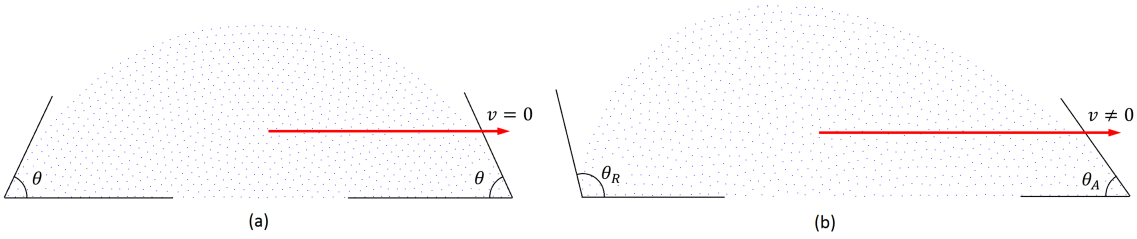

FIGURE 7.1: (a) Showing droplet at equilibrium static contact angle with $\vec{v} = 0$ (b) Contact angle hysteresis where the droplet move with $\vec{v} \neq 0$ observed by varying the advancing angle.

By setting the receding angle at $\theta_R = 150°$ and varying the advancing angle from $\theta_A = 30°$ to 150° at an increment of 10°, it is noticed that the droplet begin to move with a velocity when the difference between (θ_R - $\theta_A = 10°$). This position is supported by the experimental work of Gao and McCarthy [246] and Chaudhury and Whitesides [245] who reported that water droplet propel when θ_{Hys} is ≈ 10°. During

the simulation, the droplet velocities initially increases gradually, but later becomes relatively constant at time $t = 0.25s$ as the contact angle hysteresis increases as shown in Figure 7.2 (a).

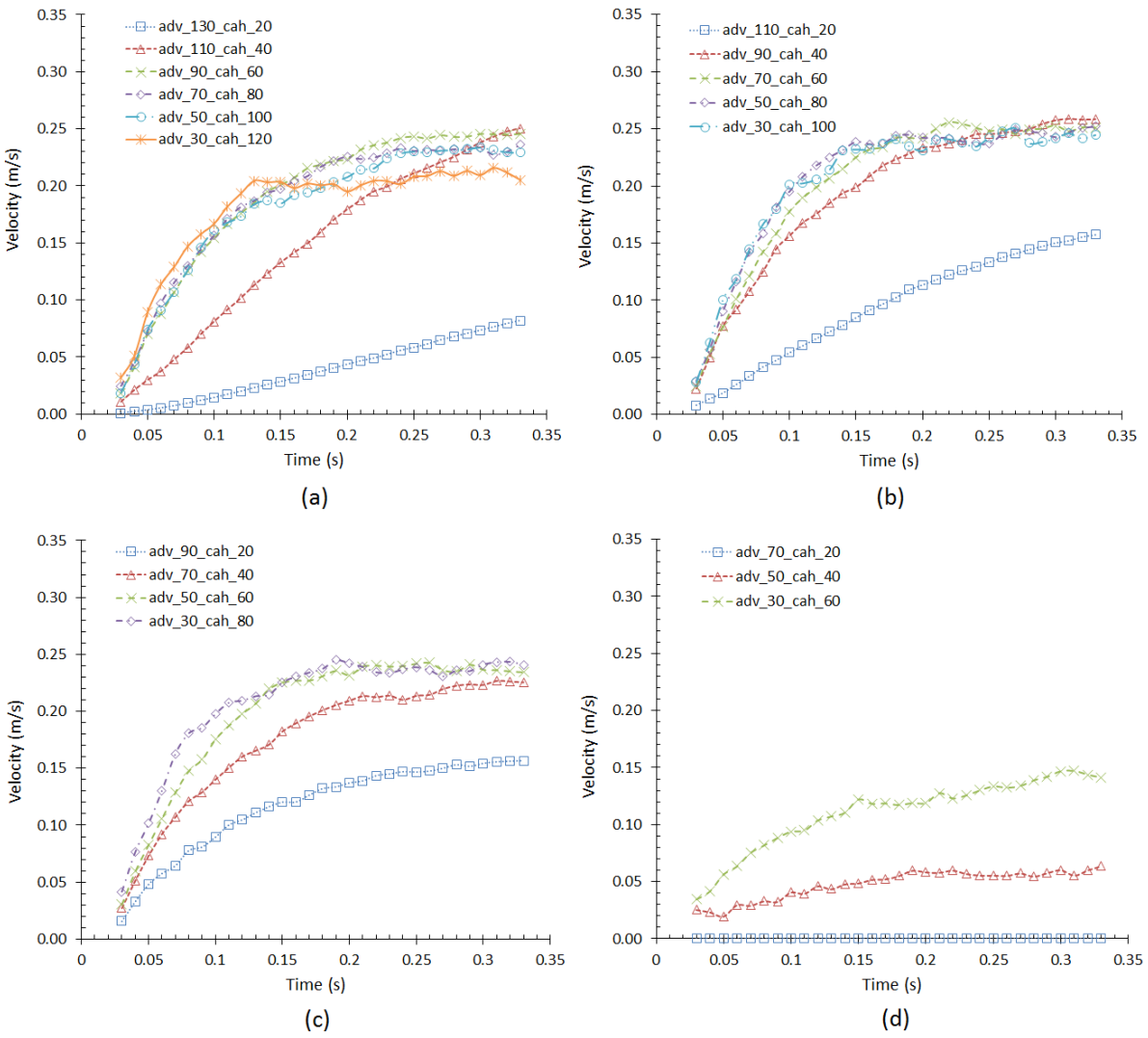

FIGURE 7.2: Showing the average velocity against time for (a) $\theta_R = 150°$, (b) $\theta_R = 130°$, (c) $\theta_R = 110°$ and (d) $\theta_R = 90°$, with varying advancing angle (θ_A), thus leading to increase hysteresis (θ_{Hys}). *Note that θ_A and θ_{Hys} represent (adv) and (cah).

Again, by setting the receding angle to $\theta_R = 130°$ and $\theta_R = 110°$ with the corresponding advancing angle varying from $\theta_A = 30°$ to $130°$ and $\theta_A = 30°$ to $110°$ respectively, with the advancing angle in both cases incremented as before, the same trend is observed as the previous as shown in Figures 7.2 (b), and (c) respectively. However, with the receding angle set at $\theta_R = 90°$ and the advancing angle varied from $\theta_A = 30°$ to $90°$, with the same incremental advancing angle as before, the same trend is also observed as the previous as shown in Figure 7.2 (d), but with the droplet not

moving when the advancing angle was 70° as indicated in Figure 7.2 (d). This may have been caused by the very low centre of mass of the droplet when the receding angle is $\theta_R = 90°$ and the advancing angle is 70°, couple with the low hysteresis value of ($\theta_{Hys} = 20°$) which represent the drag force. Once this hysteresis increases, the droplet begin to move, though slower than the previous, but still maintain a relatively constant velocity at around time $t = 0.25s$. In all the cases presented as shown in Figure 7.2, there were slight fluctuation in these velocities especially at cases with high contact angle hysteresis which may be due to the higher drag on the droplet, couple with the high centre of mass.

Using the same logic as above, a droplet of the same size is simulated with periodic motion where the receding and advancing contact angles are set at $\theta_R = 95°$ and $\theta_A = 55°$, respectively. At interval of $t = 0.08s$, these angles are interchange so as to change the direction of droplet movement. This test case is performed to showcase the future insight of the capabilities of SPH methodology compared to the experimental work by Sumino *et al.* [1]. From the simulation, the results are in good agreement by the velocity profile trend observed from SPH result and the experiment conducted by Sumino *et al.* [1] as shown in Figure 7.3 (a) and (b), respectively.

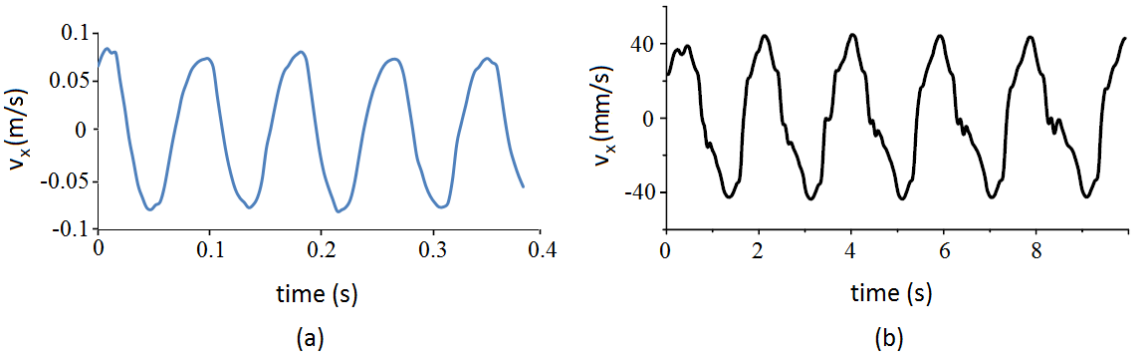

FIGURE 7.3: Showing the average periodic motion of velocity in x-direction against time for (a) SPH (b) Experiment [1], results respectively.

7.2.2 Droplet movement on a step stair substrate

The setup of this test case is similar to the droplet movement on a horizontal substrate in all aspect, except that the substrate is now configured stair-like as shown schematically in Figure 7.4. For this simulation, a 3mm × 3mm initial square shape droplet was generated on the step stair-like substrate with set static contact angle

of ($\theta_s = 160°$) on both sides by turning s_{sf}, while using the same operating physical properties as described in sub-section 6.1.1.

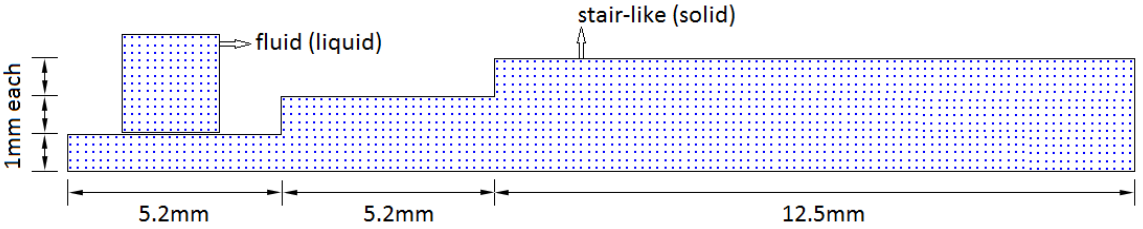

FIGURE 7.4: The schematic representation of the droplet on the stair-like substrate before surface tension force is applied.

The problem was initiated using a two-dimensional droplet with same set static contact angle on both sides where the droplet begin to spread until it reaches its equilibrium state at zero velocity ($\vec{v} = 0$). At this stage, the receding angle is set to be $\theta_R = 160°$ whereas the advancing angle is varied from $\theta_A = 160°$ to $30°$ with decreasing interval of $5°$; it was observed that the droplet begin to move when $\theta_A \leq 150°$, but could only climb or propel up the 1mm stair-like substrate when $\theta_A \leq 130°$. Again by setting the receding angle to be $\theta_R = 150°$ and varying the advancing angle from $\theta_A = 150°$ to $30°$ with decreasing interval of $5°$, the droplet begin to move at $\theta_A \leq 140°$, but could only climb the stair-like substrate when $\theta_A \leq 125°$. This procedure was repeated for receding angles of $\theta_R = 130°$, $\theta_R = 110°$ and $\theta_R = 90°$ with the advancing angle varied from $\theta_A \leq 130°$ to $30°$, $\theta_A \leq 110°$ to $30°$ and $\theta_A \leq 90°$ to $30°$ respectively with decreasing interval of $5°$. The same trend as before was observed as shown by the critical line in Figure 7.5 which represent the boundary; where to the left of it the droplet will climb whereas to the right of it the droplet will not climb. Interestingly, when the receding angle was set at $\theta_R = 90°$, the droplet begin to move at $\theta_A \leq 80°$ to $30°$ with decreasing interval of $5°$, but was unable to climb irrespective of the value of the advancing angle θ_A. The reason for this may be the low centre of gravity, couple with the fact the droplet is occupying more area were the fluid viscous is becoming more active at receding angle of $\theta_R = 90°$. This is confirmed by extrapolating Figure 7.5 backward as shown in Figure 7.6 by the dash black line where the vertical intercept by the critical line is at $\theta_R \approx 100°$. To validate this minimum receding angle for which this droplet begin to climb, a test case with receding angle $\theta_R = 100°$ and advancing angle varied from $\theta_A = 100°$ to $30°$ with decreasing interval of $5°$ was employed. It was found that the droplet could only climb when the advancing angle was $\theta_A = 30°$, but leaving small patches of droplets behind at

each foot of the stairs as shown by the droplet evolution snapshot in Figure 7.7. This observed phenomena is difficult to capture with the other numerical methods.

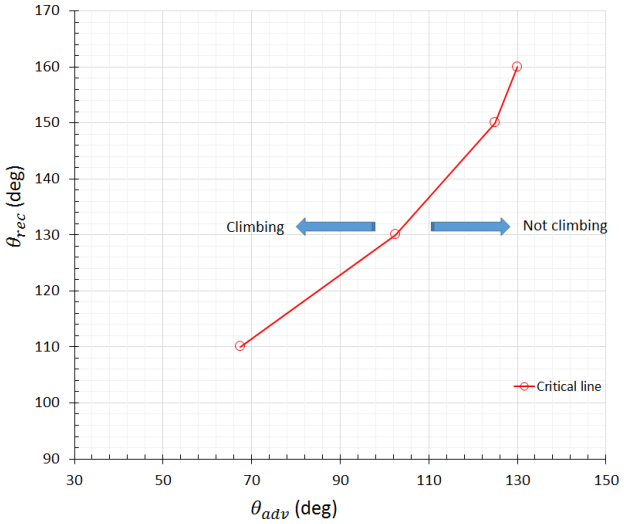

FIGURE 7.5: The critical line represent the combination of θ_R and θ_A when the droplet will climb the 1mm stair-like substrate. The arrow pointing left represent the region for climbing, while the arrow pointing right represent the region for non-climbing.

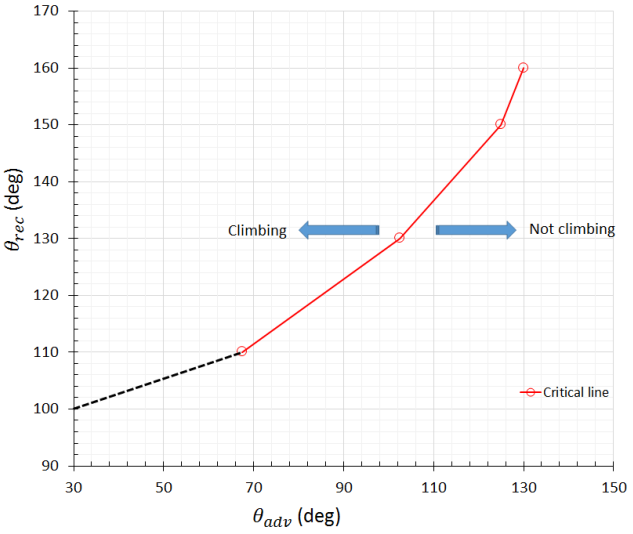

FIGURE 7.6: The extrapolated critical line represent when the line intercept the vertical axis.

Figure 7.8 shows the velocity profile for the receding and advancing angle when the droplet were able to climb the step stair-like substrate. From the velocity against time graph, when the receding angle was $\theta_R = 160°$ and advancing angle $\theta_A = 130°$,

the droplet first accelerate up to $t = 0.2s$, then decelerate when it meet the first step at $t = 0.06s$.

It then accelerate again from $t = 0.26s$ to $t = 0.36s$, but decelerate when it meet the second step at $t = 0.04s$ and finally accelerate from $t = 0.4s$ as indicated on the graph. This behaviour is expected in that energy is expended during climbing, thus leading to a reduction in velocity. The same behaviour is happening for the other receding angles $\theta_R = 150°$, $\theta_R = 130°$, $\theta_R = 110°$ and advancing angles $\theta_A = 125°$, $\theta_A = 102.5°$, $\theta_A = 67.5°$, respectively, at which the droplet were able to climb. For receding angle $\theta_R = 100°$ and advancing angle $\theta_A = 30°$, a similar situation is repeated as before, but with the velocity having a negative value. This occurred because the droplet at the stair step is struggling to climb, thus resulting in a forward and backward motion, until it escape by leaving small patches of droplets at each stair foots and then accelerate as shown in Figure 7.8 by the purple dash line represented by rec_100_adv_30.

Sumino *et al.* [1] performed several experiments, one of which was a droplet climbing a 1mm step stair-like substrate made of glass, with experimental setup as shown in Figure 7.9. From their experiment, the droplet evolution snapshot is shown in Figure 7.10 (a) which is in qualitative good agreement with our simulation in 2D as shown in Figure 7.10 (b).

7.3 Thin film flow on an incline solid substrate

For many industrial processes such as dry patch formation on heated surfaces, liquid film drainage from steam turbine stator blades, gas-liquid containing equipment in distillation and absorption, being able to characterise the flow of liquid down an incline surface is very paramount [61]. Even though the geometry is simple, a large number of hydrodynamic regimes is observed depending on the solid surface and liquid properties. Liquid flow on an incline plane to form a film is probably the best known regime, as a significant amount of research has been put into it [247]. Some notable researchers, Hartley and Murgatroyd [248], Bankoff [249], and Mikielewiez and Moszynski [250] developed energy theories for film stability and breakdown and this form the basis for subsequent work for rivulet flows. Others authors, like Hobler and Czajka [251] and Munakata *et al.* [252] dealt with the issue of determining the minimum flow rate for complete surface wetting, while a few researchers were investigating into the hydrodynamics of droplet and rivulet flows [253–257]. Tanner

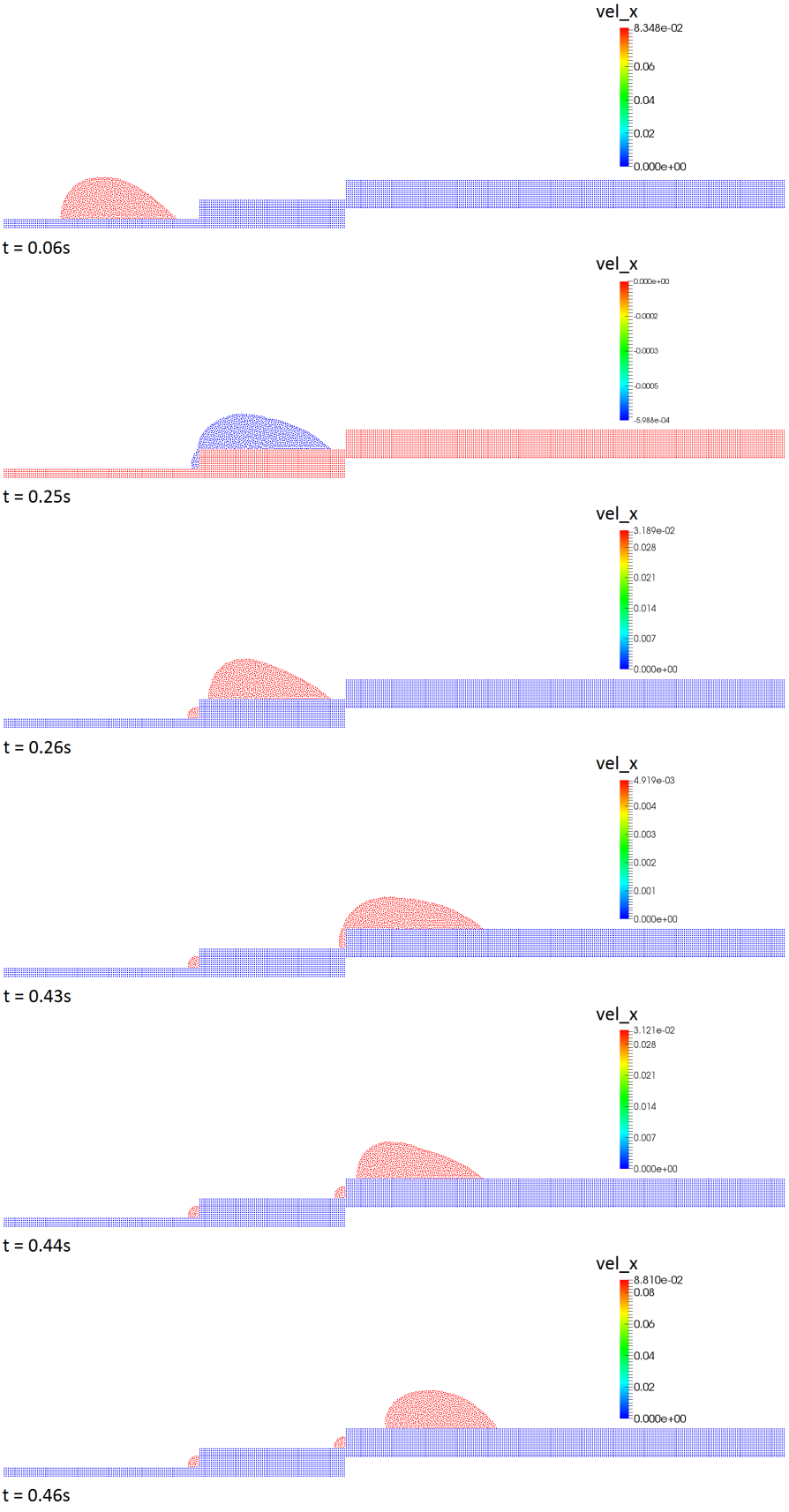

FIGURE 7.7: The evolution snapshot of droplet leaving patches of droplets during climbing 1mm stair-like substrate (where vel_x is the average velocity).

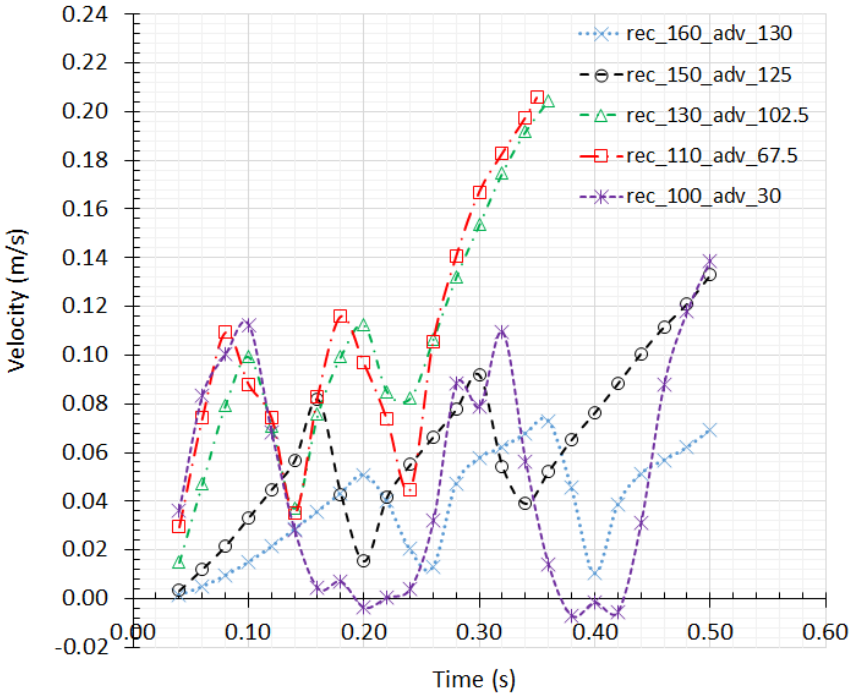

FIGURE 7.8: The velocity of droplet climbing 1mm stair-like substrate.

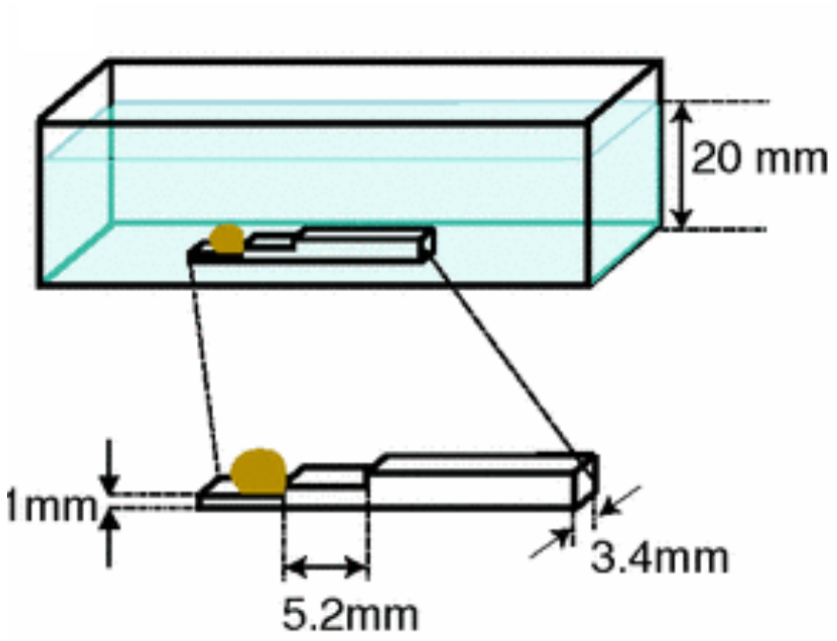

FIGURE 7.9: The experimental setup of droplet climbing 1mm stair-like substrate [1].

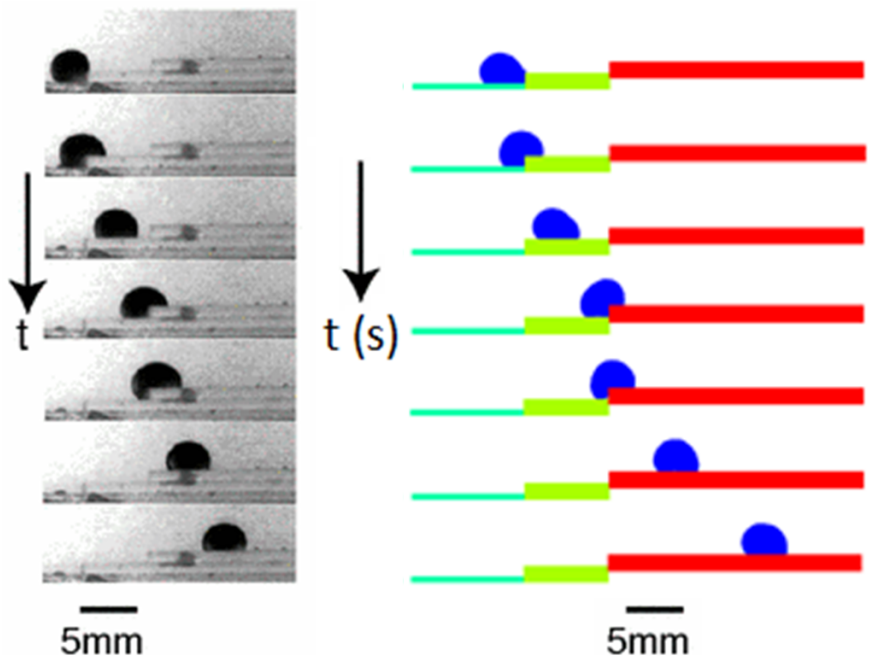

FIGURE 7.10: The evolution snapshot of droplet climbing 1mm stair-like substrate (a) Experiment [1] (b) Our SPH results.

[258] and Gorycki [259] have noticed and described qualitatively the regions where the existence and formation of droplet and linear, meandering and oscillating rivulets are dependent on the flow rate and gradient of the surface. This Chapter focuses on the formation of rivulets and its associating droplets in 2D for flow on an inclined substrate.

7.3.1 Flow of liquid on an incline solid substrate

Following from the implementation of the IIF method in Model 1 in Section 5.6.1, a substrate with $L_x = 210$mm inclined at ψ to the horizontal on which a liquid (water) flowing at velocity, v_{in}, from a source with opening $H_y = 2$mm is setup as shown in Figure 7.11. The solid substrate is made up of four particle layers, consisting of 8416 SPH particles with initial separation of $(dx = dy = 0.0001)$m. All other details of the parameter used are presented in Table 7.1. Note that for the following test cases, gravity is dominant as $B_O \gg 1$.

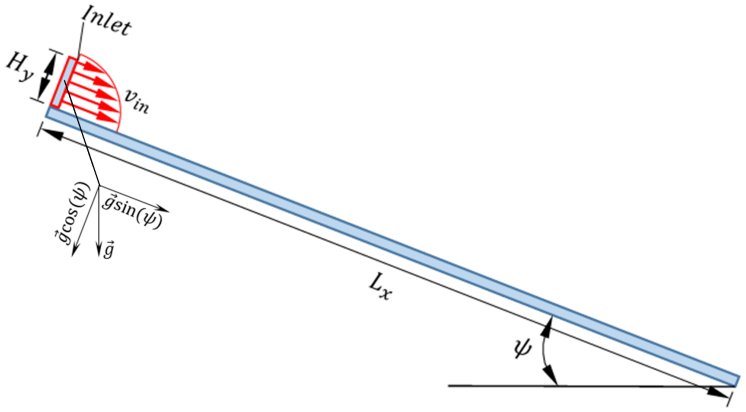

FIGURE 7.11: The schematic representation of thin film with inlet velocity v_{in} on a solid substrate at inclination ψ to the horizontal.

TABLE 7.1: Initial properties of thin film using Model 1.

Properties, symbols (Units)	**Fluid values**
Mass, m (kg)	$\rho \times dx \times dy$
Density, ρ (kg/m^3)	1000.0
Pressure, p (Pa)	0
Acceleration (gravity), $\vec{\mathbf{a}}$ (m/s^2)	0
Dynamics viscosity, μ (Pas)	10^{-3}
Sound speed, c_o (ms^{-1})	4.0,
Smoothing length, h (m)	1.3$\times$ dx
Strength of the repulsive force, D (-)	0.012
strength of the force between fluid and fluid, s_{ff} (-)	0.008
strength of the force between solid and fluid, s_{sf} (-)	0.004
Kernel, W_{ij} (m^{-3})	Quintic

7.3.1.1 Solid substrate at inclination of 30°

A constant inlet flow rate is set at varying velocities, v_{in}, 0.02, 0.1, 0.2, 0.5 and 1.0 ms^{-1}, on a solid substrate that is inclined at $\psi = 30°$. With each of these velocities, Figures 7.12 to 7.13 shows the snapshot of these rivulets profile at time 0.04s and 0.24s intervals. The developing rivulet film evolves as if flows down the inclined substrate. It clearly shows that the amount and therefore length of the rivulet increases with increasing inlet velocities. However, a necking instability where the film begin to stretch and thus, thins behind the advancing front, similar to those of Taylor instability phenomena, is observed especially when inlet are small, i.e $v_{in} \ll 1.0$ms^{-1}

At time = 0.34s in Figure 7.14, the rivulet with $v_{in} = 1.0\text{ms}^{-1}$ exits the substrate with no significant change in shape whereas the remaining flowing rivulets continue to experience necking at behind the rivulet front. It is interesting to note that the length of the advancing rivulet shaped front, in front of the point of minimum necking thickness, is of the same length (approximately 0.03m) spread across the different inlet velocities. The height of minimum necking is however smaller for lower velocities (details of this will be discussed later in this Chapter 7). At time = 0.42s in Figure 7.15, all the rivulet with $v_{in} = 0.1\text{ms}^{-1}$ and $v_{in} = 0.2\text{ms}^{-1}$ experiences significant necking observed behind the advancing rivulet front. At time = 0.50s in Figure 7.16, the rivulet with $v_{in} = 0.2\text{ms}^{-1}$ break into two at x = 0.175m with the receding end on the right pulling immediately forward toward the broken droplet (A) with a high pull due to surface tension whereas the rivulet with $v_{in} = 0.1\text{ms}^{-1}$ continue to experiences more significant necking. However, due to limitation in computational resources, the case where $v_{in} = 0.5\text{ms}^{-1}$ will be ignored in the analysis and the focus is placed on to the remaining rivulets. At time = 0.58s in Figure 7.17, the rivulets with $v_{in} = 0.2\text{ms}^{-1}$ exits the substrate without the neck breaking whereas the one with $v_{in} = 0.1\text{ms}^{-1}$ experience a breakage of the rivulet into two at x = 0.13m. The receding end on the right is immediately pulled towards the broken off droplet (B) with a large pull due to surface tension while the advancing end on the left side was propelled backward, now towards the new advancing front of the shortened rivulet.

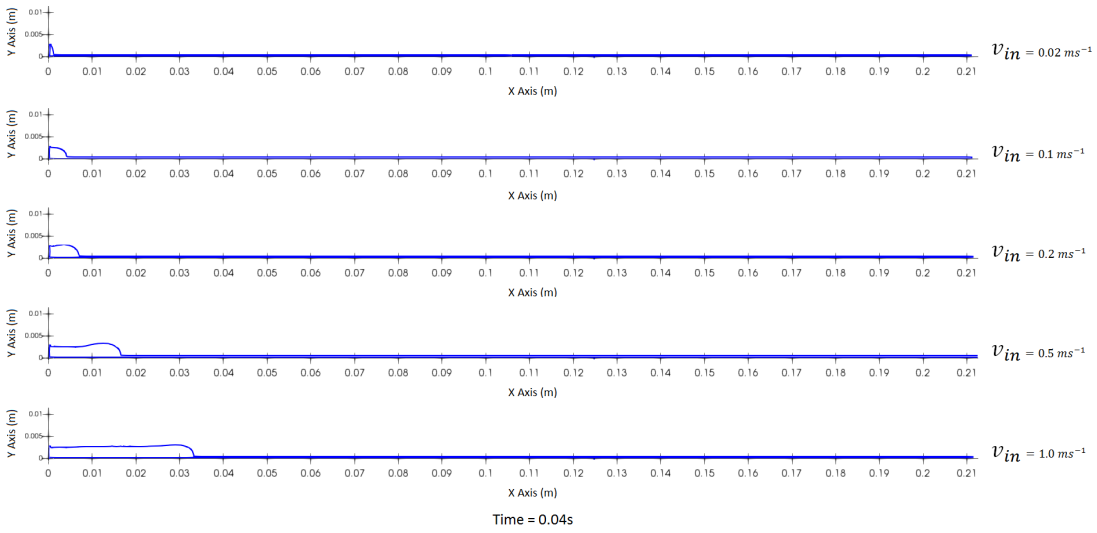

FIGURE 7.12: The evolution snapshot of thin film on a solid substrate at $\psi = 30°$ inclination using inlet velocities, 0.02ms^{-1}, 0.1ms^{-1}, 0.2ms^{-1}, 0.5ms^{-1} and 1.0ms^{-1} respectively.

This larger droplet on the right subsequently advanced forward to x = 0.185m, leaving the new and small rivulet front on the left stationary as it waits to recover sufficient

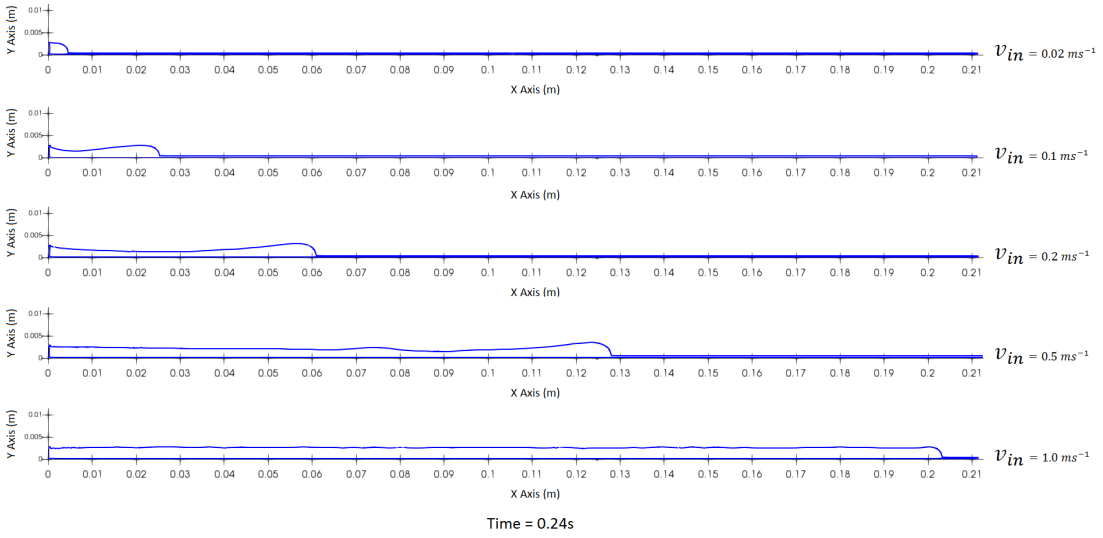

FIGURE 7.13: The evolution snapshot of thin film on a solid substrate at $\psi = 30°$ inclination using inlet velocities, 0.02ms^{-1}, 0.1ms^{-1}, 0.2ms^{-1}, 0.5ms^{-1} and 1.0ms^{-1} respectively.

volume (or mass) for the effects of gravity to ably flow down the inclined substrate, shown in Figure 7.18 at time = 0.64s. At time = 0.94s in Figure 7.19, this large droplet eventually flow out of the domain while leaving behind the bigger rivulet front with $v_{in} = 0.1\text{ms}^{-1}$ whereas the rivulet with $v_{in} = 0.02\text{ms}^{-1}$ slowly advanced forward with time, experiencing significant necking.

Since the rivulet with $v_{in} = 0.1\text{ms}^{-1}$ has exit the substrate, then focus will be on the remaining rivulet, at time = 1.14s, in Figure 7.20, where the rivulet with v_{in} = 0.02ms^{-1} began breaking up at x = 0.01m into two where on the left, sees the formation of a smaller droplet (C) attached to the now new rivulet front while on the right, the receding end catches up to the droplet at its front. The momentum of the latter carries the droplet forward (see, time = 1.20s) which then stabilized at time = 1.28s. At time = 2.00s, this droplet escapes the substrate while the rivulet front is developed again. Finally, the above process repeats itself with the breakage at the neck at time = 2.12s and subsequent flow profile similar to time = 1.28s is reformed at time = 2.24s.

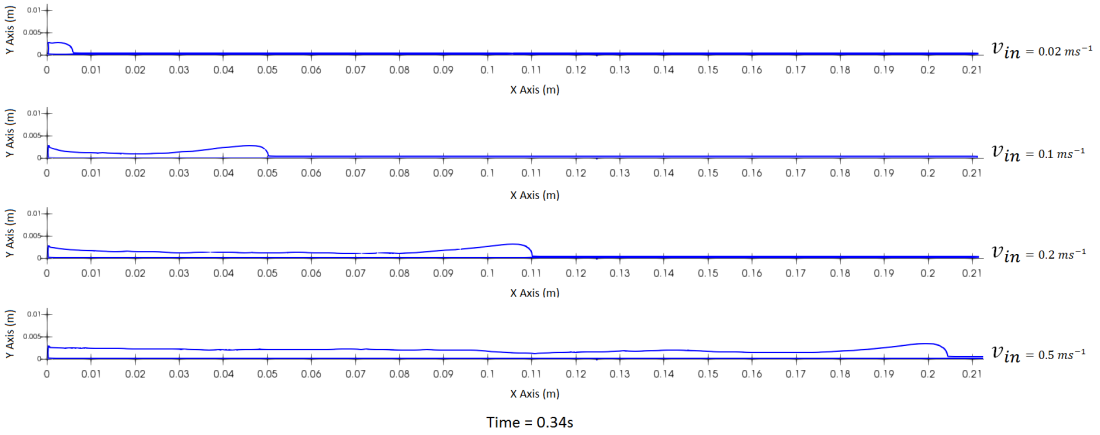

FIGURE 7.14: The evolution snapshot of thin film on a solid substrate at $\psi = 30°$ inclination using inlet velocities, 0.02ms^{-1}, 0.1ms^{-1}, 0.2ms^{-1} and 0.5ms^{-1} respectively. *Note that the rivulet with $v_{in} = 1.0\text{ms}^{-1}$ has exit the substrate.

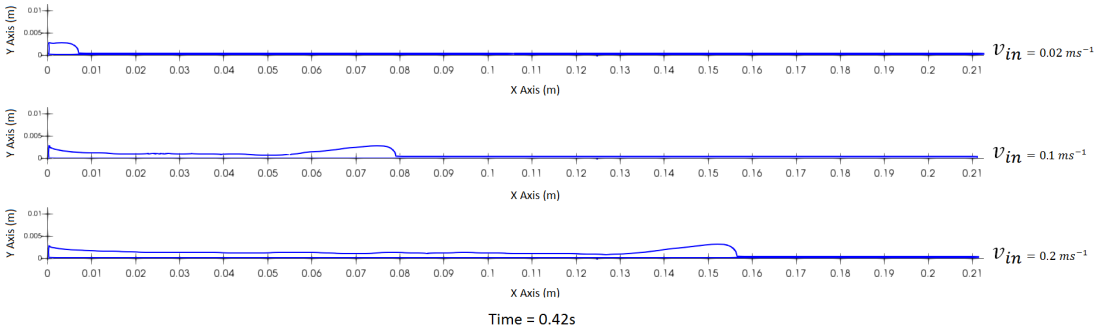

FIGURE 7.15: The evolution snapshot of thin film on a solid substrate at $\psi = 30°$ inclination using inlet velocities, 0.02ms^{-1}, 0.1ms^{-1} and 0.2ms^{-1} respectively. *Note that the rivulet with $v_{in} = 0.5\text{ms}^{-1}$ has exit the substrate.

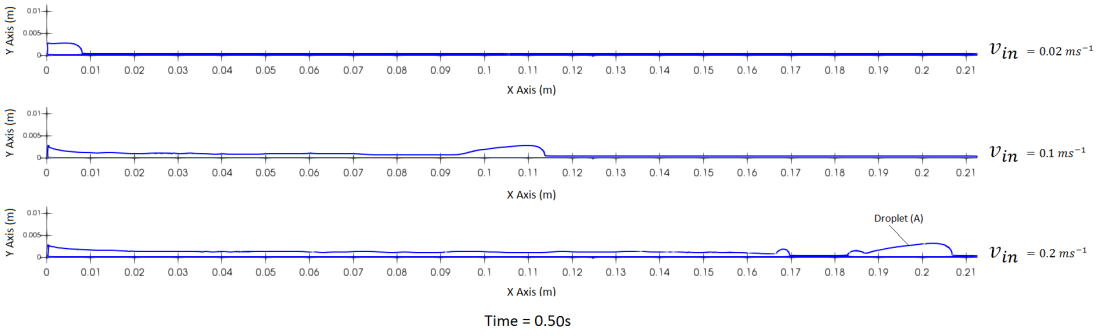

FIGURE 7.16: The evolution snapshot of thin film on a solid substrate at $\psi = 30°$ inclination using inlet velocities, 0.02ms^{-1}, 0.1ms^{-1} and 0.2ms^{-1} respectively. *Note that the rivulet with $v_{in} = 0.2\text{ms}^{-1}$ has produce the first droplet.

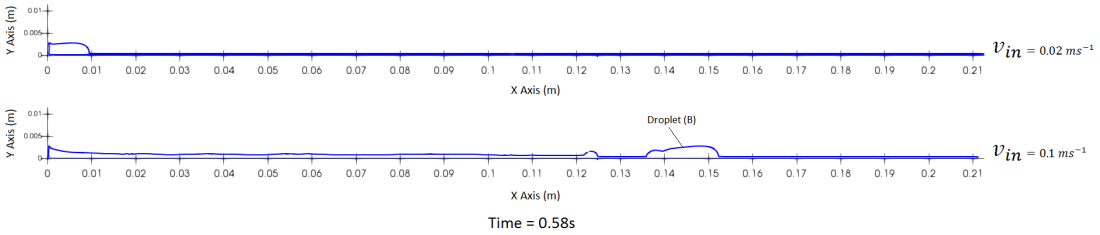

FIGURE 7.17: The evolution snapshot of thin film on a solid substrate at $\psi = 30°$ inclination using inlet velocities, 0.02ms^{-1} and 0.1ms^{-1} respectively. *Note that the rivulet with $v_{in} = 0.2\text{ms}^{-1}$ and its droplet has exit the substrate whereas the next droplet is form by rivulet with $v_{in} = 0.1\text{ms}^{-1}$.

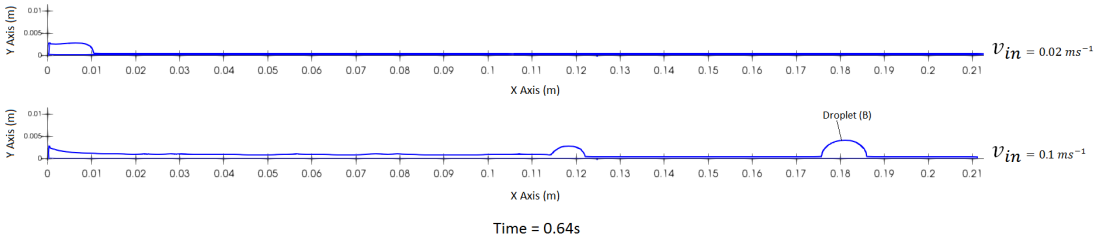

FIGURE 7.18: The evolution snapshot of thin film on a solid substrate at $\psi = 30°$ inclination using inlet velocities, 0.02ms^{-1} and 0.1ms^{-1} respectively.

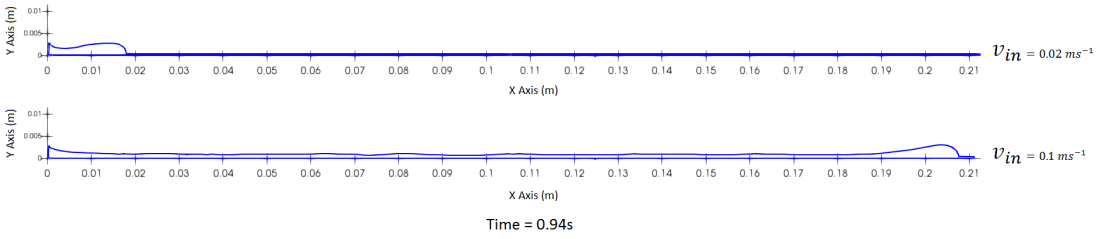

FIGURE 7.19: The evolution snapshot of thin film on a solid substrate at $\psi = 30°$ inclination using inlet velocities, 0.02ms^{-1} and 0.1ms^{-1} respectively. *Note that this droplet from $v_{in} = 0.1\text{ms}^{-1}$ has exit the substrate.

To further illustrate the phenomena that happened in the advancing front and necking of the rivulet migration at various inlet flows conditions between $v_{in} = 0.1\text{ms}^{-1}$ to 1.0ms^{-1}, Figure 7.21 (a) highlights the evolution snapshots of the position with time.

The linear profile of the velocity of the rivulet fronts is almost the same generally, whether it just coming out of either the source or after breakage, once the rivulet is fully developed. It clearly shows that the rivulet is more likely to break into droplets at lower inlet velocities, at the thinning and necking region of the rivulets moving downstream due to the effect of gravity.

For this particular case when the inclination angle is $\psi = 30°$, the breakage of the rivulets front at the necking which started at $v_{in} = 0.2\ \text{ms}^{-1}$ and lower, result in the formation of droplets in front of the new rivulets, are becoming more prominent,

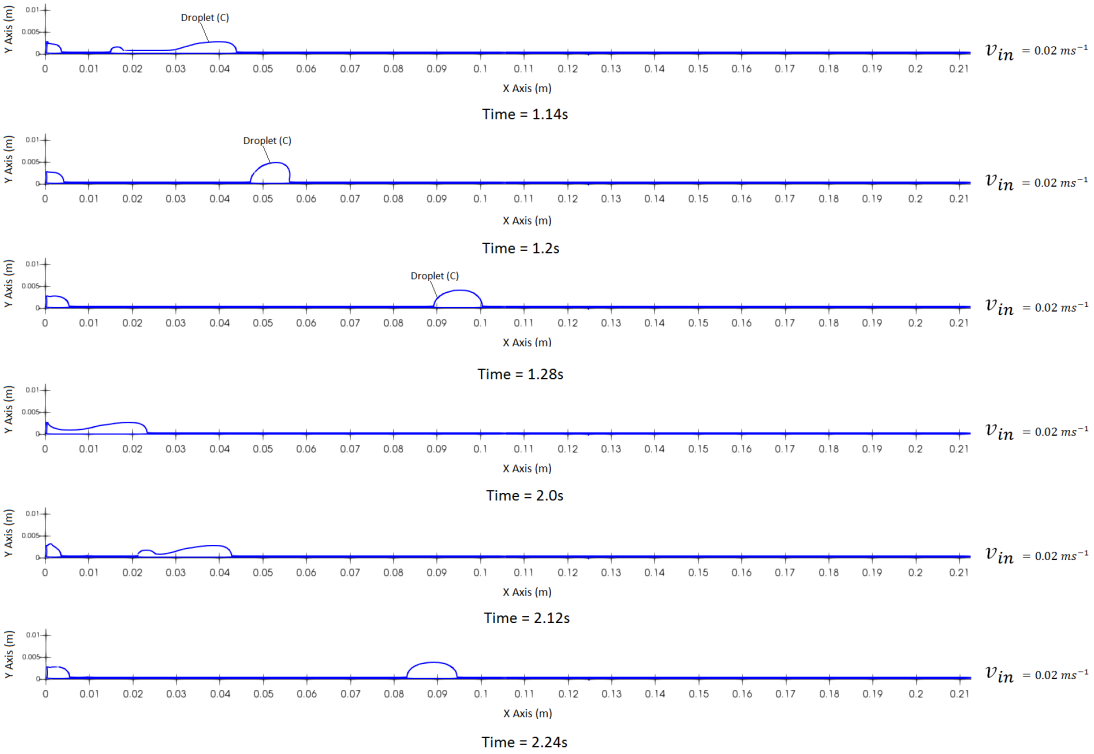

FIGURE 7.20: The evolution snapshot of thin film on a solid substrate at $\psi = 30°$ inclination using inlet velocity, 0.02ms^{-1}. *Note that the rivulet with $v_{in} = 0.1$ms^{-1} has exit the substrate.

consistent and predictable at lower inlet velocities, especially at $v_{in} = 0.02$ ms^{-1}, where the formation of disconnected droplet from the rivulet occur at almost regular intervals.

The trend shown in Figure 7.21 (b) is the necking thickness over time before the breakage occurs when $\psi = 30°$. It clearly highlight that the necking thickness at the various velocities inlet are relatively same with a value of 2.7×10^{-4}m which was found to correspond to three particle layers of fluid that is compressed as seen from the simulation (note that the particles was initially spaced at 10^{-4}m from one another). It is believed that this necking thickness is related to resolution restriction, so if the particle resolution is reduce, the necking thickness will also reduced also.

7.3.1.2 Solid substrate at inclination of 50°

This time, the solid substrate orientation is at $\psi = 50°$ to the horizontal while still maintaining the same inlet flow rate velocities at, v_{in}, 0.02, 0.1, 0.2, 0.5 and 1.0 ms^{-1}. Applying each of these velocities, Figures 7.22 shows the evolution of these rivulets profile at time = 0.16s. Just like previous observations, the rivulet film evolves as it

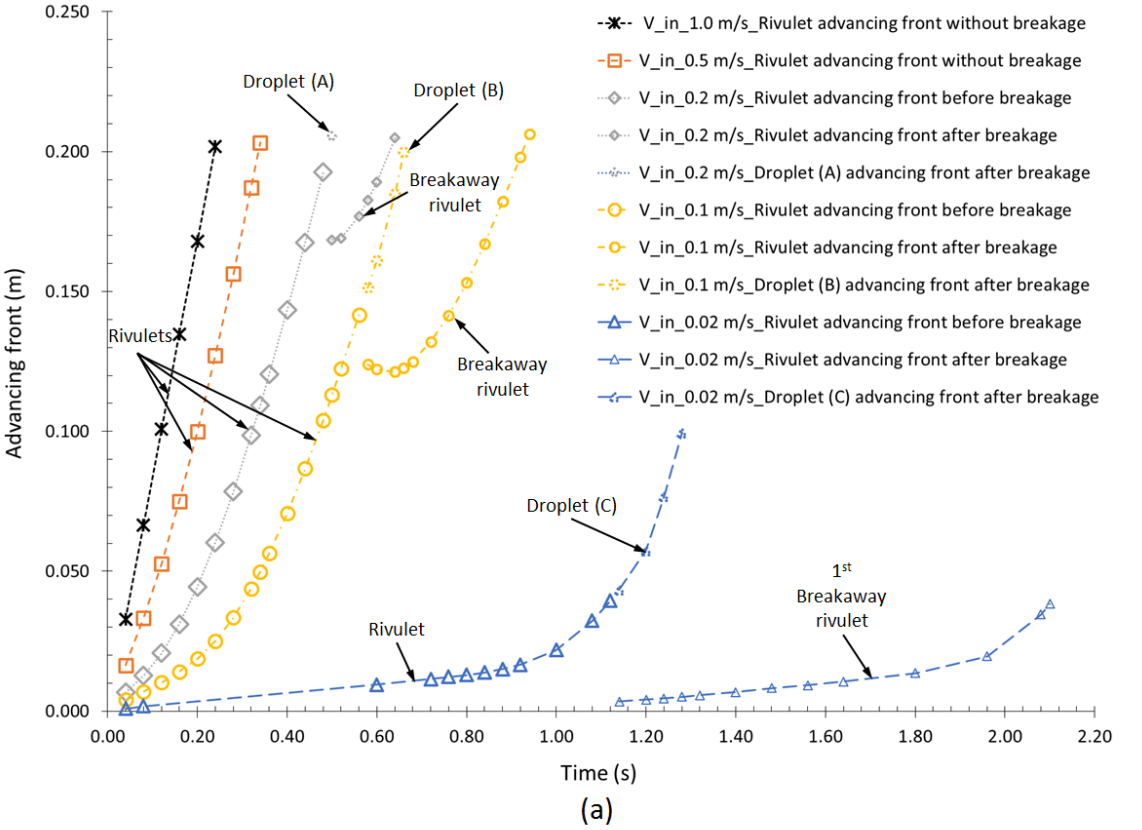

(a)

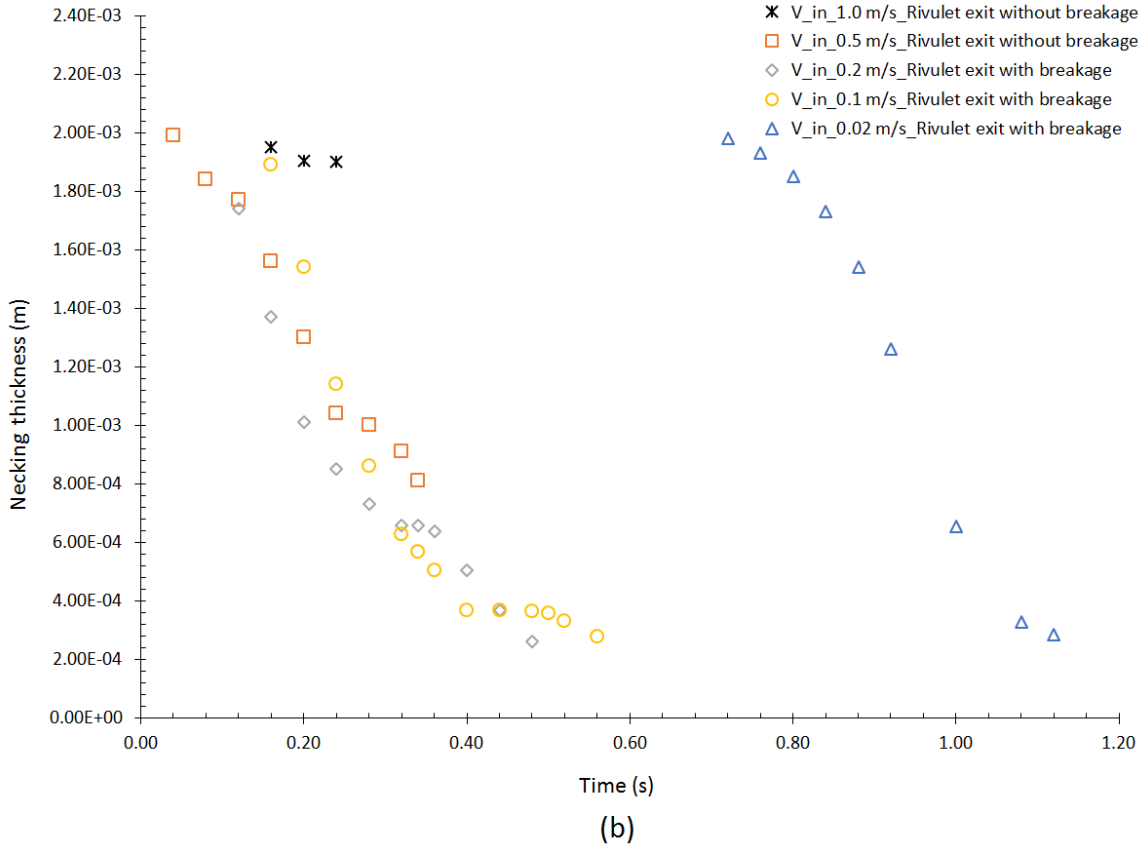

(b)

FIGURE 7.21: The evolution snapshot of (a) rivulet advancing front (b) necking thickness, at various inlet velocities between $v_{in} = 0.02\ \text{ms}^{-1}$ to $1.0\ \text{ms}^{-1}$ at $\psi = 30°$.

flow down the inclined substrate, where the amount and length of the rivulet increases with increasing velocities, with necking instability experienced especially when inlet velocities are small. These necking instabilities become more severe at time = 0.2s in Figure 7.23 especially the rivulet with $v_{in} = 0.5\text{ms}^{-1}$, with the length of the advancing rivulet shaped front , in front of point of minimum necking thickness, have the same length (approximately 0.02m) distributed across the different inlet velocities.

At time = 0.26s in Figures 7.24, the rivulet with $v_{in} = 1.0\text{ms}^{-1}$ has escape the substrate without any noticeable change in shape whereas the rivulet with $v_{in} = 0.5\text{ms}^{-1}$ undergoes breakup into droplet (A) at x $\approx$ 0.108m, which undergoes a pearling (B) and (C) (for details of these phenomena, see Subsubection 7.3.1.3), while the remaining rivulets experience observable necking. In Figure 7.25 at time = 0.32s, the receding end of the broken off droplet (A) on the right pulled the droplet forward, thus making it escape the substrate faster, but leaving behind pearling (D) whereas the new advancing rivulet front on the left side propelled backward to recover volume, then move forward consuming pearling (B) and (C) in front. At this same time, the rivulet with $v_{in} = 0.2\text{ms}^{-1}$ breakup to produce droplet (E) at x $\approx$ 0.125m, which has a behaviour similar to the one in Section 7.3.1.1 previously observed, while the remaining rivulets experiencing necking. When the time = 0.42s in Figure 7.26, the rivulet and pearling (D) with $v_{in} = 0.5\text{ms}^{-1}$ is ignored based on previous reasons in Section 7.3.1.1, whereas the newly formed rivulet front with $v_{in} = 0.2\text{ms}^{-1}$ developed fully while its droplet (E) escape the substrate, but leaving behind pearling (F). The rivulet with $v_{in} = 0.1\text{ms}^{-1}$ breakup into droplet (G) at x $\approx$ 0.11m, with the receding end of the droplet catches up to its front while its rivulet front and that of $v_{in} = 0.02\text{ms}^{-1}$, will advanced forward similar to previous behaviour observed.

At time = 0.64s in Figure 7.27, the rivulet along with the pearling (F) with $v_{in} = 0.2\text{ms}^{-1}$ have exits the substrate, whereas the rivulet with $v_{in} = 0.1\text{ms}^{-1}$ has fully developed while its droplet (G) seen at time = 0.42s has escape the substrate. However, the rivulet with $v_{in} = 0.02\text{ms}^{-1}$ is experiencing noticeable necking. When the time = 0.76s in Figure 7.28, the rivulet with $v_{in} = 0.1\text{ms}^{-1}$ has left the substrate while the one with $v_{in} = 0.02\text{ms}^{-1}$ experiencing more necking. This remaining rivulet with $v_{in} = 0.02\text{ms}^{-1}$ then break into droplet (H) at x $\approx$ 0.01m when time = 0.78s, where the receding end of the droplet catches up with the front while stabilizing at time = 0.90s. At time = 1.20s to 1.30s, this latter droplet has exits the substrate whereas the rivulet front is just developing again and at time = 1.50s, the entire process is repeated in a

similar manner as the previous Section 7.3.1.1 with the droplet stabilizing at time = 2.20s.

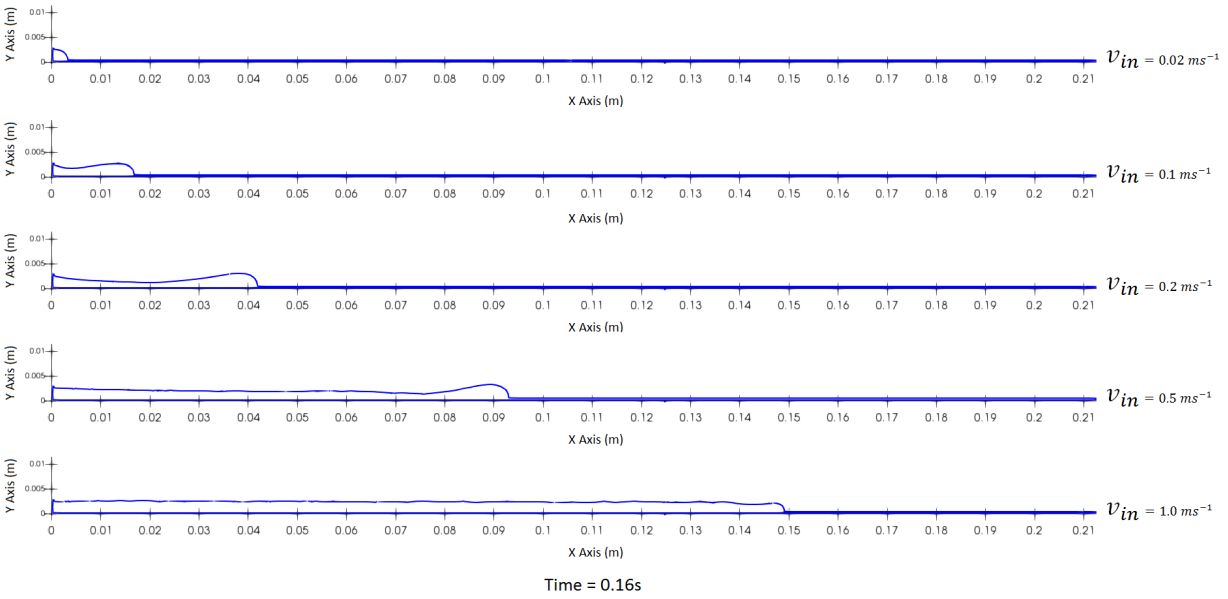

FIGURE 7.22: The evolution snapshot of thin film on a solid substrate at $\psi = 50°$ inclination using inlet velocity, $0.02ms^{-1}$, $0.1ms^{-1}$, $0.2ms^{-1}$, $0.5ms^{-1}$ and $1.0ms^{-1}$ respectively.

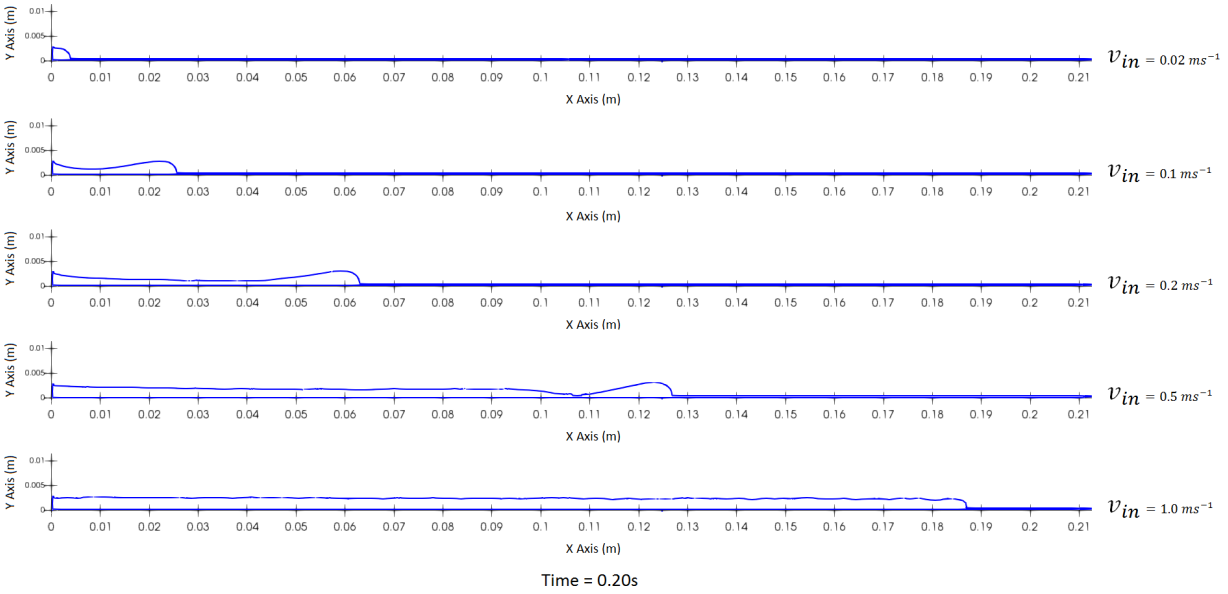

FIGURE 7.23: The evolution snapshot of thin film on a solid substrate at $\psi = 50°$ inclination using inlet velocity, $0.02ms^{-1}$, $0.1ms^{-1}$, $0.2ms^{-1}$, $0.5ms^{-1}$ and $1.0ms^{-1}$ respectively.

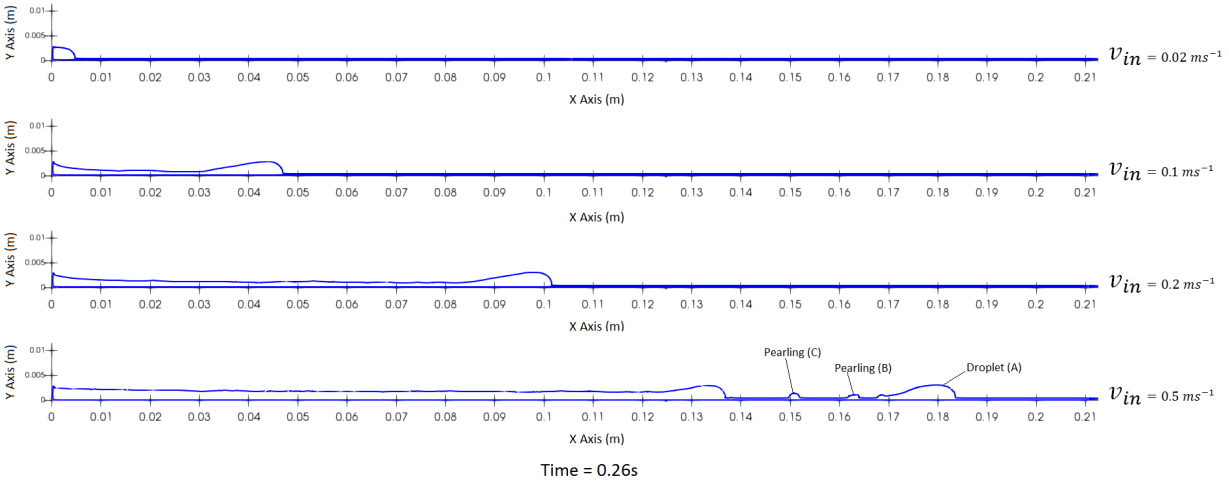

FIGURE 7.24: The evolution snapshot of thin film on a solid substrate at $\psi = 50°$ inclination using inlet velocity, 0.02ms^{-1}, 0.1ms^{-1}, 0.2ms^{-1} and 0.5ms^{-1} respectively. *Note that the rivulet with $v_{in} = 1.0\text{ms}^{-1}$ has exit the substrate.

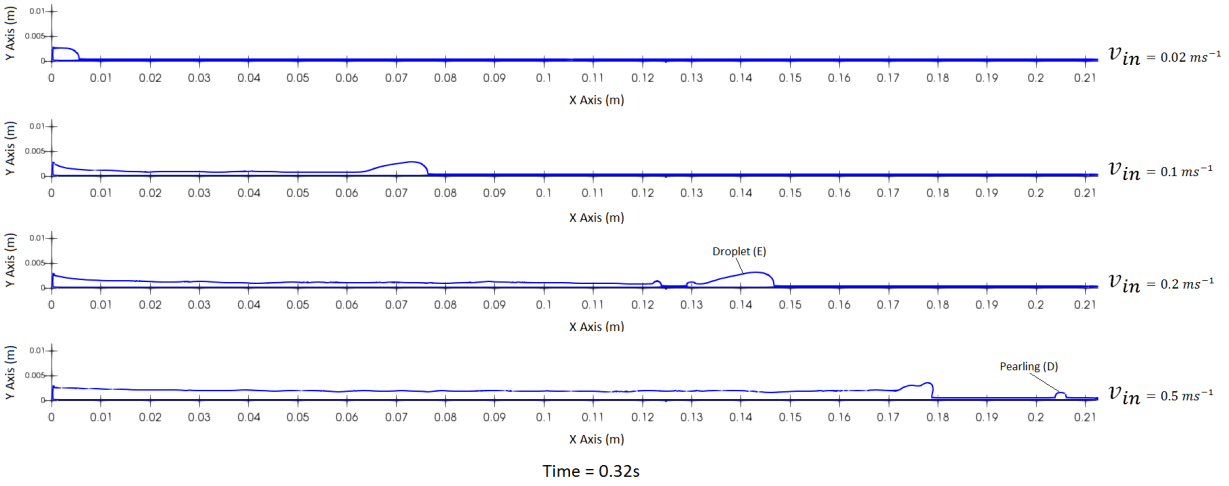

FIGURE 7.25: The evolution snapshot of thin film on a solid substrate at $\psi = 50°$ inclination using inlet velocity, 0.02ms^{-1}, 0.1ms^{-1}, 0.2ms^{-1} and 0.5ms^{-1} respectively.

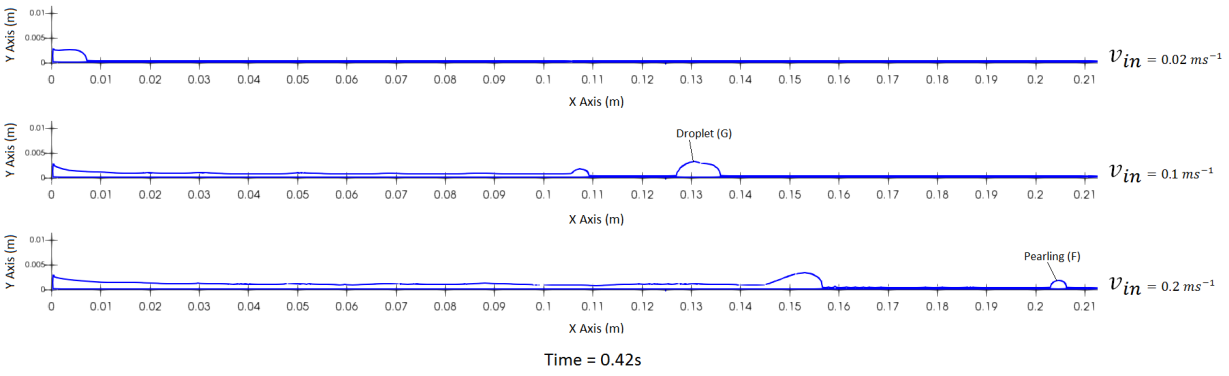

FIGURE 7.26: The evolution snapshot of thin film on a solid substrate at $\psi = 50°$ inclination using inlet velocity, 0.02ms^{-1}, 0.1ms^{-1} and 0.2ms^{-1} respectively. *Note that the rivulet with $v_{in} = 0.5\text{ms}^{-1}$ has exit the substrate.

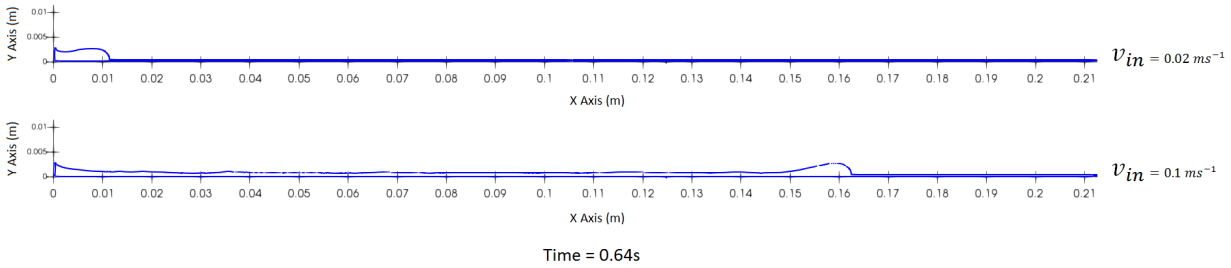

FIGURE 7.27: The evolution snapshot of thin film on a solid substrate at $\psi = 50°$ inclination using inlet velocity, 0.02ms^{-1} and 0.1ms^{-1} respectively. *Note that the rivulet with $v_{in} = 0.2\text{ms}^{-1}$ has exit the substrate.

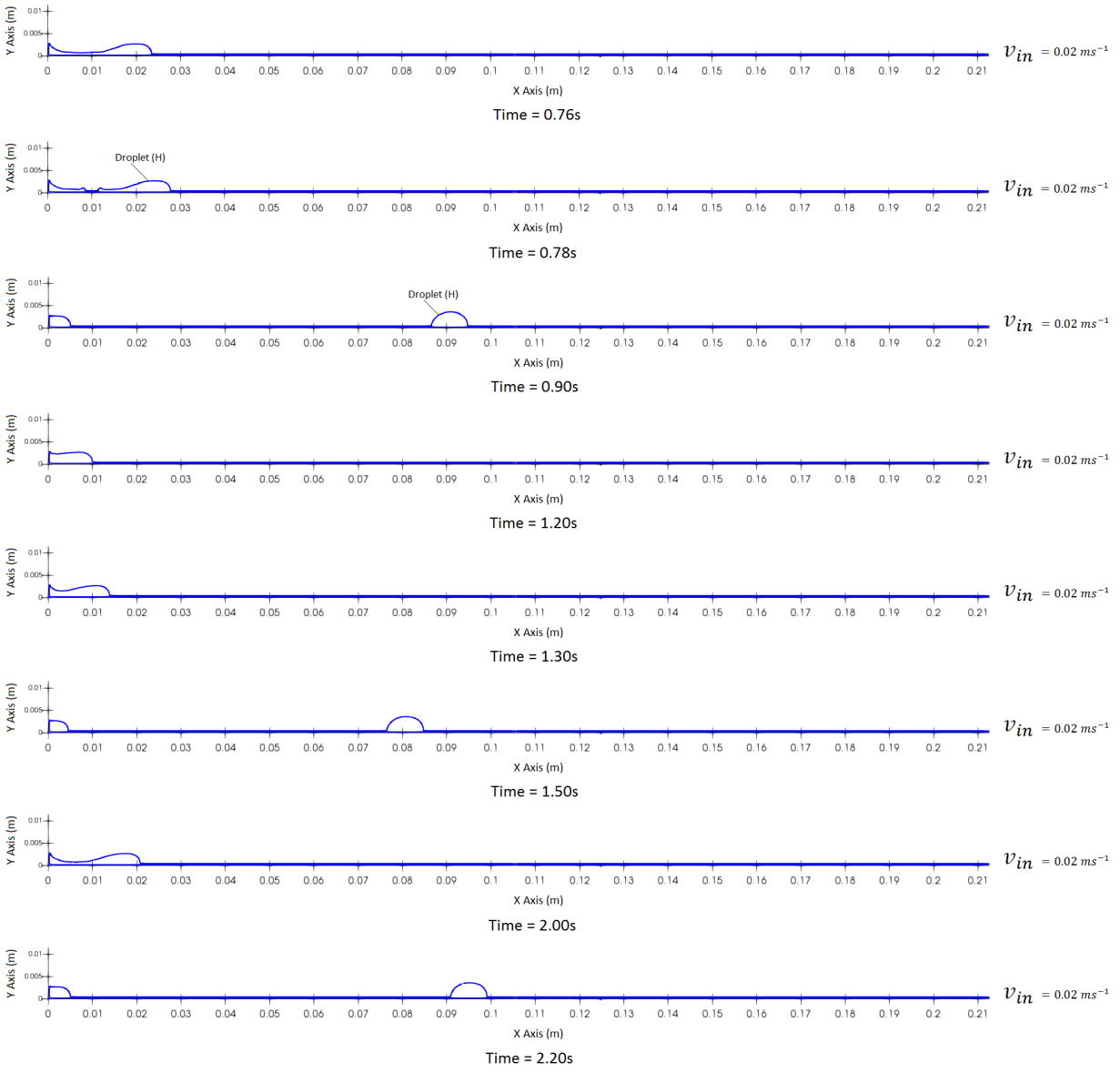

FIGURE 7.28: The evolution snapshot of thin film on a solid substrate at $\psi = 50°$ inclination using inlet velocity, 0.02ms^{-1}. *Note that the rivulet with $v_{in} = 0.1\text{ms}^{-1}$ has exit the substrate.

Figure 7.29 (a) delineate the evolution of the advancing front of migrating rivulets at different inlet flows conditions between 0.02ms^{-1} to 1.0ms^{-1}. The formation of a detached droplet due to the stability and thus, breakage of the thin film is highlighted clearly, denoting their positions in time.

The velocity of the rivulet fronts, in general, whether it originates either from the inlet or as a results of breakage, follows a linear profile as soon as the rivulet is fully developed. It clearly shows that the rivulet are more likely to break from the thinning and necking effect as inlet velocity decreases to form pearling or droplets that eventually coalescence with one another as they move downstream due to the effect of gravity.

Of particular note is the case when the inclination angle is $\psi = 50°$, breakage of the resulting rivulets and droplets from necking becomes prominent at lower inlet velocities and becomes more consistent and predictable at small velocities, for example, at $v_{in} = 0.02\text{ms}^{-1}$, where the formation of the detached droplet from the rivulet occur at relatively fixed intervals. It can also be seen that the rivulet breakage started at inlet flow rate of $v_{in} = 0.5\text{ms}^{-1}$ and lower compared to $v_{in} = 0.2\text{ms}^{-1}$ and lower for when $\psi = 30°$.

The trend shown in Figure 7.29 (b) for the necking thickness over time of the initial rivulet at $\psi = 50°$ for various inlet flow conditions is similar to $\psi = 30°$. It clearly shows that the neck thickness here decreases compared to when $\psi = 30°$. However, due to resolution restrictions, this characteristic is not observed for $v_{in} = 0.5\text{ms}^{-1}$ and higher.

7.3.1.3 Solid substrate at inclination of 70°

Consider the case when the substrate is inclined at $\psi = 70°$ to the horizontal and employing the same inlet flow velocities at v_{in}, 0.02, 0.1, 0.2, 0.5 and 1.0 ms^{-1}, respectively. Initial snapshots of the rivulet evolutions are depicted in Figure 7.30 and7.31 at time = 0.16s and 0.20s respectively. The same necking phenomena is observed as in Section 7.3.1.1 and 7.3.1.2 and is more pronounced when $v_{in} \ll 1.0$ ms^{-1}. The separation of the droplet into two, a droplet on the right and the remaining rivulet on the left, is more obvious and occurs for the $v_{in} = 0.5$ ms^{-1} case at a much earlier stage compared to the cases when the substrate inclination angle $\psi = 30°$ and 50° were used. It can be seen that for $v_{in} = 0.5$ ms^{-1}, the breakage occurs more readily and the

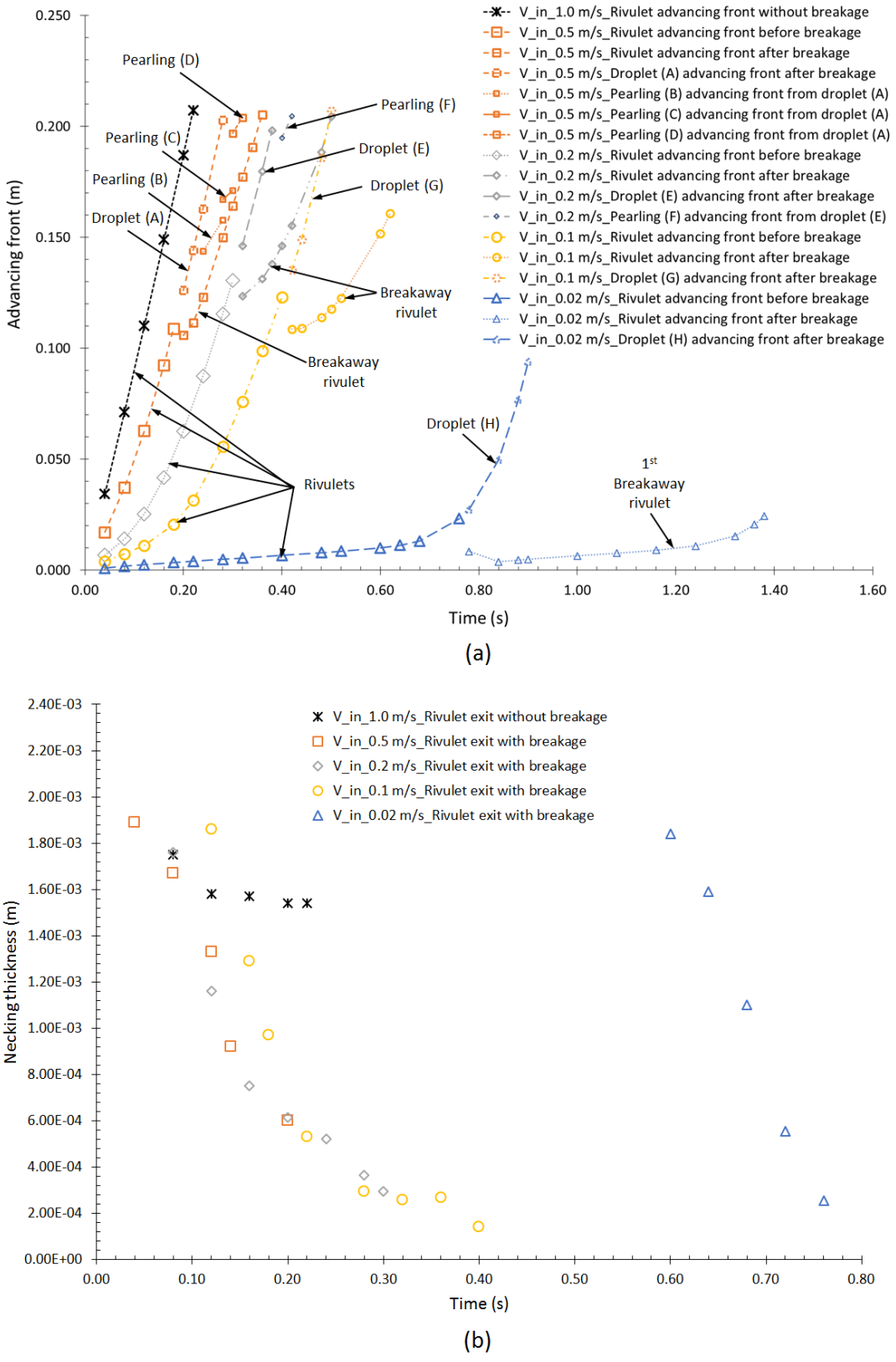

FIGURE 7.29: The evolution snapshot of (a) rivulet advancing front (b) necking thickness, at various inlet velocities between v_{in} = 0.02 ms^{-1} to 1.0 ms^{-1} at ψ = 50°.

advancing droplet (A) undergoes a pearling (B) phase. This pearling phenomena is reported by Podgorski *et al.* [260] for moving droplets down inclined surfaces. As the inclination angle increases, the droplet slides down the incline plane with increasing velocity, such that it experiences corner effect at the receding end, which developed into a cusp effect at higher inclination angle. At a certain inclination angle close to 60° [260], this droplet start to emit droplets (pearl) at the tip of the cusp and if the inclination angle is increase further, it begin to leave behind a trailing which develop into an unstable state via a Rayleigh-like instability. The current work will not focus on the formation on pearling as it lies beyond the scope of the thesis.

In Figure 7.32, at time = 0.24s, the rivulet with $v_{in} = 1.0$ ms^{-1} has exited the domain without any changes in its shape or form, and is therefore omitted from the subsequent plots. It is interesting to note that for the case where $v_{in} = 0.5$ ms^{-1}, the advancing droplet (A) leaves a second pearling (C), while the following advancing rivulet catches up to the tiny droplet (B) and encapsulates the droplet into itself, thus forming a larger rivulet front. At the same time, the rivulet with $v_{in} = 0.2$ ms^{-1} and $v_{in} = 0.1$ ms^{-1} both experiences their first breakage, creating droplets (D) and (E), respectively, due to the initial necking effects, while the rivulet with $v_{in} = 0.02$ ms^{-1} advanced forward.

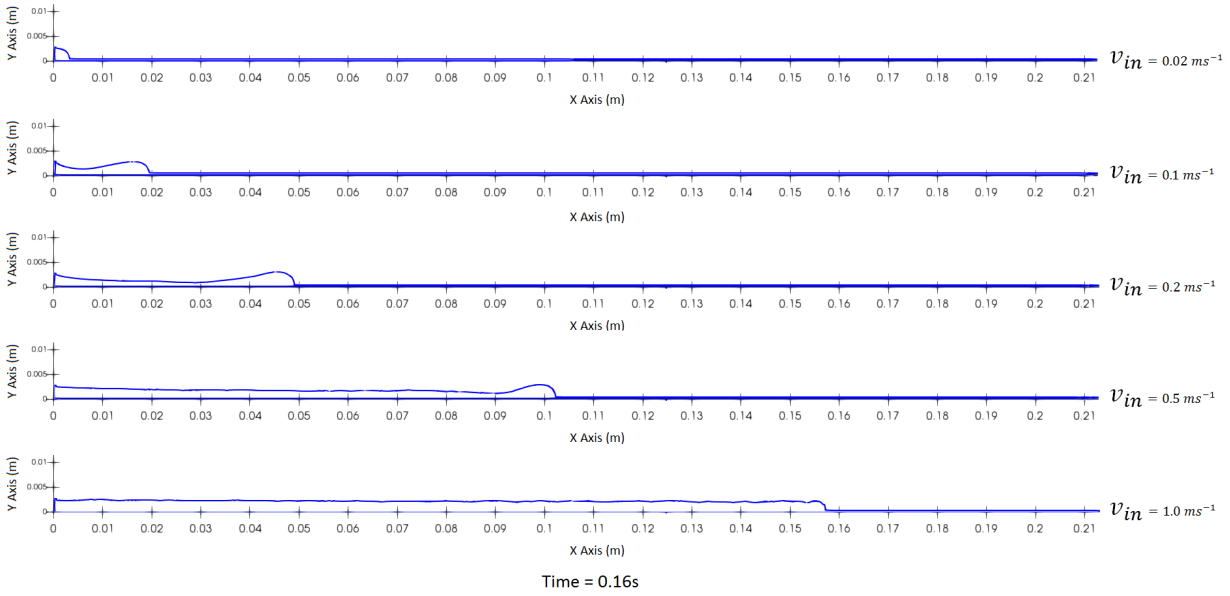

FIGURE 7.30: The evolution snapshot of thin film on a solid substrate at $\psi = 70°$ inclination using inlet velocity, 0.02ms^{-1}, 0.1ms^{-1}, 0.2ms^{-1}, 0.5ms^{-1} and 1.0ms^{-1} respectively.

At time = 0.26s, Figure 7.33 shows that for the case $v_{in} = 0.5$ ms^{-1}, the advancing droplet (A) separates further and creates pearling's (F), (G) and (H) while the advancing rivulet front move closer to pearling (C). At $v_{in} = 0.2$ ms^{-1}, droplet (D)

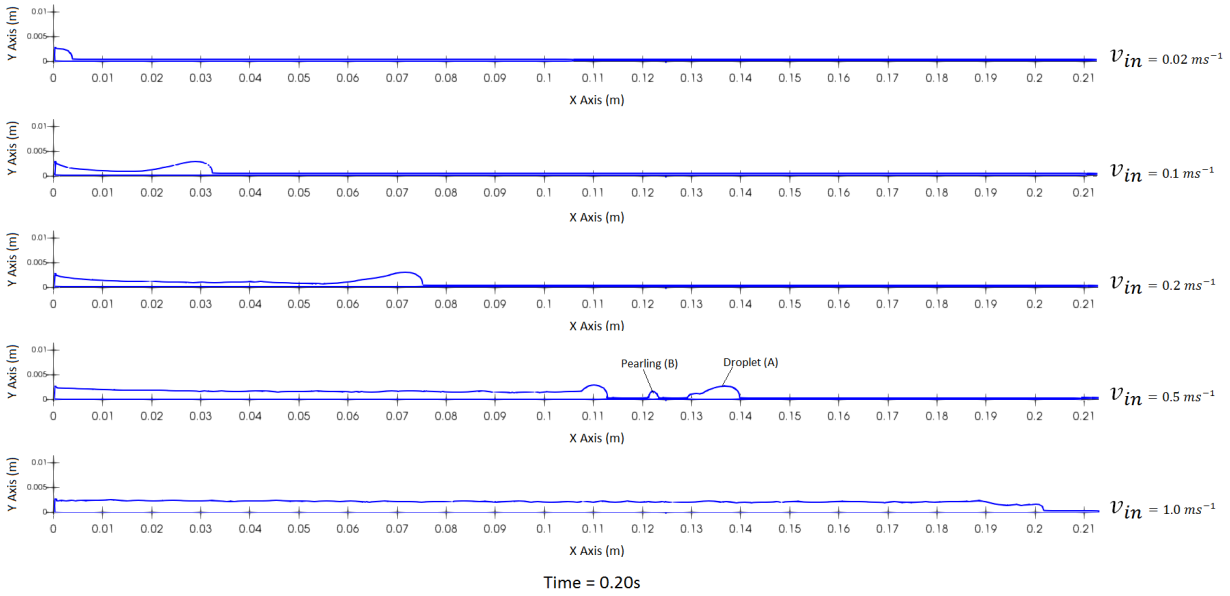

FIGURE 7.31: The evolution snapshot of thin film on a solid substrate at $\psi = 70°$ inclination using inlet velocity, 0.02ms^{-1}, 0.1ms^{-1}, 0.2ms^{-1}, 0.5ms^{-1} and 1.0ms^{-1} respectively.

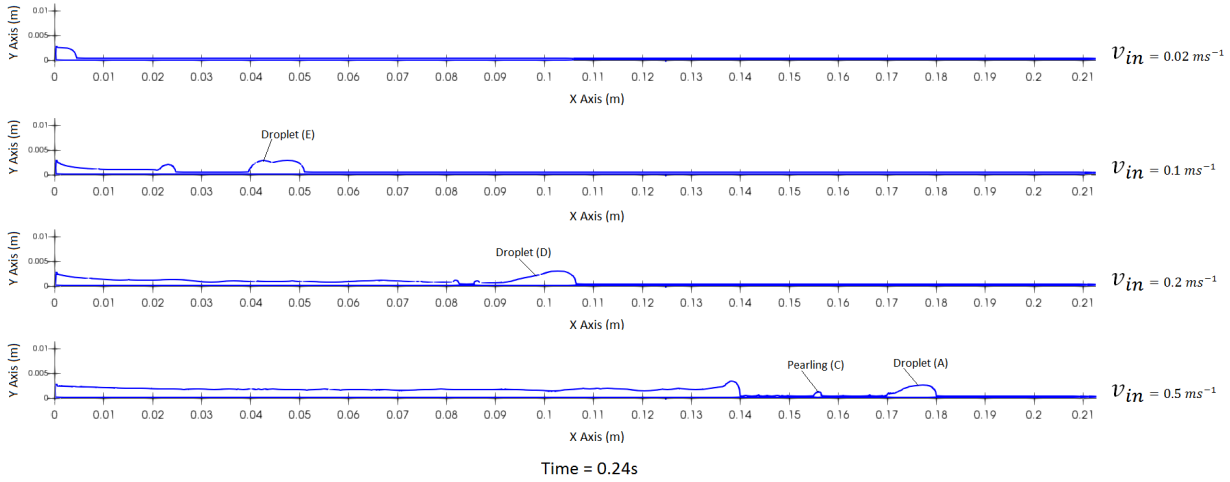

FIGURE 7.32: The evolution snapshot of thin film on a solid substrate at $\psi = 70°$ inclination using inlet velocity, 0.02ms^{-1}, 0.1ms^{-1}, 0.2ms^{-1} and 0.5ms^{-1}, respectively. *Note that the rivulet with $v_{in} = 1.0\text{ms}^{-1}$ has exit the substrate.

begins necking and stretches in preparation to leave subsequent pearling's, whereas the advancing rivulet front breaks, thus forming droplet (I) with an accompanying long tail. Droplet (E) for $v_{in} = 0.1$ ms^{-1} migrates further downstream carried by the positive momentum from the earlier breakage while the rivulet front recovers from the negative momentum effect as more of the incoming fluid increases its mass and volume to move forward. Also the rivulet with $v_{in} = 0.02$ ms^{-1} continue to advanced forward.

Figure 7.34 shows the snapshot at time = 0.32s for the case when $v_{in} = 0.5$ ms^{-1}, droplet (A) and pearlings (F) has left the domain while pearlings (G) and (H) moved closer to each besides the advancing rivulet front which continues its way forward, consuming pearlings (C) along its path. For $v_{in} = 0.2$ ms^{-1}, the model predicts the formation of multiple smaller droplets from (D) and (I). The former created pearlings (J) and (K), while the latter leaves pearlings (L). Also droplet (M) is produced by the advancing rivulet front, which stalls as it slowly replenishes its mass before moving forward again. Droplet (E) and its accompanying rivulet on the left for $v_{in} = 0.1$ ms^{-1}, continues its migration to the right of the domain. The rivulet with $v_{in} = 0.02$ ms^{-1} is still developing and continues to grow in size.

At time = 0.38s in Figure 7.35, the rivulet together with the pearlings for the case with $v_{in} = 0.5$ ms^{-1} have exited the domain without any observable shape changes. However, in the case where $v_{in} = 0.2$ ms^{-1}, the larger droplet (D) has migrated out of the right boundary but its pearlings (J) and (K) moved much slower due to their size. The ensuing larger droplet (I) catches up followed by a slow moving pearling (L) and faster moving droplet (M). The coalesce of droplet (I), pearlings (K) and (J) and similarly droplet (M) and pearlings (L) is observed in Figure 7.36 and 7.37 during which the droplet (E) escapes the domain at time = 0.43s while the rivulet front with $v_{in} = 0.1$ ms^{-1} and that of $v_{in} = 0.02$ ms^{-1} propagate to the right of the domain. The snapshot in Figure 7.38 shows parts of the merged droplet of (IKJ) exiting the domain, droplet (ML) moving forward and the formation beginnings of droplet (N) and due to the breakage at the neck, the rivulet front is pushed slightly backward. Note that the long tail of the droplet (N) increases the likelihood of breakage due to Rayleigh-Taryor-like instability. The formation of droplet (O) come as a result of the instability caused by the creation of (N) as seen in Figure 7.39 at time = 0.48s. During the same period, the rivulet with $v_{in} = 0.1$ ms^{-1} and $v_{in} = 0.02$ ms^{-1} advanced forward whereas the remaining part of the merged droplet (IKJ) with $v_{in} = 0.2$ ms^{-1} leaves the domain while droplet (ML) continues to move forward.

Figure 7.40 shows that at time = 0.56s, for the case where v_{in} = 0.2 ms^{-1}, droplet (N) has separated to create pearling (P) while itself advanced toward the product of droplet (ML) which at this time has exited the domain. Its rivulet front and droplet (O) move forward whereas for the case with v_{in} = 0.1 ms^{-1}, the rivulet breaks off at its neck and create droplet (Q) that migrate toward the right of the system. At the same time, the rivulet with v_{in} = 0.02 ms^{-1} just begin to show signs of necking. In Figure 7.41 at time = 0.70s, the droplets (N) and (Q) has exited the system whereas the bigger and faster droplet (O) has collided with the slower pearling (P) while its rivulet has advanced to the right of the domain along with the rivulet with v_{in} = 0.1 ms^{-1}. The rivulet with v_{in} = 0.02 ms^{-1} break off for the first time at the neck and this induced a positive momentum on the created droplet (R). At time = 0.74s in Figure 7.42, the colliding pearling (P) and droplet (O) both have exited the domain while its rivulet and that of v_{in} = 0.1 ms^{-1} and droplet (R) propagate to the right of the domain. From Figure 7.43 at time = 0.78s, the rivulet with v_{in} = 0.2 ms^{-1} and v_{in} = 0.1 ms^{-1} have both escaped from the substrate, thus will be eliminated from subsequent plots. The only remaining rivulet and droplet (R) with v_{in} = 0.02 ms^{-1} advanced forward and at time = 1.16s, this droplet (R) exit the substrate while the rivulet experience more necking leading to a second breakup into droplet (S) at time = 1.28s. This process is repeated again in the same similar manner as before with the droplet escaping and rivulet forming another droplet till time = 1.83s.

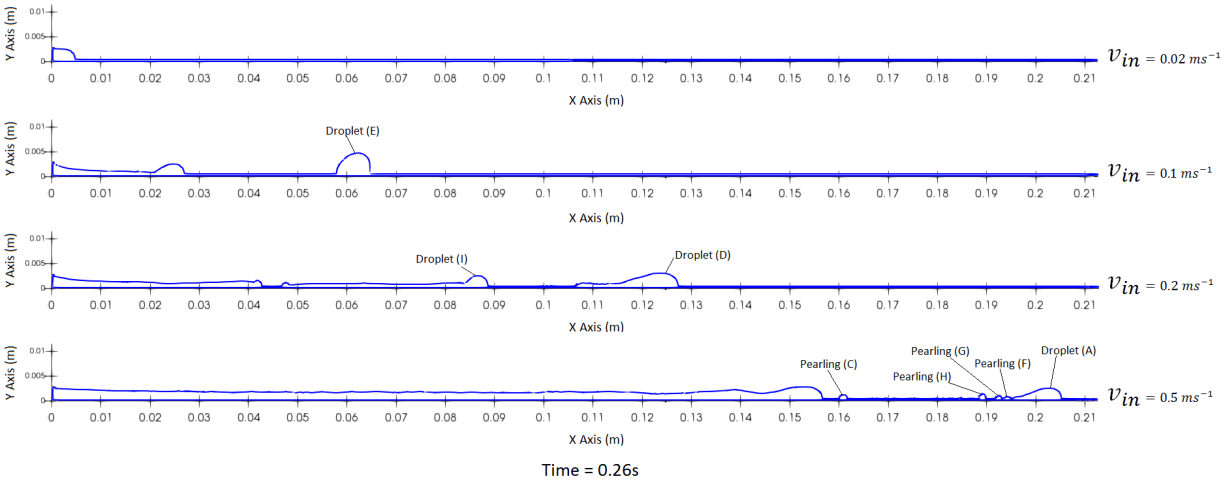

FIGURE 7.33: The evolution snapshot of thin film on a solid substrate at $\psi = 70°$ inclination using inlet velocity, 0.02ms^{-1}, 0.1ms^{-1}, 0.2ms^{-1} and 0.5ms^{-1} respectively.

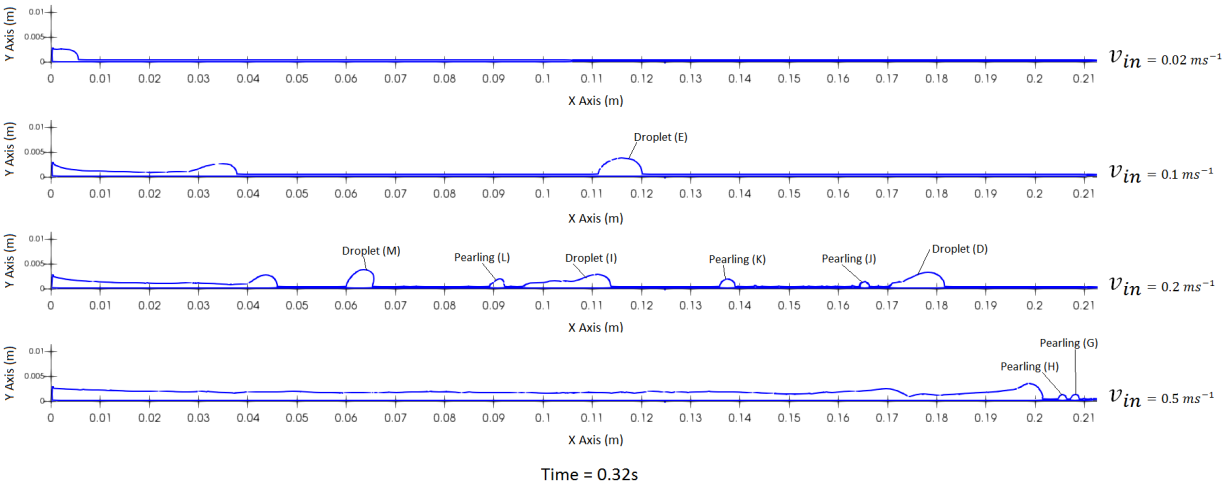

FIGURE 7.34: The evolution snapshot of thin film on a solid substrate at $\psi = 70°$ inclination using inlet velocity, 0.02ms^{-1}, 0.1ms^{-1}, 0.2ms^{-1} and 0.5ms^{-1} respectively. *Note that the bigger droplet with $v_{in} = 0.5\text{ms}^{-1}$ has exit the substrate.

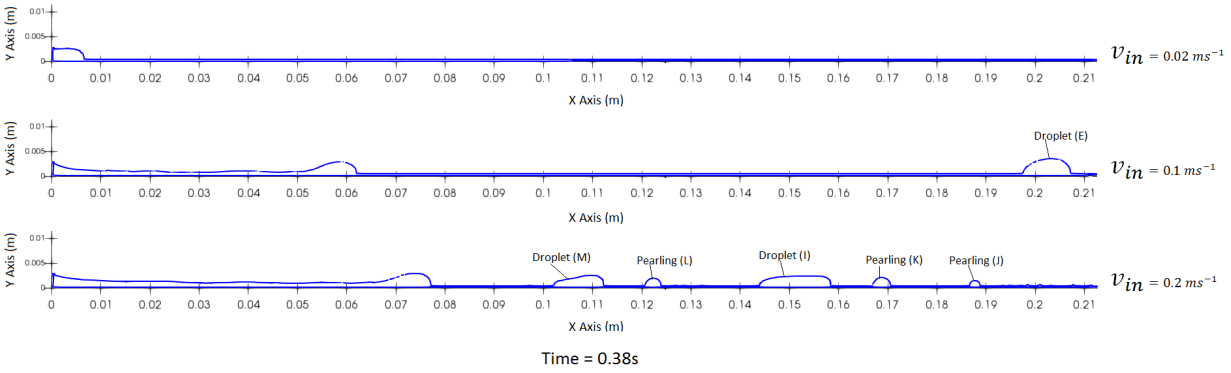

FIGURE 7.35: The evolution snapshot of thin film on a solid substrate at $\psi = 70°$ inclination using inlet velocity, 0.02ms^{-1}, 0.1ms^{-1} and 0.2ms^{-1} respectively. *Note that the rivulet together with its tiny droplets with $v_{in} = 0.5\text{ms}^{-1}$ has exit the substrate. Also the first droplet with $v_{in} = 0.2\text{ms}^{-1}$ has exit the substrate.

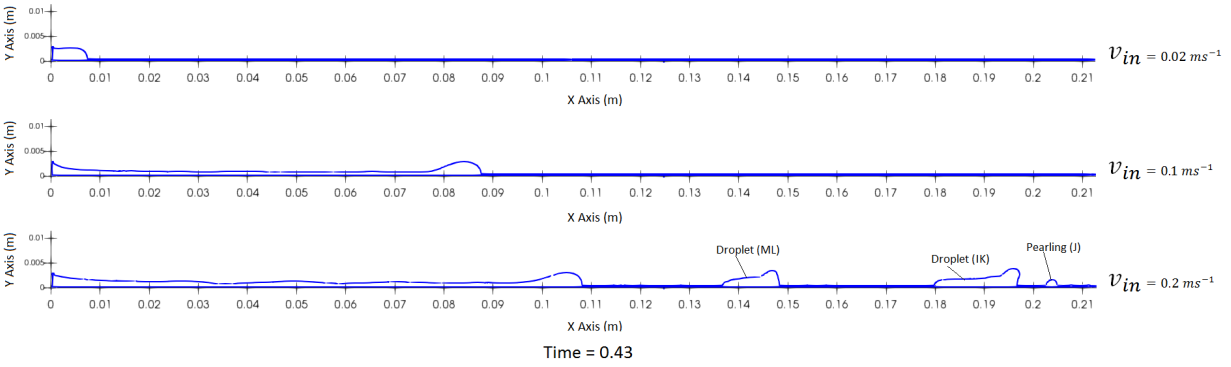

FIGURE 7.36: The evolution snapshot of thin film on a solid substrate at $\psi = 70°$ inclination using inlet velocity, 0.02ms^{-1}, 0.1ms^{-1} and 0.2ms^{-1} respectively. *Note that the first droplets with $v_{in} = 0.1\text{ms}^{-1}$ has exit the substrate.

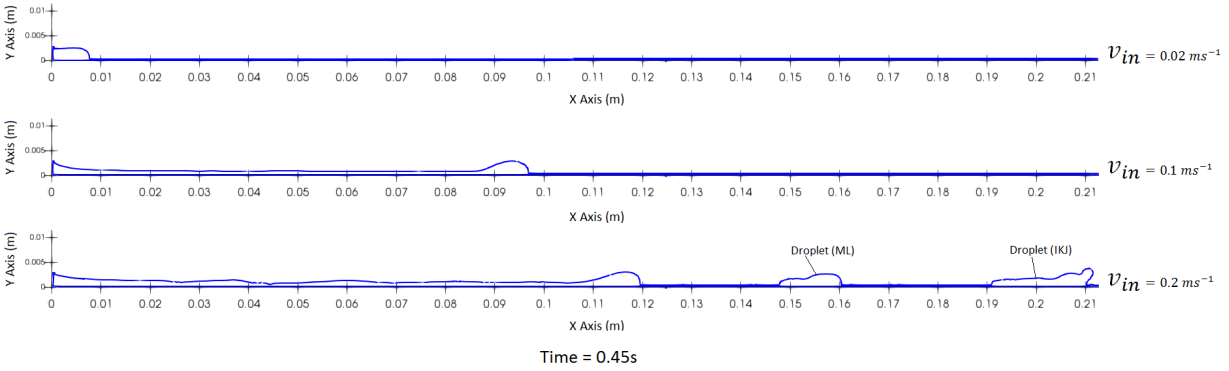

FIGURE 7.37: The evolution snapshot of thin film on a solid substrate at $\psi = 70°$ inclination using inlet velocity, 0.02ms^{-1}, 0.1ms^{-1} and 0.2ms^{-1} respectively.

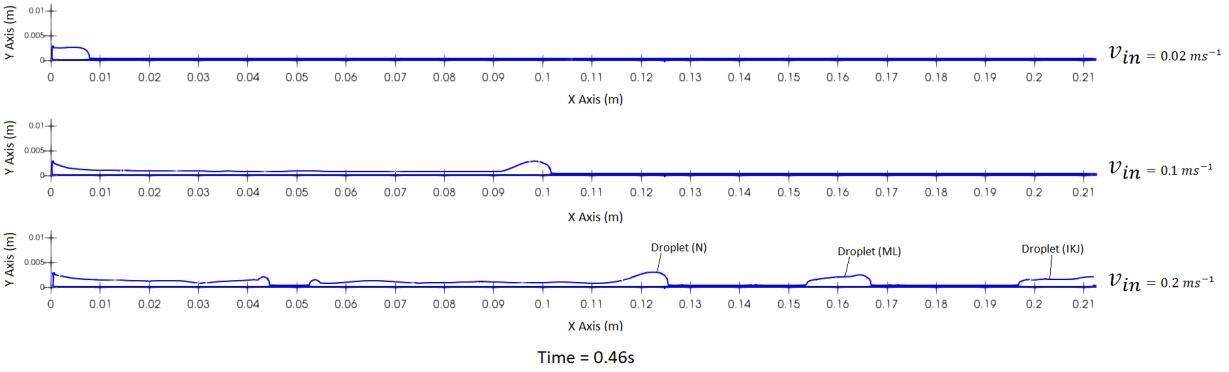

FIGURE 7.38: The evolution snapshot of thin film on a solid substrate at $\psi = 70°$ inclination using inlet velocity, 0.02ms^{-1}, 0.1ms^{-1} and 0.2ms^{-1} respectively.

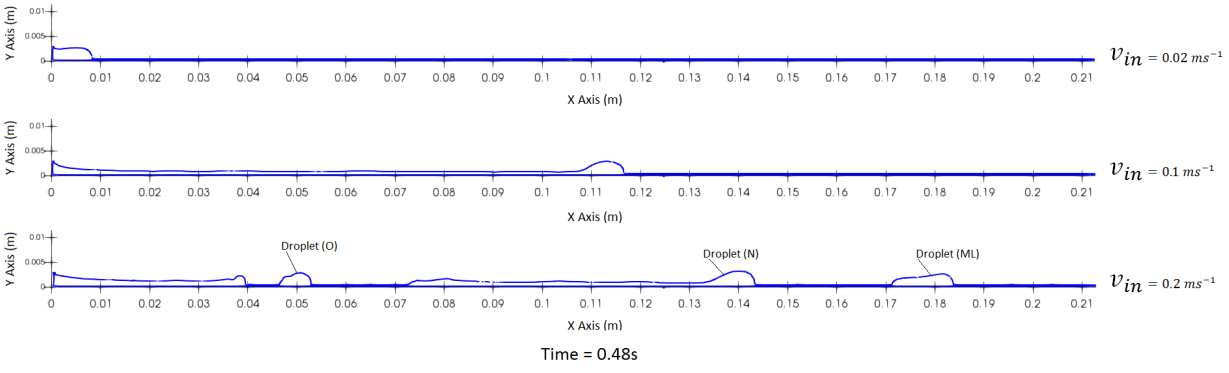

FIGURE 7.39: The evolution snapshot of thin film on a solid substrate at $\psi = 70°$ inclination using inlet velocity, 0.02ms^{-1}, 0.1ms^{-1} and 0.2ms^{-1}, respectively. *Note that more of the bigger droplet with $v_{in} = 0.2\text{ms}^{-1}$ has exit the substrate.

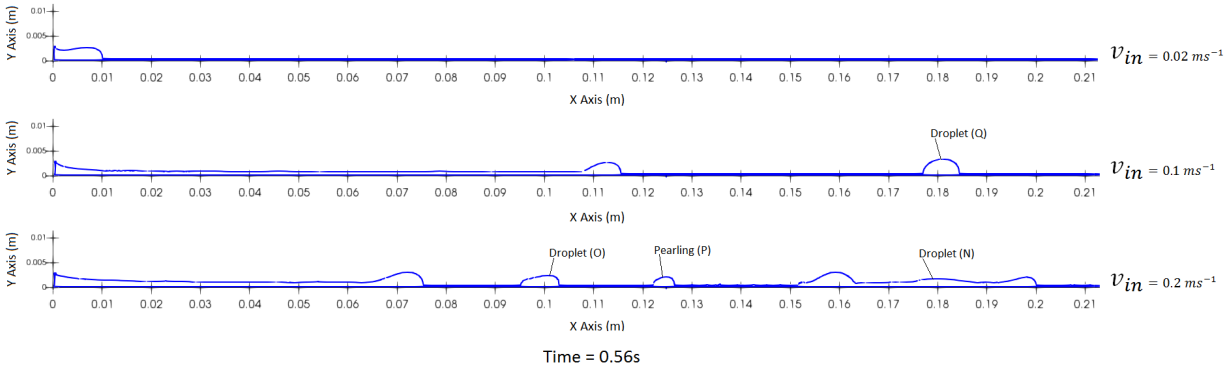

FIGURE 7.40: The evolution snapshot of thin film on a solid substrate at $\psi = 70°$ inclination using inlet velocity, 0.02ms^{-1}, 0.1ms^{-1} and 0.2ms^{-1}, respectively. *Note that more of the bigger droplet with $v_{in} = 0.2\text{ms}^{-1}$ has exit the substrate.

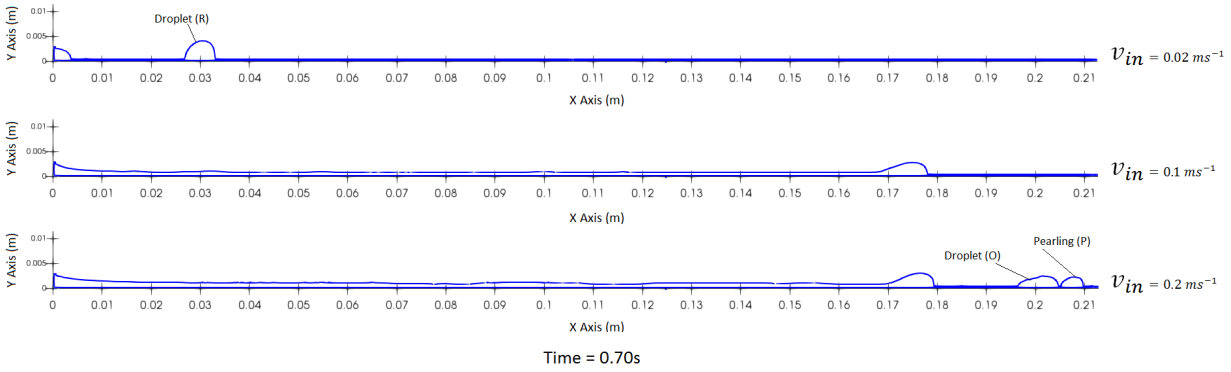

FIGURE 7.41: The evolution snapshot of thin film on a solid substrate at $\psi = 70°$ inclination using inlet velocity, 0.02ms^{-1}, 0.1ms^{-1} and 0.2ms^{-1} respectively. *Note that some of the bigger droplet with $v_{in} = 0.1\text{ms}^{-1}$ and $= 0.2\text{ms}^{-1}$ has exit the substrate.

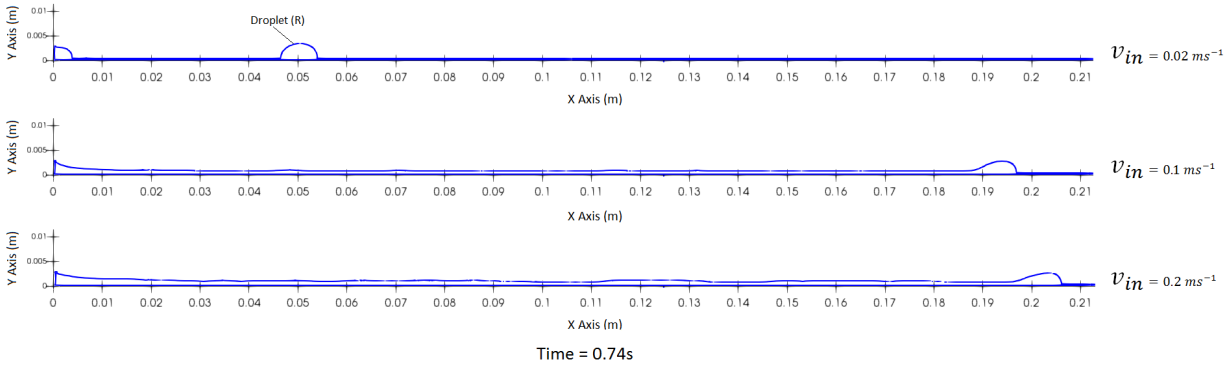

FIGURE 7.42: The evolution snapshot of thin film on a solid substrate at $\psi = 70°$ inclination using inlet velocity, 0.02ms^{-1}, 0.1ms^{-1} and 0.2ms^{-1} respectively. *Note that the last bigger droplet with $v_{in} = 0.2\text{ms}^{-1}$ has exit the substrate.

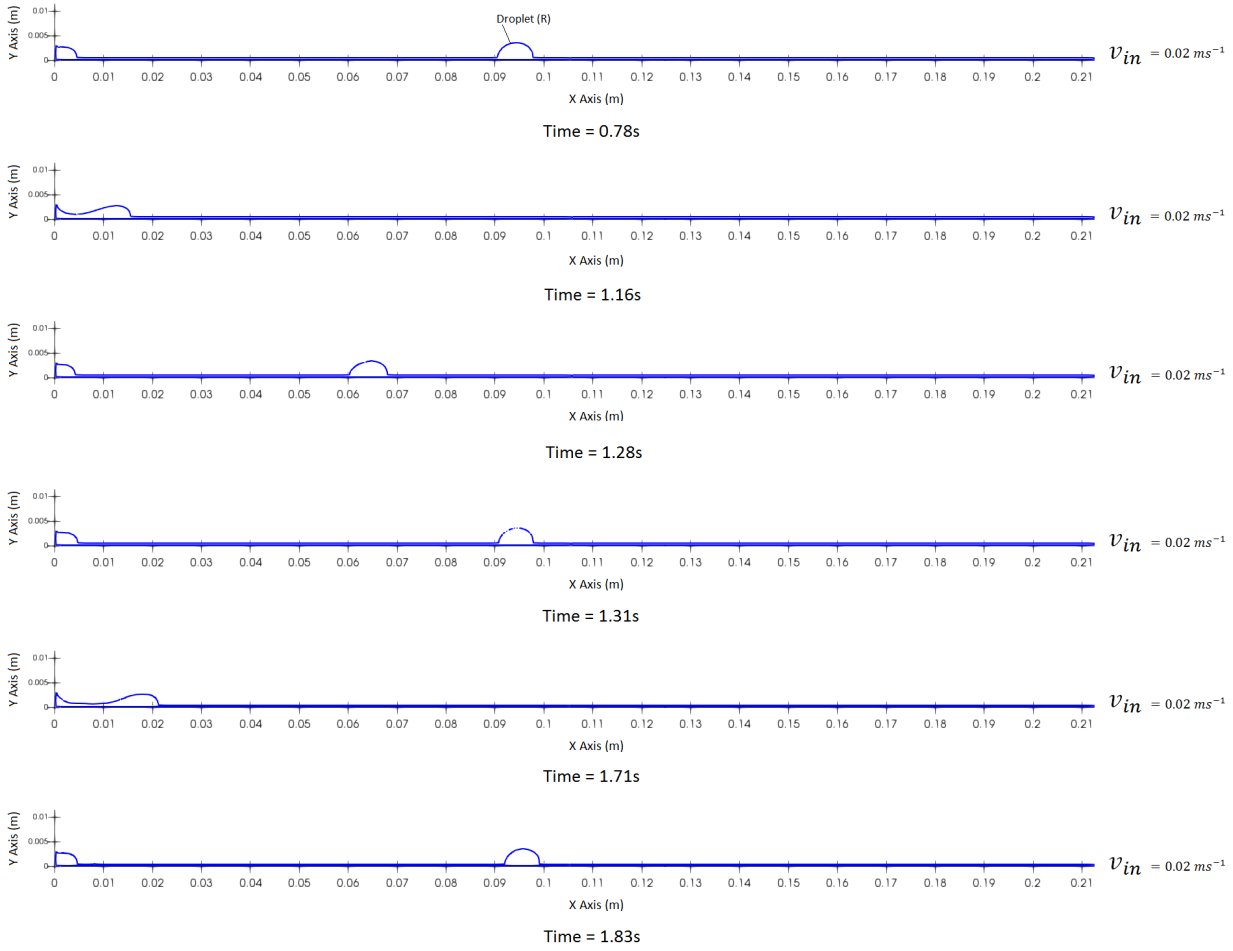

FIGURE 7.43: The evolution snapshot of thin film on a solid substrate at $\psi = 70°$ inclination using inlet velocity, 0.02ms^{-1}, 0.1ms^{-1} and 0.2ms^{-1} respectively. *Note that the rivulet with $v_{in} = 0.1\text{ms}^{-1}$ and 0.2ms^{-1} have both exit the substrate.

To have a qualitative comparison, the SPH result obtained are compared with the work of Schmuki and Laso [61] as shown in Figure 7.44 to 7.45. As it can be seen from the SPH result in Figure 7.44 (a) top view, there are different droplet types generated as the rivulet front evolves. These droplet types may be due to the higher slope of the substrate as well as the inlet flow rate of the fluid. Therefore, based on the above argument, it can be said that these SPH results are in good agreement with the experiment qualitatively.

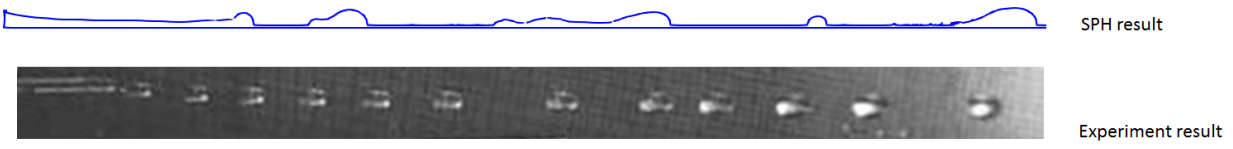

(a)

FIGURE 7.44: The evolution snapshot of rivulet, droplets results for SPH on top and experiment [61] below.

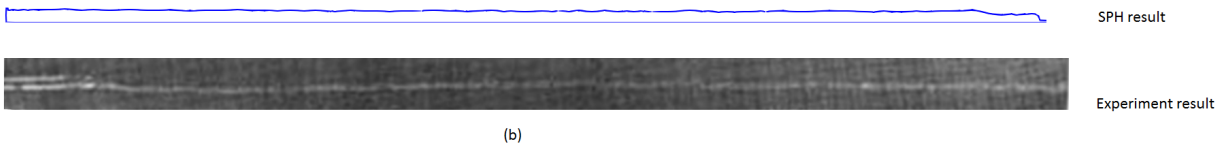

FIGURE 7.45: The evolution snapshot of straight linear rivulet result for SPH on top and experiment [61] below.

Figure 7.46 (a) shows the evolution of the advancing front of migrating rivulets at different inlet flow conditions similar to that when $\psi = 30°$. The formation of a detached droplet, similar to what happened when $\psi = 30°$ or $50°$ is clearly highlighted for this test case when $\psi = 70°$.

As clearly shown, the rivulet undergo thinning and necking, which eventually lead to breakage at lower inlet velocities to form pearling or droplets, which then coalescence with each other as they move downstream is same as what happened when $\psi = 50°$. However, at certain inlet flow rate, for example $v_{in} = 0.2$ ms^{-1}, the pearlings and droplets formations are occurring more frequently as shown in the detailed Figure 7.47 (a) to (d), where some of these pearlings and droplets combine to form bigger droplet.

Figure 7.46 (b) delineate the necking thickness with time of the initial rivulet at $\psi = 70°$ for various inlet flow conditions similar to $\psi = 30°$. Again, it clearly demonstrate that the necking effect also decrease compared to when $\psi = 30°$ or $50°$ for most of the inlet velocities. This further shows that as the inclination angle increases, the necking and thinning becomes more due to gravity effects.

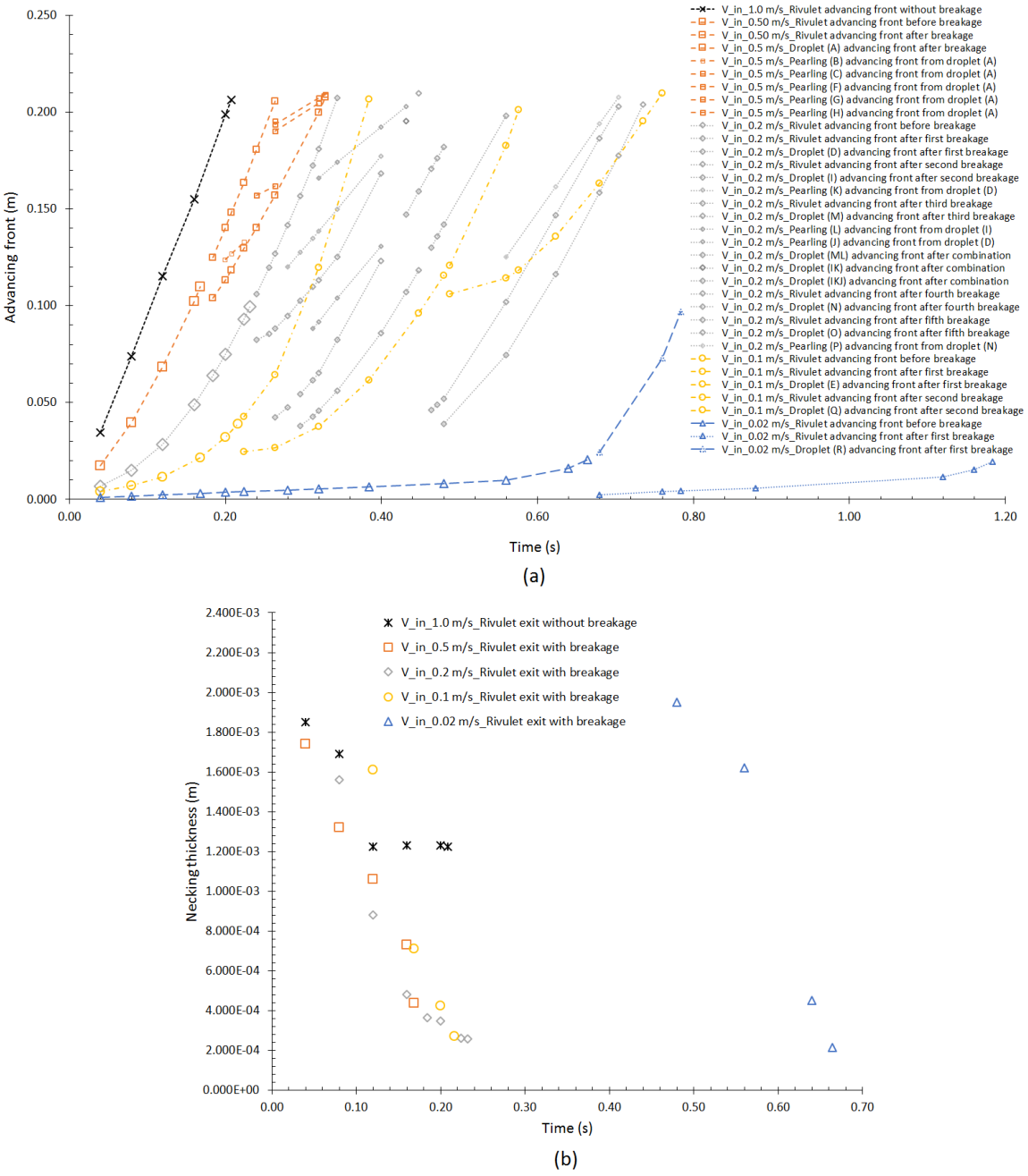

FIGURE 7.46: The evolution snapshot of (a) rivulet advancing front (b) necking thickness, at various inlet velocities between $v_{in} = 0.02\ \mathrm{ms}^{-1}$ to $1.0\ \mathrm{ms}^{-1}$ at $\psi = 70°$.

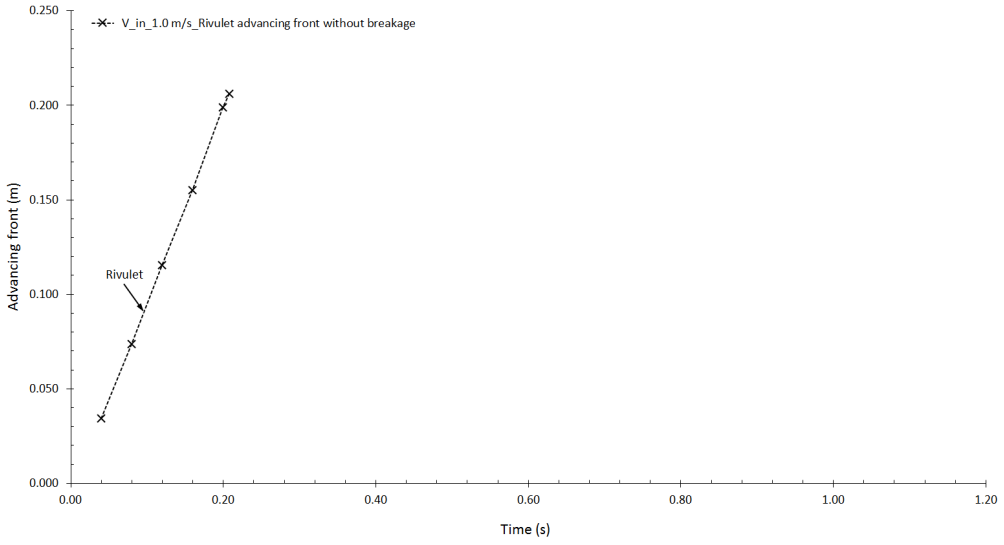
V_in_1.0 m/s_Rivulet advancing front without breakage
Rivulet
Advancing front (m)
Time (s)

(a)

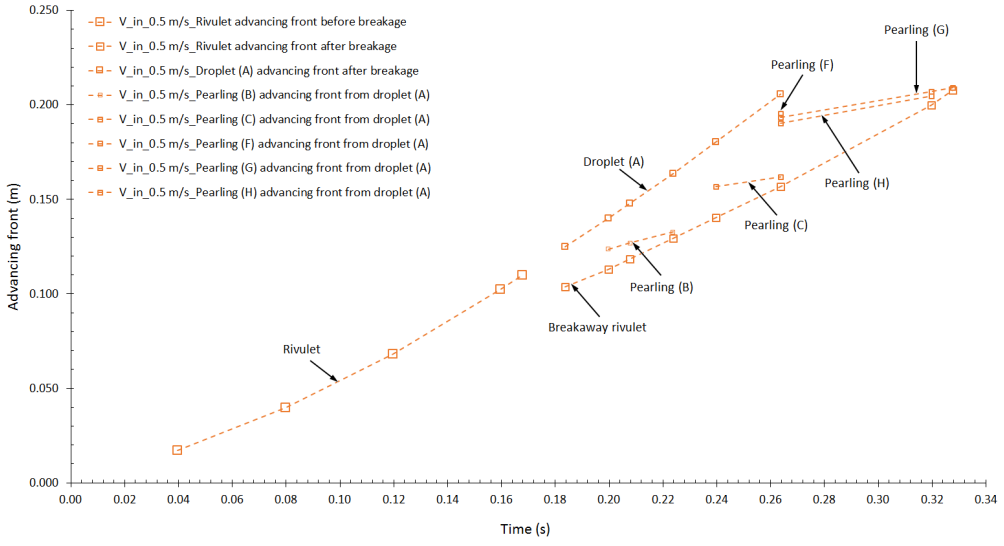
V_in_0.5 m/s_Rivulet advancing front before breakage
V_in_0.5 m/s_Rivulet advancing front after breakage
V_in_0.5 m/s_Droplet (A) advancing front after breakage
V_in_0.5 m/s_Pearling (B) advancing front from droplet (A)
V_in_0.5 m/s_Pearling (C) advancing front from droplet (A)
V_in_0.5 m/s_Pearling (F) advancing front from droplet (A)
V_in_0.5 m/s_Pearling (G) advancing front from droplet (A)
V_in_0.5 m/s_Pearling (H) advancing front from droplet (A)
Pearling (G)
Pearling (F)
Droplet (A)
Pearling (H)
Pearling (C)
Pearling (B)
Breakaway rivulet
Rivulet
Advancing front (m)
Time (s)

(b)

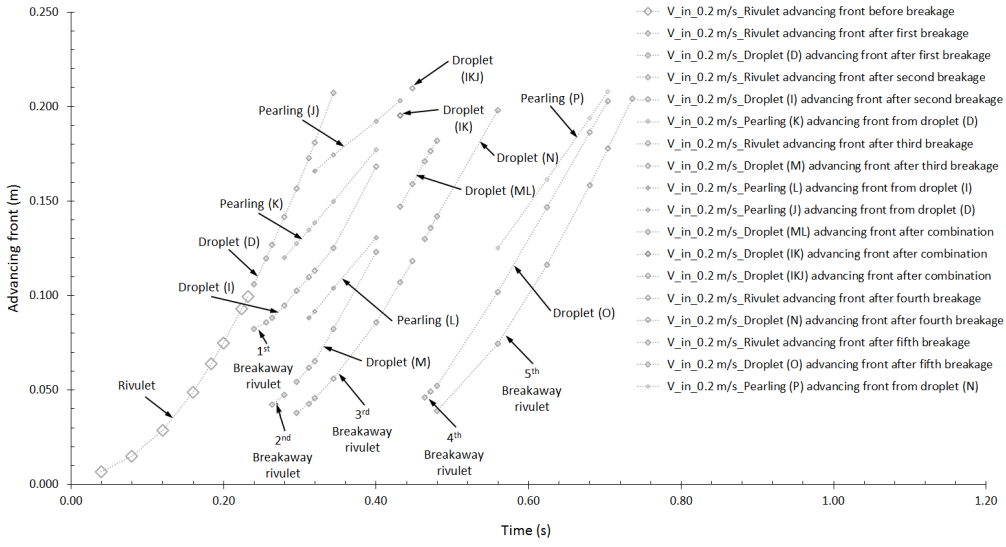
V_in_0.2 m/s_Rivulet advancing front before breakage
V_in_0.2 m/s_Rivulet advancing front after first breakage
V_in_0.2 m/s_Droplet (D) advancing front after first breakage
V_in_0.2 m/s_Rivulet advancing front after second breakage
V_in_0.2 m/s_Droplet (I) advancing front after second breakage
V_in_0.2 m/s_Pearling (K) advancing front from droplet (D)
V_in_0.2 m/s_Rivulet advancing front after third breakage
V_in_0.2 m/s_Droplet (M) advancing front after third breakage
V_in_0.2 m/s_Pearling (L) advancing front from droplet (I)
V_in_0.2 m/s_Pearling (J) advancing front from droplet (D)
V_in_0.2 m/s_Droplet (ML) advancing front after combination
V_in_0.2 m/s_Droplet (IK) advancing front after combination
V_in_0.2 m/s_Droplet (IKJ) advancing front after combination
V_in_0.2 m/s_Rivulet advancing front after fourth breakage
V_in_0.2 m/s_Droplet (N) advancing front after fourth breakage
V_in_0.2 m/s_Rivulet advancing front after fifth breakage
V_in_0.2 m/s_Droplet (O) advancing front after fifth breakage
V_in_0.2 m/s_Pearling (P) advancing front from droplet (N)
Droplet (IKJ)
Pearling (J)
Droplet (IK)
Pearling (P)
Droplet (N)
Droplet (ML)
Pearling (K)
Droplet (D)
Droplet (I)
Pearling (L)
Droplet (O)
1st Breakaway rivulet
Droplet (M)
5th Breakaway rivulet
Rivulet
3rd Breakaway rivulet
2nd Breakaway rivulet
4th Breakaway rivulet
Advancing front (m)
Time (s)

(c)

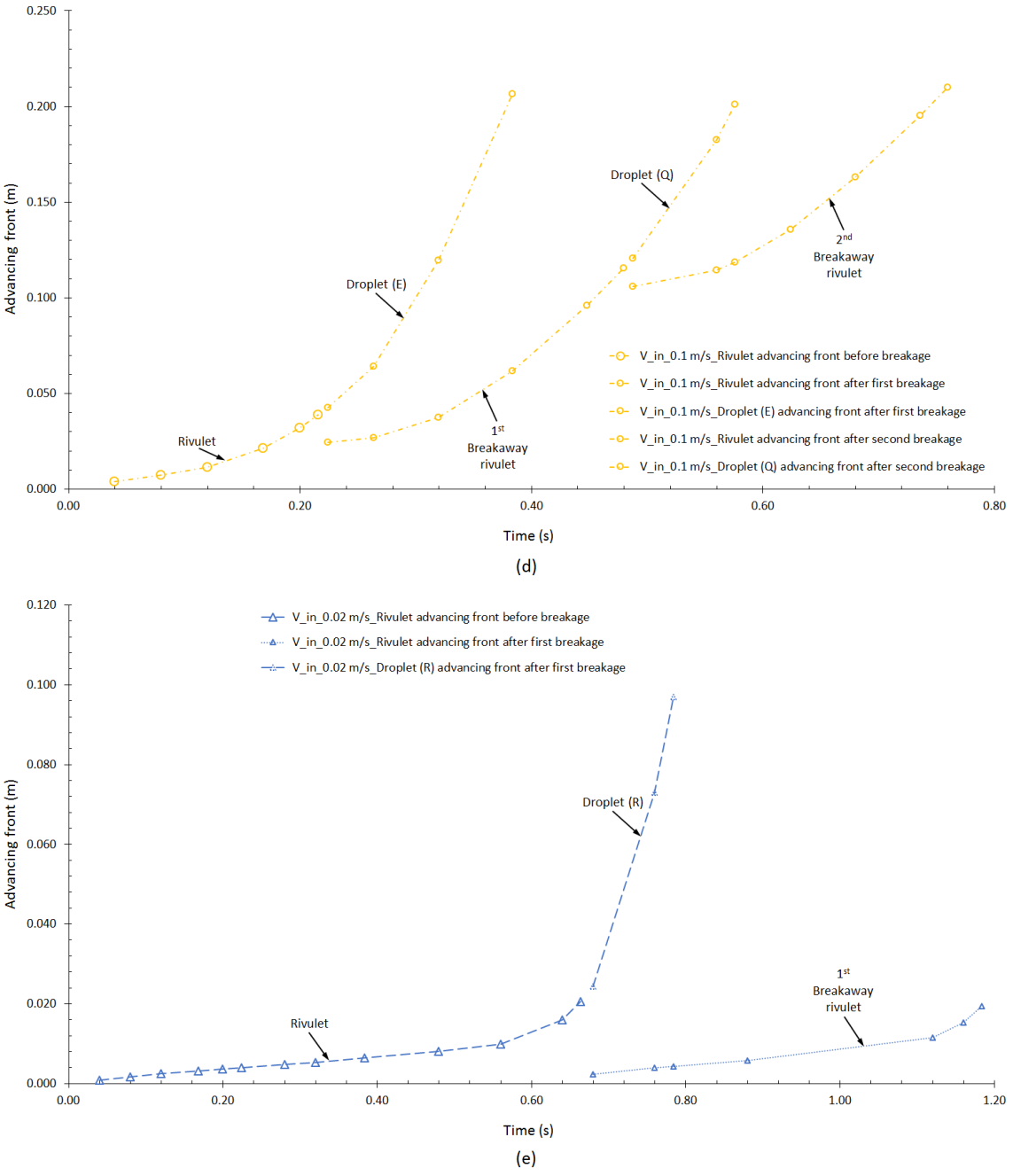

FIGURE 7.47: The exploded evolution snapshot of rivulet advancing front at various inlet velocities between $v_{in} = 0.02$ ms^{-1} to 1.0 ms^{-1} at $\psi = 70°$.

Chapter 8

Conclusion and Future Work

"Life can only be understood backwards; but it must be lived forwards."

Søren Kierkegaard, (1813-1855).

8.1 Conclusions

Contributions

- The implementation of the CSF model for single-phase with just one kernel with real fluid properties using SPH, thus saving computational time.
- The implementation of the disjoining pressure model for the first time in SPH with ease, thus leading to higher contact angle up to 130° for flow phenomena of droplet spreading.
- The application of SPH was demonstrated for droplet flow on a stair-like substrate, thus leading to the capturing of patches of small droplet at the foot of the stairs.
- The application of SPH was demonstrated for the first time on thin film flow problems. Flow phenomena such as rivulet breaking into droplets, thus leading to the formations of pearling was explored and the developed SPH methodology showed good qualitative agreements.

In this present thesis, the Weakly Compressible Smoothed Particle Hydrodynamics (WCSPH) approach for two dimensional flows is implemented here for ease of simplicity and also to highlight its capabilities. The major advantage of SPH when compared to the mesh-based traditional methods is its ability to handle large deformations especially when simulating highly non-linear flows, such as wave breaking problems, fluid interactions with structures as well as those between different multiple fluids. In the SPH model, surface tension phenomena is performed using only the single-phase (fluid) for droplet and thin film rivulet flows. Furthermore, due to SPH mesh-free nature, robustness and straightforwardness, no special treatment is required for simulating flows on wet/dry surfaces with complicated geometries. Three different kernels such as the cubic, quadratic and fourth order kernel functions (Quintic and Wendland) were used in the simulations (their applicability is dependent on the problem at hand), along with a KD-tree search algorithm is employed for finding neighbouring particles. The conservation equations in the solver are implemented and solved in a modular fashion with the option to include additional physical interactions readily. Time integration is performed using the Verlet scheme with the addition of an Euler step at every number of iterations to ensure good coupling between the kinematic components.

The developed SPH solver is validated over a series of test cases in Chapter 4 to ensure accurate physics are captured and is numerically correct. These include test cases such as particle bouncing inside a box where the dynamics boundary condition is reaffirmed and the results are compared against analytical solutions. Both the subsequent test cases for Couette flow and Poiseuille flow checks the implemented viscosity model and flow with periodic boundary conditions, while the following dam break test case examines a large free surface problem with good comparisons made against experimental ones. The lid driven cavity test case explore the flexibility of the SPH methodology with increasing Reynold numbers and is validated against known results reported in literature using mesh based methods.

The simulation of a droplet in the absence of air (vacuum) was investigated in Chapter 5 using two modified surface tension models which are IIF and CSF models. The IIF model shows that the simulated droplet appeared with unphysical rings and clustering. To resolve these issues, two different approaches (remedy) were considered; the first approach uses a quadratic kernel function only in the acceleration terms due to the pressure term; the second approach introduces the repulsive force as an external force. The latter approach showed that it works best in resolving the clumping issue,

couple with the fact that the particles within the droplet are now well ordered, and because of this, it is used in this thesis. The second IIF model explores the introduction of a kernel function into the model to approximate surface tension force; the simulated droplet was found to be too stiff, thus making it difficult to be controlled and used for real physical problems. In the CSF models, the free surfaces are tracked and this required numerous computational steps to calculate the curvature of each particle located near the free surface, but this is not necessary with the IIF approach. However, the CSF approach does not perform well with shapes with sharp corners, thus making it unphysical. It was found that using a Wendland kernel helped to reduce particle disorder and thus negating the need for an artificial repulsive force, thus making it adaptable for real phenomena. In the CSF model, a modified curvature formulation for single-phase was implemented and the results obtained agrees with theoretical results, especially at high resolution. While the CSF model does not need special treatments to resolve particle clustering unlike the IIF model, the period of droplet oscillation obtained from both models are in good agreement with analytical results.

In Chapter 6, a simple droplet spread on a horizontal substrate problem was investigated to explore wetting capabilities of the SPH methodology with varying contact angles. In this study, three approaches were proposed which are the IIF, CLF and disjoining pressure approaches. For the IIF approach, the contact angle was control by simply tuning the interaction strength (s_{sf}) between the fluid and substrate particles. Other obvious advantage of this approach is that, the free surface particles do not need to be tracked. In the CLF approach, the contact angle was control by applying CLF force to the free surface particles close to the substrate particles while the CSF approach were applied to the remaining free surface particles. For the disjoining pressure approach, the contact angle is control by applying a disjoining pressure force to both the fluid and substrate particles near the interface. This approach, is applied for the first time in SPH, and the results showed good agreement to those obtained previously from the literature. However, the disjoining pressure scheme requires tracking of the free surface and the solid-fluid interface before it can be applied.

Finally, in Chapter 7, the contact angle hysteresis was studied using the IIF method due to its simplicity and easy implementation with the added stability observed for droplet flows with very high contact angles. This approach is used to study droplet movement on a horizontal and stair-like substrate to explore the capability of the SPH methodology to capture and handle the dynamics of contact angle changes. The

results showed good qualitative agreement with those observed experimentally from experiments and further work is required to improve the accuracy of the developed scheme. The test case also investigates the flow of a thin liquid rivulet film on an inclined substrate. The results obtained showed great potential of the SPH methodology, exhibiting good physical rivulet characteristics similar to those expected from experiments. The author believe that the above test case has not been explored before, using SPH and little research was done using traditional mesh based methods due to the complex nature of the problem and difficulty with using the latter approach.

8.2 Future Work

This section profiles some suggestions that can be done to improve the developed SPH model and solver:

- In order to capture highly stable contact angle greater than 90 degrees using the CLF approach, improvements need to be made to the free surface tracking mechanism. The need to know why it is unstable at contact angles higher than 90 degrees has to be investigated.
- In the disjoining pressure approach, the small gap due to pressure differences between the substrate and droplet need to be examined in more detail so as to capture highly stable contact angle greater than 90 degrees.
- A 3-dimensional implementation of the above SPH solver and models will provide better accuracy for capturing flow with surface tension dominated effects. The extension to the third dimension is readily extendable methodology-wise, but care should be taken to ensure that the developed single phase surface tension models include these effects.
- The computational time can be speedup by implementing parallel computation using multiple CPUs or with GPUs.
- A study of droplet and thin film rivulet flows and their pearling formations on inclined planes should be examined in detail as SPH provides not only tracking of fluid evolution throughout the simulation but also within the movement of fluid within, which has vast applications in mixing and transport processes.

Appendix A

Kernels and its derivatives

A.1 Poly6 Kernel with 2D and 3D normalizer

Given the poly6 kernel with the function:

$$f = (h^2 - r^2)^3. \tag{A.1}$$

Then the poly6 kernel is given by:

$$W_{poly6}(|\mathbf{r}|, h) = \frac{1}{c} f. \tag{A.2}$$

Therefore, let the $2D$ and $3D$ normalizer be given as:

$$\alpha_{1_{2D}} = \frac{1}{c_{2D}} \quad \text{and,} \tag{A.3}$$

$$\alpha_{1_{3D}} = \frac{1}{c_{3D}} \quad \text{respectively.} \tag{A.4}$$

Now, for a **2D** case, we have:

$$
\begin{aligned}
c_{2D} &= \int_0^h 2\pi r f dr, \\
&= \int_0^h 2\pi r (h^2 - r^2)^3 dr, \\
&= \int_0^h 2\pi r (h^6 - 3h^4 r^2 + 3h^2 r^4 - r^6) dr \quad \text{by expanding } (h^2 - r^2)^3, \\
&= \int_0^h 2\pi (h^6 r - 3h^4 r^3 + 3h^2 r^5 - r^7) dr \quad \text{multiplying through by } r, \\
&= 2\pi \Big| \frac{h^6 r^2}{2} - 3\frac{h^4 r^4}{4} + 3\frac{h^2 r^6}{6} - \frac{r^8}{8} \Big|_0^h, \\
&= 2\pi \Big| \frac{4h^6 r^2 - 6h^4 r^4 + 4h^2 r^6 - r^8}{8} \Big|_0^h, \\
&= \pi \Big[\frac{4h^8 - 6h^8 + 4h^8 - h^8}{4} \Big], \\
&= \frac{\pi h^8}{4}.
\end{aligned} \tag{A.5}
$$

Since the normalizer for the $2D$ case is given as $\alpha_1 = \frac{1}{c}$, Substituting equation (A.5) into equation (A.3), we have:

$$
\alpha_{1_{2D}} = \frac{4}{\pi h^8}. \tag{A.6}
$$

Similarly, for a **3D** case, we have:

$$
\begin{aligned}
c_{3D} &= \int_0^h 4\pi r^2 f dr, \\
&= \int_0^h 4\pi r^2 (h^2 - r^2)^3 dr, \\
&= \int_0^h 4\pi r^2 (h^6 - 3h^4 r^2 + 3h^2 r^4 - r^6) dr \quad \text{by expanding } (h^2 - r^2)^3, \\
&= \int_0^h 4\pi (h^6 r^2 - 3h^4 r^4 + 3h^2 r^6 - r^8) dr \quad \text{multiplying through by } r^2, \\
&= 4\pi \Big| \frac{h^6 r^3}{3} - 3\frac{h^4 r^5}{5} + 3\frac{h^2 r^7}{7} - \frac{r^9}{9} \Big|_0^h, \\
&= 4\pi \Big| \frac{315h^6 r^3 - 567h^4 r^5 + 405h^2 r^7 - 105r^9}{3 \times 5 \times 7 \times 9} \Big|_0^h, \\
&= 4\pi \Big[\frac{315h^9 - 576h^9 + 405h^9 - 105h^9}{3 \times 5 \times 7 \times 9} \Big], \\
&= \frac{64\pi h^9}{315}.
\end{aligned} \tag{A.7}
$$

Also the normalizer for the $3D$ case is given as $\alpha_{1_{3D}} = \frac{1}{c_{3D}}$, Substituting equation (A.7) into equation (A.4), we have:

$$\alpha_{1_{3D}} = \frac{315}{64\pi h^9}. \tag{A.8}$$

So therefore, in summary the poly6 kernel $W(|\mathbf{r}|, h)$ with its $2D$ and $3D$ normalizer is given as:

$$W_{poly6}(|\mathbf{r}|, h) = \alpha_D \begin{cases} (h^2 - r^2)^3 & 0 \leq r < h, \\ 0 & \text{otherwise}, \end{cases} \tag{A.9}$$

where α_D is $\frac{4}{\pi h^8}$ in $2D$ and $\frac{315}{64\pi h^9}$ in $3D$.

A.1.1 1st Derivative of Poly6 Kernel with 2D and 3D normalizer

We have the following for a $2D$ case:

$$\begin{aligned} \nabla &= \frac{\partial}{\partial x} i + \frac{\partial}{\partial y} j, \\ \nabla &= \frac{\partial}{\partial r}\frac{\partial r}{\partial x} i + \frac{\partial}{\partial r}\frac{\partial r}{\partial y} j, \\ \nabla W &= \frac{\partial W}{\partial r}.\frac{\partial r}{\partial x} i + \frac{\partial W}{\partial r}.\frac{\partial r}{\partial y} j, \end{aligned} \tag{A.10}$$

where

$$\vec{r} = xi + yj, \qquad \text{since } r = |\vec{r}|, \text{ we have} \tag{A.11}$$

$$r = (x^2 + y^2)^{1/2}. \tag{A.12}$$

So therefore,

$$\begin{aligned}\frac{\partial W_{poly6}}{\partial r} &= \frac{\partial}{\partial r}\left(\alpha_D(h^2-r^2)^3\right), \\ &= \alpha_D\frac{\partial}{\partial r}\left((h^2-r^2)^3\right), \quad \text{factorizing out } \alpha_D \text{ as a constant,} \\ &= \alpha_D\left(3(h^2-r^2)^2.(-2r)\right), \\ &= \alpha_D\left(-6r(h^2-r^2)^2\right). \end{aligned} \tag{A.13}$$

For the derivative of r with respect to x from equation (A.12), we have:

$$\begin{aligned}\frac{\partial r}{\partial x} &= \frac{\partial}{\partial x}\left((x^2+y^2)^{1/2}\right), \\ &= \frac{1}{2}\left((x^2+y^2)^{-1/2}.(2x)\right), \\ &= \frac{x}{(x^2+y^2)^{1/2}}. \end{aligned} \tag{A.14}$$

Similarly, the derivative of r with respect to y equation (A.12), we have:

$$\frac{\partial r}{\partial y} = \frac{y}{(x^2+y^2)^{1/2}}, \tag{A.15}$$

Substituting equations (A.13), (A.14), and (A.15) into equaton (A.10), we have:

$$\begin{aligned}\nabla W_{poly6} &= \alpha_D\left[\left(-6r(h^2-r^2)^2\right).\frac{x}{(x^2+y^2)^{1/2}}i + \left(-6r(h^2-r^2)^2\right).\frac{y}{(x^2+y^2)^{1/2}}j\right], \\ &= \alpha_D\frac{(-6r(h^2-r^2)^2)}{(x^2+y^2)^{1/2}}\left[xi+yj\right] \quad \text{where } r/(x^2+y^2)^{1/2} \text{ cancel out.} \end{aligned} \tag{A.16}$$

This therefore lead to:

$$\begin{aligned}\nabla W_{poly6} &= \alpha_D\left(-6(h^2-r^2)^2\right)\vec{r}, \\ &= -6\alpha_D(h^2-r^2)^2\vec{r}. \end{aligned} \tag{A.17}$$

The $2D$ normalizer for the first derivative of poly6 kernel ∇W from equation (A.17) will be given as:

$$\begin{aligned}\alpha_{2_{2D}} &= -6 \times \alpha_{1_{2D}}, \\ &= -6 \times \frac{4}{\pi h^8}, \\ &= -\frac{24}{\pi h^8}. \end{aligned} \tag{A.18}$$

For a $3D$ case:

$$\begin{aligned}\nabla &= \frac{\partial}{\partial x}i + \frac{\partial}{\partial y}j + \frac{\partial}{\partial z}k, \\ \nabla &= \frac{\partial}{\partial r}\frac{\partial r}{\partial x}i + \frac{\partial}{\partial r}\frac{\partial r}{\partial y}j + \frac{\partial}{\partial r}\frac{\partial r}{\partial z}k, \\ \nabla W &= \frac{\partial W}{\partial r}.\frac{\partial r}{\partial x}i + \frac{\partial W}{\partial r}.\frac{\partial r}{\partial y}j + \frac{\partial W}{\partial r}.\frac{\partial r}{\partial z}k, \end{aligned} \tag{A.19}$$

where

$$\vec{r} = xi + yj + zk, \tag{A.20}$$

$$\begin{aligned} r &= |\vec{r}|, \\ r &= (x^2 + y^2 + z^2)^{1/2}. \end{aligned} \tag{A.21}$$

Also the derivative of r with respect to z from equation (A.21), we have:

$$\frac{\partial r}{\partial z} = \frac{z}{(x^2 + y^2 + z^2)^{1/2}}. \tag{A.22}$$

Now, following from equation (A.16) by introducing the z component for the $3D$ case, we have

$$\begin{aligned} \nabla W_{poly6} &= \alpha_D \frac{(-6r(h^2 - r^2)^2)}{(x^2 + y^2 + z^2)^{1/2}} [xi + yj + zk] \\ &\quad \text{where } r/(x^2 + y^2 + z^2)^{1/2} \text{ cancel out,} \\ \text{Therefore,} \quad \nabla W_{poly6} &= \alpha_D \left(-6(h^2 - r^2)^2\right) \vec{r}, \\ &= -6\alpha_D (h^2 - r^2)^2 \vec{r}. \end{aligned} \tag{A.23}$$

The $3D$ normalizer for the first derivative of poly6 kernel ∇W_{poly6} from equation (A.23) will be given as:

$$\begin{aligned} \alpha_{2_{3D}} &= -6 \times \alpha_{1_{3D}}, \\ &= -6 \times \frac{315}{64\pi h^9}, \\ &= -\frac{945}{32\pi h^9}. \end{aligned} \tag{A.24}$$

So therefore, in summary the first kernel derivative $\nabla W_{poly6}(|\mathbf{r}|, h)$ with its $2D$ and $3D$ normalizer is given as:

$$\nabla W_{poly6}(|\mathbf{r}|, h) = \alpha_D \begin{cases} (h^2 - r^2)^2 \vec{r} & 0 \leq r < h, \\ 0 & \text{otherwise}, \end{cases} \tag{A.25}$$

where α_D is $-\frac{24}{\pi h^8}$ in $2D$ and $-\frac{945}{32\pi h^9}$ in $3D$.

A.1.2 2st Derivative of Poly6 Kernel with 2D and 3D normalizer

For a $2D$ case, we have:

$$\begin{aligned} \nabla \cdot \nabla W_{poly6} &= \left(\frac{\partial}{\partial x} i + \frac{\partial}{\partial y} j\right) \cdot \left(\alpha_D (h^2 - r^2)^2 \vec{r}\right) \\ &\quad \text{Substituting } \vec{r} = xi + yj \text{ and re-arranging, gives,} \\ &= \alpha_D \left[\left(\frac{\partial}{\partial x} i + \frac{\partial}{\partial y} j\right) \cdot \left((h^2 - r^2)^2 (xi + yj)\right)\right], \quad \text{expanding} \\ &= \alpha_D \left[\left(\frac{\partial}{\partial x} i + \frac{\partial}{\partial y} j\right) \cdot \left((h^2 - r^2)^2 xi + (h^2 - r^2)^2 yj\right)\right] \\ &\quad \text{where } \alpha_D \text{ is a constant,} \\ &= \alpha_D \left[\left(\frac{\partial}{\partial x} i\right) \left((h^2 - r^2)^2 xi\right) + \left(\frac{\partial}{\partial y} j\right) \left((h^2 - r^2)^2 yj\right)\right]. \end{aligned} \tag{A.26}$$

Considering first the x component dot product and leting it be A_x, we have:

$$\begin{aligned} A_x &= \left(\frac{\partial}{\partial x} i\right) \cdot \left((h^2 - r^2)^2 xi\right) \quad \text{since } i^2 = 1, \text{ we have} \\ &= \frac{\partial}{\partial x}\left((h^2 - r^2)^2 x\right). \end{aligned} \tag{A.27}$$

Now, applying product rule to the left hand side of equation (A.27) and letting $(h^2 - r^2)^2$ be u and x be v, then:

$$A_x = u\frac{dv}{dx} + v\frac{du}{dx}, \tag{A.28}$$

Since,

$$\begin{aligned} v &= x, \\ \frac{dv}{dx} &= 1. \end{aligned} \tag{A.29}$$

Also:

$$\begin{aligned} u &= (h^2 - r^2)^2, \quad \text{substituting } r^2 = x^2 + y^2, \text{ gives} \\ &= (h^2 - (x^2 + y^2))^2, \\ \frac{du}{dx} &= 2 \times (h^2 - (x^2 + y^2)) \times (-2x), \\ &= -4x \times (h^2 - (x^2 + y^2)) \quad \text{replacing } x^2 + y^2 \text{ with } r^2, \text{ gives} \\ &= -4x(h^2 - r^2). \end{aligned} \tag{A.30}$$

Substituting equation (A.29), (A.30) and the expression for u and v into equation (A.28), we have:

$$\begin{aligned} A_x &= (h^2 - r^2)^2(1) + (x)(-4x(h^2 - r^2)), \\ &= (h^2 - r^2)^2 - 4(h^2 - r^2)x^2. \end{aligned} \tag{A.31}$$

Similarly from equation (A.31), its follow that:

$$A_y = (h^2 - r^2)^2 - 4(h^2 - r^2)y^2. \tag{A.32}$$

So therefore, Substituting equation (A.31), (A.32) into equation (A.26), we have:

$$\begin{aligned}
\nabla \cdot \nabla W_{poly6} &= \alpha_D \left[A_x + A_y\right], \\
&= \alpha_D \left[(h^2 - r^2)^2 - 4(h^2 - r^2)x^2 + (h^2 - r^2)^2 - 4(h^2 - r^2)y^2\right], \\
&= \alpha_D \left[2(h^2 - r^2)^2 - 4((h^2 - r^2)(x^2 + y^2))\right], \\
&\quad \text{replacing } x^2 + y^2 \text{ with } r^2, \text{ gives} \\
&= \alpha_D \left[2(h^2 - r^2)^2 - 4(h^2 - r^2)r^2\right], \\
\nabla^2 W_{poly6} &= 2\alpha_D \left[(h^2 - r^2)^2 - 2(h^2 - r^2)r^2\right]. \qquad \text{(A.33)}
\end{aligned}$$

The $2D$ normalizer for the second derivative of poly6 kernel $\nabla^2 W$ from equation (A.33) will be given as:

$$\begin{aligned}
\alpha_{3_{2D}} &= 2 \times \alpha_{2_{2D}}, \\
&= 2 \times -\frac{24}{\pi h^8}, \\
&= -\frac{48}{\pi h^8}. \qquad \text{(A.34)}
\end{aligned}$$

For a $3D$ case, it follow that from equation (A.26), we have:

$$\begin{aligned}
\nabla \cdot \nabla W_{poly6} &= \alpha_D \left[\frac{\partial}{\partial x} i \cdot \left((h^2 - r^2)^2 xi\right) + \frac{\partial}{\partial y} j \cdot \left((h^2 - r^2)^2 yj\right)\right. \\
&\quad \left. + \frac{\partial}{\partial z} k \cdot \left((h^2 - r^2)^2 zk\right)\right]. \qquad \text{(A.35)}
\end{aligned}$$

Therefore for A_z its follow from equation (A.31), that we have:

$$A_z = (h^2 - r^2)^2 - 4(h^2 - r^2)z^2. \qquad \text{(A.36)}$$

So therefore, Substituting equation (A.31), (A.32), and (A.36) into equation (A.35), we have:

$$\begin{aligned}
\nabla^2 W_{poly6} &= \alpha_D \left[A_x + A_y + A_z\right], \\
&= \alpha_D \left[(h^2 - r^2)^2 - 4(h^2 - r^2)x^2 + (h^2 - r^2)^2 - 4(h^2 - r^2)y^2 \right. \\
&\quad \left. + (h^2 - r^2)^2 - 4(h^2 - r^2)z^2\right], \\
&= \alpha_D \left[3(h^2 - r^2)^2 - 4(h^2 - r^2)(x^2 + y^2 + z^2)\right], \\
&\quad \text{replacing } x^2 + y^2 + z^2 \text{ with } r^2 \text{ gives,} \\
&= \alpha_D \left[3(h^2 - r^2)^2 - 4(h^2 - r^2)r^2\right]. \qquad \text{(A.37)}
\end{aligned}$$

The $3D$ normalizer for the second derivative of poly6 kernel $\nabla^2 W_{poly6}$ from equation (A.37) will be given as:

$$\begin{aligned}
\alpha_{3_{3D}} &= 1 \times \alpha_{2_{3D}}, \\
&= -\frac{945}{32\pi h^9}, \\
&= -\frac{945}{32\pi h^9}. \qquad \text{(A.38)}
\end{aligned}$$

So therefore, in summary the second kernel derivative $\nabla^2 W_{poly6}(|\mathbf{r}|, h)$ with its $2D$ normalizer is given as:

$$\nabla^2 W_{poly6}(|\mathbf{r}|, h) = \alpha_D \begin{cases} (h^2 - r^2)^2 - 2r^2(h^2 - r^2) & 0 \leq r < h, \\ 0 & \text{otherwise}, \end{cases} \qquad \text{(A.39)}$$

where α_D is $-\frac{48}{\pi h^8}$ in $2D$

While the second kernel derivative $\nabla^2 W_{poly6}(|\mathbf{r}|, h)$ with its $3D$ normalizer is given as

$$\nabla^2 W_{poly6}(|\mathbf{r}|, h) = \alpha_D \begin{cases} 3(h^2 - r^2)^2 - 4r^2(h^2 - r^2) & 0 \leq r < h, \\ 0 & \text{otherwise}. \end{cases} \qquad \text{(A.40)}$$

where α_D is $-\frac{945}{32\pi h^9}$ in $3D$.

A.2 Spiky Kernel with 2D and 3D normalizer

Given the spiky kernel with the function

$$f = (h - r)^3. \tag{A.41}$$

Then the spiky kernel is given by

$$W_{spiky}(|\mathbf{r}|, h) = \frac{1}{c} f, \tag{A.42}$$

where $1/c$ is the normalizer. Let the $2D$ and $3D$ normalizer be given as

$$\alpha_{1_{2D}} = \frac{1}{c_{2D}}, \quad \text{and} \tag{A.43}$$

$$\alpha_{1_{3D}} = \frac{1}{c_{3D}} \quad \text{respectively.} \tag{A.44}$$

Now, for a **2D** case, we have:

$$\begin{aligned}
c_{2D} &= \int_0^h 2\pi r f dr, \\
&= \int_0^h 2\pi r (h - r)^3 dr, \quad \text{by expanding } (h-r)^3, \text{ we have} \\
&= \int_0^h 2\pi r (h^3 - 3h^2 r + 3hr^2 - r^3) dr, \quad \text{multiplying through by } r, \text{ we have} \\
&= \int_0^h 2\pi (h^3 r - 3h^2 r^2 + 3hr^3 - r^4) dr, \\
&= 2\pi \Big| \frac{h^3 r^2}{2} - 3\frac{h^2 r^3}{3} + 3\frac{hr^4}{4} - \frac{r^5}{5} \Big|_0^h, \\
&= 2\pi \Big| \frac{10h^3 r^2 - 20h^2 r^3 + 15hr^4 - 4r^5}{20} \Big|_0^h, \\
&= 2\pi \Big[\frac{10h^5 - 20h^5 + 15h^5 - 4h^5}{20} \Big], \\
&= \frac{\pi h^5}{10}.
\end{aligned} \tag{A.45}$$

Since the normalizer for the $2D$ case is given as $\alpha_{1_{2D}} = \frac{1}{c_{2D}}$, Substituting equation (A.45) into equation (A.43), we have:

$$\alpha_{1_{2D}} = \frac{10}{\pi h^5}. \tag{A.46}$$

Similarly, for a **3D** case, we have:

$$\begin{aligned}
c_{3D} &= \int_0^h 4\pi r^2 f dr, \\
&= \int_0^h 4\pi r^2 (h-r)^3 dr, \quad \text{by expanding } (h^2-r^2)^3, \text{ we have} \\
&= \int_0^h 4\pi r^2 (h^3 - 3h^2 r + 3hr^2 - r^3) dr, \quad \text{multiplying through by } r^2, \text{ we have} \\
&= \int_0^h 4\pi (h^3 r^2 - 3h^2 r^3 + 3hr^4 - r^5) dr, \\
&= 4\pi \Big| \frac{h^3 r^3}{3} - 3\frac{h^2 r^4}{4} + 3\frac{hr^5}{5} - \frac{r^6}{6} \Big|_0^h, \\
&= 4\pi \Big| \frac{20h^3 r^3 - 45h^2 r^4 + 36hr^5 - 10r^6}{60} \Big|_0^h, \\
&= 4\pi \Big[\frac{20h^6 - 45h^6 + 36h^6 - 10h^6}{60} \Big], \\
&= \frac{\pi h^6}{15}.
\end{aligned} \tag{A.47}$$

Also the normalizer for the $3D$ case is given as $\alpha_{1_{3D}} = \frac{1}{c_{3D}}$, Substituting equation (A.47) into equation (A.44), we have:

$$\alpha_{1_{3D}} = \frac{15}{\pi h^6}. \tag{A.48}$$

So therefore, in summary the spiky kernel $W_{spiky}(|\mathbf{r}|, h)$ with its $2D$ and $3D$ normalizer is given as:

$$W_{spiky}(|\mathbf{r}|, h) = \alpha_D \begin{cases} (h-r)^3 & 0 \le r < h, \\ 0 & \text{otherwise}, \end{cases} \tag{A.49}$$

where α_D is $\frac{10}{\pi h^5}$ in $2D$ and $\frac{15}{\pi h^6}$ in $3D$.

A.2.1 1st Derivative of Spiky Kernel with it 2D and 3D normalizer

Recall from equation (A.10) that for a $2D$ case, we have:

$$\nabla W = \frac{\partial W}{\partial r}.\frac{\partial r}{\partial x}i + \frac{\partial W}{\partial r}.\frac{\partial r}{\partial y}j. \tag{A.50}$$

where

$$\vec{r} = xi + yj, \qquad \text{since } r = |\vec{r}|, \text{ we have} \tag{A.51}$$

$$r = (x^2 + y^2)^{1/2}. \tag{A.52}$$

So therefore:

$$\begin{aligned} \frac{\partial W_{spiky}}{\partial r} &= \frac{\partial}{\partial r}\left(\alpha_D(h-r)^3\right), \\ &= \alpha_D\frac{\partial}{\partial r}\left((h-r)^3\right), \quad \text{factorizing out } \alpha_D \text{ as a constant,} \\ &= \alpha_D\left(3(h-r)^2.(-1)\right), \\ &= -3\alpha_D(h-r)^2. \end{aligned} \tag{A.53}$$

For the derivative of r with respect to x, we have:

$$\begin{aligned} \frac{\partial r}{\partial x} &= \frac{\partial}{\partial x}\left((x^2+y^2)^{1/2}\right), \\ &= \frac{1}{2}\left((x^2+y^2)^{-1/2}.(2x)\right), \\ &= \frac{x}{(x^2+y^2)^{1/2}}. \end{aligned} \tag{A.54}$$

Similarly, the derivative of r with respect to y, we have:

$$\frac{\partial r}{\partial y} = \frac{y}{(x^2+y^2)^{1/2}}. \tag{A.55}$$

Substituting equations (A.53), (A.54), and (A.55) into equaton (A.50) we have:

$$\begin{aligned}\nabla W_{spiky} &= \alpha_D \left[\left(-3(h-r)^2\right) . \frac{x}{(x^2+y^2)^{1/2}} i + \left(-3(h-r)^2\right) . \frac{y}{(x^2+y^2)^{1/2}} j \right], \\ &= \alpha_D \frac{(-3(h-r)^2)}{(x^2+y^2)^{1/2}} [xi + yj] \quad \text{substituting } \vec{r} = (xi + yj) \text{ and} \\ &\quad r = (x^2+y^2)^{1/2}, \text{ we have,} \\ &= -3\alpha_D \frac{(h-r)^2}{r} \vec{r}. \end{aligned} \tag{A.56}$$

This therefore lead to:

$$\nabla W_{spiky} = -3\alpha_D \frac{(h-r)^2}{r} \vec{r}. \tag{A.57}$$

The $2D$ normalizer for the first derivative of spiky kernel ∇W_{spiky} from equation (A.57) will be given as:

$$\begin{aligned}\alpha_{2_{2D}} &= -3 \times \alpha_{1_{2D}}, \quad \text{where } \alpha_{1_{2D}} \text{ is from } \textit{equation } (A.46) \\ &= -3 \times \frac{10}{\pi h^5}, \\ &= -\frac{30}{\pi h^5}. \end{aligned} \tag{A.58}$$

For a $3D$ case, recall from equation (A.19) that:

$$\nabla W = \frac{\partial W}{\partial r} . \frac{\partial r}{\partial x} i + \frac{\partial W}{\partial r} . \frac{\partial r}{\partial y} j + \frac{\partial W}{\partial r} . \frac{\partial r}{\partial z} k, \tag{A.59}$$

where

$$\vec{r} = xi + yj + zk, \quad \text{since } r = |\vec{r}|, \text{ we have} \tag{A.60}$$

$$r = (x^2 + y^2 + z^2)^{1/2}. \tag{A.61}$$

Also the derivative of r with respect to z, we have:

$$\frac{\partial r}{\partial z} = \frac{z}{(x^2+y^2+z^2)^{1/2}}, \tag{A.62}$$

Now, following from equation (A.56) by introducing the z component for the $3D$ case, we have:

$$\begin{aligned}
\nabla W_{spiky} &= \alpha_D \frac{(-3(h-r)^2)}{(x^2+y^2+z^2)^{1/2}}\,[xi+yj+zk] \quad \text{where } r=(xi+yj+zk) \\
&\quad \text{and } r=(x^2+y^2+z^2)^{1/2}, \\
\nabla W_{spiky} &= -3\alpha_D \frac{(h-r)^2}{r}\vec{r}.
\end{aligned} \tag{A.63}$$

The $3D$ normalizer for the first derivative of spiky kernel ∇W_{spiky} from equation (A.63) will be given as:

$$\begin{aligned}
\alpha_{2_{3D}} &= -3 \times \alpha_{1_{3D}}, \quad \text{where } \alpha_{1_{3D}} \text{ is from } \textit{equation } (A.48) \\
&= -3 \times \frac{15}{\pi h^6}, \\
&= -\frac{45}{\pi h^6}.
\end{aligned} \tag{A.64}$$

So therefore, in summary the first kernel derivative $\nabla W_{spiky}(|\mathbf{r}|,h)$ with its $2D$ and $3D$ normalizer is given as:

$$\nabla W_{spiky}(|\mathbf{r}|,h) = \alpha_D \begin{cases} \frac{(h-r)^2}{r}\vec{r} & 0 \le r < h, \\ 0 & \text{otherwise}, \end{cases} \tag{A.65}$$

where α_D is $-\frac{30}{\pi h^5}$ in $2D$ and $-\frac{45}{\pi h^6}$ in $3D$.

A.2.2 2st Derivative of Spiky Kernel with 2D and 3D normalizer

For a $2D$ case:

$$\begin{aligned}
\nabla \cdot \nabla W_{spiky} &= \left(\frac{\partial}{\partial x}i + \frac{\partial}{\partial y}j\right) \cdot \left(\alpha_D \frac{(h-r)^2}{r}\vec{r}\right) \quad \text{where } \vec{r} = xi + yj \text{ and} \\
&\text{re-arranging gives,} \\
&= \alpha_D \left[\left(\frac{\partial}{\partial x}i + \frac{\partial}{\partial y}j\right) \cdot \left(\frac{(h-r)^2}{r}(xi + yj)\right)\right], \quad \text{expanding} \\
&= \alpha_D \left[\left(\frac{\partial}{\partial x}i + \frac{\partial}{\partial y}j\right) \cdot \left(\frac{(h-r)^2}{r}xi + \frac{(h-r)^2}{r}yj\right)\right] \\
&\text{where } \alpha_D \text{ is a constant} \\
&= \alpha_D \left[\left(\frac{\partial}{\partial x}i\right)\left(\frac{(h-r)^2}{r}xi\right) + \left(\frac{\partial}{\partial y}j\right)\left(\frac{(h-r)^2}{r}yj\right)\right]. \quad \text{(A.66)}
\end{aligned}$$

Considering first the x component dot product of equation (A.66) and leting it be A_x, we have:

$$\begin{aligned}
A_x &= \left(\frac{\partial}{\partial x}i\right) \cdot \left(\frac{(h-r)^2}{r}xi\right) \quad \text{since } i^2 = 1, \text{ we have} \\
&= \frac{\partial}{\partial x}\left(\frac{(h-r)^2}{r}x\right). \quad \text{(A.67)}
\end{aligned}$$

Now, using product rule, let $\frac{(h-r)^2}{r}$ be u and x be v then:

$$A_x = u\frac{dv}{dx} + v\frac{du}{dx}. \quad \text{(A.68)}$$

Since

$$\begin{aligned}
v &= x, \\
\frac{dv}{dx} &= 1. \quad \text{(A.69)}
\end{aligned}$$

Also:

$$\begin{aligned}
u &= \frac{(h-r)^2}{r}, \quad \text{expanding } (h-r)^2 \text{ and simplifying, gives} \\
&= \frac{h^2}{r} - 2h + r, \quad \text{substituting } r^2 = x^2 + y^2, \text{ gives} \\
&= \frac{h^2}{(x^2+y^2)^{1/2}} - 2h + (x^2+y^2)^{1/2}, \\
\frac{du}{dx} &= \frac{-1}{2} \times \frac{h^2}{(x^2+y^2)^{3/2}} \times (2x) + \frac{1}{2} \times (x^2+y^2)^{-1/2} \times (2x), \quad \text{cancelling out} \\
&\quad \text{likes terms, gives,} \\
&= -\frac{h^2 x}{(x^2+y^2)^{3/2}} + \frac{x}{(x^2+y^2)^{1/2}} \quad \text{replacing } x^2+y^2 \text{ with } r^2, \text{ gives} \\
&= -\frac{h^2 x}{r^3} + \frac{x}{r}. \qquad \text{(A.70)}
\end{aligned}$$

Substituting equation (A.69), (A.70) and the expression for u and v into equation (A.68), we have:

$$\begin{aligned}
A_x &= \frac{(h-r)^2}{r} + x \times \left(-\frac{h^2 x}{r^3} + \frac{x}{r} \right), \\
&= \frac{(h-r)^2}{r} - \frac{h^2 x^2}{r^3} + \frac{x^2}{r}. \qquad \text{(A.71)}
\end{aligned}$$

Similarly from equation (A.71), its follow that:

$$A_y = \frac{(h-r)^2}{r} - \frac{h^2 y^2}{r^3} + \frac{y^2}{r}. \qquad \text{(A.72)}$$

So therefore, Substituting equation (A.71), and (A.72) into equation (A.66), we have:

$$\begin{aligned}
\nabla \cdot \nabla W_{spiky} &= \alpha_D \left[A_x + A_y \right], \\
&= \alpha_D \left[\frac{(h-r)^2}{r} - \frac{h^2 x^2}{r^3} + \frac{x^2}{r} + \frac{(h-r)^2}{r} - \frac{h^2 y^2}{r^3} + \frac{y^2}{r} \right], \\
&= \alpha_D \left[2\frac{(h-r)^2}{r} - \frac{h^2}{r^3}(x^2+y^2) + \frac{(x^2+y^2)}{r} \right], \quad \text{replacing } x^2+y^2 \\
&\quad \text{with } r^2, \text{ gives,} \\
&= \alpha_D \left[2\frac{(h-r)^2}{r} - \frac{h^2}{r^3}(r^2) + \frac{(r^2)}{r} \right], \quad \text{simplifying, gives} \\
\nabla^2 W_{spiky} &= \alpha_D \left[\frac{2(h-r)^2 - (h^2 - r^2)}{r} \right]. \qquad \text{(A.73)}
\end{aligned}$$

The $2D$ normalizer for the second derivative of spiky kernel $\nabla^2 W_{spiky}$ from equation (A.73) will be given as:

$$\begin{aligned}
\alpha_{3_{2D}} &= 1 \times \alpha_{2_{2D}}, \quad \text{where } \alpha_{2_{2D}} \text{ is from } \textit{equation } (A.58), \\
&= 1 \times -\frac{30}{\pi h^5}, \\
&= -\frac{30}{\pi h^5}.
\end{aligned} \tag{A.74}$$

For a $3D$ case, it follow that from equation (A.66), we have:

$$\begin{aligned}
\nabla \cdot \nabla W_{spiky} &= \alpha_D \left[\frac{\partial}{\partial x} i \cdot \left(\frac{(h-r)^2}{r} xi \right) + \frac{\partial}{\partial y} j \cdot \left(\frac{(h-r)^2}{r} yj \right) \right. \\
&\quad \left. + \frac{\partial}{\partial z} k \cdot \left(\frac{(h-r)^2}{r} zk \right) \right].
\end{aligned} \tag{A.75}$$

Therefore for A_z its follow from equation (A.71), that we have:

$$A_z = \frac{(h-r)^2}{r} - \frac{h^2 z^2}{r^3} + \frac{z^2}{r}. \tag{A.76}$$

So therefore, Substituting equation (A.71), (A.72), and (A.76) into equation (A.75), we have:

$$\begin{aligned}
\nabla^2 W_{spiky} &= \alpha_D \left[A_x + A_y + A_z \right], \\
&= \alpha_D \left[\frac{(h-r)^2}{r} - \frac{h^2 x^2}{r^3} + \frac{x^2}{r} + \frac{(h-r)^2}{r} - \frac{h^2 y^2}{r^3} + \frac{y^2}{r} + \frac{(h-r)^2}{r} \right. \\
&\quad \left. - \frac{h^2 z^2}{r^3} + \frac{z^2}{r} \right], \\
&= \alpha_D \left[3\frac{(h-r)^2}{r} - \frac{h^2}{r^3}(x^2+y^2+z^2) + \frac{(x^2+y^2+z^2)}{r} \right], \quad \text{replacing,} \\
&\quad x^2+y^2+z^2 \text{ with } r^2 \text{ gives,} \\
&= \alpha_D \left[\frac{3(h-r)^2}{r} - \frac{h^2}{r^3}(r^2) + \frac{(r^2)}{r} \right], \quad \text{simplifying gives,} \\
&= 2\alpha_D \left[\frac{(h-r)(h-2r)}{r} \right].
\end{aligned} \tag{A.77}$$

The $3D$ normalizer for the second derivative of spiky kernel $\nabla^2 W_{spiky}$ from equation (A.77) will be given as:

$$\begin{aligned} \alpha_{3_{3D}} &= 2 \times \alpha_{2_{3D}}, \quad \text{where } \alpha_{2_{3D}} \text{ is from } \textit{equation } (A.64) \\ &= 2 \times -\frac{45}{\pi h^6}, \\ &= -\frac{90}{\pi h^6}. \end{aligned} \tag{A.78}$$

So therefore, in summary the second spiky kernel derivative $\nabla^2 W_{spiky}(|\mathbf{r}|, h)$ with its $2D$ normalizer is given as:

$$\nabla^2 W_{spiky}(|\mathbf{r}|, h) = \alpha_D \begin{cases} \frac{(h-r)(h-3r)}{r} & 0 \leq r < h, \\ 0 & \text{otherwise}, \end{cases} \tag{A.79}$$

where α_D is $-\frac{30}{\pi h^5}$ in $2D$.

While the second spiky kernel derivative $\nabla^2 W_{spiky}(|\mathbf{r}|, h)$ with its $3D$ normalizer is given as:

$$\nabla^2 W_{spiky}(|\mathbf{r}|, h) = \alpha_D \begin{cases} \frac{(h-r)(h-2r)}{r} & 0 \leq r < h, \\ 0 & \text{otherwise}, \end{cases} \tag{A.80}$$

where α_D is $-\frac{90}{\pi h^6}$ in $3D$.

A.3 Viscosity Kernel with 2D and 3D normalizer

Given the viscosity kernel with the function:

$$f = -\frac{r^3}{2h^3} + \frac{r^2}{h^2} + \frac{h}{2r} - 1. \tag{A.81}$$

Then the viscosity kernel is given by:

$$W_{viscosity}(|\mathbf{r}|, h) = \frac{1}{c} f, \tag{A.82}$$

where $1/c$ is the normalizer. Let the $2D$ and $3D$ normalizer be given as:

$$\alpha_{1_{2D}} = \frac{1}{c_{2D}}, \quad \text{and} \tag{A.83}$$

$$\alpha_{1_{3D}} = \frac{1}{c_{3D}} \quad \text{respectively.} \tag{A.84}$$

Now, for a **2D** case, we have:

$$\begin{aligned}
c_{2D} &= \int_0^h 2\pi r f dr, \\
&= \int_0^h 2\pi r \left(\frac{-r^3}{2h^3} + \frac{r^2}{h^2} + \frac{h}{2r} - 1 \right) dr, \quad \text{multiplying through by } r\text{, we have} \\
&= \int_0^h 2\pi \left(\frac{-r^4}{2h^3} + \frac{r^3}{h^2} + \frac{hr}{2r} - r \right) dr, \quad \text{cancelling out like terms, we have} \\
&= \int_0^h 2\pi \left(\frac{-r^4}{2h^3} + \frac{r^3}{h^2} + \frac{h}{2} - r \right) dr, \\
&= 2\pi \Big| \left(\frac{-r^5}{10h^3} + \frac{r^4}{4h^2} + \frac{hr}{2} - \frac{r^2}{2} \right) \Big|_0^h, \\
&= \pi \left(\frac{-h^5}{5h^3} + \frac{h^4}{2h^2} + \frac{h^2}{1} - \frac{h^2}{1} \right), \\
&= \pi \left(\frac{-h^2}{5} + \frac{h^2}{2} + h^2 - h^2 \right), \\
&= \pi \Big[\frac{-2h^2 + 5h^2}{10} \Big], \\
&= \frac{3\pi h^2}{10}.
\end{aligned} \tag{A.85}$$

Since the normalizer for the $2D$ case is given as $\alpha_{1_{2D}} = \frac{1}{c_{2D}}$, Substituting equation (A.85) into equation (A.83), we have:

$$\alpha_{1_{2D}} = \frac{10}{3\pi h^2}. \tag{A.86}$$

Similarly, for a **3D** case, we have:

$$\begin{aligned}
c_{3D} &= \int_0^h 4\pi r^2 f dr, \\
&= \int_0^h 4\pi r^2 \left(\frac{-r^3}{2h^3} + \frac{r^2}{h^2} + \frac{h}{2r} - 1\right) dr, \quad \text{multiplying through by } r^2, \text{ we have} \\
&= \int_0^h 4\pi \left(\frac{-r^5}{2h^3} + \frac{r^4}{h^2} + \frac{hr^2}{2r} - r^2\right) dr, \quad \text{cancelling out likes terms} \\
&= \int_0^h 4\pi \left(\frac{-r^5}{2h^3} + \frac{r^4}{h^2} + \frac{hr}{2} - r^2\right) dr, \\
&= 4\pi \Big| \left(\frac{-r^6}{12h^3} + \frac{r^5}{5h^2} + \frac{hr^2}{4} - \frac{r^3}{3}\right) \Big|_0^h, \\
&= 4\pi \Big| \left(\frac{-h^6}{12h^3} + \frac{h^5}{5h^2} + \frac{h^3}{4} - \frac{h^3}{3}\right) \Big|_0^h, \\
&= 4\pi \Big[\left(\frac{-h^3}{12} + \frac{h^3}{5} + \frac{h^3}{4} - \frac{h^3}{3}\right) \Big], \\
&= 4\pi \left(\frac{-5h^3 + 12h^3 + 15h^3 - 20h^3}{60}\right), \\
&= \frac{2\pi h^3}{15}.
\end{aligned} \tag{A.87}$$

Also the normalizer for the $3D$ case is given as $\alpha_{1_{3D}} = \frac{1}{c_{3D}}$, Substituting equation (A.87) into equation (A.84), we have:

$$\alpha_{1_{3D}} = \frac{15}{2\pi h^3}. \tag{A.88}$$

So therefore, in summary the viscosity kernel $W_{viscosity}(|\mathbf{r}|, h)$ with its $2D$ and $3D$ normalizer is given as:

$$W_{viscosity}(|\mathbf{r}|, h) = \alpha_D \begin{cases} -\frac{r^3}{2h^3} + \frac{r^2}{h^2} + \frac{h}{2r} - 1 & 0 \leq r < h, \\ 0 & \text{otherwise}, \end{cases} \tag{A.89}$$

where α_D is $\frac{10}{3\pi h^2}$ in $2D$ and $\frac{15}{2\pi h^3}$ in $3D$.

A.3.1 1st Derivative of Viscosity Kernel with 2D and 3D normalizer

Recall also that from equation (A.10) that for a $2D$ case, we have:

$$\nabla W = \frac{\partial W}{\partial r}.\frac{\partial r}{\partial x}i + \frac{\partial W}{\partial r}.\frac{\partial r}{\partial y}j, \tag{A.90}$$

where

$$\vec{r} = xi + yj, \qquad \text{since } r = |\vec{r}|, \text{ we have} \tag{A.91}$$

$$r = (x^2 + y^2)^{1/2}. \tag{A.92}$$

So therefore:

$$\begin{aligned}
\frac{\partial W}{\partial r} &= \frac{\partial}{\partial r}\left(\alpha_D\left(-\frac{r^3}{2h^3} + \frac{r^2}{h^2} + \frac{h}{2r} - 1\right)\right), \\
&= \alpha_D \frac{\partial}{\partial r}\left(-\frac{r^3}{2h^3} + \frac{r^2}{h^2} + \frac{h}{2r} - 1\right), \quad \text{factorizing out } \alpha_D \text{ as a constant,} \\
&= \alpha_D\left(-\frac{3r^2}{2h^3} + \frac{2r}{h^2} + \frac{-h}{2r^2}\right).
\end{aligned} \tag{A.93}$$

For the derivative of r with respect to x from equation (A.92), we have:

$$\begin{aligned}
\frac{\partial r}{\partial x} &= \frac{\partial}{\partial x}\left((x^2 + y^2)^{1/2}\right), \\
&= \frac{1}{2}\left((x^2 + y^2)^{-1/2}.(2x)\right), \\
&= \frac{x}{(x^2 + y^2)^{1/2}}.
\end{aligned} \tag{A.94}$$

Similarly, the derivative of r with respect to y equation (A.92), we have:

$$\frac{\partial r}{\partial y} = \frac{y}{(x^2 + y^2)^{1/2}}. \tag{A.95}$$

Substituting equations (A.93), (A.94), and (A.95) into equaton (A.90), we have:

$$\begin{aligned}\nabla W &= \alpha_D \left[\left(-\frac{3r^2}{2h^3}+\frac{2r}{h^2}+\frac{-h}{2r^2}\right).\frac{x}{(x^2+y^2)^{1/2}}i\right.\\ &\quad \left.+\left(-\frac{3r^2}{2h^3}+\frac{2r}{h^2}+\frac{-h}{2r^2}\right).\frac{y}{(x^2+y^2)^{1/2}}j\right],\\ &= \alpha_D\left(-\frac{3r^2}{2h^3}+\frac{2r}{h^2}+\frac{-h}{2r^2}\right)\left(\frac{xi+yj}{(x^2+y^2)^{1/2}}\right)\\ &\quad \text{where } r/(x^2+y^2)^{1/2} \text{ cancel out.}\end{aligned} \tag{A.96}$$

This therefore lead to:

$$\begin{aligned}\nabla W &= \alpha_D\left(-\frac{3r}{2h^3}+\frac{2}{h^2}-\frac{h}{2r^3}\right)\vec{r},\\ &= \frac{1}{h^2}\alpha_D\left(-\frac{3r}{2h}+2-\frac{h^3}{2r^3}\right)\vec{r}.\end{aligned} \tag{A.97}$$

The $2D$ normalizer for the first derivative of viscosity kernel $\nabla W_{viscosity}$ from equation (A.97) will be given as:

$$\begin{aligned}\alpha_{2_{2D}} &= \frac{1}{h^2}\times\alpha_{1_{2D}},\\ &= \frac{1}{h^2}\times\frac{10}{3\pi h^2},\\ &= \frac{10}{3\pi h^4}.\end{aligned} \tag{A.98}$$

For a $3D$ case, recall also that from equation (A.19) that:

$$\nabla W = \frac{\partial W}{\partial r}.\frac{\partial r}{\partial x}i+\frac{\partial W}{\partial r}.\frac{\partial r}{\partial y}j+\frac{\partial W}{\partial r}.\frac{\partial r}{\partial z}k, \tag{A.99}$$

where

$$\vec{r} = xi+yj+zk, \quad \text{since } r=|\vec{r}|, \text{ we have} \tag{A.100}$$

$$r = (x^2+y^2+z^2)^{1/2}. \tag{A.101}$$

Also the derivative of r with respect to z from equation (A.101), we have:

$$\frac{\partial r}{\partial z} = \frac{z}{(x^2+y^2+z^2)^{1/2}}, \tag{A.102}$$

Now, following from equation (A.97) by introducing the z component for the $3D$ case, we have

$$\begin{aligned} \nabla W &= \alpha_D \left(-\frac{3r^2}{2h^3} + \frac{2r}{h^2} + \frac{-h}{2r^2}\right) \frac{(xi+yj+zk)}{(x^2+y^2+z^2)^{1/2}}, \quad \text{where} \\ & \quad r/(x^2+y^2+z^2)^{1/2} \text{ cancel out} \\ \text{Therefore,} \quad \nabla W &= \alpha_D \left(-\frac{3r}{2h^3} + \frac{2}{h^2} - \frac{h}{2r^3}\right) \vec{r}, \\ &= \frac{1}{h^2}\alpha_D \left(-\frac{3r}{2h} + 2 - \frac{h^3}{2r^3}\right) \vec{r}. \end{aligned} \tag{A.103}$$

The $3D$ normalizer for the first derivative of viscosity kernel $\nabla W_{viscosity}$ from equation (A.103) will be given as:

$$\begin{aligned} \alpha_{2_{3D}} &= \frac{1}{h^2} \times \alpha_{1_{3D}}, \\ &= \frac{1}{h^2} \times \frac{15}{2\pi h^3}, \\ &= \frac{15}{2\pi h^5}. \end{aligned} \tag{A.104}$$

So therefore, in summary the first kernel derivative $\nabla W_{viscosity}(|\mathbf{r}|, h)$ with its $2D$ and $3D$ normalizer is given as:

$$\nabla W_{viscosity}(|\mathbf{r}|, h) = \alpha_D \begin{cases} \left(-\frac{3r}{2h} + 2 - \frac{h^3}{2r^3}\right) \vec{r} & 0 \le r < h, \\ 0 & \text{otherwise}, \end{cases} \tag{A.105}$$

where α_D is $\frac{10}{3\pi h^4}$ in $2D$ and $\frac{15}{2\pi h^5}$ in $3D$.

A.3.2 2st Derivative of Viscosity Kernel with 2D and 3D normalizer

For a $2D$ case, we have:

$$\begin{aligned}
\nabla \cdot \nabla W &= \left(\frac{\partial}{\partial x}i + \frac{\partial}{\partial y}j\right) \cdot \left(\alpha_D \left(-\frac{3r}{2h} + 2 - \frac{h^3}{2r^3}\right)\vec{r}\right) \quad \text{Substituting } \vec{r} = xi + yj, \\
&\quad \text{and re-arranging, gives} \\
&= \alpha_D \left[\left(\frac{\partial}{\partial x}i + \frac{\partial}{\partial y}j\right) \cdot \left(-\frac{3r}{2h} + 2 - \frac{h^3}{2r^3}\right)(xi + yj)\right], \quad \text{expanding} \\
&= \alpha_D \left[\left(\frac{\partial}{\partial x}i + \frac{\partial}{\partial y}j\right) \cdot \left(\left(-\frac{3r}{2h} + 2 - \frac{h^3}{2r^3}\right)xi + \left(-\frac{3r}{2h} + 2 - \frac{h^3}{2r^3}\right)yj\right)\right] \\
&\quad \text{where } \alpha_D \text{ is a constant,} \\
&= \alpha_D \left[\left(\frac{\partial}{\partial x}i\right) \cdot \left(-\frac{3r}{2h} + 2 - \frac{h^3}{2r^3}\right)xi + \left(\frac{\partial}{\partial y}j\right) \cdot \left(-\frac{3r}{2h}\right.\right. \\
&\quad \left.\left. + 2 - \frac{h^3}{2r^3}\right)yj\right]. \qquad \text{(A.106)}
\end{aligned}$$

Considering first the x component dot product and leting it be A_x, we have:

$$\begin{aligned}
A_x &= \left(\frac{\partial}{\partial x}i\right) \cdot \left(-\frac{3r}{2h} + 2 - \frac{h^3}{2r^3}\right)xi \quad \text{since } i^2 = 1, \text{ we have} \\
&= \frac{\partial}{\partial x}\left(\left(-\frac{3r}{2h} + 2 - \frac{h^3}{2r^3}\right)x\right). \qquad \text{(A.107)}
\end{aligned}$$

Now, applying product rule to the left hand side of equation (A.107) and letting $\left(-\frac{3r}{2h} + 2 - \frac{h^3}{2r^3}\right)$ be u and x be v, then:

$$A_x = u\frac{dv}{dx} + v\frac{du}{dx}. \qquad \text{(A.108)}$$

Since:

$$\begin{aligned}
v &= x, \\
\frac{dv}{dx} &= 1. \qquad \text{(A.109)}
\end{aligned}$$

Also:

$$\begin{aligned}
u &= -\frac{3r}{2h} + 2 - \frac{h^3}{2r^3}, \quad \text{substituting } r^2 = x^2 + y^2, \text{ gives} \\
&= -\frac{3(x^2+y^2)^{1/2}}{2h} + 2 - \frac{h^3}{2(x^2+y^2)^{3/2}}, \\
\frac{du}{dx} &= \frac{1}{2} \times \left(-\frac{3(x^2+y^2)^{-1/2}}{2h} \right) \times (2x) - \frac{-3}{2} \times \left(\frac{h^3}{2(x^2+y^2)^{5/2}} \right) \times (2x), \\
&= -\frac{3x}{2h(x^2+y^2)^{1/2}} + \frac{3h^3 x}{2(x^2+y^2)^{5/2}} \quad \text{replacing } x^2+y^2 \text{ with } r^2, \text{ gives} \\
&= \frac{3x}{2r}\left(-\frac{1}{h} + \frac{h^3}{r^4} \right). \qquad \text{(A.110)}
\end{aligned}$$

Substituting equation (A.109), (A.110) and the expression for u and v into equation (A.108), we have:

$$\begin{aligned}
A_x &= \left(-\frac{3r}{2h} + 2 - \frac{h^3}{2r^3} \right) \times (1) + (x) \times \left(\frac{3x}{2r}\left(-\frac{1}{h} + \frac{h^3}{r^4} \right) \right), \\
&= -\frac{3r}{2h} + 2 - \frac{h^3}{2r^3} + \frac{3x^2}{2r}\left(-\frac{1}{h} + \frac{h^3}{r^4} \right), \\
&= -\frac{3r}{2h} + 2 - \frac{h^3}{2r^3} - \frac{3x^2}{2hr} + \frac{3h^3x^2}{2r^5}. \qquad \text{(A.111)}
\end{aligned}$$

Similarly from equation (A.111), its follow that:

$$A_y = -\frac{3r}{2h} + 2 - \frac{h^3}{2r^3} - \frac{3y^2}{2hr} + \frac{3h^3y^2}{2r^5}. \qquad \text{(A.112)}$$

So therefore, Substituting equation (A.111), (A.112) into equation (A.106), we have:

$$\begin{aligned}
\nabla \cdot \nabla W &= \alpha_D \left[A_x + A_y \right], \\
&= \alpha_D \left[-\frac{3r}{2h} + 2 - \frac{h^3}{2r^3} - \frac{3x^2}{2hr} + \frac{3h^3x^2}{2r^5} - \frac{3r}{2h} + 2 - \frac{h^3}{2r^3} - \frac{3y^2}{2hr} + \frac{3h^3y^2}{2r^5} \right], \\
&= \alpha_D \left[-\frac{3r}{h} + 4 - \frac{h^3}{r^3} - \frac{3(x^2+y^2)}{2hr} + \frac{3h^3(x^2+y^2)}{2r^5} \right], \quad \text{replacing } x^2+y^2 \\
&\quad \text{with } r^2, \text{ gives} \\
&= \alpha_D \left[-\frac{3r}{h} + 4 - \frac{h^3}{r^3} - \frac{3r}{2h} + \frac{3h^3}{2r^3} \right], \\
\nabla^2 W &= \alpha_D \left[-\frac{9r}{2h} + \frac{h^3}{2r^3} + 4 \right]. \qquad \text{(A.113)}
\end{aligned}$$

The $2D$ normalizer for the second derivative of viscosity kernel $\nabla^2 W_{viscosity}$ from equation (A.113) will be given as:

$$\begin{aligned} \alpha_{3_{2D}} &= 1 \times \alpha_{2_{2D}}, \\ &= 1 \times \frac{10}{3\pi h^4}, \\ &= \frac{10}{3\pi h^4}. \end{aligned} \tag{A.114}$$

For a $3D$ case, it follow that from equation (A.106), we have:

$$\begin{aligned} \nabla \cdot \nabla W &= \alpha_D \left[\left(\frac{\partial}{\partial x} i \right) \cdot \left(-\frac{3r}{2h} + 2 - \frac{h^3}{2r^3} \right) xi + \left(\frac{\partial}{\partial y} j \right) \cdot \left(-\frac{3r}{2h} + 2 - \frac{h^3}{2r^3} \right) yj \right. \\ &\quad \left. + \left(\frac{\partial}{\partial z} k \right) \cdot \left(-\frac{3r}{2h} + 2 - \frac{h^3}{2r^3} \right) zk \right]. \end{aligned} \tag{A.115}$$

Therefore for A_z its follow from equation (A.111), that we have.

$$A_z = -\frac{3r}{2h} + 2 - \frac{h^3}{2r^3} - \frac{3z^2}{2hr} + \frac{3h^3 z^2}{2r^5}. \tag{A.116}$$

So therefore, Substituting equation (A.111), (A.112), and (A.116) into equation (A.115), we have:

$$\begin{aligned} \nabla^2 W &= \alpha_D \left[A_x + A_y + A_z \right], \\ &= \alpha_D \left[-\frac{3r}{2h} + 2 - \frac{h^3}{2r^3} - \frac{3x^2}{2hr} + \frac{3h^3 x^2}{2r^5} - \frac{3r}{2h} + 2 - \frac{h^3}{2r^3} - \frac{3y^2}{2hr} + \frac{3h^3 y^2}{2r^5} - \frac{3r}{2h} \right. \\ &\quad \left. + 2 - \frac{h^3}{2r^3} - \frac{3z^2}{2hr} + \frac{3h^3 z^2}{2r^5} \right], \\ &= \alpha_D \left[-\frac{9r}{2h} + 6 - \frac{3h^3}{2r^3} - \frac{3(x^2+y^2+z^2)}{2hr} + \frac{3h^3(x^2+y^2+z^2)}{2r^5} \right], \quad \text{replacing,} \\ &\quad x^2 + y^2 + z^2 \text{ with } r^2 \text{ gives,} \\ &= \alpha_D \left[-\frac{9r}{2h} + 6 - \frac{3h^3}{2r^3} - \frac{3r^2}{2hr} + \frac{3h^3 r^2}{2r^5} \right], \\ &= \alpha_D \left[-\frac{9r}{2h} + 6 - \frac{3h^3}{2r^3} - \frac{3r}{2h} + \frac{3h^3}{2r^3} \right], \\ &= \alpha_D \left[-\frac{6r}{h} + 6 \right], \\ &= 6\alpha_D \left[-\frac{r}{h} + 1 \right]. \end{aligned} \tag{A.117}$$

The $3D$ normalizer for the second derivative of viscosity kernel $\nabla^2 W_{viscosity}$ from equation (A.117) will be given as:

$$\begin{aligned} \alpha_{3_{3D}} &= 6 \times \alpha_{2_{3D}}, \\ &= 6 \times \frac{15}{2\pi h^5}, \\ &= \frac{45}{\pi h^5}. \end{aligned} \tag{A.118}$$

So therefore, in summary the second kernel derivative $\nabla^2 W_{viscosity}(|\mathbf{r}|, h)$ with its $2D$ normalizer is given as:

$$\nabla^2 W_{viscosity}(|\mathbf{r}|, h) = \alpha_D \begin{cases} -\frac{9r}{2h} + \frac{h^3}{2r^3} + 4 & 0 \leq r < h, \\ 0 & \text{otherwise}, \end{cases} \tag{A.119}$$

where α_D is $\frac{10}{3\pi h^4}$ in $2D$.

While the second kernel derivative $\nabla^2 W_{viscosity}(|\mathbf{r}|, h)$ with its $3D$ normalizer is given as:

$$\nabla^2 W_{viscosity}(|\mathbf{r}|, h) = \alpha_D \begin{cases} -\frac{r}{h} + 1 & 0 \leq r < h, \\ 0 & \text{otherwise}, \end{cases} \tag{A.120}$$

where α_D is $\frac{45}{\pi h^5}$ in $3D$.

Appendix B

C++ Programming Code

This is not included here. Check the CD inside

Appendix C

Descriptive formulation

C.1 Unit surface normal direction correction

The Figure C.1 below shows the exploded view of how to resolve the unit surface normal direction of interface fluid particles close to the solid boundary.

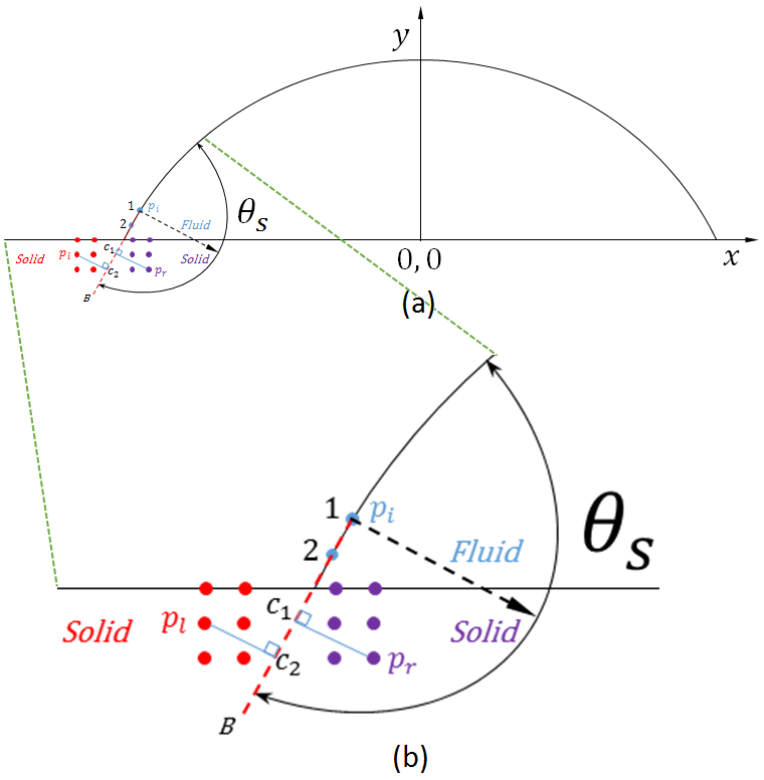

FIGURE C.1: The correction of the unit normal direction implementation for the interface fluid particles close to the substrate, where summation is taken over the search angle θ_s (a) Complete assembly correction view (b) Exploded view.

To achieve this, an algorithm that can get the correct neighbour list of interested interface fluid particles p_i within the search angle (θ_s) without including the red substrate particles at the negative x axis is presented. The same can be replicated at the positive x axis since there is symmetric by assumption.

From the Figure C.1, the negative part of x axis, where the two interface fluid particles close to the substrate are label 1 and 2 were first considered. Now, taking p_i at particle 1, as the interface fluid particle of interest and drawing an imaginary line represented by the red dotted line from particle 1 to point B through particle 2, the particles at the solid wall are now divided into the red particles (p_l) at the left and the purple particles (p_r) at the right. There is also a possibility that some of the solid particles may lie on this imaginary line. The next task was to draw a perpendicular line from either the purple particles (p_r) or red particles (p_l) to meet the red line at points c_1 and c_2 respectively. The coordinate of these points c_1 and c_2 are now compared with the purple particles (p_r) and red particles (p_l) positions respectively. If the purple particles x coordinate position ($p_r \geq x$ coordinate position of c_1), when this happen, the substrate particle is considered as a neighbour to the fluid particle p_i of interest, while for the red substrate particles (p_l) they are discarded. Also, for the the positive part of x axis, the purple particles x coordinate position ($p_r \leq x$ coordinate position of c_1), when this happen, the substrate particle is considered as a neighbour to the fluid particle p_i of interest, while the red substrate particles (p_l) are discarded.

C.2 Mathematical derivation of the algorithms

For the mathematical formulation, let the coordinate of the existing interface particles at 1 and 2 be (x_1, y_1) and (x_2, y_2) respectively. Since these positions are known, then, the gradient between these two points 1 and 2 will be given as:

$$m_1 = \frac{y_2 - y_1}{x_2 - x_1} \tag{C.1}$$

From the theory of mathematic, the product of any two perpendicular line must give negative unity. With this, it follows that if a line is drawn from point p_r to be perpendicular to the red line represented by (p_i to B) meeting it at c_1 as shown in Figure C.1 b, then the gradient m_2 of the line represented by (p_r to c_1) will be given as:

$$m_2 = \frac{-1}{m_1} \tag{C.2}$$

Letting the coordinate of points p_r be (x_3, y_3) and c_1 be (x_4, y_4), then the following equations hold:

$$\frac{y_1 - y_4}{x_1 - x_4} = m_1 \quad \text{representing equation for line from point 1 to } c_1 \tag{C.3}$$

$$\frac{y_3 - y_4}{x_3 - x_4} = m_2 \quad \text{representing equation for line from point } p_r \text{ to } c_1 \tag{C.4}$$

From equation C.3 and C.4, the only unknown is the coordinate at point c_1 given as (x_4, y_4). We are only interested in the x coordinate of c_1 given as (x_4), so making y_4 the subject formular from equation C.3 gives:

$$y_4 = y_1 - m_1(x_3 - x_4) \tag{C.5}$$

Substitute y_4 from equation C.5 into equation C.4, given the following:

$$y_3 - (y_1 - m_1(x_3 - x_4)) \quad = \quad m_2(x_3 - x_4), \tag{C.6}$$

$y_3 - y_1 + m_1x_3 - m_1x_4 = m_2x_3 - m_2x_4$, expanding and collecting like terms, give

$$m_2x_4 - m_1x_4 \quad = \quad m_2x_3 - y_3 + y_1 - m_1x_3,$$

$$x_4 \quad = \quad \frac{y_1 - y_3 + m_2x_3 - m_1x_3}{m_2 - m_1}, \tag{C.7}$$

Similarly, the same can be done for point c_2 by letting the coordinate of points p_l be (x_5, y_5) and c_2 be (x_6, y_6), then x_6 is given as:

$$x_6 = \frac{y_1 - y_5 + m_2 x_5 - m_1 x_5}{m_2 - m_1}, \tag{C.8}$$

Now, as a general rule for the left side of the droplet, if the x intercept of point c_1 is less than or equal to the substrate particle x position at point p_r, then these substrate particles are selected as a neighbour list to the interested interface particle p_i, else it is discarded. Also, if the x intercept of point c_2 is less than or equal to the substrate particle x position at point p_l, then these substrate particles are selected as a neighbour list to the interested interface particle p_i, else it is discarded. Similarly, this rule is reverse for the right side of the droplet.

Appendix D

Force balance of the contact angle of a drop edge at equilibrium

The stationary equilibrium of a drop edge is illustrated in Figure D.1 below

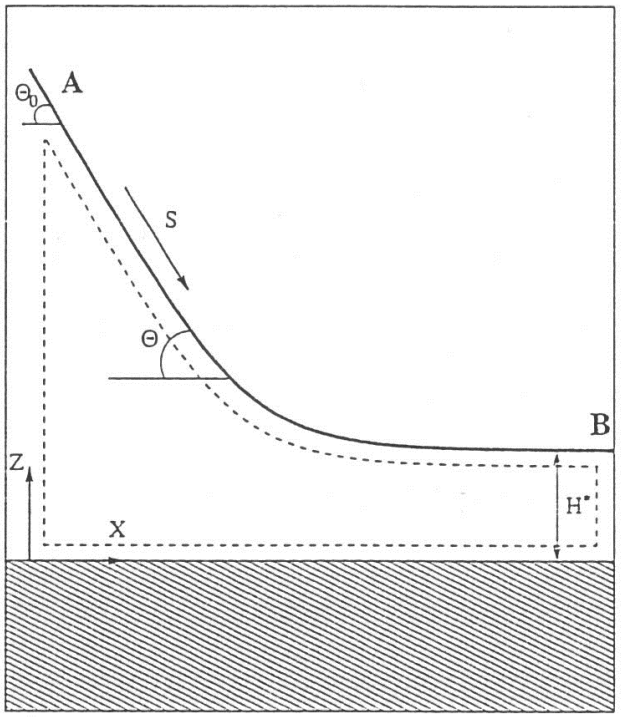

FIGURE D.1: Equilibrium contact angle at the drop edge

Using the same similar approach as Schwartz [83], it is easy to analyse the basic force balance in relation to the equivalent line tension with the disjoining pressure model previously described in Chapter 6. Because of the fact that the analysis is restricted

to the drop edge, only the two-dimensional case will be considered. The labelled point A in Figure D.1 is assumed to be far away from the substrate such that its height H is a multiple of H^*, and as such is at infinity with its been zero at that point.

Once the contact angle θ_0 is at equilibrium, the inclination at point A will remain constant, thus making pressure jump generated by the curvature of the surface to be zero. Furthermore, the total pressure at point A will also be zero. Similarly, at point B close to the precursor film, the inclination θ and it rate of change both are zero with its $\Pi(H)$ also zero at this point.

Performing an integral force balance in the X direction on the area cover by the dashed line in Figure D.1, and knowing that the total pressure at the vertical faces A and B are zero, the following holds

$$0 = \int_{H^*}^{\infty} P(H)dH = \int_{H^*}^{\infty} \frac{d\theta}{dS} dH - \int_{H^*}^{\infty} \Pi(H)dH \tag{D.1}$$

where S is the arc length measured along the free-surface. Since $\frac{dH}{dS} = sin\theta$, the above equation yield

$$0 \;=\; \sigma cos\theta|_0^{\theta_0} - \int_{H^*}^{\infty} \Pi(H)dH, \tag{D.2}$$

or

$$\sigma cos\theta_0 \;=\; \sigma - E_d(\infty), \tag{D.3}$$

where $E_d(H)$ is the local disjoining energy density and $E_d(\infty)$ is similar to the spreading coefficient. Equation (D.3) is the disjoining model similar to the Young's equation (6.1).

Using the two-term disjoining model, the constant B from equation (6.11) will take the place of θ_0 in equation (D.2) and will yield

$$B = \frac{(n-1)(m-1)}{H^*(n-m)}\sigma(1-cos\theta_0), \tag{D.4}$$

Bibliography

[1] Y. Sumino, N. Magome, T. Hamada, and K. Yoshikawa. Self-running droplet: Emergence of regular motion from non-equilibrium noise. *Physical Review Letters*, 94:068301, 2005.

[2] Alejandro Jacobo Cabrera Crespo. PhD Thesis: Application of the Smoothed Particle Hydrodynamics model SPHysics to free-surface hydrodynamics. (ISSN 978-0-19-965552-6), 2008.

[3] S. B. G. O'Brien and L. E. W. Schwartz. Theory and Modeling of Thin Film Flows. *Encyclopedia of Surface and Collidal Science*, pages 5283–5297, 2002.

[4] J. J. Monaghan and A. Kocharyan. SPH simulation of multi-phase flow. *Computer Physics Communications*, 87:225–235, 1995.

[5] Alexender Oron, Stephen H. Davis, and S. George Bankoff. Long scale evolution of thin films. *Reviews of Modern Physics*, 69:931–980, 1997.

[6] R. V. Craster and O. K. Matar. Dynamics and stability of thin liquid films. *Reviews of Modern Physics*, 81:1131–1198, 2009.

[7] S. Veremieiev, H. M. Thompson, and P. H. Gaskell Y. C. Lee. Inertia thin film flow on planer surfaces featuring topography. *Computer & Fluids*, 39:431–450, 2010.

[8] Herbert E. Huppert. The propagation of two-dimensional and axisymmetric viscous gravity currents over a rigid horizontal surface. *J . Fluid Mech.*, 121: 43–58, 1982.

[9] Mark A. Hallworth, Herbert E. Huppert, Jeremy C. Phillips, and R. Stephen J. Sparks. Entrainment into two-dimensional and axisymetric turbulent gravity currents. *J. Fluid Mech.*, 308:289–311, 1996.

[10] T. Maxworthy, J. Leilich, J. E. Simpson, and E. H. Meiburg. Propagation of a gravity current into a linearly stratified fluid. *J. Fluid Mech.*, 453:371–394, 2002.

[11] Roger T. Bonnecaze, Herbert E. Huppert, and John R. Lister. Particle-driven gravity currents. *J. Fluid Mech.*, 250:339–369, 1993.

[12] Herbert E. Huppert and John E. Simpson. The slumping of gravity currents. *J. Fluid Mech.*, 99:785–799, 1980.

[13] T. Martonen, Z. Zhang, Y. Yang, and G. Bottei. Airway surface irregualrities promote particle diffusion in the human lung. *J. Fluid Mech.*, 59(1):5–14, 1995.

[14] Frank F. Espinosa and Roger D. Kamm. Thin Layer Flows Due to Surface Tension Gradients over a Membrane Undergoing Nonuniform, Periodic Strain. *Annals of Biomedical Engineering*, 25:913–925, 1997.

[15] Ashutosh Sharma and Rajesh Khanna. Pattern Formation in Unstable Thin Liquid Films. *Physical Review Letters*, 81(16):3463–3466, 1998.

[16] A. Sharma and E. Ruckenstein. The Role of Lipid Abnormalities, Aqueous and Mucus Deficiencies in the Tear Film Breakup, and Implications for Tear Substitutes and Contact Lens Tolerance. *Journal of Colloid and Interface Science*, 111(1):8–34, 1986.

[17] A. M. Tartakovsky, Kim F. Ferris, and P. Meakin. Lagrangian particle model for multiphase flows. *Computer Physics Communications*, 180:1874–1881, 2009.

[18] G. R. Liu and M. B. Liu. Smoothed Particle Hydrodynamics: A Meshfree Particle Method. *World Scientific Publishing Co. Inc.*, 149:135–143, 2003.

[19] J. J. Monaghan. Smoothed Particle Hydrodynamics. *Annu. Rev. Astron. Astrophysic*, 30:543–574, 1992.

[20] Jingqi Miao, Glenn J. White, M. A. Thompson, and Richard P. Nelson. An Investigation on the Morphological Evolution of Bright-Rimmed Clouds (BRCs). *The Astrophysical Journal*, 692(1):382–401, 2009.

[21] A. Ashrafi, M. A. Golozar, and S. Mallakpour. Morphological investigations of polypropylene coatings on stainless steel. *Synthetic Metals*, 156(1):1280–1285, 2006.

[22] Accessed on 22th of Febraury 2017. URL http://web.mit.edu/nnf/education/wettability/intro.html.

[23] A. Frohn and N. Roth. Dynamics of Droplets. *Springer-Verlag Berlin Heidelberg, Germany*, 2000.

[24] F. Brochard-Wyart P. G. de Gennes and D. Quere. Capillarity and Wetting Phenomena: Drops, Bubbles, Pearls Waves. springer. 2002.

[25] M. Dupeyrat and E. Nakache. 205-direct conversion of chemical energy into mechanical energy at an oil water interface. *Bioelectrochemistry and Bioenergetics*, 5(1):134–141, 1978.

[26] T. Takahashi, H. Yui, and T. Sawada. Direct observation of dynamic molecular behaviour at a water/nitrobenzene interface in a chemical oscillation system. *The Journal of Physical Chemistry B.*, 106(9):2314–2318, 2002.

[27] R. C. Weast. editor. CRC Handbook of Chemistry and Physics. CRC press. *CRC press, Boca Raton, 66th edition*, 1985.

[28] A. W. Adamson. Physical Chemistry of Surfaces. *John Wiley and Sons Inc., New York, 4th edition*, 1982.

[29] J. J. Bikerman. Physical Surfaces. *Academic Press, New York*, 1970.

[30] T. Lida and R. I. L. Guthrie. The Physical Properties of Liquid Metals. *Clarendon Press. Oxford*, 1988.

[31] Accessed on 22th of Febraury 2017. URL http://hyperphysics.phy-astr.gsu.edu/hbase/surten.html.

[32] Accessed on 4th of March 2017. URL https://en.wikipedia.org/wiki/Tears_of_wine.

[33] T. A. Ghezzehei. Constraints for flow regimes on smooth fracture surfaces. *Water Resources Research*, 40:W11503, 2004.

[34] A. Das and P. K. Das. Simulation of Drop Movement over an Inclined Surface Using Smoothed Particle Hydrodynamics. *Langmuir*, 25(19):11459–11466, 2009.

[35] J. C. Berg. Wettability. Surfactant Science Series. *Marcel Dekker Inc., New York*, 49, 1993.

[36] J. L. Moillet. Waterproofing and Water-repellency. *Elsevier, Amsterdam*, 1963.

[37] Chapter1.pdf Accessed on 18th of Febraury 2014. URL http://static.ifp.tuwien.ac.at/homepages/Personen/duenne_schichten/pdf/t_p_ds_.

[38] Accessed on 21st of Febraury 2014. URL http://www.wisegeek.com/what{-}is{-}a{-}substrate.htm.

[39] K. Seshan. Handbook of Thin-Film Deposition Processes and Techniques: Principles, Methods, Equipment and Applications, Second Edition. *William Andrew Publishing, New York, U.S.A*, (ISBN 0-8155-1442-5):707–718, 2012.

[40] P. H. Gaskel, P. K. Jimack, M. Sellier, H. M. Thompson, and M. C. T. Wilson. Gravity-driven flow of continuous thin liquid films on non-porous substrates with topography. *J. Fluid Mech.*, 509:253–280, 2004.

[41] M. M. J. Decre and J. C. Baret. Gravity-driven flows of viscous liquids over two-dimensional topographies. *J. Fluid Mech.*, 487:147–166, 2003.

[42] J. Liu, J. B. Schneider, and J. P. Gollub. Three dimensional instabilities of film flows. *Phys. Fluids*, 7:55–58, 1995.

[43] N. Didden and T. Maxworthy. The viscous spreading of plane and axisymmetric gravity currents. *J. Fluid Mech.*, 121:27–42, 1982.

[44] M. Fermigier, L. Limat, J. E. Wesfreid, P. Boudinet, and C. Quilliet. Two-dimensional patterns in Rayleigh-Taylor instability of a thin-layer. *J. Fluid Mech.*, 236:349–383, 1992.

[45] T . P. Hynes. Stability of thin films. *Ph.D. thesis, Cambridge University*, 1978.

[46] Chapter1.pdf. Accessed on 18th of February 2014. URL http://static.ifp.tuwien.ac.at/homepages/Personen/duenne_schichten/pdf/t_p_ds_.

[47] S. J. Baxter, H. Power, K. A. Cliffe, and S. Hiberd. Three-dimensional thin film flow over and around an obstacle. *Physica of Fluids*, 21:032102–23, 2009.

[48] M. G. Blyth and C. Pozrikidis. Film flow down an inclined plane over a three-dimensional obstacle. *Physics of Fluids*, 18:052104–1–14, 2006.

[49] U. Thiele and E. Knobloch. Thin liquid films on a slightly inclined heated plate. *Physica D.*, 190:213–248, 2004.

[50] S. J. VanHook, M. F. Schatz, J. B. swift, W. D. McCormick, and H. L. Swinney. Longwavelength-surface-tension-driven benard convection: Experiment and theory. *J. Fluid Mech.*, 345:45–78, 1997.

[51] A. Oron and S. G. Bankoff. Dewetting of a heated surface by an evaporating liquid film under conjoining/disjoining pressures. *J. Colloid Interface Sci.*, 218: 152–166, 1999.

[52] A. Oron and S. G. Bankoff. Dynamics of a condensing liquid film under conjoining/disjoining pressures. *Phys. Fluids*, 218:1107–1117, 2001.

[53] J. B. Grotberg. Pulmonary flow and transport phenomena. In: Lumley JL, Dyke M Van, Reed HL (eds). *Annual Reviews of Fluid Mechanics. Annual Reviews, Palo Alto, Calif.*, pages 529–571, 1994.

[54] D. A. Edwards, H. Brenner, and D. T. Wasan. Interfacial Transport Processes and Rheology. *Butterworth-Heinemann, Boston*, 1991.

[55] T. Podgorski. Dry arches within flowing films. *Phys. Fluids, doi: 10.1063/1.869956*, 11(282):845, 1999.

[56] P. G. de Gennes. Wetting: Statistics and Dynamics. *Rev. Mod. Phys.*, 57(3): 827–863, 1985.

[57] T. D. Blake and K. J. Ruschak. A maximum speed of wetting Nature. (282): 489–491, 1979.

[58] L. M. Hocking, W. R. Debler, and K. E. Cook. Three dimensional instabilities of film flows. *Phys. Fluids*, 11:307, 1999.

[59] S. Kalliadasis, C. Bielarz, and G. M. Homsy. Steady free-surface thin film flows over topography. *Physics of fluids*, 12(8):1889–1898, 2000.

[60] S. Kalliadasis and G. M. Homsy. Stability of free-surface thin-film flows over topography. *J. Fluid Mech. Cambridge University Press*, 448(8):387–410, 2001.

[61] P. Schmuki and M. Laso. On the stability of rivulet flow. *J. Fluid Mech.*, 215: 125–143, 1990.

[62] A. M. Worthington. On the forms assumed by drops of liquids falling vertically on a horizontal plate. *Proceedings of the Royal Society of London*, 25:261–272, 1876.

[63] A. M. Worthington. A second paper on the forms assumed by drops of liquids falling vertically on a horizontal plate. *Proceedings of the Royal Society of London*, 25:498–503, 1877.

[64] A. M. Worthington. A study of splashes. *Longsman, Green*, 25, 1908.

[65] Z. Levin and P. V. Hobbs. Splashing of water drops on solid and wetted surfaces: Hydrodynamics and charge separation. *Philos. Trans. R. Soc. London*, 269 (1200):555–585, 1971.

[66] A. L. Yarin and D. A. Weiss. Impact of drops on solid surfaces: self-similar capillary waves, and splashing as a new type of kinetics discontinuity. *Journal of Fluid Mechanics*, 283:141–173, 1995.

[67] S. Chandra and C. T. Avedisian. On the collision of a droplet with a solid surface. *Proceedings of the Royal Society of London*, 13(432), 1991.

[68] J. Fukai, Y. Shiiba, T. Yamamoto, O. Miyatake, D. Poulikakos, C. M. Megaridis, and Z. Zhao. Wetting effects on the spreading of a liquid droplet colliding with a flat surface: experiments and modeling. *Physics of fluids*, 7(236), 1995.

[69] J. Fukai, Z. Zhao, D. Poulikakos, C. M. Megaridis, and O. Miyatake. Modeling of the deformation of a liquid droplet impinging upon a flat surface. *Physics of fluids*, 5(2588), 1993.

[70] J. F. Gao and A. A. Sonin. Precise deposition of molten microdrops: The physics of digital microfabrication. *Proceedings of the Royal Society of London*, 444(533), 1994.

[71] N. Hatta, H. Fujimoto, and H. Takuda. Deformation process of a water droplet impinging on a solid surface. *Transactions of the ASME: Journal of Fluids Engineering*, 117(394), 1995.

[72] B. S. Dooley, A. E. Warncke, M. Gharib, and G. Tryggvason. Vortex ring generation due to the coalescence of a water drop at a free surface. *Experiments in Fluids*, 22(5):369–374, 1997.

[73] J. Shin and T. A. McMahon. The tuning of a splash. *Physics of Fluids: A*, 2 (8):1312–1317, 1990.

[74] G. B. Foote. The water drop rebound problem: dynamics of collision. *Journal of the Atmospheric Science*, 32(5):390–402, 1975.

[75] N. Hatta, H. Fujimoto, K. Kinoshita, and H. Takuda. Experimental study of deformation mechanism of a water droplet impinging on hot metalic surfaces above the leidenfrost temperature. *Transactions of the ASME: Journal of Fluids Engineering*, 119(5):692–699, 1997.

[76] T. Mao, D. C. Kuhn, and H. Tran. Spread and rebound of liquid droplets upon impact on flat surfaces. *AIChE Journal*, 43(9):2169–2179, 1997.

[77] M. Passandideh-Fard, Y. M. Qiao, S. Chandra, and J. Mostaghimi. Capillary effects during droplet impact on a solid surface. *Physics of Fluids*, 8(3):650–659, 1996.

[78] N. Savva, S. Kalliadasis, and G. A. Pavliotis. Two-dimensional droplet spreading over random topographical substrates. *Phys. Rev. Lett.*, 104(084501), 2010.

[79] B. Muller, M. Riedel, R. Michel, S. M. De Paul, R. Hofer, D. Heger, and D. Grutzmacher. Impact of nanometer-scale roughness on contact-angle hysteresis and globulin adsorption. *J. Vac. Sci. Technol. B*, 19(5):1715–1720, 2001.

[80] R. H. Dettre and R. E. Johnson. Contact angle hysteresis. II. contact angle measurements on rough surfaces. *Adv. Chem. Ser.*, 43:136–144, 1964.

[81] P. H. Gaskel, Y. Y. Koh, P. K. Jimack, M. Sellier, H. M. Thompson, and M. C. T. Wilson. Thin film flow over substrates with topography. *Presented at the 12th International Coating Science and Technology Symposium September, Rochester, New York*, pages 20–22, 2004.

[82] L. W. Schwartz and R. R. Eley. Simulation of Droplet Motion on Low-Energy and Heterogeneous Surfaces. *J. of Colloid and Interface Science*, 202(5):173–188, 1998.

[83] L. W. Schwartz. Hysteretic Effects in Droplet Motions on Heterogeneous Substrates: Direct Numerical Simulation. *Langmuir*, 14(5):3440–3453, 1998.

[84] A. Y. Malkin, I. Masalova, P. Slatter, and K. Wilson. Effect of droplet size on the rheological properties of highly-concentrated w/o emulsions. *Rheologica acta*, 43(6):584–591, 2004.

[85] G. R. Liu and M. B. Liu. Smoothed Particle Hydrodynamics. *Ed. Singapore: World Scientific Publishing Co. Pte. Ltd.*, 2009.

[86] Y. Jaluria and K. E. Torrance. Computational Heat Transfer. *2nd ed. London: Taylor & Francis*, 2003.

[87] F. B. Hildebrand. Introduction to Numerical Analysis. *McGraw-Hill, New York*, 1956.

[88] S. C. Chapra and R. P. Canale. Introduction to Numerical Analysis. *McGraw-Hill, New York*, 1988.

[89] J. Meek. A brief history of the beginning of the finite element method. *International Journal for Numerical Methods in Engineering*, 39:3761–3774, 1996.

[90] J. Argyris. Numerical Methods in Engineering. *Int. J. Numer. Meth. Engng.*, 60:1633–1637, 2004.

[91] R. W. Clough. The finite element in plan stress analysis. *In: Proceedings of the 2nd ASCE Conference on Electronic Computation, Pittsburgh, PA*, 1960.

[92] R. L. Courant. The Finite-Element Method, Part 1:. *IEEE Antennas and Propagation Magazine*, 49(2), 2007.

[93] O. C. Zienkiewicz. The birth of the finite element method and of computational mechanics. *Int. J. Numer. Meth. Engng.*, 60:3–10, 2004.

[94] J. Fish and T. Belytschko. A First Course in Finite Elements. *Chichester: John Wiley & Sons Ltd*, 2007.

[95] J. R. LeVeque. Finite Volume Methods for Hyperbolic Problems. *Cambridge University Press, United Kingdom*, 2002.

[96] E. F. Toro. Riemann Solvers and Numerical Methods for Fluid Dynamics: A Practical Introduction. *Third Edition, Springer, London New York*, 1999.

[97] R. Eymard, T. Gallouet, and R. Herbin. Finite Volume Methods. *Marseille*, 2003.

[98] L. B. Lucy. A numerical approach to the testing of the fission hypothesis. *The Astronomical Journal*, 82(12), 1977.

[99] R. A. Gingold and J. J. Monaghan. Smoothed Particle Hydrodynamics: Theory and application to non-spherical stars. *Royal Astronomical Societyl, Monthly Notices*, 181:375–389, 1977.

[100] D. Violeau. Fluid Mechanics and the SPH Method: Theory and Applications. *Oxford University Press, United Kingdom, ISBN*, 2012.

[101] J. P. Morris, P. J. Fox, and Yi Zhu. Modeling Low Reynolds Number Incompressible Flows Using SPH. *Journal of Computational Physics*, (136):214–226, 1997.

[102] K. Szewc, K. Walczewska-Szewc, and M. Olejnik. Is the motion of a single SPH particle droplet/solid physically correct? *Computational Physics (arXiv:1602.07902v1)*, 25 Feb 2016 .

[103] L. D. G. Sigalotti, H. López, and L. Trujillo. An adaptive SPH method for strong shocks. *Journal of Computational Physics*, 228:5888–5907, 2009.

[104] S. J. Cummins and M. Rudman. An SPH projection method. *J. Comput. Phys.*, 152:584–607, 1999.

[105] S. Shao and E. Lo. Incompressible SPH method for simulating Newtonian and non-Newtonian flows with free surface. *Advances in Water Resources*, 26:787–800, 2003.

[106] R. Xu. An Improved Incompressible Smoothed Particle Hydrodynamics Method and Its Application in Free-Surface Simulations. *Ph.D., University of Manchester*, 2009.

[107] J. J. Monaghan. Simulating free surface flows with SPH. *Journal of Computational Physics*, 110:399–406, 1994.

[108] J. W. Swegle. SPH behavior in tension. *Memo*, 110, 13th August 1992.

[109] W. Benz and E. Asphaug. Explicit 3D continuum fracture modeling with Smoothed Particle Hydrodynamics. *In Proceedings of Twenty-fourth Lunar and Planetary Science Conference*, pages 99–100, 1993.

[110] R. Di Lisio, Istituto Astronomico, E. Grenier, and M. Pulvirenti. The Convergence of the SPH Method. *Computers Math. Applic.*, 35(1/2):95–102, 1998.

[111] B. B. Moussa. On the convergence of SPH method for scalar conservation laws with boundary conditions. *Methods and Applications of Analysis*, 13(1):029–062, 2006.

[112] J. J. Monaghan. Why Particle Method Work. *SIAM J. SCI. STAT. COMPUT.*, 3(4):422–433, 1982.

[113] D. Wood. Collapse and fragmentation of isothermal gas clouds. *Mon. Not. R. Astr. Soc.*, 194:201–218, 1981.

[114] G. V. Bicknell. Tthe Equation of Motion of Particles in Smoothed Particle Hydrodynamics. *SIAM J. SCI. STAT. COMPUT.*, 12(5):1198–1206, 1991.

[115] P. W. Randles and L. D. Libersky. Smoothed Particle Hydrodynamics: Some recent improvements and applications. *Comput Methods Appl Mech Engrg*, 139 (1):375–408, 1996.

[116] J. Pozorski and A. Wawrenczuk. SPH computation of incompressible viscous flows. *Journal of Theoretical and Applied Mechanics*, 40(4):917–937, 2002.

[117] M. Ellero, M. Serran, and P. Espanol. Incompressible smooth particle hydrodynamics. *Journal of Computational Physics*, 226:1731–1752, 2007.

[118] X. Y. Hu and Adam. An incompressible mult-iphase SPH method. *Journal of Computational Physics*, 227:264–278, 2007.

[119] X. Y. Hu and Adam. A constant density approach for incompressible multiphase SPH. *Journal of Computational Physics*, 228:2082–2091, 2009.

[120] R. H. Durisen, R. A. Gingold, and A. P. Boss. Dynamic Fission Instabilities in Rapidly Rotating $n=\frac{3}{2}$ Polytropes: A Comparision of Results from Finite-difference and Smoothed Particle Hydrodynamics Codes. *The Astronimical Journal*, (305):281–308, 1986.

[121] P. Berezik. Modeling the star formation in galaxies using the chemodynamical SPH code. *Astronomy and Astrophysics*, (360):76–84, 2000.

[122] P. Berezik and I. G. Kolesnik. Smoothed Particle Hydrodynamics and its applications to astrophysical problem. *Kinematics and Physics of Celestial Body*, (9):1–11, 1993.

[123] P. Berezik and I. G. Kolesnik. Gas dynamical model for the triaxial protogalaxy collapse. *Astronomy and Astrophysical Transactions*, (16):163–185, 1998.

[124] J. J. Monaghan and J. C. Lattanzio. A simulation of the collapse and fragmentation of cooling molecule clouds. *The Astronomical Journal*, (375):177–189, 1991.

[125] A. E. Evrad. Beyond N-body: 3D cosmological gas dynamics. *Astronomical Soc*, (235):911–931, Mon. Not. R 1988.

[126] P. R. Shapiro, H. Martel, J. V. Villumen, and J. Owen. Adaptive Smoothed Particle Hydrodynamics with Application to Cosmology: Methodology. *The Astronomical Journal*, (103):269–330, 1996.

[127] J. J. Monaghan. Modelign the universe. *In Proceedings of the Astronomical Society of Australia*, (18):233–237, 1990.

[128] W. Benz. Smoothed Particle Hydrodynamics: A review, Numerical Modeling of Stellar Pulsation: Problems and Prospects. *In Proceedings of Nato Workshop, Les Arcs, France*, page 269, 1989.

[129] W. Benz. Applications of Smoothed Particle Hydrodynamics SPH to Astrophysical Problems. *Computer Physics Communications*, (48):130–139, 1988.

[130] W. Benz. Smoothed Particle Hydrodynamics: A review, Numerical Modeling of Nonlinear Stellar Pulsation: Problems and Prospects Kluwer Acad. *Boston Publ*, pages 269–288, 1990.

[131] J. Faber and F. A. Rasio. Post Newtonian SPH Calculations of Binary Neutron Stars Coalescence, Methods and First Results. *Physical Review D.*, (62):1–23, 2000.

[132] J. Faber and J. B. Manor. Post Newtonian SPH Calculations of Binary Neutron Stars Coalescence, II Mass-Ratio, equation of state and spin and First Results. *Physical Review D.*, (63):1–16, 2001.

[133] A. R. Frederic and C. L. James. Smoothed Particle Hydrodynamics calculations of stellar interactions. *Journal of Computational and Applied Mathematics*, (109):213–230, 1999.

[134] M. Herant and W. Benz. Hydrodynamical instabilities and mixing in SN1987A-Two-dimensional simulations of the first 3 months. *The Astronomical Journal*, 370:81–84, 1991.

[135] M. Nagasawa, T. Nakamura, and S. M. Miyama. Three-dimensional hydrodynamical simulations of type II supernova - Mixing and fragmentation of ejecta. *Astronomical Society of Japan*, 40:691–708, 1988.

[136] J. J. Monaghan and A. Kos. Solitary Waves on a Cretan Beach. *J. Waterway Port, Coastal and Ocean Engineering*, 125:145–154, 1999.

[137] J. J. Monaghan and A. Kos. Scott Russells Wave Generator. *Physics of Fluids*, 12:622–630, 2000.

[138] J. J. Monaghan. Gravity currents and solitary waves. *Physica D*, 98:523–533, 1996.

[139] J. J. Monaghan, R. F. Cas, A. Kos, and Hallworth. Gravity currents descending a ramp in a stratified tank. *Journal Fluid Mechanics*, 379:39–70, 1999.

[140] J. K. Chen, J. E. Beraun, and T. C. Carney. A corrective Smoothed Particle Hydrodynamic Method for boundary value problems in heat conduction. *Computer Methods in Applied Mechanics and Engineering*, 46:231–252, 1999.

[141] J. W. Swegle and S. Attaway. On the feasibility of using Smoothed Particle Hydrodynamics for underwater explosion calculation. *Computational Mechanics*, 17:151–168, 1995.

[142] G. J. Philips and J. J. Monaghan. Anumericla method for three-dimensional simulations of collapsing, isothermal, magnetic gas clouds. *Astr. Soc*, 216:883–895, 1985.

[143] R. F. Stellingwerf and R. E. Peterkin. Smooth Particle Magnetohydrodynamics. *Technical report, Albuquerque: Mission Res*, 1990.

[144] A. Habe. Status rep. super computing Japan. *Ed. T. Nakamura, M. Nagasawa National Lab. High Energy Phys.*

[145] G. R. Johnson, R. A. Stryk, and S. R. Beissel. SPH for high velocity impact computations. *Comput Methods Appl Mech Engrg*, 139(1–4):347–373, 1996.

[146] W. Benz and E. Asphaug. Impact simulationwith fracture. *I. Methods and tests*, 107:98–116, 1994.

[147] J. Bonet and S. Kuasegaram. Corrections and stabilization of Smooth Partilce Hydrodynamics methods with applications in metal forming simulations. *International Journal for Numerical Methods in Engineering*, 47:1189–1214, 2000.

[148] W. Benz and E. Asphaug. Simulation of brittle solids using Smooth Particle Hydrodynamics. *Computer Physics Communications*, 87:253–265, 1995.

[149] K. Szewc, J. Pozorskia, and J. P. Minierb. Analysis of the incompressibility constraint in the Smoothed Particle Hydrodynamics Method Physics. *flu-dyn with Preprint submitted to Elsevier on the 27th October*, 2011.

[150] J. U. Brackbill, D. B. Kothe, and C. Zemach. A continuum method for modelling surface tension. *J. Comput. Phys.,*, (100):335–354, 1992.

[151] S. Nugent and H. A. Posch. Liquid drops and surface tension with smoothed particle applied mechanics. *Phys. Rev. E.*, 62(4):4968–4975, 2000.

[152] A. M. Tartakovsky and P. Meakin. Modeling of surface tension and contact angles with Smoothed Particle Hydrodynamics. *PHYSICAL REVIEW E 72*, (026301), 2005.

[153] M. Muller, D. Charypar, and M. Gross. Particle-Based Fluids Simulation for inter-active Applications. *Eurographics/SIGGRAPH Symposium on Computer Animation*, pages 154–372, 2003.

[154] H. Lopez and L. D. G. Sigalotti. Oscillation of viscous drops with Smoothed Particle Hydrodynamics. *Physical Review E*, 73:051201, 2006.

[155] N. Akinci, G. Akinci, and M. Teschner. Versatile Surface Tension and Adhesion for Smoothed Particle Hydrodynamics Fluids. *ACM Transactions on Graphics TOG-Proceedings of ACM SIGGRAPH Asia*, 32, 2013.

[156] F. Macia, M. Antuono, and A. Colagrossi. Benefits of using a Wendland kernel for free-surface flows. *6th International SPHERIC workshop, Hamburg, Germany*, 2011.

[157] D. A. Fulk. A Numerical Analysis of Smoothed Particle Hydrodynamics, PhD thesis, School of Engineering Air University. 1994.

[158] G. R. Liu and M. B. Liu. Smoothed Particle Hydrodynamics: An Overview and Recent Developments. *Archives Computationa Methods Engineering*, 17 (1):25–76, 2010.

[159] Jiannong Fang, Aurèle Parriaux, Martin Rentschler, and Christophe Ancey. Improved SPH methods for simulating free surface flows of viscous fluids. *Applied Numerical Mathematics*, 59:251–271, 2009.

[160] J. J. Monaghan. Smoothed Particle Hydrodynamics. *Rep. Prog. Phys.*, (1703–1759), 2005.

[161] J. J. Monaghan and J. C. Lattanzio. A refined particle method for astrophysical problems. *Astronomy and Astrophysics*, 149(1):135–143, 1985.

[162] G. R. Johnson and S. R. Beisse. Normalized smoothing functions for SPH impact computations. *Int J. Numer Methods Eng.*, 39(16):2725–2741, 1996.

[163] A. Panizzo, T. Capone, and R. A. Dalrymple. Accuracy of kernel derivatives and numerical schemes in SPH. *Submitted to Journal of Computational Physics*, 2007.

[164] J. P. Morris. A study of the stability properties of SPH. *Applied Mathematics Report and Preprints, Monash University*, 1994.

[165] J. P. Morris. Analysis of Smoothed Particle Hydrodynamics with Applications. *PhD thesis, Department of Mathematics Monash University*, 1996.

[166] J. Monaghan. An introduction to SPH. *Computer Physics Communications*, 48 (1):89–96, January 1988.

[167] J. Bonet and T. S. L. Lok. Variational and momentum preservation aspects of Smooth Partilce Hydrodynamics formulations. *Computer Methods in Applied Mechanics and Engineering*, 180:97–115, 1999.

[168] Accessed on 28th of February, 2014. URL http://en.wikipedia.org/wiki/Derivation_of_the_Navier%E2%80%93Stokes_equations.

[169] S. Barbara. Incompressible fluid simulation and advanced surface handling with SPH. *PhD thesis, Faculty of Economics, Business Administration and Information Technology. The University of Zurich: Zurich*, 2010.

[170] J. K. Chen, J. E. Beraun, and C. J. Jih. An improvement for tensile instability in Smoothed Particle Hydrodynamics. *Comput Mech*, 23(4):279–287, 1999.

[171] J. K. Chen and J. E. Beraun. A generalized Smoothed Particle Hydrodynamics method for nonlinear dynamic problems. *Comput Methods Appl Mech Engrg*, 23(4):225–239, 2000.

[172] A. Ferrari, M. Dumbser, E. F. Toro, and A. Armanini. A new 3D parallel SPH scheme for free-surface flows. *Computers and Fluids*, 38:1203–1217, 2009.

[173] A. Mahdavi and N. Talebbeydokhti. A hybrid solid boundary treatment algorithm for Smoothed Particle Hydrodynamics SPH. *Scientia Iranica*, 22:1457–1469, 2015.

[174] Z. Mingyn. Smoothed Particle Hydrodynamics in Materials Processing, Code Delopment and Applications, PhD thesis, Mechanical Engineering, Stony Brook Univeristy, May. 2007.

[175] J. J. Monaghan. Heat conduction with discontinuous conductivity. *Applied Mathematics Report and Reprint, Monash University*, page 18, 1995.

[176] J. J. Monaghan and R. A. Gingold. Shock simulation by the particle method SPH. *J. Comput. Phys.*, 52:374–89, 1983.

[177] G. K. Batchelor. Introduction to fluid dynamics. *Cambridge University Press*, 1974.

[178] A. Mokos. Multi-phase Modelling of Violent Hydrodynamics Using Smoothed Particle Hydrodynamics (SPH) on Graphics Processing Units (GPUs). *PhD thesis, School of Mechanical, Aerospace and Civil Engineering. The University of Manchester: Manchester*, 2013.

[179] S. J. Lind, R. Xu, P. K. Stansby, and B. D. Rogers. Incompressible Smoothed Particle Hydrodynamics for free-surface flows: A generalised diffusion-based algorithm for stability and validations for impulsive flows and propagating waves. *Journal of Computational Physics*, 231:1499–1523, 2012.

[180] A. J. Chorin. Numerical solution of the Navier-Stokes equations. *Mathematics of Computation*, 22:745–762, 1968.

[181] A. Khayyer, H. Gotoh, and S. D. Shao. Corrected incompressible SPH method for accurate water-surface tracking in breaking waves. *Coastal Engineering*, 55: 236–250, 2008.

[182] Jon Louis Bentley. Kd -Trees for Semidynamic Point Sets. *AT&T Bell Laboratories, SCG 90 Proceedings of the sixth annual symposium on Computational geometry*, (ISBN:0-89791-362-0):187–197, 1990.

[183] J. J. Monaghan. On the problem of penetration in particle methods. *Journal of Computational Physics*, 82:1–15, 1989.

[184] J. Kordilla. Flow transport in saturated and unsaturated fractured porous media: Development of Particle-based modelling approaches. PhD, Georg-August-Universitat Gottingen. 2009.

[185] Accessed on 9th of April 2014. URL http://en.wikipedia.org/wiki/Explicit_and_implicit_methods.

[186] William H. Press, Saul A. Teukolsky, William T. Vetterling, and Brian P. Flannery. Numerical Recipes in C, The Art of Scientific Computing, Second Edition. *Cambridge University Press, New York*, (ISBN 0-521-43108-5):707–718, 1988 1992.

[187] Loup Verlet. "Computer "Experiments" on Classical Fluids. I. Thermodynamical Properties of Lennard-Jones Molecules". *Physical Review*, 159:98–103, 1967. URL http://link.aps.org/doi/10.1103/PhysRev.159.98.

[188] Piet Hut, Jun Makino, and Steve McMillan. Building a better leapfrog. *The Astronomical Journal, April 20*, 443:93–96, 1995.

[189] Piet Hut, Yoko Funato, Junichiro Makino, and Steve McMillan. Time Symmetrization Meta-Algorithms: 12th "Kingston meeting". *Computational Astrophysics, ASP Conference Series*, 123, 1997.

[190] Rusty Rook, Mehmet Yildiz, and Sadik Dost. Modelling Transient Heat Transfer Using SPH and Impilcit Time Integration. *Numerical Heat Transfer, Part B: Fundamental: An International Journal of Computation and Methodology*, (51):1–23, 2007.

[191] Tuncer Cebeci. Convective Heat Transfer. *Springer*, (ISBN 0-9668461-4-1), 2002.

[192] J. Crank and P. Nicolson. A practical method for numerical evaluation of solutions of partial differential equations of the heat conduction type. *Proc. Camb. Phil. Soc.*, 43(1):50–67, 1947.

[193] Courant R., Friedrichs K., and Lewy H. (English 1956). On the Partial Difference Equations of Mathematical Physics. *AEC Computing and Applied Mathematics Centre, AEC Research and Development Report, , New York, NYO7689*, 1928.

[194] P. W. Cleary and J. J. Monaghan. Conduction Modelling Using Smoooth Particle Hydrodynamics. *J. Comput. Phys.*, 148:235–236, 1999.

[195] Lv Cunjing. Wetting states of two-dimensional drops under gravity. *arXiv:1705.03548v2 [physics.flu-dyn] with Preprint submitted to Elsevier on the 1st June*, 2017.

[196] A. J. C. Crespo, M. Gmez-Gesteira, and Robert A. Dalrymple. Boundary conditions generated by dynamic particles in SPH methods. *CMC-TECH SCIENCE PRESS-*, 5(3):173, 2007.

[197] Y. Zhu, P. J. Fox, and J. P. Morris. A pore-scale numerical model for flow through porous media. *International Journal for Numerical and Analytical Methods in Geomechanics*, (23):881–904, 1999.

[198] S. Adami, X. Y. Hu, and N. A Adams. A transport-velocity formulation for smoothed particle hydrodynamics. *Journal of Computation Physics*, (241):292–307, 2013.

[199] A. Leroy, D. Violeau, M. Ferrand, and C. Kassiotis. Unified semi-analytical wall boundary conditions applied to 2D incompressible SPH. *Journal of Computation Physics, Elsevier*, (261):106–129, 2014.

[200] B. D. Rogers. 3rd benchmark test: 2-D lid-driven flow without gravity,. *Spheric Community*, 2006. URL http://wiki.machester.ac.uk/spehric/.

[201] U. Ghai, K. Ghai, and C. Shin. High-Re Soolutions for incompressible flow using the Navier-Stokes equations and a multigrid method. *Journal of Computation Physics*, 48(3):387–411, 1982.

[202] S. Koshizuka and Y. Oka. Moving-particle semi-implicit method for fragmentation of compressible fluid. *Nuclear Science Engineering*, 123:421–434, 1996.

[203] D. Violeau and R. Issa. Numerical Modelling of Complex Turbulent Free-Surface Flows with SPH Method: An Overview. *Int. J. Numer. Meth. Fluid*, 53:277–304, 2006.

[204] W. Dehnen and H. Aly. Improving convergence in smoothed particle hydrodynamics simulations without pairing instability. *Mon. Not. R. Astron. Soc.*, (425):1068–1082, 2012.

[205] J. P. Hunter. Surface tension in Smoothed particle hydrodynamics. *Honours thesis. Math. Dep., Monash Univ.*, 1992.

[206] P. Meakin and A. M. Tartakovsky. A Smoothe Particle Hydrodynamics model for miscible flow in three-dimensional fractures and the two-dimensional Rayleigh-taylor instability. *J. Comput. Phys.*, 2005.

[207] A. M. Tartakovsky and A. Panchenko. Pairwise force Smoothed Particle Hydrodynamics model for multiphase flow: surface tension and contact angles line dynamics. *Journal of Computational Physics*, 305:1119–1146, 2015.

[208] J. P. Morris. Simulating surface tension with smoothed particle hydrodynamics. *Int. J. Numer. Meth. Fluids,*, 33(3):333–353, 15 th June 2000.

[209] E. Lee, C. Mouline, R. Xu, D. Violeau, D. Laurence, and P. Stansby. Comparisons of weakly compressible and truly incompressible algorithms for the SPH mesh free particle method. *Journal of Computation Physics*, 227(18):8417–8436, 2008.

[210] S. Adami, X. Y. Hu, and N. A. Adams. A new surface-tension formulation for multi-phase sph using a reproducing divergence approximation. *Journal of Computation Physics*, 229:5011 – 5021, 2010.

[211] M. Zhang. Simulation of surface tension in 2D and 3D with smoothed particle hydrodynamics method. *J. of Comp. Phys.*, 229:7238–7259, 2010.

[212] S. Chandrasekhar. The oscillations of a viscous liquid globe. *Proc. Lond. Math. Soc.*, 9:141–149, 1959.

[213] S. Chandrasekhar. Hydrodynamic and Hyrdromagnetic Stability. *Clarendon*, pages 466–477, 1961.

[214] W. H. Reid. The oscillations of a viscous liquid drop. *Q. Appl. Maths*, 18:86–89, 1960.

[215] A. Prosperetti. Viscous effects on perturbed spherical flows. *Q. Appl. Maths*, 35:339–352, 1977.

[216] A. Prosperetti. Normal-mode analysis for the oscillations of a viscous liquid drop immersed in another liquid. *J. Mec.*, 19:149–182, 1980a.

[217] A. Prosperetti. Tree oscillations of drops and bubbles: the initial-value problem. *J. Fluid, Mech.*, 100:333–347, 1980b.

[218] R. S. Valentine, N. F. Sather, and W. J. Heideger. The motion of drops in various media. *Chem. Engng Sci.*, 20:719–728, 1965.

[219] M. Strani and F. Sabetta. Viscous oscillations of a supported drop in an immiscible fluid. *J. Fluid, Mech.*, 189:397–421, 1988.

[220] Lord Rayleigh. On the capillary phenomena of jets. *Proc. R. Soc. Lond.*, 29: 71–97, 1879.

[221] H. Lamb. Hydrodynamics. 6th edn. *Cambridge University Press*, 29:473–475, 1932.

[222] N. Ashgriz and M. Movassat. Handbook of Atomization and Sprays Theory and Applications. *Springer New York Dordrecht Heidelberg London, ISBN978-1-4419-7263-7*, page 125, 2011.

[223] R. E. Apfel, Y. Tian, J. Jankovsky, T. Shi, X. Chen, R. Glynn Holt, E. Trinh, A. Croonquist, K. C. Thornton, A. Sacco, C. Coleman, F. W. Leslie, and D. H. Matthiesen. Free Oscillations and Surfactant Studies of Superdeformed Drops in Microgravity. *Physical Review Letters*, pages 78–10, 1997.

[224] Accessed on 22nd of February 2017. URL https://en.wikipedia.org/wiki/Contact_angle#Typical_contact_angles.

[225] W. Barthlott and C. Neinhuis. Purity of the sacred lotus, or escape from contamination in biological surfaces. *Planta*, 202:1–8, 1997.

[226] T. Young. Philosophical transactions of the royal society of London. 1805.

[227] G. Zhou, W. Ge, and J. Li. A revised surface tension model for macro-scale particle methods. *Powder Technology*, 183:21–26, 2008.

[228] J. Kordilla, A.M. Tartakovsky, and T. Geyer. Aj Smoothed Particle Hydrodynamics Model for droplet and film flow on smooth and rough fracture surfaces. *Advances in Water Resources*, 59:1–14, 2013.

[229] M. Huber, F. Keller, W. Sackel, M. Hirschler, and P. Kunz. On the physically based modelling of surface tension and moving contact lines with dynamics contact angles on the continuum scale. *Journal of Computational Physics*, 310: 459–477, 2016.

[230] V. S. Mitlin. On dewetting conditions. *Colloid Surf. A*, 89:97–101, 1994.

[231] B. V. Deryagin. *Kolloidn Zh*, 17:191, 1995.

[232] G. F. Teletzke. Thin liquid films: molecular theory and hydrodynamic implications. *PhD Thesis Submitted to the University of Minnesota*, 1983.

[233] M. Sellier. The Numerical Simulation of Thin Film Flow over Heterogeneous Substrates. *PhD Thesis Submitted to the University of Leeds*, 2003.

[234] P. Ehrhard and S. H. Davis. Non-isothermal spreading of liquid drops on horizontal plates. *J. Fluid Mech.*, 229:365–388, 1991.

[235] N. V. Churaev and V. D. Sobolev. Prediction of contact angle on the basis of the frumkin-derjaguin approach. *Adv. Colloid Interface Sci.*, 61:1–16, 1995.

[236] V. S. Mitlin and N. V. Petviashvili. Nonlinear dynamics of dewetting-kinetically stable structures. *Phys. Lett. A*, 192:323–326, 1994.

[237] L. H. Tanner. The spreading of silicone oil drops on horizontal surface. *Journal of Physics D: Applied Physics*, 12:1473–1984, 1979.

[238] M. D. Lelah and A. Marmur. Spreading kinetics of drops on glass. *Journal of Colloid and Interface Science*, 82:518–525, 1981.

[239] R. E. Johnson and R. H. Dettre. Wetting of low energy surfaces. In: Berg. J. C. (Ed.), Wettability. pages 1–74.

[240] L. Feng, S. Li, Y. Li, H. Li, L. Zhang, J. Zhai, Y. Song, B. Liu, L. Jiang, and D. Zhu. "Superhydrophobic surfaces: from natural to artificial". *Advanced materials*, 14:1857, 2002.

[241] R. Blossey. "Self-cleaning surfaces-virtual realities". *Nature Materials*, 2:301, 2003.

[242] Thermal Analysis & Surface Solution GmbH. Accessed on 8th June 2017. URL http://thass.net.

[243] H. P. Greenspan. On the motion of a small viscous droplet that wets a surface. *Journal of Fluid Mechanics*, 84:125–143, 1978.

[244] C. D. Bain and G. M. Whitesides. A study of contact angle of the acid-base behaviour of monolayers containing w-mercaptocarboxylic acids adsorbed on gold: An example of reactive spreading. *Langmuir*, 5:1370–1378, 1989.

[245] M. K. Chaudhury and G. M. Whitesides. How to make water run uphill. *Science*, 256:1539, 1992.

[246] L. Gao and T. J. McCarthy. Contact Angle Hysteresis Explained. *Langmuir*, 22:6234–6237, 2006.

[247] W. Nusselt. Die Oberflachenkondensation des Wasserdampfes. *Z. Verein deutscher Ingenieure*, 60:541, 1916.

[248] D. E. Hartley and W. Murgatroyd. Criteria for the break-up of thin liquid layers flowing isothermally over solid surfaces. *J. Heat Mass Transfer*, 7:1003–1015, 1964.

[249] S. G. Bankoff. Minimum thickness of a draining film. *J. Heat Mass Transfer*, 14:2143–2146, 1971.

[250] J. Mikielewicz and J. R. Moszynski. Minimum thickness of a liquid film flowing vertically down a solid surface. *J. Heat Mass Transfer*, 14:771–776, 1976.

[251] T. Hobler and J. Czajka. Minimum wetting rate of a flat surface. *Chemia Stosow*, 2B:169–186, 1968.

[252] T. Munakata, K. Watanabe, and K. Miyashita. Minimum wetting rate on wetted-wall column. correlation over wide range of liquid viscosity. *J . Chem. Engng Japan*, 8(6):440–444, 1975.

[253] G. D. Towell and L. B. Rothfeld. Hydrodynamics of rivulet flow. *AIChE J*, 12 (5):972, 1966.

[254] J. Kern. Zur hydrodynamik der rinnsale. *Verfahrenstechnik*, 3(10):425–430, 1969.

[255] T. Nakagawa and J. C. Scott. Stream meanders on a smooth hydrophobic surface. *J . Fluid Mech.*, 149:89–99, 1984.

[256] A. Doniec. Laminar flow of a liquid down a vertical solid surface. Maximum thickness of liquid rivulet. *PhysicoChem. Hydrodyn*, 5(2):143–152, 1984.

[257] V. E. B. Dussan. On the ability of drops or bubbles to stick to non-horizontal surfaces of solids. Part 2. small drops of bubbles having contact angles of arbitrary size. *J. Fluid Mech.*, 151:1–20, 1985.

[258] W. F. Tanner. Helicoidal flow, a possible cause of meandering. *J. Geophys. Res.*, 63(3):993, 1960.

[259] M. A. Gorycki. Hydraulic drag: a meander-initiating mechanism. *Bull. Geol. Soc. Am.*, 84:175–186, 1973.

[260] T. Podgorski, J. M. Flesselles, and L. Limat. Corners, Cusps, and Pearls in Running Drops. *Physical Review Letters*, 87(3), 2001.